Design of the Micro Vertex Detector of the CBM experiment: Development of a detector response model and feasibility studies of open charm measurement

Dissertation zur Erlangung des Doktorgrades
der Naturwissenschaften

vorgelegt beim Fachbereich Physik
der Johann Wolfgang Goethe - Universität
in Frankfurt am Main

Thèse presentée pour obtenir le grade de Docteur
de l'Université de Strasbourg

Discipline: Physique

Christina Anna Dritsa
aus/née à Athènes

Frankfurt/Strasbourg (2011)
(D30)

Vom Fachbereicht Physik der
Johann Wolfgang Goethe - Universität als Dissertation angenommen.

Dekan: Prof. D.-H. Rischke

Gutachter:
Dr. habil. F. Rami, Institut Pluridisciplinaire Hubert Curien, Strasbourg
Prof. Dr. P. Senger, Goethe Universität, Frankfurt am Main

Contents

List of Figures

List of Tables

Deutsche Zusammenfassung

Einführung

Das Compressed Baryonic Matter Experiment (CBM) ist eines der zentralen Experimente der zukünftigen, internationalen Facility for Antiproton and Ion Research (FAIR), das zurzeit in Darmstadt aufgebaut wird. Das Fixed-Target Schwerionenexperiment mit einer Strahlenergie von 10 bis 45 $AGeV$ dient dazu, das Phasendiagramm der Kernmaterie im Bereich höchster baryonischer Dichten und moderater Temperaturen zu untersuchen. Dieser Bereich ist zum gegenwärtigen Zeitpunkt sowohl im Hinblick auf experimentelle Daten als auch im Hinblick auf ein theoretisches Verständnis weitgehend unerschlossen. Besondere wissenschaftliche Schwerpunkte liegen in der Suche nach dem postulierten Phasenübergang erster Ordnung zwischen der hadronischen und der partonischen Materie, nach dem kritischen Punkt des Phasendiagramms, nach Anzeichen für die vorhergesagte Wiederherstellung der Chiralen Symmetrie, exotischen Materieformen und die Vermessung der Zustandsgleichung der Kernmaterie.

Das verbesserte Verständnis im Hinblick auf die Struktur und der Eigenschaften der durch die Schwerionenstöße erzeugten Feuerbälle soll dazu dienen, die Theorie der starken Wechselwirkung zu testen. Darüber hinaus wird vermutet, dass die Ergebnisse zur Modellbildung im Hinblick auf die Eigenschaften von kompakten Astrophysikalischen Objekten wie zum Beispiel Neutronensternen beitragen können.

Open-Charm-Teilchen (d.h. Teilchen mit einem Charm-Quark) gehören zu den entscheidenden Sonden, die im CBM-Experiment zum Einsatz kommen sollen. Man erwartet dass die Produktion und der Transport dieser Teilchen während der Schwerionenkollision sollten besonders sensibel auf Veränderungen der Dichte der Kernmaterie sowie auf einen Phasenübergang zu partonischer Materie reagieren. Darüber hinaus wird erwartet, dass die Masse dieser Teilchen im nuklearen Medium verändert wird, wodurch sich auch ihre Produktionswirkungsquerschnitte ändern. Dieser Effekt sollte im Energiebereich von FAIR besonders ausgeprägt sein, da hier die für die Teilchenproduktion verfügbare Energie nur wenig über dem notwendigen Minimum liegt. Nicht zuletzt wurde eine Sprung in der relativen Produktionsrate von D-Mesonen und Charmonium als eine starke Signatur für einen Phasenübergang von normaler hadronischer Materie zum Quark-Gluon-Plasma

(QGP) vorgeschlagen, wodurch der erwartete Phasenübergang im Energiebereich von FAIR nachgewiesen werden könnte.

Fragestellung:

Das CBM-Experiment hat es sich zur Aufgabe gestellt, erstmals Open-Charm-Teilchen, die im Feuerballs einer Schwerionenkollision bei Strahlenergien von $10 - 45\ AGeV$ erzeugt wurden, nachzuweisen. Um bei dieser geringen Energie eine hinreichende Zahl dieser Teilchen zu erzeugen, wird ein besonders intensiver Ionenstrahl und eine hohe Kollisionsrate benötigt. Dies wird durch den hohen Strahlstrom des SIS-300 Beschleunigers von FAIR sichergestellt, der einen Strahl mit bis zu 10^9 Schwerionen (Au) pro Sekunde zur Verfügung stellt. Um die Open-Charm-Teilchen vor dem komplexen Hintergrund des zerfallenden Feuerballs zu rekonstruieren, wird ein neuartiger, hochpräziser und äußerst leichter Vertexdetektor benötigt. Dieser soll die Open-Charm-Teilchen durch Identifikation und Abgrenzung der Zerfallsvertices vom primären Kollisionsvertex identifizieren. Die messtechnische Herausforderung besteht darin, die Abgrenzung der Vertices trotz der kurzen Flugstrecke der Open-Charm-Teilchen (einige 100 μm im Laborbezugssystem) zuverlässig umzusetzen. Wegen der niedrigen Produktionswirkungsschnitte der Teilchen muss der Detektor hierfür gleichzeitig sehr ratenfest sein und die für die Hintergrundunterdrückung notwendige, extreme Sensitivität aufweisen.

Um diese technologisch widersprüchlichen Ziele zu erreichen, wird ein hoch präziser, extrem leichter, strahlenharter und schneller Mikrovertexdetektor (MVD) benötigt. Dieser soll auf Basis der Monolithic Active Pixel Sensoren (MAPS) umgesetzt werden. Diese neuartigen Pixel sind besonders dünn ($< 0.05\%\ X0$) und vermessen Teilchenbahnen mit einer ungewöhnlich präzisen Ortsauflösung von nur wenigen Mikrometern. Um den Anforderungen im Hinblick auf die Ratenfestigkeit gerecht zu werden, wurden ihre Strahlenhärte und Auslesegeschwindigkeit wurden in den letzten Jahren kontinuierlich gesteigert. Hierdurch wurde eine Zeitauflösung von 100 μs und eine Toleranz gegen eine nicht-ionisierende Strahlung von $10^{13}\ n_{eq}/cm^2$ erreicht. Weitere Verbesserungen sind bis zur Konstruktionsphase des MVD absehbar. Die Auslesezeit der Sensoren sollte bis dahin um einen Faktor 3 auf 30 μm reduziert werden und absehbar dürfte eine Strahlentoleranz von $10^{14}\ n_{eq}/cm^2$ erreicht werden.

Die vorliegende Doktorarbeit leistet einen Beitrag zur Entwicklung eines Designkonzeptes für den MVD. Sie prüft ob das derzeit favorisierte Konzept des MVD geeignet ist, die gestellte Messaufgabe zu lösen. Um diese Frage mit Hilfe von Detektorsimulationen zu beantworten, wurden im Rahmen dieser Arbeit das Ansprechverhalten eines MAPS-Prototypen systematisch vermessen und auf Basis von Messdaten ein Simulationsmodell für MAPS entwickelt. Nachfolgend die Teilchenrekonstruktion simuliert.

Charakterisierung der Sensoren:

Grundsätzlich war das Ansprechverhalten von MAPS, die von geladene Teilchen getroffen werden, bereits im Vorfeld dieser Arbeit wohlbekannt. Allerdings beschränkten sich die meisten Studien auf einen Spezialfall in dem die Teilchen senkrecht zur Sensorebene einfallen. Das Ansprechverhalten für andere Trajektorienwinkel war bislang nur wenig bekannt.

Um dem abzuhelfen wurde mit dem MAPS Prototypen MIMOSA-17 eine Strahlzeit am CERN-SPS durchgeführt. Hierzu wurde ein 120 GeV/c Pionenstrahl mit verschiedenen Einfallwinkeln ($0° - 75°$ relativ zur normalen der Sensorebene) auf den Sensor gelenkt. Das Ansprechverhalten Sensoren wurden durch Vermessung verschiedene Leistungsparameter (z.B. die Form und Größe der verschiedenen Pixelcluster sowie die von den verschiedenen Pixeln gesammelte Signalladung) charakterisiert und als Funktion des Einfallwinkels des Strahls ausgewertet.

Dabei wurde festgestellt dass die Form der Signalamplituden innerhalb eines Clusters bei einem Einfallswinkel von $\theta = 0°$ durch eine Lorentz-Funktion beschrieben werden kann. Bei höheren Einfallswinkeln skalierte die gesamte, in einem Cluster gesammelte Ladung proportional zur Länge der Teilchenspur im sensitiven Volumen des Sensors, d.h. proportional zu $1/cos(\theta)$. Gleichzeitig verlängert sich der Cluster entlang der Projektion der Teilchenspur.

Simulationsmodell für MAPS:

Auf Basis dieser Informationen wurde ein Simulationsmodell für die Sensoren entwickelt, das das Ansprechen von MAPS auf einfallende Teilchen beschreibt. Um seiner Aufgabe, der Simulation des MVD bei den erwarteten, sehr hohen Besetzungsdichten, gerecht zu werden, musste dieses Modell die Pixelstruktur und die endliche Auslesezeit der Sensoren beschreiben. Um das erwartete Verschmelzen von Hitclustern akkurat darzustellen, wurde eine exakte Beschreibung der Zahl und Signalamplitude der zu den Clustern zugehörigen Pixel angestrebt. Hierbei wurde besonderer Wert auf eine gute Beschreibung der Peripherie der Cluster gelegt, da diese bei Verschmelzungsprozessen eine dominierende Rolle spielen. Die relativ hohe Zahl von Trajektoren, die die Sensoren mit flachen Einfallswinkeln treffen, legte es darüber hinaus nahe, eine gute Beschreibung der Cluster über einen weiten Winkelbereich zu fordern.

Bei der Entwicklung des Simulationsmodells wurde zunächst ein existierendes Modell erprobt, das im Vorfeld der Arbeit für Simulation von MAPS im Kontext des International Linear Collider (ILC) Experiments zum Einsatz gekommen war. Der Output dieses Modells, das nachfolgend als Gauß-Modell bezeichnet werden soll, wurde mit den vorhandenen Messdaten verglichen. Dabei wurde festgestellt, dass das Modell bei geeigneter Wahl der Parameter die durchschnittliche Anzahl der aktivierten Pixel im Cluster gut wiedergibt. Eine genauere Untersuchung zeigte jedoch, dass die Form der Cluster und die Ladung in den einzelnen Pixeln nicht mit einer Präzision reproduziert werden, die für eine zuverlässige Simulation der Clusterverschmelzung notwendig wäre. Die offensichtliche Ursache für diese Beobachtung liegt darin, dass das Gauß-Modell ursprünglich für klassische, verarmte Detektoren entwickelt wurde. Diese sammeln die Signalladung überwiegend mittels Drift. Die Sensoren der MAPS sind hingegen nicht verarmt und sammeln die Signalladung durch eine subtile Mischung aus mikroskopischen Einbauspannungen und thermischer Diffusion. Diese Abweichung zwischen Modell und Realität konnte durch Anpassung der Modellparameter nicht überbrückt werden. Das Modell wurde daher als zu unpräzise verworfen.

Um die Genauigkeit des Simulationsmodells zu erhöhen wurde ein neuer Ansatz gewählt. Dieser verzichtet darauf, die Ladungssammlung im Sensor detailliert beschreiben zu wollen und beschränkt sich auf eine Parametrisierung der gemessenen Eigenschaften des Sensors. Das so entwickelte Modell, das nachfolgend als Lorentz-Modell bezeichnet werden

soll, simuliert die Teilchendetektion wie folgt: Die Signalladung, die im aktiven Volumen des Sensors freigesetzt wird, wird als Zufallszahl auf Basis einer Landau-Verteilung generiert. Diese Landau-Verteilung wurde an die entsprechenden experimentellen Messdaten angepasst. Die Ladung wird auf eine gewisse Anzahl von Trajektoriensegmenten aufgeteilt. Von dort wird sie entsprechend einer Lorentz-Funktion auf die Pixel verteilt. Die Parameter dieser Funktion werden hierbei so gewählt, dass sie die beobachtete Form der Cluster wiedergeben. Obwohl sowohl die Landau- als auch die Lorentz-Funktion an Messdaten für einen senkrechten Teilcheneinfall angepasst worden waren, zeigte es sich, dass das Modell das Ansprechverhalten der Sensoren für Teilchen mit einem Einfallwinkel von 0° bis zu 75° mit einer Genauigkeit von besser als 10% beschreibt.

Einmal ausgearbeitet wurde das Simulationsmodell in das Simulationsframework des CBM-Experimentes (CBMROOT) integriert. Hierbei wurde die Software dergestalt erweitert, dass auch ein Pile-up von mehreren Kernkollisionen während der Integrationszeit des Detektors dargestellt werden kann. Darüber hinaus wurde eine Methode entwickelt, die zahlreichen Delta-Elektronen, die vom Schwerionenstrahl aus dem Target geschlagen werden, mit vertretbarer Rechenzeit in der Simulation zu berücksichtigen. Bezüglich des Aufbaus der internen Ansprechschwelle der MAPS wurde die Simulation von verschiedenen technischen Optionen (ADC, Diskriminator) ermöglicht. Verfollständigt wurde die Software durch die Entwicklung eines Cluster-Finder-Algorithmus, der einfach zusammenhängende Cluster von beliebiger Form und Größe finden kann.

Simulationsstudien

Nachdem das Simulationsmodell entwickelt und gegen Messdaten getestet war, wurde es zur Simulation einer Rekonstruktion von Open-Charm-Teilchen eingesetzt. Diese Simulationen wurden mit CBMROOT durchgeführt. Hierbei wurde der MVD und das Silicon-Tracking-System (STS) des CBM-Experimentes im Detail beschrieben. Die der Teilchenidentifikation dienenden Detektoren von CBM konnten nur vereinfacht dargestellt werden.

In der Simulation wurde die Rekonstruktion von D^0-Teilchen, die in zentralen Au-Au Kollision mit einer Strahlenergie von 25 AGeV, nachgestellt. Als Zerfallskanal wurde der D^0-Zerfall in ein (π,K)-Paar gewählt, der bereits früher zur Beurteilung der Sensitivität von CBM zum Einsatz gekommen war. Die Rekonstruktionsstrategie beruhte auf der Identifikation des sekundären Zerfallsvertex der D^0-Teilchen und der Abgrenzung dieses Vertex vom primären Vertex der Schwerionenkollision. In einer ersten Simulation wurde angenommen, dass die Kollisionsrate von CBM an die Zeitauflösung des MVD angepasst wird. Hierdurch wird ein Pile-up im MVD vermieden und man erhält eine Kollisionsrate von etwa 3×10^4 Kollisionen pro Sekunde.

Es wurde festgestellt, dass Vertexauflösung des MVD unter diesen Umständen bei etwa 40 μm liegt. Die Impulsauflösung des Detektorsystems wurde mit 1,2% ermittelt, wodurch die Auflösung für die Invariante Masse der D^0-Teilchen bei 12 MeV/c^2 liegt. Die Effizienz der Spurrekonstruktion für Teilchen mit einem Impuls von mehr als 1 GeV/c lag bei $\sim$ 95%. Für das Signal der D^0 Teilchen wurde ein Signal-Hintergrund-Verhältnis von $2.0^{+1.4}_{0.6}$ bzw. $10.8^{+8.0}_{-3.5}$ beobachtet, wobei eine Produktionsmultiplizität von 3.74×10^{-5} für HSD

bzw. 2.05×10^{-4} für SHM zu Grunde gelegt wurden. Die Rekonstruktionseffizient für D^0-Teilchen (einschließlich der Detektorakzeptanz, der Effizienz der Spurrekonstruktion und der Effizienz der verschiedenen Schnitte) lag bei etwa 2%.

Zur Berechnung der Zahl der rekonstruierten Teilchen wurde davon ausgegangen, dass CBM binnen eines Betriebsjahres 5×10^6 Sekunden "Strahl auf Target" haben wird. Unter der Annahme von SHM-Multiplizitäten reicht dies aus, um $9,6 \times 10^3$ $(D^0 + \overline{D^0})$ zu rekonstruieren. Unter der Annahme von SHM-Multiplizitäten sinkt diese Zahl auf $1,7 \times 10^3$. Die Signifikanz der Teilchensignale liegt demnach bei $48.0^{+2.4}_{-2.2}$ (SHM) and $17.2^{+1.6}_{-1.4}$ (HSD). Zu beachten ist bei diesen Ergebnissen, dass die volle Leistungsfähigkeit der Teilchenidentifikationsdetektoren von CBM berücksichtigt wurde: Es wurde davon ausgegangen, dass Protonen mit Hilfe des Flugzeitdetektors (TOF) von CBM unterdrückt werden können. Ferner wurde angenommen, dass das TOF eine Identifikation von Pionen und Kaonen mit einem Impuls von weniger als $3,5$ GeV/c ermöglicht und dass der RICH-Detektor und die TRD-Detektoren des Experiments Elektronen zuverlässig unterdrücken.

Angesichts der Ergebnisse für HSD-Multiplizitäten stellt man fest, dass das Physikpotential von CBM im Wesentlichen auf Messungen der absoluten und relativen Produktionsmultiplizitäten der Open-Charm-Teilchen beschränkt ist. Das Potential könnte wesentlich erweitert werden, sofern es gelingt würde, die Zählstatistik des Experiments zu erhöhen. Diese Überlegung motivierte eine zweite Studie, bei der geprüft wurde, ob der hochgranulare Vertexdetektor in der Lage ist, einen Pile-up von 5 Kollisionen während seiner Integrationszeit zu verarbeiten. Sofern dies erfüllt ist, könnte man die Kollisionsrate des Experimentes um einen Faktor 5 auf einen Wert von $1,5 \times 10^5$ pro Sekunde steigern und eine Zählstatistik von $7,5 \times 10^{10}$ zentralen Kollisionen pro Jahr erreichen. In der Studie wurde jeodch beobachtet, dass die Rekonstruktionseffizienz für D^0-Teilchen auf 0,7% sinkt. Auf Grund der erhöhten Kollisionsrate können dennoch bei HSD-Multiplizitäten $3,2 \times 10^3$ $(D^0 + \overline{D^0})$ pro Jahr rekonstruiert werden. Bei SHM-Multiplizitäten erwartet man jährlich $1,7 \times 10^4$ rekonstruierte $(D^0 + \overline{D^0})$. Das Signal-zu-Hintergrund-Verhältnis für D^0-Mesonen liegt bei $0,43^{+0.18}_{-0.11}$ und die Signifikanz des Signals bei $15.6^{+2.8}_{-2.2}$ (HSD).

Diskussion der Resultate:

Die Resultate der Studien legen nahe, dass eine Erhöhung der Kollisionsrate von 3×10^4 auf $1,5 \times 10^5$ Kollisionen pro Sekunde das Physikpotential von CBM nicht signifikant erhöht. Dieses unerwartete Ergebnis entsteht offensichtlich dadurch, dass die hohen Besetzungsdichten des MVD die Teilchenrekonstrution behindern. Die Rekonstruktionseffizienz sinkt und das Signal-zu-Hintergrundverhältnis sinken beinahe um einen Faktor 5 wodurch der positive Effekt der zusätzlichen Zählstatistik aufgehoben wird. Die Signifikanz der Teilchensignal bleibt, unter Berücksichtigung der statistischen Unsicherheiten der Simulation, unverändert.

Dennoch zeigt die Studie beeindruckend die Robustheit des grundsätzlichen Detektorkonzepts von CBM. Dies gilt insbesondere für Strahlenergien über 25 $AGeV$ und sofern sich die SHM-Multiplizitäten als zutreffend erweisen. Sollten sich die kleineren HSD-Multiplizitäten als realistisch herausstellen, müsste man für die Messung die Sensitivität des Detektors voll ausschöpfen.

Der Studie zu Folge ist die Leistungsfähigkeit des Dektorsystems vor allem durch die angenommenen Grenzen der Ratenfestigkeit der Sensoren beschränkt. Eine weitere Einschränkung entsteht dadurch, dass die Spurrekonstruktionsalgorithmen zum zum Zeitpunkt der Simulation noch nicht vollständig für die Verarbeitung der sehr hohen Teilchenmultiplizitäten im Vertexdetektor optimiert waren. Eine Reihe von Optimierungsschritten sollten in der Lage sein, die Leistungsfähigkeit des Experiments deutlich zu steigern. So sollte es in einem gewissen Maß möglich sein, verschmolzene Teilchencluster im MVD zu erkennen und nachträglich zu trennen. Hierdurch sollte es den Spurrekonstruktionsalgorithmen ermöglicht werden, einem Cluster mehrere Tracks zuzuordnen, was bisher nicht möglich war. Die Detektorhardware könnte dadurch verbessert werden, dass der MVD um eine dritte Station erweitert wird. Diese Station war ursprünglich vorgesehen, sie wurde im Rahmen von Kostensenkungsmaßnahmen aus den Plänen entfernt. Dies erweiterte jedoch den Abstand zwischen dem MVD und der ersten STS-Station auf 20 cm. Es ist naheliegend zu vermuten, dass dieser sehr hohe Abstand die Spurverfolgung vom STS zum MVD nachhaltig behindert.

Zuletzt sollte angemerkt werden, dass die in der Simulation verwendeten Leistungsdaten das beste Verständnis im Jahr 2009 bezüglich der Leistungsdaten von Sensoren mit Baujahr 2015 repräsentieren. Auf Grund mehrerer unerwarteter technologischer Durchbrüche in der Halbleiterindustrie wurden die diese Entwicklungsziele in einigen Bereichen bereits von Sensoren aus dem Jahr 2011 übertroffen und die Grundlagen für weitere Leistungssteigerungen gelegt. Es erscheint daher nicht ausgeschlossen, dass die für die hier diskutierten Messungen verfügbaren, zukünftigen Sensoren die in dieser Arbeit angesetzten Leistungsdaten noch deutlich übertreffen.

Introduction

The Compressed Baryonic Matter experiment (CBM), planed at the future international accelerator Facility for Antiproton and Ion Research (FAIR) in Darmstadt, aims at investigating the nuclear matter phase diagram in the region of high net baryonic densities and moderate temperatures. This region is to a large extent unexplored in detail both experimentally and theoretically.

Among the primary goals of this experiment are the search for the predicted first order phase transition between hadronic matter and and partonic matter, the search for the critical point, the search for signatures of chiral symmetry restoration, the search for new forms of matter and the study of nuclear matter equation-of-state in the energy range between 10 and 45 $AGeV$.

The strong interaction theory will profit from gaining a better understanding of the structure and the properties of strongly interacting matter at high baryon densities [50]. Moreover, the matter which will be produced under these extreme conditions of baryon densities is of particular interest for the study of compact astrophysical objects such as neutron stars [51].

The study of the production and propagation of open charm in the heavy ion collisions is one of the main physics topics of the CBM experiment. Observables related to open charm particles (i.e. particles containing one charm quark and one light quark) are expected to be particularly sensitive to the high density effects and to the deconfinement phase transition.

At large net baryon densities, the mass of open charm particles is expected to be modified in the nuclear medium. In consequence, their production cross section is expected to be modified. This effect should be particularly enhanced close to their kinematical threshold which is located at FAIR energies. On the other hand, the relative yield of D-mesons and charmonium has been suggested recently as a signature of the deconfinement phase transition. This might appear as a sudden drop in the excitation function of the $J/\Psi/D$ ratio at a beam energy corresponding to the onset of QGP formation which is expected to take place in the FAIR energy range.

The CBM experiment will measure open charm particles in heavy ion collisions for the first time in the energy range below 45 $AGeV$. The measurement of open charm particles

close to their production threshold calls for high intensity beams. FAIR will be able to deliver high intensity beams, up to 10^9 ions/second (for Au beams). Moreover, given the small average decay length of open charm particles, a new generation highly precise and thin vertex detector is needed. The latter will offer the possibility to identify and separate the decay vertex of open charm from the primary collision vertex.

The detection of open charm particles in CBM is based on the reconstruction of their decay vertex and its distinction from the primary collision vertex. The average life time of these open charm particles like D-mesons is very short, in the order of a picosecond, which corresponds to a decay length of several 100 μm in the laboratory frame. This makes their detection particularly challenging and imposes strong constraints on the detection system which has to be able to identify the D-mesons by reconstructing their decay vertex in an environment of high track density. Moreover, the low production multiplicities of D-mesons impose the use of high beam intensities which would allow measuring sufficient statistics.

Therefore, a highly precise, low material budget, radiation tolerant and fast vertex detector is required for open charm reconstruction in CBM. This Micro Vertex Detector (MVD) of CBM will be equipped with Monolithic Active Pixel Sensors (MAPS), because they provide a low material budget (below 0.05% X_0) and are highly precise (spatial resolution close to 1 μm). Substantial progresses have been achieved over the last years mainly in terms of their radiation tolerance and readout speed. Today, MAPS have reached a readout speed of $\sim 100\ \mu s$ and a radiation tolerance of $\gtrsim 10^{13} n_{eq}/cm^2$. Further improvements are expected in the coming years, before the construction phase of the detector which is planned to start in 2015. The readout speed is expected to be improved by a factor of 3 reaching $\sim 30\ \mu s$ and the radiation tolerance is also expected to be further improved, reaching $\sim 10^{14} n_{eq}/cm^2$).

The present thesis is a contribution to the design and development of the Micro Vertex detector of the CBM experiment. It deals with three main aspects. The first one concerns the experimental characterisation of the response of MAPS sensors to the passage of charged particles. The second one consists in the development of a realistic MVD detector response model. Finally, the third aspect is a detailed simulation study of the feasibility of open charm measurements.

The characterisation of MAPS response to charged particles is regularly performed in beam. Until recently, only particles impinging vertically the detector have been studied. The poor knowledge of the MAPS sensors' response to inclined particles motivated the realisation of a dedicated beam test, with a sensor called MIMOSA-17, at the CERN-SPS with 120 GeV/c pions impinging the sensor at various incident angles (0°-75°). The purpose of this test was to characterise the sensor's response in terms of cluster properties (such as cluster size and charge) position resolution and cluster shape. These properties were studied for all incident angles measured. Having this information available made the development and evaluation of a detector response model possible.

A detector response model, accounting for the particular response of MAPS sensors to inclined particles, did not exist and had therefore to be developed. Such a model should provide the possibility to simulate, among others, the granular structure of MAPS and their readout time. A particular focus had to be laid on the response of MAPS to inclined particles since they represent a substantial fraction of all impinging particles on the MVD. When particles impinge the detector with high incident angles they tend to cross a larger number of pixels which fire and increase thus the detector occupancy.

Based on the input provided, a detector response model was developed and evaluated. A particular challenge was to describe with good accuracy the response of the detector even for particles with high incident angles, given that the mechanism of charge collection and cluster formation in MAPS is highly complex. After this model was developed and validated with the beam test data, it was implemented in the global simulation framework of CBM and used for extended simulations.

The purpose of the simulation studies was to assess the feasibility of open charm measurements in nucleus-nucleus collisions with the CBM detector. Special focus was given in using realistic detector response. Detailed simulations were carried out for central Au + Au collisions at an incident energy of 25 $AGeV$. The expected performances for open charm particle reconstruction (purity, efficiency) were benchmarked using the D^0 meson in its hadronic decay channel leading to a (π^+, K^-) pair and an estimate of the expected statistics during a typical CBM run period was obtained. The possibility to pile up several collisions in the MVD detector was investigated taking into account the limited read out speed of MAPS sensors.

The thesis is organised as follows:

The first chapter is an introduction to high energy heavy ion physics. Particular emphasis is given to the importance of measuring open charm in heavy ion collisions in the FAIR energy range. In Chapter 2 the future FAIR accelerator and the CBM experiment and its physics goals are presented. Chapter 3 focuses on the conceptual design of the Micro-Vertex detector of CBM. A compilation of information on the predicted features of the MVD, such as the time resolution the radiation hardness, the material budget and readout time is presented. Chapter 4 concerns the beam tests performed at the CERN-SPS with the goal to benchmark the MAPS sensors' response to particles impinging the detector with a wide range of incident angles. The experimental setup is described and the analysis of the experimental data is performed. In Chapter 5 the development of a detector response model for MAPS is presented. Based on the results of the beam test experiment, we develop and benchmark a detector response model for MAPS sensors. The performance and the limits of this model are discussed. In Chapter 6, detailed simulation studies are presented in order to demonstrate the feasibility of open charm measurements in CBM and to evaluate the physics potential of the experiment.

CHAPTER 1

High Energy Heavy Ion Collisions

One frontier of modern physics is at the particle level, below atomic or nuclear scales, and experiments using particles of high energy are necessary to pursue the search of an understanding of the nature of matter. Much of the present research in physics is devoted to the study of matter with special emphasis on details of the behaviour of matter in conditions of extreme pressure and/or temperatures. How the world came to be as it is?, what is the nature of the forces which govern it? These are the most fundamental questions that may be approached through observation and experiment.

This chapter starts with a description of our current understanding on the building elements of matter and the forces that govern our universe. The most relevant questions in high energy heavy ion research, in particular those related to confinement and chiral symmetry, are introduced next. This is followed by a discussion on the nuclear matter phase diagram, and how to probe it by means of experiment. In the last part, the current knowledge on the hot and dense nuclear matter is summarised and the open questions are discussed. A particular emphasis is given to the importance of open charm measurements.

1.1 Basic constituents of matter and their interactions

1.1.1 Constituents of matter

Our present understanding of the elementary particles and forces in nature is described by the Standard Model [1]. The first step of the Standard Model was established in 1960, when Glashow Weinberg and Salam formulated the electroweak force theory. The latter is a way to combine the electromagnetic and nuclear weak interactions in a unique description. Several years later, the discovery of neutral weak currents established this theory as standard description of the electroweak interactions. According to the Standard Model, matter is composed from twelve basic building blocks called fundamental particles, governed by four fundamental forces. Particles in the Standard Model are generally separated in fermions

and bosons and the forces in 4 types: electromagnetic, weak, strong and gravity. Fermions are elementary particles of spin-1/2 and consist the building blocks of matter. The interaction among the particles is mediated by bosons which are particles with spin 1. Fermions are classified, according to how they interact, into quarks (up, down, charm, strange, top, bottom) and leptons (electron, μ, τ and the corresponding 3 neutrinos). Quarks carry electric and colour charge and can interact with the electromagnetic and strong interaction respectively. They also carry a weak isospin which allows them to interact with the weak force too. The leptons cannot interact with the strong force because they do not carry colour charge. They all interact with the weak force and only three of them (e, μ, τ) carry electric charge which allows them to interact with the electromagnetic force.

Although the Standard Model includes the strong interaction and the electroweak interaction, it does not include the gravitational interaction. The corresponding force carrier, the *graviton* has not been observed.

The weak force is carried by the Z or W boson, while photons are mediating the electromagnetic interaction. The strong interaction between quarks is mediated by gluons which carry a colour charge and this allows them to interact among themselves. The theory that describes the strong interaction is called Quantum Chromodynamics (QCD). A summary of the current knowledge on the elementary particles is given in Table 1.1.

Even though the Standard Model is currently the best description we have of the subatomic world, it does not explain the complete picture. Today it is still under investigation the way quarks and gluons interact via the strong force. Basic concepts of the strong interaction, such as the phenomenon of confinement (why are quarks not observed as free particles?) and the origin of the mass of hadrons (why is a hadron much heavier than the sum of the masses of its constituent quarks?), are not understood.

1.1.2 The strong interaction

The strong interaction between partons is described by the QCD Lagrangian:

$$\mathcal{L}_{QCD} = \sum_{j=0}^{n_f} \underbrace{\overline{\psi}_j i\gamma^\mu(\partial_\mu}_{1} \underbrace{- igA_\mu)\psi_j}_{2} \underbrace{- m_j^0\overline{\psi}_j\psi_j}_{3} \underbrace{- \frac{1}{2}TrG_{m\nu}G^{m\nu}}_{4} \tag{1.1}$$

The sum is on the quark flavours, n_f. The first term (1) corresponds to the kinetic energy of a quark field (ψ). The second term expresses the interaction between a quark field ψ and the gluon field A_μ. Next term (3) is the term of quark mass. The last term (4) demonstrates that gluons also interact with themselves and not only with quarks.

The way it is constructed, QCD possesses a lot of symmetries which may be translated in a conservation of a corresponding quantity, as stated by Noether's theorem. These symmetries and their breaking is dictating the structure of the vacuum and the properties of strongly interacting matter. Some of the features of QCD that are most relevant for heavy-ion collisions are described below.

FERMIONS (constituents of matter)						
Generation	QUARKS			LEPTONS		
	symbol	*(name)*	electric charge	*symbol*	*(name)*	electric charge
1st	**u**	*(up)*	2/3	ν_e	*(electron neutrino)*	0
	d	*(down)*	-1/3	e	*(electron)*	-1
2nd	**c**	*(charm)*	2/3	ν_μ	*(muon neutrino)*	0
	s	*(strange)*	-1/3	μ	*(muon)*	-1
3d	**t**	*(top)*	2/3	ν_τ	*(tau neutrino)*	0
	b	*(bottom)*	-1/3	τ	*(tau)*	-1

BOSONS (force carriers)			
symbol	*name*	*electric charge*	*color charge*
γ	photon	0	0
g	gluon	0	8
Z	Z	0	0
W	W	± 1	0

Table 1.1: *Building blocks of matter (see text) [2].*

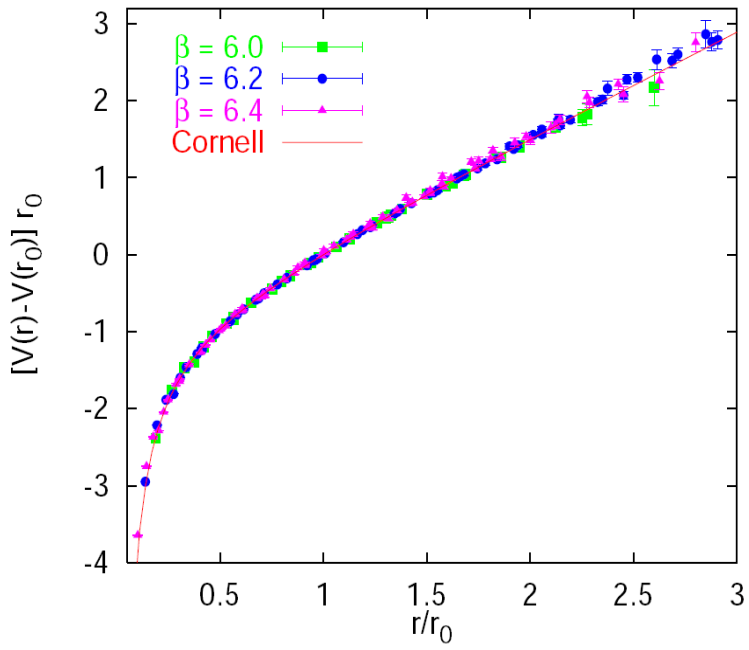

Figure 1.1: *The potential between two quarks obtained in lattice QCD simulations, for different temperatures ($\beta \sim T^{-1}$), and normalised to $V(r_0) = 0$ [3].*

Confinement and asymptotic freedom

A single free quark has never been observed. Quarks exist only confined in "colourless" or "white" objects, the hadrons. In QCD, the potential between a heavy quark and its corresponding antiquark, separated by a distance r, is described in a simple approach by the Cornell potential [3]

$$V_{qq}(r) = -\frac{e}{r} + \sigma r \tag{1.2}$$

where σ is the string tension and e is the Euler's number. r_0 is the value of the radius of the quark-antiquark pair for which $V(r_0) = 0$.

Figure 1.1 shows the quark-antiquark potential as a function of the separation distance as obtained in lattice QCD simulations. The curve represents the Cornell parametrisation, in Equation 1.2, with e=0.295. At normal temperatures ($T \sim 0$) and nuclear densities ($\rho_0 \sim 0.17\ GeV/fm^3$), when two quarks are separated from each other, the second term in Equation 1.2 dominates and the potential between them tends to infinity. This scenario describes the *colour confinement* of quarks and implies that one cannot observe a free quark: quarks are always bound within hadrons. On the other hand, when two quarks approach very much each other, then the first term of the potential, the coulombian term, dominates and the potential linear term tends to minus infinity.
The only way quarks can be free is if they are all in short distances from one another. Conditions under this regime are called "asymptotic freedom", which is another characteristic feature of QCD. As it will be discussed in Section 1.3, such conditions could be achieved in high energy heavy ion collisions.

Chiral Symmetry

The *chiral symmetry* is an important symmetry derived from the QCD Lagrangian. When the spin of a quark is oriented to the same direction as its momentum then it is said that the quark has a *right chirality*, or it is *right-handed*. Correspondingly, when the spin orientation is opposite to the momentum then the quark has *left chirality* or is *left-handed*. Be ψ_R a right handed quark and ψ_L a left handed quark, respectively defined as: $\psi_R = \frac{1}{2}(1-\gamma_5)\psi$ and $\psi_L = \frac{1}{2}(1+\gamma_5)\psi$, then, it holds $\psi = \psi_R + \psi_L$. If the Lagrangian of Equation 1.1 is calculated under the transformation $\psi \rightarrow \psi_R + \psi_L$, it is possible to demonstrate that the combination of terms (1) and (2) of Equation 1.1 couples only states of same chirality:

$$i\overline{\psi}O\psi = i\overline{\psi_R}O\psi_R + i\overline{\psi_L}O\psi_L \tag{1.3}$$

While the mass term (3) couples different chirality states:

$$m\overline{\psi}\psi = m(\overline{\psi_R}\psi_L + \overline{\psi_L}\psi_R) \tag{1.4}$$

The outcome of this transformation tells us that when two *massless* quarks interact, their chirality and flavour are conserved. On the other hand, if the term of mass is introduced then the Lagrangian breaks the chiral symmetry, i.e. the chirality is not conserved. This means that in the case of massless quarks, only right handed quarks can interact with each other and only left-handed quarks are allowed to interact with left-handed quarks. In the case of massive quarks, the interaction between right and left handed quarks is allowed, as indicated by the term (3) in Equation 1.1. An important consequence of the spontaneous chiral symmetry breaking is the existence of a massless mode, the Goldstone boson. Chiral symmetry predicts for every particle the existence of a mirror particle with the same mass. Most of the observed mass of light quarks is generated by the spontaneous breaking of the chiral symmetry. This is illustrated in Figure 1.2 where the mass of quarks is shown in the QCD vacuum and the Higgs vacuum. A substantial part of the mass of the light quarks, (u, d, s) is generated by the spontaneous chiral symmetry breaking. The mass of the heavier quarks, (c, b, τ) is practically not affected by the effect of spontaneous chiral symmetry breaking.

A natural way to explore the phenomena discussed above (confinement and chiral symmetry), is to heat and compress nuclear matter. At high temperatures and densities, one expects a new phase of matter. a quark gluon plasma, where quark and gluons are deconfined and chiral symmetry might be completely restored.

1.2 Phase diagram

In this section, we first introduce some commonly used terms about the phase diagram of matter. For this purpose, the simple example of phase diagram of water is employed. Next, the corresponding features on the QCD phase diagram and some of the open questions will be presented. The section ends with our current knowledge of the QCD phase diagram from lattice simulations.

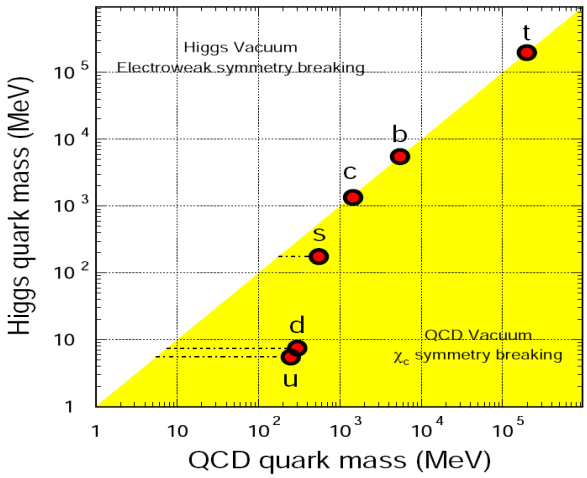

Figure 1.2: *Quark masses in the QCD vacuum and the Higgs vacuum [4]. A large fraction of the light quark masses is due to the chiral symmetry breaking in the QCD vacuum.*

1.2.1 Phase diagram of water: general features

A *phase diagram* in physical science is a type of chart used to show conditions at which thermodynamically distinct phases of a substance can occur at equilibrium. One distinguishes in general three phases: solid, liquid, gas. The most common representation is in the temperature-pressure plane (T, p) on which the phases are separated by three transition lines. Common features of a phase diagram are lines of equilibrium or phase boundaries, which refer to lines that mark conditions under which multiple phases can coexist at equilibrium. Phase transitions occur along lines of equilibrium. Figure 1.3 shows the phase diagram of water, in pressure-temperature plane; the lines of equilibrium or phase boundaries between the three phases of solid, liquid, and gas are shown. The line of transition between liquid and gas ends at a *critical point*. For pressure higher than the one corresponding to the critical point, one cannot distinguish between liquid and gas. One refers to as a supercritical fluid. In water, the critical point occurs at a temperature $T_c = 647.096\ K$ and pressure $p_c = 22.064\ MPa$. The three lines also meet at a point called the *triple point*. At the triple point, the three phases of matter, e.g. gas, liquid, solid, coexist in thermodynamic equilibrium. The coordinates of this point are characteristic for the substance under study.

A phase transition is an n^{th} order phase transition if the n^{th} derivative of the free energy, $\frac{\partial^n F}{\partial T^n}$ is discontinuous while all its lower derivatives in T are continuous. An example of first order phase transition is the liquid gas transition of water. If $\frac{\partial F}{\partial T}$ is discontinuous as a function of temperature, then there is a *1^{st} order phase transition*. If the free energy F of the system and its first derivative $\frac{\partial F}{\partial T}$ are continuous but the second derivative $\frac{\partial^2 F}{\partial T^2}$ (related to specific heat) is discontinuous, then we talk about *a second order phase transition*. For example, a second order phase transition occurs when a crystal lattice is changing configuration from a symmetric state to a non symmetric state, in a discontinuous way, as the temperature changes, while the crystal remains in a solid state. Note that the energy

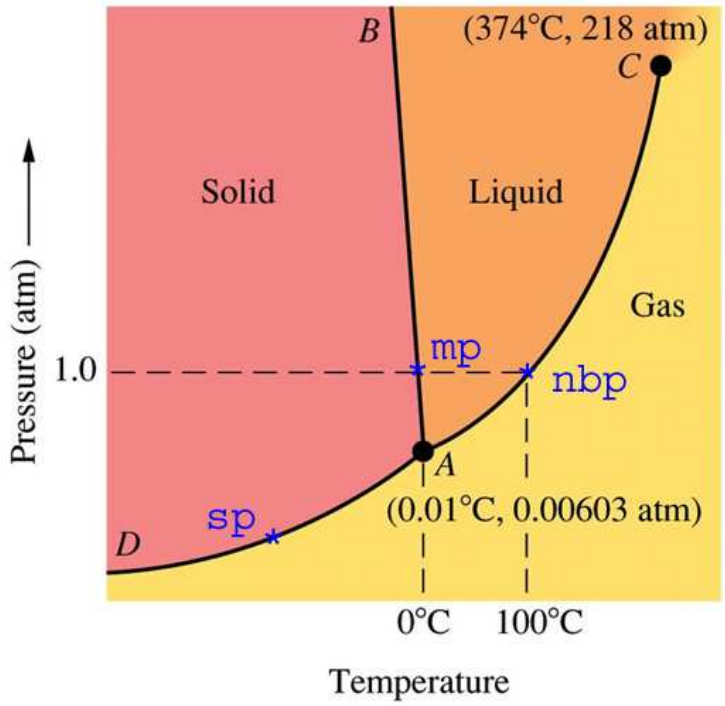

Figure 1.3: *Typical phase diagram of water. The light yellow shaded area corresponds to the gaseous phase of water. The orange area is the region of water in liquid form and the red is the solid phase area. The lines mark the transition among phases. Point C is the critical point and point A is the triple point.*

density is related to $\frac{\partial F}{\partial T}$:

$$\epsilon = \frac{E}{V} = \frac{F + T\frac{\partial F}{\partial T}}{V} \tag{1.5}$$

Therefore, in a first order phase transition, the energy density is discontinuous as a function of the temperature.

1.2.2 Phase diagram of nuclear matter

Many of the various facets of normal matter are also expected to appear in the strongly interacting regime. Some of the states of nuclear matter are illustrated in Figure 1.4.

The phase diagram of nuclear matter is commonly described in the plane of temperature (T) versus baryon chemical potential (μ_B) or net baryon density (ρ_B). The baryochemical potential, μ_B, is the energy needed in order to add a particle to the system and is related to the net baryon density, ρ_B:

$$\rho_B \simeq 4 \times \left(\frac{m \times T}{2\pi}\right)^{3/2} \times \left(e^{(\mu_B - m)/T} - e^{(-\mu_B - m)/T}\right) \tag{1.6}$$

where m is the particle mass.

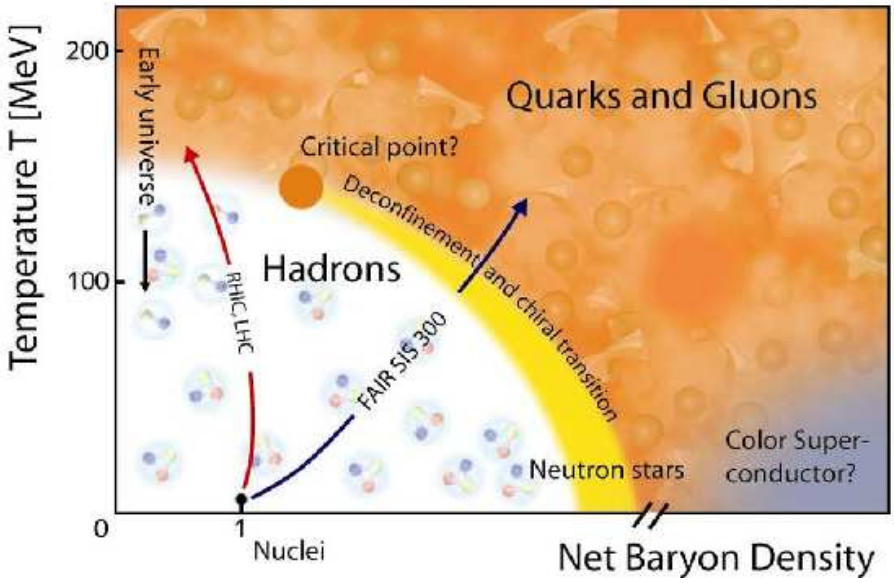

Figure 1.4: *Sketch of the phase diagram of strongly interacting matter plotted as a function of the temperature and the net baryon density [5].*

Nuclei in their ground state (i.e. $T = 0\ MeV$ and $\rho_B = 0.17\ nucleons/fm^3$) behave very similar to a liquid. At finite temperature and density, a transition from liquid to gas occurs. At moderate temperatures and densities above the liquid-gas transition, nucleons that are excited to short-lived states (baryonic resonances) emit mesons in their decay. At higher temperatures, the energy available to the system is high enough to allow also creation of particle-antiparticle pairs. This mixture of baryons, antibaryons and mesons is called hadronic matter. The corresponding region is represented by the white colour on the phase diagram on Figure 1.4.
At very high temperatures or baryonic densities, a phase transition from hadronic matter to quark-gluon matter is predicted to take place: quarks and gluons are no longer confined into hadrons ("deconfinement") forming a new state of matter: the Quark-Gluon Plasma (QGP). To create this deconfined partonic matter, one needs to increase the energy density of the nuclear system above a certain critical energy density (ε_C) where the average distance between quarks becomes sufficiently small (asymptotic freedom) so that confinement disappears (see Section 1.1.2). There are two possible ways to achieve this: either by compressing cold nuclear matter or by heating the matter at zero net baryon density. The heating process consists in increasing the temperature of the system, which can be achieved at high energies. In the compressing mode, one tries to increase, in a given volume, the baryon number density. It is therefore possible to map out the nuclear phase diagram in the (T, ρ_B) plane, by compressing or heating or by combinations of both.

For high temperatures, and low net baryonic densities, it is generally accepted that the transition to QGP is smooth, without discontinuity, also known as *crossover*. In the region of high net baryon densities, model calculations predict a first order phase transition from hadronic matter to the QGP with a phase coexistence region in between (yellow band in Figure 1.4). The existence of a critical point in this region (red point in the figure), where

the transition changes its nature from continuous to discontinuous, is also predicted. For extremely high densities and relatively low temperatures, a colour superconductor phase, in which quark-quark pairs condensate in a similar way as Cooper pairs, is predicted.

The exploration of this phase diagram is not only important for the understanding of QCD, but it has also strong implications in cosmology and for astrophysical compact objects. The matter at zero net baryon density and high temperatures is believed to have existed in the early universe a few microseconds after the Big Bang. At zero temperature and high net baryon densities, one expects a deconfined high density phase predicted to exist in the interior of neutron stars.

It is hoped that the experimental study of the nuclear matter phase diagram, in particular the study of phase transitions, the deconfined matter, as well as the existence and location of the critical endpoint, will provide answers to some of the most fundamental open questions of modern high energy physics:

- What are the properties of strong interaction?
- Why are quarks not observed as free particles?
- How do hadrons acquire their mass?
- What are the properties of hadrons in dense baryonic matter?

Experimentally, one needs to vary the temperature and/or the net baryonic density in order to create hot and dense matter. In high energy heavy ion collisions, such conditions can be reached, as the energy lost by the colliding nuclei is deposited in the vicinity of centre of mass. This makes heavy ion collisions an excellent tool to probe the phase diagram. Before discussing the use of heavy ion collisions in laboratory, it is useful to discuss in detail the predictions of QCD for the phase diagram.

1.2.3 QCD phase diagram from lattice simulations

The approach of QCD calculations differs depending on the energy domain. At high momentum transfers ($\gg 1\ GeV$), the strong coupling is reduced with decreasing distances. This means that higher order terms in strong interaction can be treated as perturbations. This is the approach of *perturbative* QCD, pQCD. At lower momentum transfers, where the strong coupling constant is large, the application of pQCD approach is not possible any more. In this domain, only numerical simulations can be performed. This is the motivation for *lattice* QCD, the only method that allows predictions of low energy QCD. The simulations are based on the formulation in terms of path integral of quantum field theory. A periodic lattice of space-time coordinates is introduced. The simulations are performed in a way to calculate known observables, e.g. hadron masses, when the size of the lattice tends to 0. A detailed description of lattice QCD simulations can be found in literature [6]. Here we only briefly discuss some predictions of such calculations that are relevant for the deconfinement phase transition.

Lattice QCD calculations at zero baryochemical potential on the variation of the energy density as a function of the temperature are shown on Figure 1.5 [6]. In this figure, different predictions based on different assumptions on the number of quark flavours are presented. The abrupt change in the energy density in a short temperature range ($\sim 150 - 200\ MeV$) is a typical indication that the system exhibits a phase transition and can be interpreted as

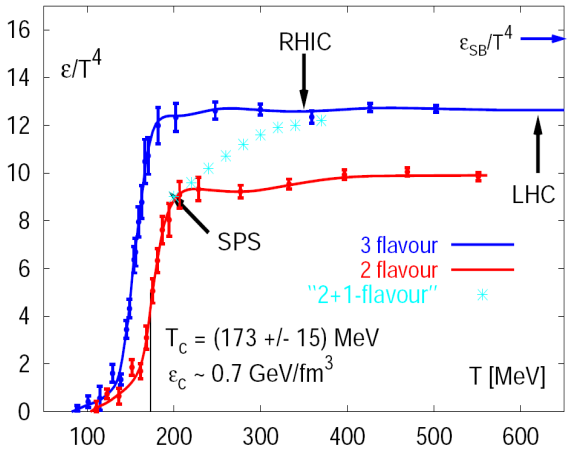

Figure 1.5: *Energy density scaled to the fourth power of the temperature as a function of the temperature from lattice QCD calculations for various number of quark flavours [6]. The values corresponding to the results obtained for an ideal gas are indicated by the arrows.*

being due to the deconfinement, i.e. the liberation of quark and gluon degrees of freedom. The minimum temperature needed for a phase transition is called the *critical temperature*, T_c, which lies, according to various theoretical works (see for example [7, 8] and references therein), in the range from 150 to 200 MeV. For example, the LQCD calculations of reference [7] predict a value of $T_c \sim 173\ MeV$ for two flavours, corresponding to an energy density of 700 MeV/fm^3 which is about four times the energy density of ordinary nuclei (170 MeV/fm^3).

Figure 1.6 illustrates the effect of deconfinement of quarks above the critical temperature. It shows the results of lattice QCD studies for the heavy quark potential for different fractions of the critical temperature. The band of lines corresponds to the potential as described in Equation 1.2. As the temperature increases, the potential decreases beyond distances $r \sim 0.25$ fm and at $T > T_c$ the potential flattens. Under these conditions, the reduced potential allows quarks to move freely for larger distances that substantially exceed the typical size of hadrons. The modification of the heavy quark potential is explained by an effect similar to the Debye screening for electric charge: the charge colour screening effect. In Debye screening, the electrons are preferably surrounded by opposite charge carriers, the positrons, decreasing the charge "seen" by a relatively distant probe. In the colour screening, a quark of a certain charge, e.g. red colour, is surrounded preferably by quarks of same charge (red). As a consequence, the colour charge appears to be smaller at smaller distances and the strength of the interaction is decreased. This effect is known as *deconfinement* of quarks.

Simulations on the lattice are difficult for a system with a finite net baryochemical potential. However, significant progress has been made in the recent years in this domain. An example of calculations [8] is presented in Figure 1.7, which shows the phase transition between a hadronic gas and a QGP. On one hand, the transition is predicted to be a

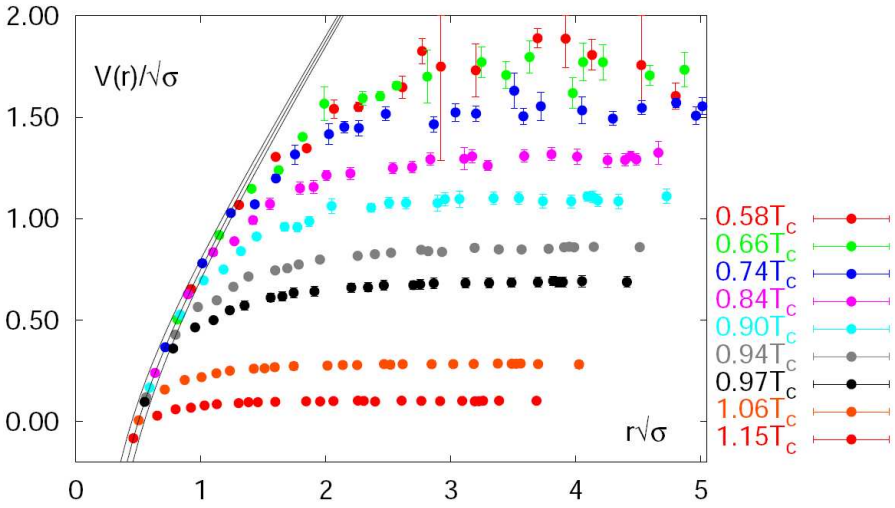

Figure 1.6: *The potential between two quarks obtained in lattice QCD simulations [7]. The effective potential between two quarks in units of* $\sqrt{\sigma}$ *(*σ *is the string tension) as function of distance for different fractions of the temperature* T_c*.* $r\sqrt{\sigma} = 1$ *corresponds to* $r \sim 0.5$ *fm.*

smooth crossover for vanishing μ_B and high temperatures; on the other hand, for increasing μ_B and moderate temperatures the predicted transition is of first order. The calculations of Figure 1.7 predict the existence of a critical point, separating crossover from 1^{st} order transition, at $T = 162 \pm 2\ MeV$ and $\mu_B = 360 \pm 40\ MeV$ with $n_f = 2 + 1$[1]. Near this critical point one expects a second order phase transition, like it holds for water.

It should be noted that the location of the critical point is subject of large uncertainties due to limitations in the present calculations, and even its existence is still debated. There are mainly two theoretical approaches to predict the location of the critical point: lattice QCD and models. Figure 1.8 summarises the results obtained from lattice QCD calculations (green symbols) and different theoretical models (black symbols). As can be seen, the predictions for the critical point cover a very wide range in temperature and baryochemical potential. This figure is used to illustrate in the best way that there is a wide region of predictions about the critical point, and no experimental information is yet available. Lattice QCD points (in green) predict the critical point, if it exists, at 400 $MeV \lesssim \mu_B \lesssim$ 800 MeV and temperatures around 150-200 MeV.

1.3 Probing the QCD phase diagram in Heavy Ion Collisions

High energy heavy ion collisions are expected to create extended volumes of matter at extreme temperatures and densities. This offers a unique possibility to explore the QCD

[1] n_f is the number of quark flavours used for the calculation

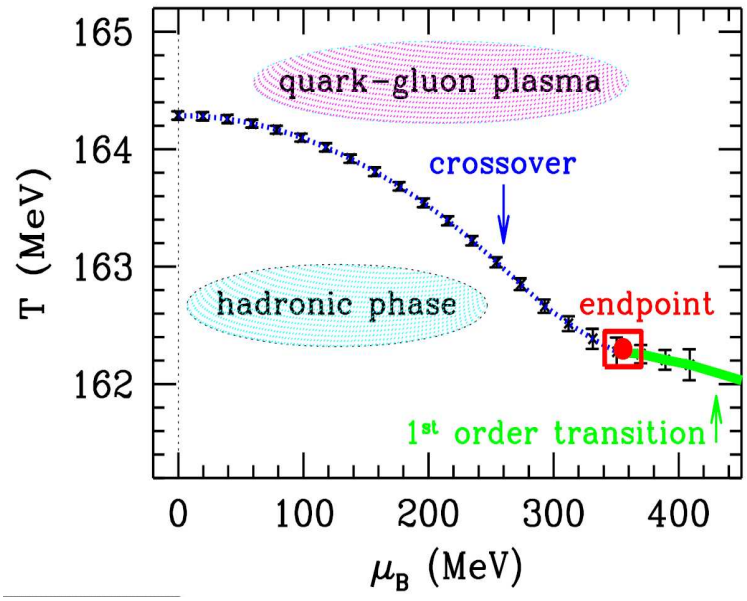

Figure 1.7: *Lattice QCD results for the phase diagram in the temperature versus baryonic chemical potential plane [8]. The box indicates the uncertainties on the location of the critical endpoint within these calculations.*

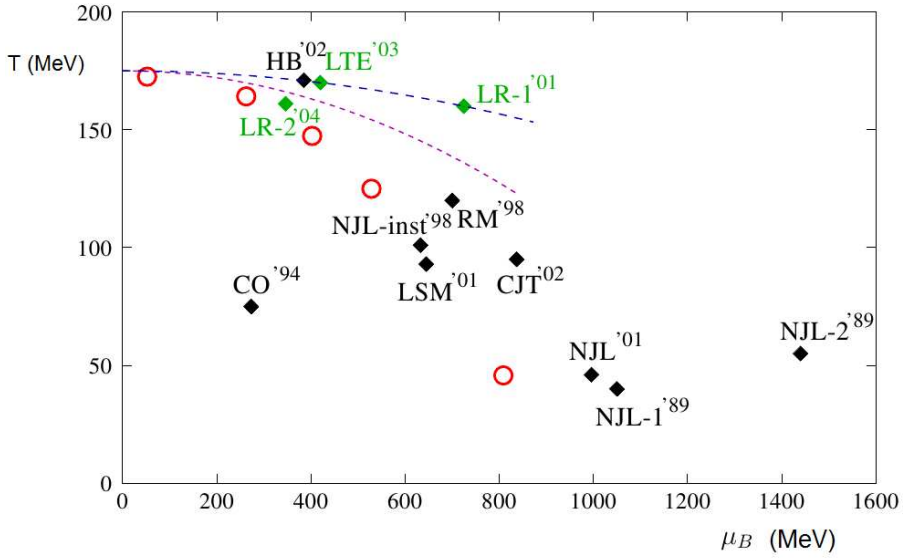

Figure 1.8: *Theoretical predictions of the critical point [9]. The red circles indicate the location of the freeze-out temperature at various collision energies.*

phase diagram in controlled laboratory conditions. Experiments with heavy ion beams have been performed for about three decades at different accelerator facilities worldwide. The Alternating Gradient Synchrotron (AGS) located at Brookhaven National Laboratory (BNL), has been one of the world's premiere accelerators. The AGS started, in 1986, a heavy ion

program first with ^{16}O and ^{28}Si beams (at incident energies up to 15 $GeV/nucleon$) and then with Au beams (up to 12 $GeV/nucleon$). The CERN[2], Super-Proton Synchrotron (SPS) started also, in 1986, being used as a heavy ion accelerator to carry out experiments with ^{16}O and ^{32}S beams at incident energies up to 200 GeV/nucleon and was later on upgraded to produce Pb beams (up to 160 GeV/nucleon). The experimental collaborations at CERN produced significant results, summarised in a CERN press release in 2000, claiming the discovery of a new state of matter [10] with several signatures that would be expected in the presence of a QGP matter. During the same year, the Relativistic Heavy Ion Collider (RHIC) at BNL started its research program with heavy ion collisions at a maximum energy of $\sqrt{s_{NN}} = 200\ GeV$. Nowadays, the Large Hadron Collider (LHC) at CERN is colliding two beams head-on at very high energy ($\sqrt{s_{NN}} = 5.5\ TeV$). It is estimated that the temperatures reached with LHC collisions will be of the order of 500 MeV. However, the net baryon densities achieved are expected to be small. In order to study the properties of nuclear matter at high baryon densities, lower energies like the ones used at the future Facility for Antiproton and Ion Research (FAIR) are more appropriate.

	AGS	AGS	SPS	SPS	RHIC	RHIC	LHC	FAIR
Starting year	1986	1992	1986	1994	2000	2001	2008	2018
A_{max}	^{28}Si	^{197}Au	^{32}S	^{208}Pb	^{197}Au	^{197}Au	^{208}Pb	^{197}Au
$\sqrt{s_{NN}}$ $[GeV]$	5.4	4.7	19.2	17.2	130	200	5500	9

Table 1.2: *High energy heavy-ion accelerator facilities. The maximum energy for each accelerator is given in terms of the centre-of-mass energy per nucleon pair.*

The future FAIR facility planned at GSI in Darmstadt (Germany) will perform heavy ion collisions in the energy range $\sqrt{s_{NN}} = 2 - 9\ GeV$. The FAIR project is distinguished by its possibility to provide the highest beam intensities (up to 10^9 ions/s) in this energy range. A description of the FAIR facility will be given in Chapter 2.

Table 1.2 summarises the the maximum energy for each accelerator facility, expressed in terms of the centre-of-mass energy per nucleon pair ($\sqrt{s_{NN}}$).

1.3.1 Evolution of a High Energy Heavy Ion Collision

Figure 1.9 illustrates the space-time evolution of a high energy heavy ion collision. Two collision scenarios are considered depending on the energy density of the collision. The left-hand side corresponds to the case where the energy density is not sufficiently high for the formation of QGP (i.e. a purely hadronic scenario), while the right-hand side shows the

[2]European Organisation for Nuclear Research (French: Centre Européen pour la Recherche Nucléaire), located in Geneva, Switzerland.

expected collision evolution above the threshold energy density for the creation of QGP, as described in [11] and [12]. In the scenario with QGP formation (right-hand side of

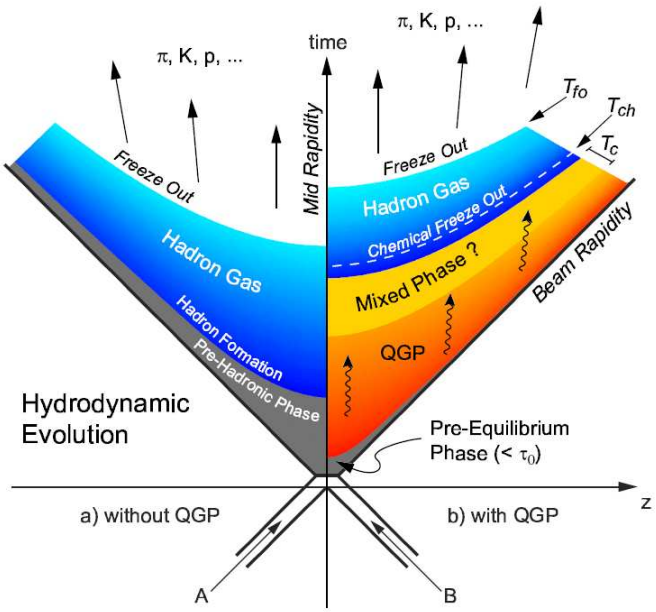

Figure 1.9: *Illustration of the space-time evolution of the fireball [13]. The left-hand side shows the evolution in the case of a purely hadronic scenario (i.e. no QGP formation) while the right-hand side illustrates the expected evolution of the system including QGP formation.*

Figure 1.9) there is a pre-equilibrium phase of $\tau \sim 1$ fm/c (time given in the centre-of-mass frame) during which the partons of the medium interact strongly. The produced partons rescatter both elastically and inelastically equipartitioning the deposited energy. If the energy density is sufficiently high, after some time a local thermal equilibrium is established, forming the QGP phase (region in red colour). In a next step the QGP expands collectively and cools down to temperatures around the critical temperature, T_c, reaching the hadronization stage in which hadrons are formed from the quarks and gluons. Before the complete transformation to a hadron gas, there is a passage through a mixed phase composed of deconfined quarks and hadrons. This phase is represented by a yellow shaded band.

In the hadronic stage, the hadrons interact inelastically until the system reaches the chemical freeze-out when inelastic collisions stop. At this point, the energy density is not sufficient to change the yields of the the different species. The gas of hadrons then continues to interact through elastic collisions as it further expands and cools until the point where the relative distance between particles exceeds the range of the strong interaction so that elastic collisions among them cease to take place. This point is called kinetic (or thermal) freeze-out. At this moment, the kinematical properties of the particles, in particular their momentum distributions, are no longer modified and are fixed. Therefore, the conditions of the thermal freeze-out are reflected in the transverse momentum spectra of the emitted

particles. The system evolves in free hadrons that fly to the detection system. In this scenario, the chemical and thermal freeze-out take place in two different moments in time, but this idea is under discussion.

1.3.2 Freeze-out conditions in high energy heavy ion collisions

The temperature (T_{ch}) and the baryon chemical potential (μ_B) at the moment of chemical freeze-out, when the particle yields are fixed, can be determined from the analysis of the measured particle ratios within the statistical thermal model [89]. The latter describes successfully particle production in heavy-ion collisions using as main input parameters T_{ch} and μ_B. Figure 1.10 shows the pairs of (T_{ch}, μ_B) extracted by fitting the data obtained at different collision energies from the SIS energy range up to the highest RHIC energies. It is interesting to note here, that the baryon chemical potential decreases smoothly from SIS up to RHIC energies, while the chemical freeze-out temperature increases rapidly and reaches a limiting value of about 160 MeV[3].

The chemical freeze-out points (Figure 1.10) are good indicators of the nuclear system at the last stage of its evolution when the particles cease to interact with each other. To probe the hot and dense stages of the collision, one needs to measure observables that are particularly sensitive to the early moments of the collision, such as charmed particles, di-leptons and direct photons. The importance of this type of observables for the study of the deconfinement phase transition and high baryon density effects will be discussed later in this chapter.

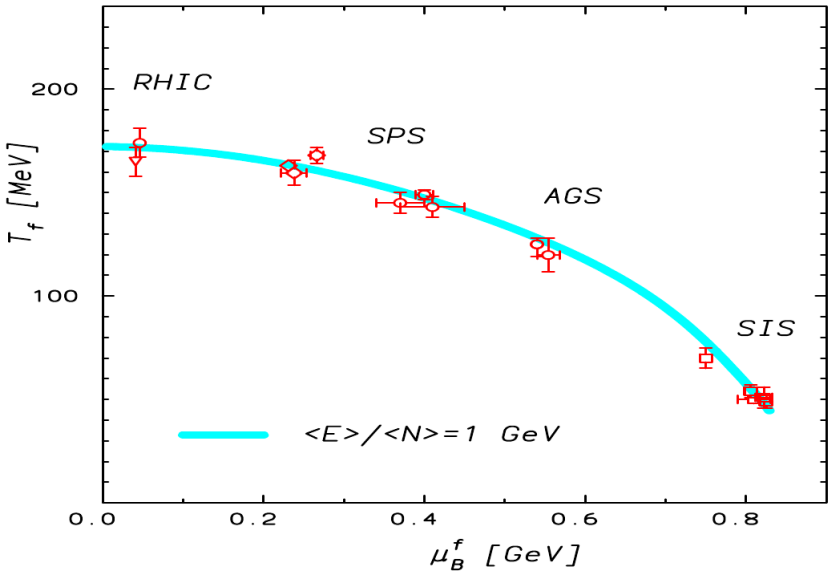

Figure 1.10: *Experimental values of the chemical freeze-out points derived from a statistical model analysis of data ranging from SIS to RHIC energies. The curve corresponds to a fixed energy per hadron of 1 GeV in the hadronic gas model. The figure is taken from [15].*

[3]We will come back on this issue in the next section

1.3.3 Expected collision trajectories in the phase diagram

If the initial energy is sufficient, the collision of two nuclei can lead to the creation of matter with very high temperatures and/or baryonic densities. The collision trajectory on the T-μ_b plane as calculated by a 3-fluid hydrodymanics model [85] is illustrated in Figure 1.11 for Pb + Pb collisions at incident energies ranging from 5 *AGeV* (top AGS energy) to 158 *AGeV* (top SPS energy). In these calculations, the nuclear system reaches equilibration after a certain time. This is indicated by the thick parts of the trajectory lines while the thin lines represent the pre-equilibrium phase of the collision.

The lightgrey shaded region corresponds to the boundary of the phase transition from the hadronic phase to the QGP. The star-symbol is the critical end-point predicted by the lattice QCD calculations [8] discussed in the previous section. The time instants expressed in the centre of mass frame of the colliding nuclei, are indicated by the numbers near the trajectories. The dotted line is the experimental freeze-out curve.

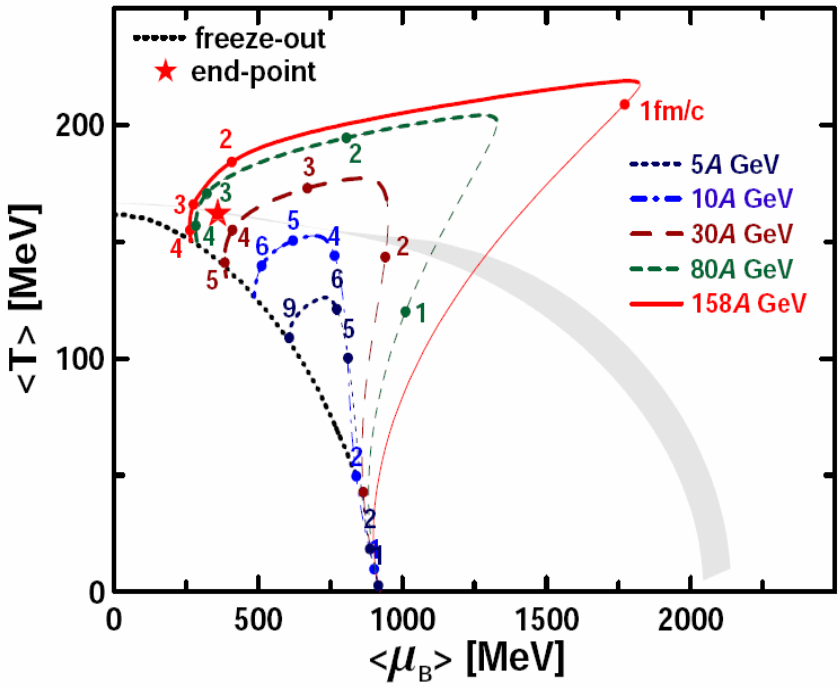

Figure 1.11: *Dynamical trajectories for central Pb-Pb collisions in the QCD phase diagram calculated with a 3-fluid dynamics model. The calculations are shown for different incident energies from 5 to 158 AGeV. [85].*

Figure 1.11 shows that the energy range above 30 *AGeV* is relevant for the search for the expected deconfinement phase transition and for the QCD critical end-point. Note, however, that these calculations should be taken with caution since they strongly depend on the used equation of state, which in this case is purely hadronic.

The exploration of the deconfinement transition and the location of a potential endpoint are among the main scientific goals of the future Compressed Baryonic Matter (CBM)

experiment.

1.3.4 Nuclear stopping power

In laboratory, hot and dense nuclear matter can be generated with a wide range of temperatures and densities by colliding atomic nuclei at high energies. What happens to the colliding system so that nuclear matter is created either with high temperatures or with high baryonic densities? How can we experimentally explore different regions of the nuclear matter phase diagram? These two questions are related to the degree of stopping attained during the collision.

In a collision between two heavy nuclei, the energy source comes from the kinetical energy of the incident nucleons. This energy will be partially deposited in the system via multiple inelastic collisions among nucleons and will be split in a compressional part and and a thermal part. The latter is used to produce new particles. Because the energy lost by the colliding nuclear matter is deposited in the vicinity of the centre of mass with the production of hadrons, high energy heavy ion collisions provide an excellent tool to produce regions of very high energy densities.

The nuclear stopping power is the degree of stopping of the incident nucleus when it impinges on the nuclear matter or another nucleus. This effect plays an important role in heavy-ion collisions. It determines basic parameters, such as the energy density, which governs the collision dynamics, and the extent to which conditions are favourable for the formation of a deconfined partonic phase. Experimentally, the degree of stopping can be evaluated from the measurement of the net rapidity distribution of the baryons. The rapidity, y, is the equivalent of the longitudinal speed in classical kinematics:

$$y = \frac{1}{2} \ln \frac{1+\beta_l}{1-\beta_l} \tag{1.7}$$

with $\beta_l = v_l/c$, where c is the speed of light.
Figure 1.12 illustrates schematically the degree of stopping for three different collision scenarios. The upper panel shows a fictive scenario, where the nuclei are completely transparent to each other: they traverse each other without interacting. In this case the rapidity does not change. In the second scenario (mid-panel), the nuclei are partially decelerated. The rapidity distribution is only slightly different than the initial one. The energy density and temperature increase leading to the creation of quark-antiquark pairs and consequently to the production of mesons (essentially) and baryons in the mid-rapidity region (gray area in the Figure). As the nucleons are not completely stopped, the net baryonic density is low in the mid-rapidity region (and high at $y/y_p \approx \pm 1$). The last scenario (lower panel) corresponds to a full stopping situation of the incoming nuclei, leading to an accumulation of the initial baryons at the point of impact and, therefore, to a high net baryon density in the mid-rapidity region.

The experimental results in Figure 1.13 illustrate nicely the above mentioned cases. The measured rapidity distribution of net protons is shown for different energy domains: AGS, SPS and RHIC. As can be seen in this figure, the net baryon density at mid-rapidity decreases with increasing collision energies, which indicates a decrease of the amount of stopping from AGS to RHIC.

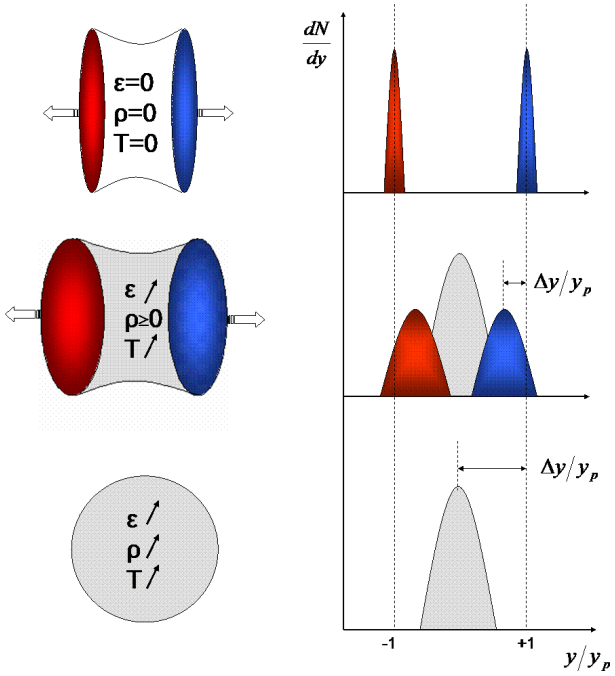

Figure 1.12: *Illustration of the nuclear stopping power as reflected by the shape of the net baryon rapidity distribution in central nucleus-nucleus collisions. The rapidity of baryons is normalised to the rapidity of the projectile in the centre-of-mass system (y_p).*

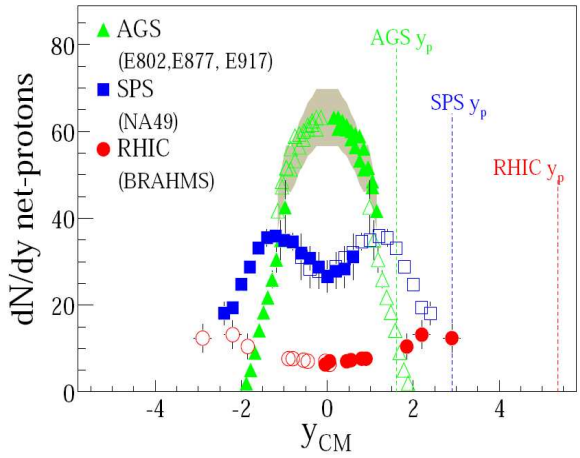

Figure 1.13: *Rapidity density of net protons (i.e. number of protons minus number of antiprotons) measured at AGS, SPS, and RHIC (BRAHMS) for central nucleus-nucleus collisions [16].*

By varying the energy of the colliding ions, one can then probe experimentally different regions of the QCD phase diagram. The region of high temperature and small baryon chemical potential is accessible at the very high energies provided by RHIC and LHC,

while the high μ_B and moderate T region can be probed at centre of mass energies in the range of 5 - 10 $AGeV$ (accessible at SPS, RHIC and the future FAIR accelerator).

In the two following sections, we summarise briefly some of the important experimental facts obtained so far from high energy heavy ion experiments at SPS and RHIC. The purpose here is not to present an exhaustive review on the subject, the intention is just to give an idea of what has been learned to date from these studies at both low μ_B (Section 1.4) and high μ_B (Section 1.5).

1.4 Experimental study of the QCD phase diagram at low μ_B

The first experimental studies of the deconfinement phase transition in heavy ion collisions started in 1986 at the CERN-SPS. At the top SPS energy ($\sqrt{s_{NN}}$ = 17 GeV for Pb+Pb), the baryochemical potential is relatively low, $\mu_B \simeq 300$ MeV, and the chemical freeze-out temperature is about 170 MeV (see Figure 1.10). This temperature is close to the critical temperature predicted by lattice QCD calculations (Section 1.2.3).

The SPS experiments measured different potential signatures of the deconfinement phase transition. The main observations concern strangeness enhancement, charmonium suppression and the initial energy density. The results obtained in these experiments are all consistent with the formation of a QGP phase. This was summarised in a CERN press release published in 2000 [10] where it was stated that:

> "CERN's Heavy Ion program presented compelling evidence for the existence of a new state of matter in which quarks, instead of being bound up into more complex particles such as protons and neutrons, are liberated to roam freely. ... The combined data coming from the seven experiments[4] on CERN's Heavy Ion program have given a clear picture of a new state of matter. This result verifies an important prediction of the present theory of fundamental forces between quarks. It is also an important step forward in the understanding of the early evolution of the universe. We now have evidence of a new state of matter where quarks and gluons are not confined."

One of the main experimental findings at CERN/SPS energies was the anomalous suppression of charmonium (J/Ψ). The latter phenomenon was proposed as a signature of QGP in 1986 by Matsui and Satz [17]. It has been suggested that pairs of $c\bar{c}$ are screened in a hot QGP and the creation of a bound state, i.e. J/Ψ, is prevented. In the case of nucleon-nucleon collisions, where QGP is not expected to be formed, the screening effect does not take place. The result is a suppression of J/Ψ in nucleus-nucleus collisions.

Such suppression was indeed observed by the NA50 experiment in central Pb+Pb collisions at an incident energy of 158 $AGeV$ [18]. Figure 1.14 shows the ratio $\sigma_{J/\Psi}/\sigma_{DY}$, of the cross sections for J/Ψ and the Drell-Yan process as a function of the path length in cold nuclear matter L. The results show a normal absorption (ratio ~ 1) of J/Ψ in p-A collisions, while an anomalous J/Ψ suppression is observed in central Pb+Pb collisions (i.e., L large).

[4] NA44, NA45, NA49, NA50, NA52, WA97 / NA57 and WA98.

This suppression phenomenon becomes more pronounced as a function of the path length. More recent results obtained by the NA60 experiment (the successor of NA50) confirmed these observations in the case of In+In collisions at 158 *AGeV* [19].

It is worthwile to note that the interpretation of the observed J/Ψ anomalous suppression as a signature of the transition to the QGP is not yet settled. Indeed, other conventional mechanisms based on J/Ψ absorption by comoving hadrons might also contribute significantly to the observed effect if the J/Ψ absorption cross sections are in the order of a few mb [20, 21].

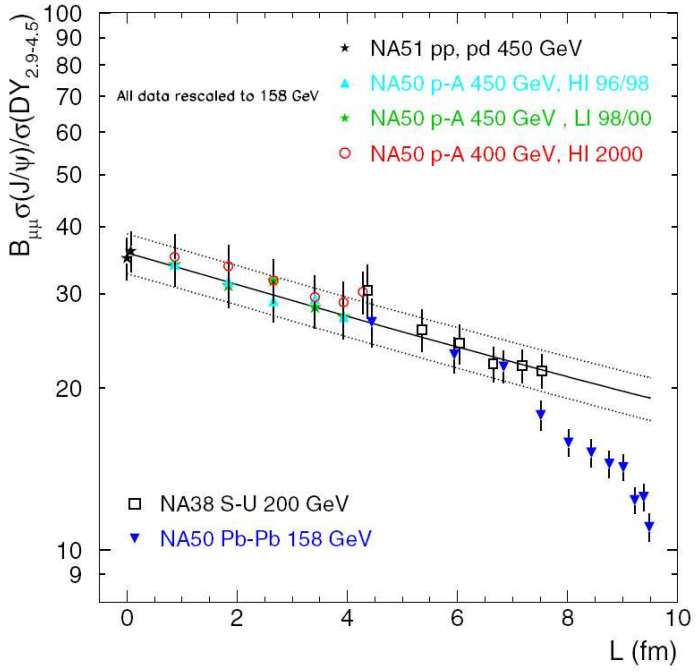

Figure 1.14: *The ratio $\sigma_{J/Psi}/\sigma_{DY}$ of the cross sections for J/Ψ and the Drell-Yan process as a function of L, the average path in nuclear matter [22]. $B_{\mu\mu}$ is the branching ratio of the $J/\Psi \rightarrow \mu^+\mu^-$ decay channel.*

Few years after the above mentioned CERN press release, RHIC announced the discovery of a state of matter referred to as sQGP, for strongly interacting QGP [23, 24, 25]. This finding is particularly interesting as it differs from the theoretical expectations in so far that the matter discovered at RHIC behaves more like a perfect liquid, rather like an ideal gas as it was expected. The constituents of this new state of matter, the sQGP, are strongly interacting. This explains the presence of the letter s in sQGP.

One of the key signatures attributed to the presence of the QGP at RHIC is the so called jet-quenching phenomenon. This is illustrated in Figure 1.15, which shows azimuthal angular correlations between a high-p_t leading hadron (selected as a trigger particle) and other particles from the same event, measured in Au+Au, d+Au and p+p collisions. These results show a strong suppression of one of the jets in head-on Au+Au collisions, while the same analysis in p+p and d+Au collisions showed no such effect. In order to understand the effect of jet suppression and the conclusion derived, a short explanation follows. Jets

originate from the scattering of high energy parton pairs, which create showers of quarks and gluons along their trajectory. If a pair of jets is formed in the outer layers of the fireball, then one jet scatters through almost the entire medium while the other one is rapidly exiting the fireball. The result is that one jet is suffering much more energy loss than the other one, creating thus the phenomenon called jet suppression. Hence, the jet suppression might reflect the slowing down, or quenching, of the partons as they propagate through the formed medium, consisting of a dense quark-gluon plasma.

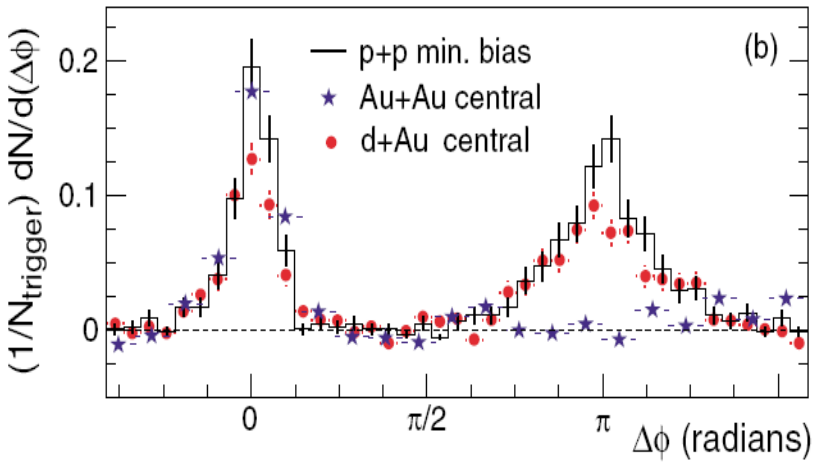

Figure 1.15: *Azimuthal angular correlations between a high-p_t leading hadron (selected as a trigger particle) and other particles from the same event, measured in central Au+Au collisions, central d+Au and pp collisions at $\sqrt{s_{NN}} = 200$ GeV [26]. $N_{trigger}$ is the number of high p_t particles.*

Other important RHIC results refer to a) the observation of a large elliptic flow, which is consistent with hydrodynamics calculations [27] and b) the existence of a universal scaling of the elliptic flow with the number of valence quarks [28, 29]. Both results demonstrate that the medium created in RHIC collisions has partonic degrees of freedom.

It is interesting to point out that no discontinuity is observed for the evolution of experimental observables from top-SPS energies to RHIC, which is consistent with a crossover transition.

The LHC, in CERN, has started operation in autumn 2009 and will extend heavy-ion collision studies at much higher energies than SPS and RHIC ($\sqrt{s_{NN}} = 5.5$ TeV).

1.5 Experimental study of the QCD phase diagram at high μ_B

Collisions of heavy ions with relatively modest incident energies (20-40 $AGeV$) can achieve high net baryon densities, as shown by transport model calculations[5]. Contrary to

[5]As we will see in the next chapter, model calculations show that for high energy heavy ion collisions, the densities can reach up to ~ 10 times the normal density

the high temperature regime, this energy domain has been, so far, only scarcely investigated. The NA49 experiment at CERN/SPS has measured Pb+Pb collisions in this energy range, that corresponds to roughly $\sqrt{s_{NN}} = 5 - 10$ GeV.

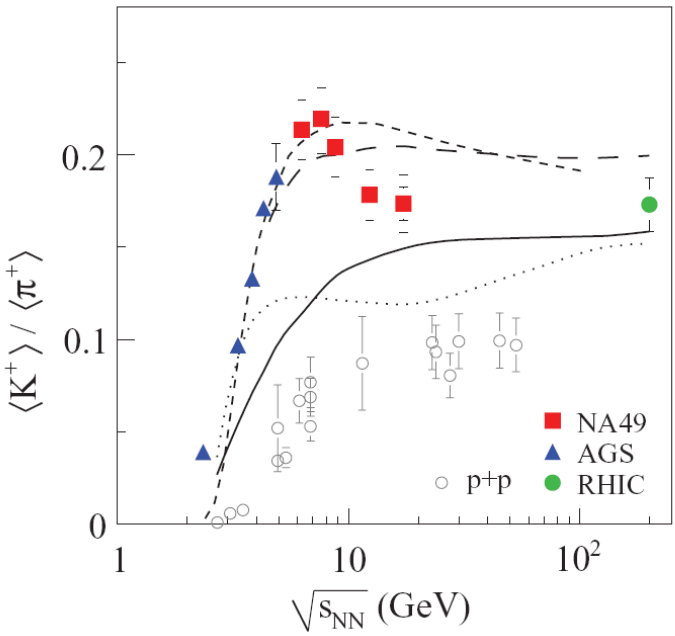

Figure 1.16: *Energy dependence of the K^+/π^+ ratio [30].*

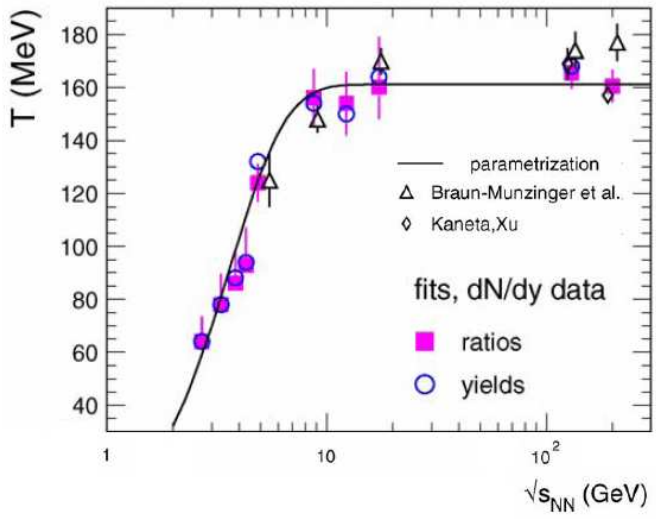

Figure 1.17: *Chemical freeze-out temperature as a function of energy. A saturation is observed above $\sqrt{s_{NN}} \geq 8$ GeV [31].*

Results from the NA49 collaboration show that particle multiplicities globally rise with the collision energy [30]. Interesting structures, however, become visible in particle ratios,

kinetic properties and particle correlations [30]. Together they give strong hints that a partonic phase is reached in A+A collisions at about 30 $AGeV$ beam energy ($\sqrt{s_{NN}}$ = 7.6 GeV). An example of these results is illustrated in Figures 1.16 for the K^+/π^+ ratio. The latter exhibits a pronounced peak close to $\sqrt{s_{NN}} = 7 - 8\ GeV$, which is absent in proton-proton collisions where the creation of a hot and dense medium is not expected. The presence of this peak cannot be explained by equilibrium hadron gas models [32] and microscopic transport calculations [33]. The NA49 collaboration interprets these results as an evidence for the onset of deconfinement.

On the other hand, Figure 1.17 illustrates the saturation of the chemical freeze-out temperature at $T \sim 160\ MeV$ for centre of mass energies above $\sqrt{s_{NN}} \approx 8$ GeV [34]. The saturation of the temperature is characteristic of a phase transition: when the phase boundary is reached, the additional energy goes into "melting" the hadrons and thus leads to the formation of QGP.

It should be noted that the SPS results mentioned above are restricted only to bulk observables. More detailed investigations of this energy domain with penetrating probes are expected to provide useful information concerning several fundamental questions:

- Onset of deconfinement: At which collision energy does hadronic matter start to be deconfined in partonic medium?
- Nature of the phase transition: If the phase transition at this energy range is of first order (as expected from LQCD calculations) then non-monotonic behaviour of the excitation functions of many sensitive observables should be observed.
- QCD critical endpoint: Is there a critical endpoint? Where is it located?
- Explore (or discover) new forms of matter at high net baryonic densities (quarkyonic matter [35], colour superconductivity [165]).
- What are the properties of hadrons in dense baryonic matter? Is the chiral symmetry restored at very high baryon densities?
- What is the equation of state (EOS) of the dense nuclear matter?

Several experimental programs, to a large extent complementary, are or will be addressing the questions listed above. Some details on these programs are given in Table 1.3.

$\sqrt{s_{NN}}$ $[GeV]$	μ_B range $[MeV]$	Experiment	Collision rate (Hz)
5-200	<540	STAR, PHENIX at RHIC	1 -10^3
4.5-17.3	220-580	NA61/SHINE at SPS	10^2
3-9	360-700	MPD at NICA	10^4
2-9	380-780	CBM at FAIR	10^7

Table 1.3: *Overview of present (PHENIX, STAR, SHINE) and future experiments (NICA, CBM) exploring the high μ_B region of the QCD phase diagram. SHINE is the SPS Heavy Ion and Neutrino Experiment [37]. MPD is the Multi Purpose Detector [38].*

All listed experiments will be able to investigate bulk observables in more detail than has been done so far. Rare probes such as di-leptons and charm production will only

become accessible at FAIR where measurements at very high collision rates will be possible. Figure 1.18 shows the particle multiplicities times the branching ratio for different hadrons. The multiplicities are calculated for central Au+Au collisions at 25 $AGeV$ using either the HSD transport code [39, 40] or the statistical hadronisation model [41]. For the vector

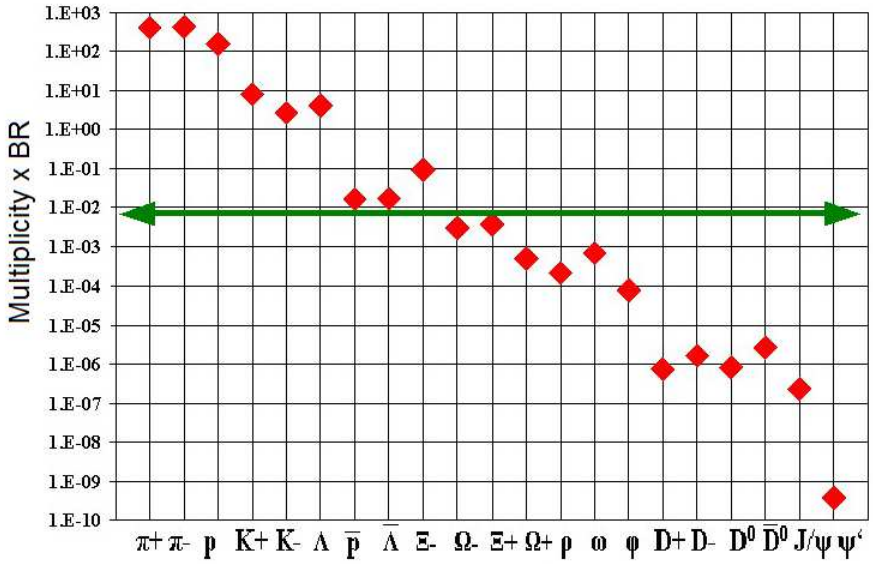

Figure 1.18: *Particle multiplicities times the branching ratio (BR) for central Au+Au collisions at* 25 *AGeV [42] (see text). The area below the horizontal arrow indicates the particles that have not yet been measured in in heavy ion collisions in the energy range close to* 25 *AGeV.*

mesons ($\rho, \omega, \phi, J/\Psi, \Psi'$) the decay into lepton pairs is assumed. For D-mesons ($D^{\pm}, D^0, \overline{D}^0$) the branching ratio corresponds to the hadronic decay into pions and kaons. The area below the horizontal arrow indicates the particles that have not yet been measured in heavy ion collisions in the FAIR energy range. Observables based on these particles are commonly named as rare observables. Most of them carry important information about the first stages of the collision, since they are produced only during this stage. Charm and open charm in particular, is one of the most challenging to measure.

1.6 Open charm

Charm production in high-energy heavy ion collisions is one of the hot topics of both theory and experiment. Because of the large mass, charm quarks are produced mainly in the early stage of relativistic heavy ion collisions, with a formation time[6]:

$$\tau \sim 1/2m_c \sim 0.1\ fm \tag{1.8}$$

Thus, observables related to charmed hadrons (i.e. containing one or more charm quarks) may constitute powerful probes of the hot and dense nuclear matter formed in these colli-

[6]Using 1 $GeV^{-1} \approx 0.2\ fm$ in the natural units system with $c = \hbar = 1$

sions. For example, through the charm quark energy loss, charm flow, and J/Ψ production (suppression or enhancement), one can learn much about the QGP.

In the fireball, a large fraction of charm quarks gets recombined in open charm hadrons, such as D-mesons (containing one light quark in addition to the c quark) and the Λ_c baryon (made of two light quarks and a charm quark). Intuitively, this can be explained by the fact that $c\bar{c}$ pairs are most of the time produced back to back and fly away from each other. This makes it more probable to recombine with light quarks and produce an open charm bound state, rather than hidden charm.

Figure 1.19 [43] shows the total charm cross section as a function of the collision centre of mass energy, as measured by various experiments. In order to compare with results from pp collisions, those for d+Au and Au+Au collisions are divided by the number of binary collisions, N_{coll}. No data on open charm production exist below a c.m. energy ($\sqrt{s_{NN}}$) of 20 GeV. Note here the very low production cross section in the energy range corresponding to FAIR ($\sqrt{s_{NN}} \leq 9$ GeV), which is close to the kinematical threshold.

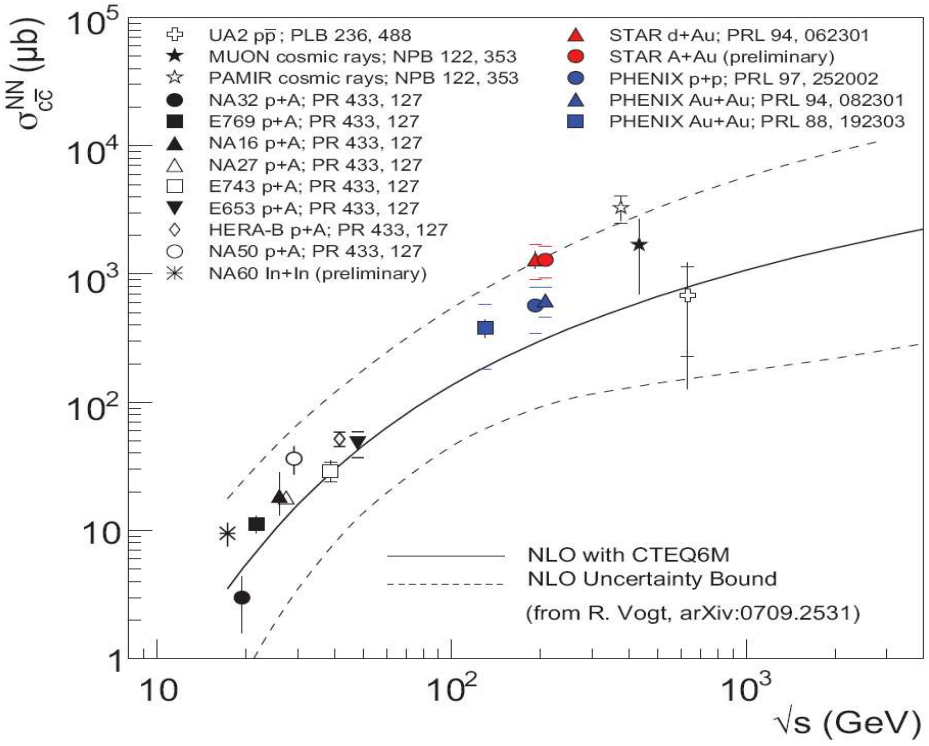

Figure 1.19: *Compilation of data of total charm production cross section ($\sigma_{c\bar{c}}$) scaled to the number of binary collisions covering a broad range of centre of mass energies [43]. The solid line corresponds to QCD NLO calculations and the dashed lines show the uncertainties of the calculation.*

Before discussing the importance of measuring open charm at FAIR and the underlying physics motivations, we will summarise briefly the present knowledge on the total charm production cross section.

1.6.1 Charm production cross section

The charm production cross section is generally evaluated from perturbative pQCD calculations. This is justified by the fact that the charm quark mass ($m_c \simeq 1.5\ GeV/c^2$) is a few times the QCD energy scale $\Lambda_{QCD} \simeq 0.2$ GeV, such that the c-quark can be treated as a heavy particle.

Several mechanisms can produce charm in perturbative QCD (pQCD). Among them are those involving gluon fusion ($g + g \rightarrow c + \overline{c}$), which dominate at high energies, and quark annihilation ($q + \overline{q} \rightarrow c + \overline{c}$). The associated Feynman diagrams at leading order are depicted in Figure 1.20.

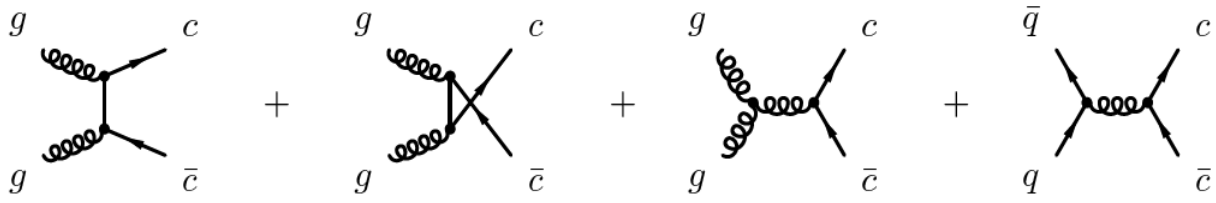

Figure 1.20: *Feynman diagrams for charm production.*

The cross section of the charm production has been calculated with leading order (LO) and next-to-leading order (NLO) perturbative QCD (pQCD) [44]. Because the charm quark is not heavy enough, the next-to-leading order (NLO) corrections are important, as indicated by the theoretical K-factor [44]:

$$\frac{\sigma_{LO} + \sigma_{NLO}}{\sigma_{LO}} \sim 3 \tag{1.9}$$

The above mentioned pQCD calculations allow determining the cross section between two partons. Once this partonic cross section is known, the charm cross section in hadron-hadron collisions can be obtained from the convolution of the partonic cross-sections with the parton distribution functions inside the hadrons [44].

For pA collisions, charm production, being dominantly a hard process, is expected to depend on the number of binary collisions. The scaling from pp to pA collisions is generally expressed as:

$$\sigma(pA \rightarrow c\overline{c}) = A^{\alpha}\sigma(pp \rightarrow c\overline{c}) \tag{1.10}$$

where alpha = 1 would correspond to a perfect binary collision scaling, which means that in this case there are no nuclear effects beyond the expected geometrical scaling. The A dependence comes from the Glauber model [45] calculation for the average number of binary collisions integrated over the collision impact parameter.

Available data [46] on charm production in p-A collisions seem to support a simple binary scaling (i.e. $\alpha \sim 1$) with respect to p-p collisions. These data were however obtained using indirect methods. Their sensitivity to deviations with respect to perfect binary scaling ($\alpha = 1$) might be quite limited due to large uncertainties. More precise data, from direct measurements, are needed for detailed studies of nuclear effects in p-A collisions. Such

studies are currently carried-out at RHIC by investigating the role of Cronin effects [47] and nuclear shadowing [48], and will be also undertaken at lower energies at FAIR. Detailed measurements of p-A collisions are important for understanding the contribution of initial state effects in A-A collisions.

For nucleus-nucleus collisions, one expects that the total charm cross section will also scale as a function of the number of binary collisions provided that the collision process between the two nuclei can be described by a simple superposition of nucleon-nucleon interactions. In this case, the binary scaling can be expressed as:

$$\sigma(AB \rightarrow c\bar{c}) = AB\sigma(NN \rightarrow c\bar{c}) \tag{1.11}$$

Experimentally, the charm production cross section in nucleus-nucleus collisions has been evaluated so far only indirectly via semi-leptonic decays, by studying dilepton spectra (NA38/NA50 at SPS) [46] or single lepton spectra (PHENIX [27], STAR [27] at RHIC). These indirect measurements require subtracting all other sources of leptons, which is subjected to large uncertainties. This renders difficult the interpretation of the results based on this kind of measurements.

Direct measurements of open charm (via hadronic decays) require the use of high precision vertex detectors. Such measurements will be possible in the near future at RHIC with the upgrades of STAR and PHENIX vertex detectors and also at the future FAIR facility with the CBM Micro-Vertex detector (see Chapter 3). The latter will allow open charm hadrons to be measured close to their production threshold.

In the following section, we will discuss in more detail the perspectives for charm physics in A-A collisions at FAIR with the CBM detector and we will focus essentially on open charm production which is the main physics topic of the present thesis. For hidden charm studies with CBM, we refer the reader to the CBM Physics Book [42].

1.6.2 Open charm at FAIR energies

The CBM experiment will measure open charm hadrons, via their hadronic decays, at low energies close to their production threshold. The CBM experimental program will include detailed measurements of open charm in p-p, p-A and A-A collisions over the full FAIR energy range: incident energies going up to 90 GeV for p-p and p-A collisions and up to 45 $AGeV$ for A-A collisions [7]. Details on the experimental methods envisaged for performing such challenging measurements will be given in Chapter 3.

The measurements of the total charm cross section at these low energies, where no data are available so far, are required for a good understanding of the charm production mechanism at threshold energies. They will provide a crucial test for pQCD calculations at low energy where their validity is questionable. Such measurements are also needed as an important input in the theoretical models, in particular those used in heavy-ion collisions for the interpretation of signatures of a possible deconfinement phase transition (e.g. J/Ψ suppression).

[7] The SIS-300 will provide high-energy ion beams of maximum energies around 45 GeV per nucleon for Ne^{10+} beams and close to 35 GeV per nucleon for fully stripped U^{92+} beams.

Beyond the total charm cross section, open charm production is also expected to be particularly sensitive to the properties of the dense and hot medium created in nucleus-nucleus collisions. Indeed, detailed measurements of charmed hadrons can provide valuable information on the nature of this medium and on the deconfinement phase transition. Furthermore, the experimental study of open charm production at FAIR energies, close to the kinematical threshold, presents a great interest for the investigation of in medium modifications of hadron properties. The sensitivity of open charm observables to each of the two above mentioned phenomena, occurrence of the QGP and in-medium properties of hadrons, is discussed in more detail below.

Sensitivity to the deconfinement phase transition

The production of charmed hadrons in nucleus-nucleus collisions depends strongly on the nature (partonic or hadronic) of the medium in which they are formed. Measurements of excitation functions of charmed hadrons could therefore provide direct evidence for the deconfinement phase transition, which is expected to occur within the FAIR energy range. This is illustrated in Figure 1.21, which shows the predictions of two different theoretical models, HSD and SHM, for the ratio of J/Ψ to $(D + \overline{D})$ in central Au+Au collisions as a function of the collision centre of mass energy per nucleon pair. One observes a striking difference between the two theoretical predictions: the J/Ψ to $(D + \overline{D})$ ratio differs by a large factor of about 5 at c.m. energies of 7-8 GeV where, as we have seen previously (Section 1.2.3), the onset of deconfinement is expected to take place. This large difference is due to the different assumptions used by the two models. HSD is a hadronic transport model [39, 40] which calculates the J/Ψ meson and the D($\overline{D}$) meson production excitation functions by means of independent parameterisations which are fitted to experimental data. On the other hand, the SHM model assumes that there is complete dissociation of charmonium in the quark gluon plasma, followed by statistical production of J/Ψ mesons and open charm particles during hadronisation [42].

In HSD, the charm production mechanism proceeds via the creation of pairs of charmed hadrons (e.g. $D^+ - D^-$), while in SHM charmed hadrons are produced through a partonic scenario recombining the charmed quarks created in the first hard collisions. These two different mechanisms involve different production thresholds, which explains the difference observed in their predictions (Figure 1.21). For example, the lowest threshold for charm production in hadronic collisions is defined by the process $p + p \rightarrow \overline{D} + \Lambda_c + p$ resulting in a value of $\sqrt{S_{thr}} = 5.07\ GeV$. In SHM, the lowest threshold is defined by the process $p+p \rightarrow p+p+c\bar{c}$ resulting in a value of $\sqrt{S_{thr}} = 4.5\ GeV$. Due to these different threshold definitions in the cross section parametrisations, the abundance of $c\bar{c}$ pairs in SHM is about 7 times higher than the abundance of $D\overline{D}$ and $\overline{D}\Lambda_c$ pairs in HSD at a collision energy of $\sqrt{S_{NN}} = 7\ GeV$. Note that in SHM the J/Ψ over $(D+\overline{D})$ ratio is independent of the total abundance of c and $\bar{c}$ quarks in the fireball (at least at FAIR energies where this number is small), and depends only on the temperature and the baryon chemical potential [49].

Thus, it appears that the J/Ψ to $(D + \overline{D})$ ratio is sensitive to the deconfinement phase transition and a careful measurement of the excitation function of this ratio should exhibit a discontinuity in the energy range where the onset of the deconfinement takes place. Note that this observable, being a ratio, is independent from the assumption of the $c\bar{c}$ production

cross section assumed in the SHM calculations. Experimentally, this observable has also the advantage to be measurable (in CBM) with good accuracy.

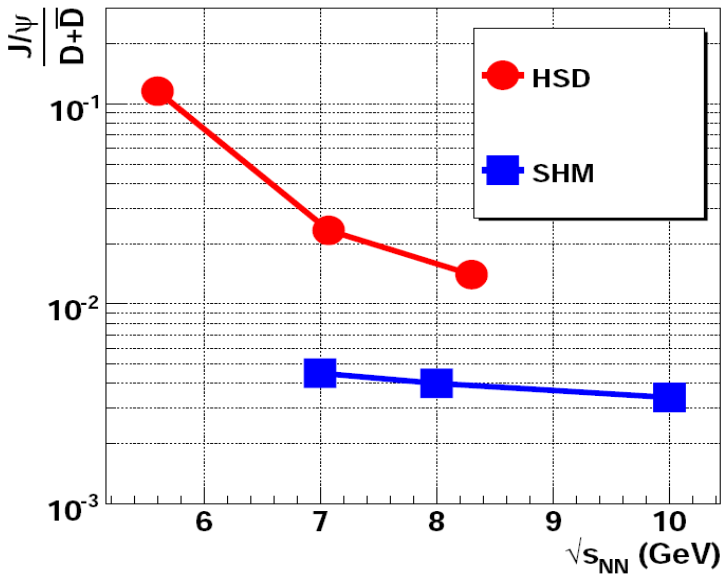

Figure 1.21: *Theoretical predictions for the ratio of J/Ψ over $(D + \overline{D})$ in central Au+Au collisions as a function of the centre of mass energy per nucleon pair [42].*

The elliptic flow of open charm particles might provide another experimental evidence for the QGP phase transition. Indeed, this observable is also very sensitive to the degrees of freedom of the medium at the early stage of the collision. The observation of a strong elliptic flow for open charm would indicate the creation of a partonic medium [42].

The study of open charm is also of great importance for the interpretation of charmonium measurements in nucleus-nucleus collisions. Measurements of open charm hadrons are essential for an accurate estimate of the total charm cross section[8], i.e. the number of $c\overline{c}$ pairs created in the hard collisions, which is the natural reference for charmonium studies. The observation of an anomalous suppression of charmonium is considered as a potential signature of the QGP formation (see Section 1.4): a suppression in the J/Ψ yield is expected due to colour screening effects. Nevertheless, alternative scenarios explaining J/Ψ suppression in a hadronic medium (e.g. absorption on hadronic comovers [102, 103]) are not yet ruled out. Measurements of open charm hadrons can contribute to a better understanding of this suppression phenomenon.

Sensitivity to in-medium modifications of hadron properties

Open charm production in nucleus-nucleus collisions at FAIR energies offers the possibility to investigate the modifications of the properties (e.g. masses and widths) of hadrons when embedded in dense nuclear medium. The study of these in-medium effects is of particular interest as it can be related to the partial restoration of chiral symmetry, i.e. a

[8]Most of the charmed quarks created in the hard collisions appear in the final state as open charm hadrons.

decrease of the $< q\bar{q} >$ condensate of the nonperturbative vacuum as a function of the net baryon density [94]. Note that for open charm hadrons, the in-medium changes are mainly associated with the light quark condensate.

Why open charm at FAIR is a good probe for in-medium effects?

As discussed earlier, charm can be produced only at the very early stage of a heavy-ion collision. This is particularly true at FAIR energies because of the proximity of the charm production threshold. This makes the production of open charm highly sensitive to in-medium effects. The study of these in-medium effects is, in addition, particularly interesting at FAIR energies where very high baryon densities (up to about 10 times the normal nuclear matter density) can be reached during the early evolution of a nucleus-nucleus collision.

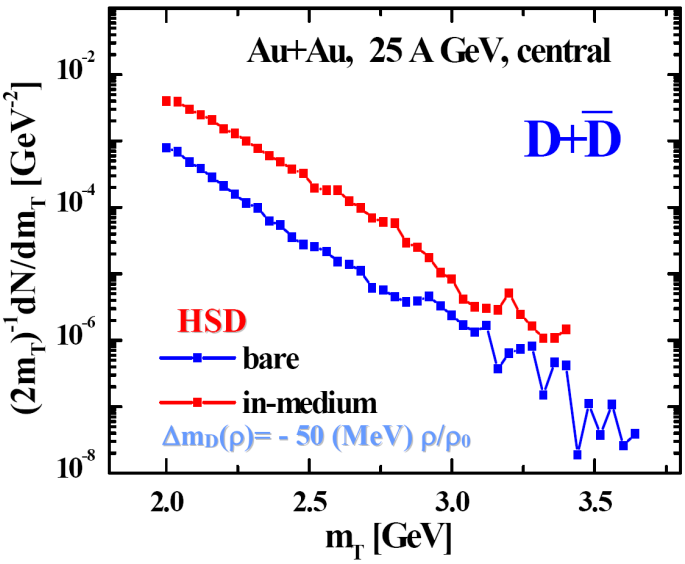

Figure 1.22: *Transverse mass spectra of $(D+\overline{D})$ in the HSD model, for central Au+Au collisions at 25 $AGeV$, with and without the inclusion of in-medium effects [104].*

What are the relevant observables?

The excitation function of open charm particles is very steep in the threshold energy region (see Figure 1.19). Therefore, a change in the effective mass of these particles would translate into a substantial modification of their yield. This is illustrated in Figure 1.22 showing the transverse mass spectra of $(D+\overline{D})$ mesons as calculated by the HSD transport model for central Au + Au collisions at an incident energy of 25 $AGeV$. The calculations are shown with (red colour) and without (blue colour) taking into account in-medium effects, which are introduced as an attractive DN potential (i.e. a mass shift of $-50 \times \rho/\rho_0$ MeV). As can be seen in the figure, the calculations with the mass shift give an enhancement of the D-meson yield by almost an order of magnitude with respect to the bare mass case.

The physics topics discussed above (deconfinement phase transition and in-medium modifications of hadron properties) require the measurements of open charm hadrons in nucleus-nucleus collisions, but also in p-p and p-A collisions. Elementary p-p reactions serve as a baseline for A-A, while p-A is important for the evaluation of the contribution of initial

state effects to the observed phenomena in A-A. As mentioned earlier, CBM will measure all these 3 types of systems at FAIR using the same experimental setup.

CHAPTER 2

The Compressed Baryonic Matter experiment

The exploration of the behaviour of nuclear matter under conditions of high net baryonic densities and moderate temperatures is the motivation of the Compressed Baryonic Matter (CBM) experiment, which will be located at the future Facility of Antiproton and Ion Research (FAIR), in Darmstadt. Among the main goals of CBM are the exploration of the first order deconfinement phase transition, the search for the critical point of the QCD phase diagram, and the study of the modifications of hadrons properties in dense matter. In this chapter we will begin with a short description of the FAIR project and its main scientific objectives. Then we will present the research program of the CBM experiment, its main goals and the various relevant observables. Finally a focus will be given on the description of the CBM detector setup and its different components.

2.1 The FAIR facility

The Facility for Antiproton and Ion Research (FAIR) is a new accelerator complex currently under construction at the GSI Helmholtz Centre for Heavy Ion Research in Darmstadt, Germany. FAIR will offer a large variety of beams, from antiprotons to heavy nuclei, which combine high intensity and excellent quality. Beam intensities of 10^{13} particles/sec for protons and 10^{9} particles/sec for Au-ions are foreseen. The concept of FAIR has been developped within a large international collaboration. Figure 2.1 shows a schematic view of its current design. The blue part corresponds to the present facility and the red one to the future installations. FAIR will be composed of two superconducting synchrotrons, SIS-100 and SIS-300, each with a circumference of 1084 meters. The main motivation for the double synchrotron is the possibility for parallel operation of up to four research programs. This will ensure high beam availability for the experiments, and in particular for CBM. for which this feature is extremely important. The goal of the SIS-100 synchrotron, with a magnetic rigidity of 100 Tm, is to achieve an intensity of up to 5×10^{11} ions per second for uranium beams (U^{28+}) at 2.7 GeV per nucleon. For protons, the foreseen intensity is of 4×10^{13}

particles per second for beam energy of 29 GeV. The high-intensity proton beams, which are required for antiproton production, will be supplied by a future separate proton linac as injector to the SIS-18 synchrotron. The SIS-300 synchrotron, with a magnetic rigidity of 300 Tm, will provide U^{92+} (fully stripped) beams up to 34 GeV per nucleon with an intensity of 3×10^{11} ions/s. Equation 2.1 allows to calculate the energy per nucleon (E/A) which can be reached for each ion with atomic mass A and atomic number Z:

$$E/A = \sqrt{(0.3 \times B \times r \times Z/A)^2 + m^2} - m \tag{2.1}$$

where $B \times r$ is the beam rigidity and m is the mass of a nucleon. For example, a ^{197}Au ion ($Z/A = 79/197$) at SIS-300 ($B \times r = 300$ Tm) will have a maximum energy of 35 GeV per nucleon while at SIS-100 it could not reach an energy higher than 11 GeV per nucleon.

The existing GSI accelerators UNILAC and SIS-18 will be upgraded in order to serve as an injector. The high-intensity beams will be extracted over periods of 10-100 seconds in quasi-continuous mode, as the complex detector systems used for nucleus-nucleus collisions experiments can accept up to $10^8 - 10^9$ particles per second. Slow extraction from the SIS-100 is an option for extending the flexibility of parallel operation for experiments.

Several research programs will be carried out at FAIR. They are distinguished into 3 major scientific areas: 1) nuclear structure, 2) astrophysics and reactions (NUSTAR), atomic physics, plasma physics and applications (APPA) and 3) quantum chromodynamics and hadron physics (QCD), in which CBM is included. A detailed description of this new facility can be found in reference [113].

2.2 The CBM research program and relevant observables

The Compressed Baryonic Matter experiment is a heavy-ion fixed target experiment planned at the future international accelerator FAIR. It aims at investigating the properties of nuclear matter at high baryonic densities and moderate temperatures, a region of the phase diagram that has been so far only scarcely explored both experimentally and theoretically. The research program of CBM is complementary to the heavy ion programs at RHIC and at LHC which address the physics of the early universe at low baryon densities and high temperatures.

The high μ_B region of the phase diagram can be explored by means of heavy ion collisions in an energy range of 10 - 40 $AGeV$, as shown in Figure 2.2, in which the *chemical freeze-out* line is depicted for Au-Au collisions, as expected on the temperature and net baryonic density plane. The numbers refer to beam energies (in GeV per nucleon). The available energy at the RHIC collider (solid squares) is expressed as a sum of the energy of each beam in the laboratory (2+2 up to 100+100 $AGeV$). For FAIR, (energy range (10-45 $AGeV$)) the numbers refer to the kinetic energy of the incident beam on a stationary target. The highest baryonic densities at chemical freeze-out are reached for incident energies between 20 and 40 $AGeV$ corresponding to centre of mass energies per nucleon pair ($\sqrt{s_{NN}}$) in the range 6-10 GeV. For this reason, CBM is designed to operate in this energy range. In this region, CBM will search for the phase boundary between hadronic and partonic matter, the QCD critical point and for modifications of hadron properties in dense matter serving

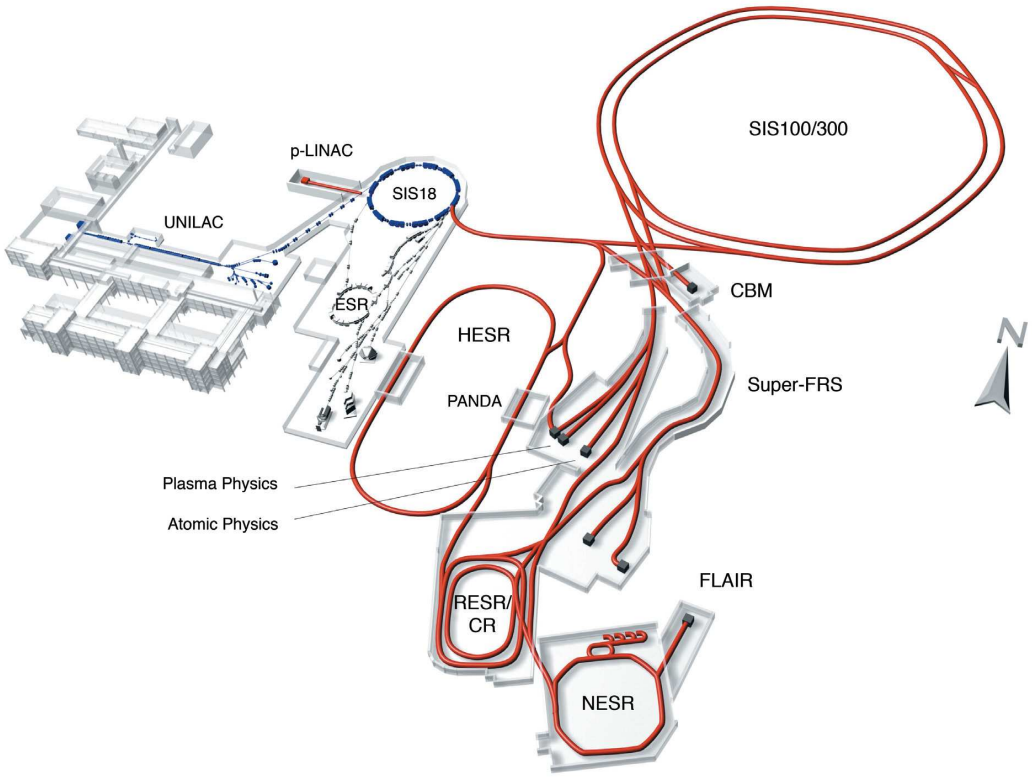

Figure 2.1: *Layout of the existing GSI facility (UNILAC,SIS-18, ESR) on the left and the planned FAIR facility on the right: the superconducting synchrotrons SIS-100 and SIS-300, the collector ring CR, the accumulator ring RESR, the new experimental storage ring NESR, the superconducting fragment separator Super-FRS, the proton linac (p-LINAC) and the high energy antiproton storage ring HESR. The location of the PANDA (anti-proton annihilation at Darmstadt), the FLAIR (facility for low-energy antiproton research) and the CBM experiments are also shown.*

as signatures of the chiral symmetry restoration. The study of the equation of state of the nuclear matter at high baryon densities is also among the main goals of CBM.

The CBM experiment will be able to investigate simultaneously a large number of observables including those associated with rare particles which have not been measured so far in heavy-ion collisions in the energy range below 45 $AGeV$.

The modification of the effective mass of D-mesons in dense matter is expected to lead to a modification of their production yield. Therefore, the relative abundance of D-mesons is an interesting observable for investigating chiral symmetry restoration.

The production of hidden charm (J/Ψ) is expected to be sensitive to the properties of the created dense matter. The J/Ψ suppression is generally considered as a signature of the QGP formation [17], but alternative interpretations are also argued [102, 103]. Measurements of this observable in CBM might shed light on this question. Moreover, the J/Ψ to $(D + \overline{D})$ ratio is also an interesting observable for providing information about the

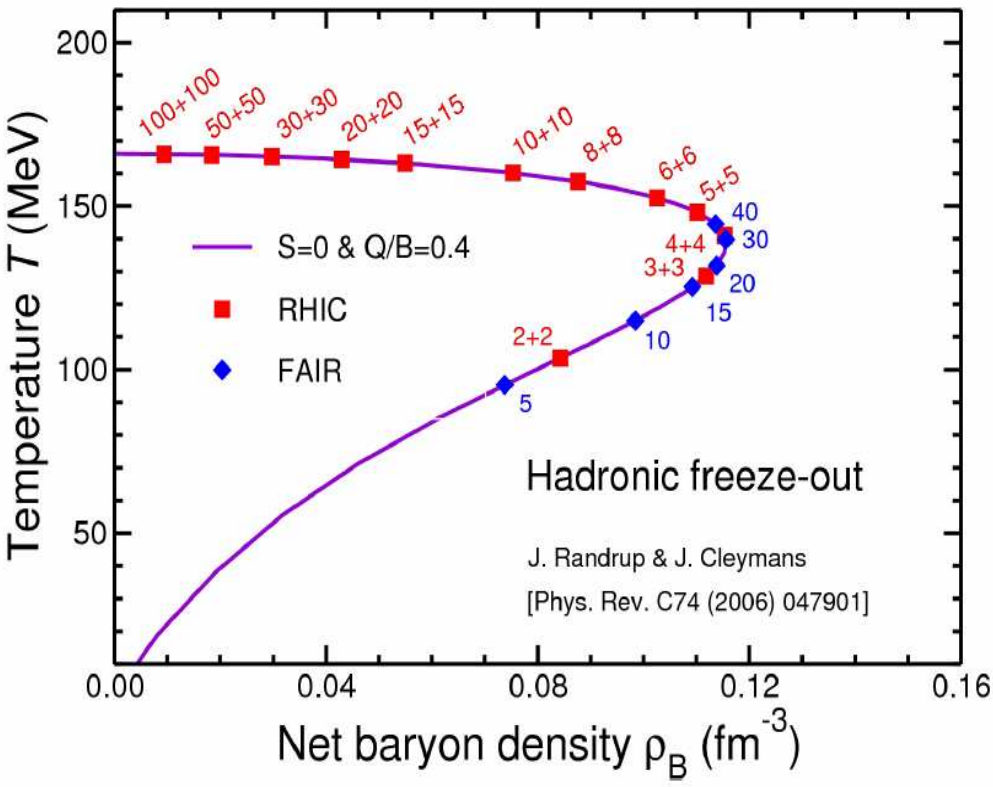

Figure 2.2: *The chemical freeze-out line as expected on the (T, ρ) plane. The line is obtained from the statistical model with the values of μ_B and T that have been extracted from the experimental data in reference [96]. The curve corresponds to Au+Au collisions. The figure is taken from reference [95].*

deconfinement phase transition (see Section 1.6.2).

The relative and absolute abundances of strange particles could be used as possible signature for the quark gluon plasma formation. For example, it has been discussed in Figure 1.16 that an interesting structure of the K^+/π^+ ratio is observed for nucleus-nucleus at beam energies in the range 20 - 40 $AGeV$. The presence of such a structure cannot be reproduced by hadronic models and has motivated further investigation of this energy range [117].

Event-by-event fluctuations are closely related to phase transitions and the QCD critical point. The term event-by-event fluctuations, refers to the study of a given observable measured on an event-by-event basis and its fluctuations over the ensemble of the events. An event-by-event measurement of hadron ratios, for example, is expected to provide evidence of a phase transition, as shown by lattice QCD calculations [118].

It has been argued [120] that event-by-event fluctuations directly reflect thermodynamic properties of the system near its critical point. Especially higher moments (skewness, kurtosis) of the fluctuations are expected to be particularly sensitive in the vicinity of the critical point [121].

The magnitude of the elliptic flow gives information about the interaction strength or

interaction rate of the early medium. In consequence, the elliptic flow of emitted particles and in particular of open charm mesons, is expected to be sensitive to the degrees of freedom of the medium at the early stage [42].

The observation of thermal radiation from the collision zone would give direct experimental access to the fireball temperature [122]. In particular, the transverse momentum spectra of direct photons are suggested to provide information on the (highest) temperature of the system.

Heavy particles containing strange quarks like $\phi(s\bar{s})$ mesons and hyperons (Ξ^0 $(uss), \Xi^-(dss)$ Ω (sss)) are produced in the high temperature and high density phase but have low interaction cross-sections with hadronic matter. Their yields, momentum, and angular distributions are expected to be affected by the conditions inside the reaction zone.

Short lived vector mesons decaying into dilepton pairs (e^+, e^- or μ^+, μ^-) interact with the particles in the collision region only with electromagnetic interaction. Therefore, leptons have a large mean free path in the medium and carry information on the thermodynamical state of the medium at the moment of their production. From the invariant mass distribution of the dilepton pairs one can extract the in-medium spectral functions of the vector mesons, which contain information on the effect of chiral symmetry restoration [123].

CBM will be operated in two phases: the first phase will start at the SIS-100 synchrotron, planned to be operational in the year 2017. At SIS-100, CBM will measure pp, pA (up to 29 GeV incident protons) and A+A collisions (up to 11 $AGeV$ for Au+Au and up to 14 $AGeV$ for Ca+Ca). The second phase, during which the physics program will be completed, will include measurements of A+A collisions at the SIS-300 synchrotron. The maximum energy achieved at SIS-300 will be 35 $AGeV$ for Au beam and 89 GeV for proton beam.

2.3 The CBM detection system

The measurement of rare probes imposes the need for very high beam intensities and long running periods. The aim in the CBM experiment is to operate the detectors at reaction rates up to 10 MHz. Such high interaction rates will induce problems of high particle flux and radiation hardness. On the other hand, the high particle track multiplicity environment in nucleus-nucleus collisions at FAIR energies (about 1000 charged particles in central Au+Au collisions at 25 $AGeV$) requires highly granular detectors.

The detectors and their readout electronics should be fast, radiation hard and should cover a large acceptance with full azimuthal coverage. The data acquisition system should be efficient and fast.

The track reconstruction algorithms should provide high precision and fast online tracking, with high efficiency and excellent momentum resolution. A very good particle identification capability both for hadrons and leptons is required.

The above mentioned requirements should be fulfilled in a wide range of energies (10-45 $AGeV$) and for various system sizes (p+p, p+A, A+A) in order to achieve the physics goals of CBM.

A schematic view of the proposed detector concept is shown in Figure 2.3. In the present design, CBM has two detector configurations: one is specialised for electron identification (electron configuration) and the second is specialised for muon identification (muon configuration). Both setups are not compatible as the muon measurements require efficient particle absorbers which would not allow for electron measurements.

The two detector configurations (see Figure 2.3) have in common a high resolution Micro Vertex Detector (MVD), a Silicon Tracking System (STS), a Transition Radiation Detector (TRD), a Time-Of-Flight (TOF) system made of Resistive Plate Chambers (RPC) and a Projectile Spectator Detector (PSD). In the electron configuration, a Ring Imaging Cherenkov detector (RICH), and an Electromagnetic Calorimeter (ECAL) are foreseen for electron identification, while for the muon configuration they are replaced by a Muon Chamber (MUCH).

The MVD serves for a precise determination of primary and secondary vertices and the STS allows charged particle track reconstruction. The task of the TOF is to provide identification of hadrons by measuring their time-of-flight. The TRD detector will permit charged particle tracking and the identification of high energy electrons and positrons. The RICH detector will identify electrons and will provide suppression of pions in the momentum range of electrons from low-mass vector-meson decays. The ECAL will be used for the identification of electrons and photons.

The various detector components of CBM are designed to cover laboratory polar angles from 2.5° to 25°. The acceptance of the CBM detector on the transverse momentum versus the rapidity plane for central Au+Au collisions at 25 $AGeV$ is shown in Figure 2.4. Three representative particle species are shown: pions, kaons and protons with at least 4 hits in the STS planes. 60% of $\pi^{\pm}$ produced in a central collision are in the CBM acceptance. For $K^{\pm}$ and protons this number becomes 80% and 95% respectively .

2.3.1 The Micro Vertex Detector (MVD)

The Micro-Vertex Detector together with the Silicon Tracking System are the core components of the CBM detection system. The MVD must be located as close as possible to the interaction point and will be therefore exposed to high particle rates, up to 10^{10} particles per second[1]. Silicon pixel detectors are foreseen in order to keep the occupancy at an acceptable level (below 1%). The MVD stations should be highly granular (pixel size of $\sim 20 \times 20\ \mu m^2$) and very thin (a thickness of few 100 μm). Both requirements can be fulfilled by the technology of Monolithic Active Pixel Sensors (MAPS). However, the MVD detector layers will be also exposed to high radiation doses: up to $10^{15}\ n_{eq}/cm^2$ per run year[2], for a beam intensity of 10^9 ions per second and assuming a 1% interaction target. The radiation hardness and read-out speed of present MAPS detectors still need to be improved in order to meet the requirements of CBM. This is currently the object of intensive R&D activities in the collaboration [55]. A detailed description of the CBM-MVD and the foreseen MAPS technology will be given in the next chapter.

[1] This number concerns only the particles issued from the collision; the knock-on electrons are not included.
[2] The CBM run year is estimated to $5 \times 10^5\ s$, approximately 2 months (see Chapter 6).

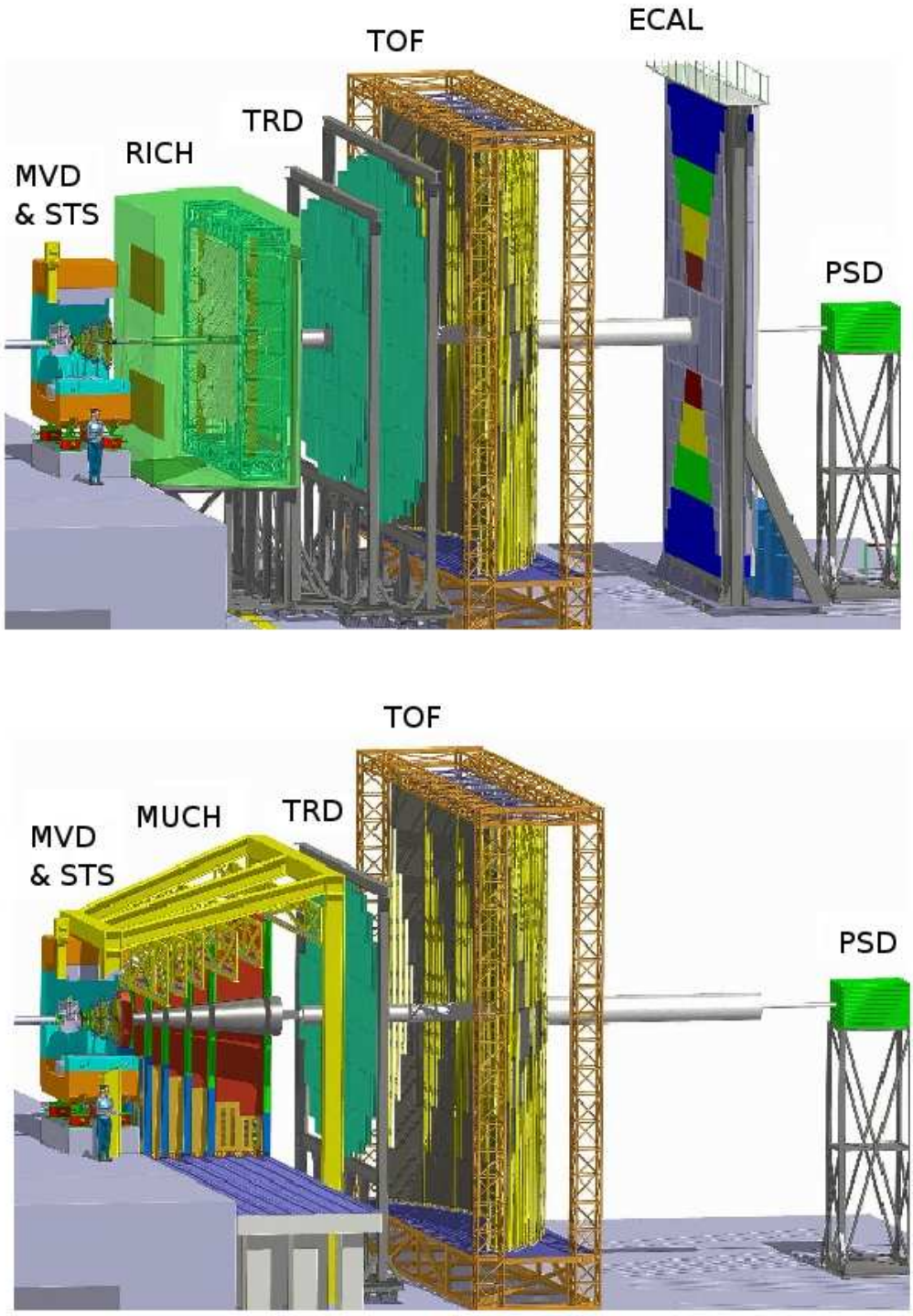

Figure 2.3: *Schematic view of the CBM experiment. The beam direction is from left to right. Following the target, there is the Micro Vertex Detector (MVD) and the Silicon Tracking System (STS). Both are located inside the dipole magnet (orange). The electron setup is shown in the top panel: The detectors situated more downstream are the RICH (green), three TRD stations (cyan, one close behind the RICH), a time-of-flight (TOF) detector and an electromagnetic calorimeter (ECAL). The muon setup is shown in the bottom panel. In the place of RICH there is a Muon Chamber (MUCH) and the ECAL is not present.*

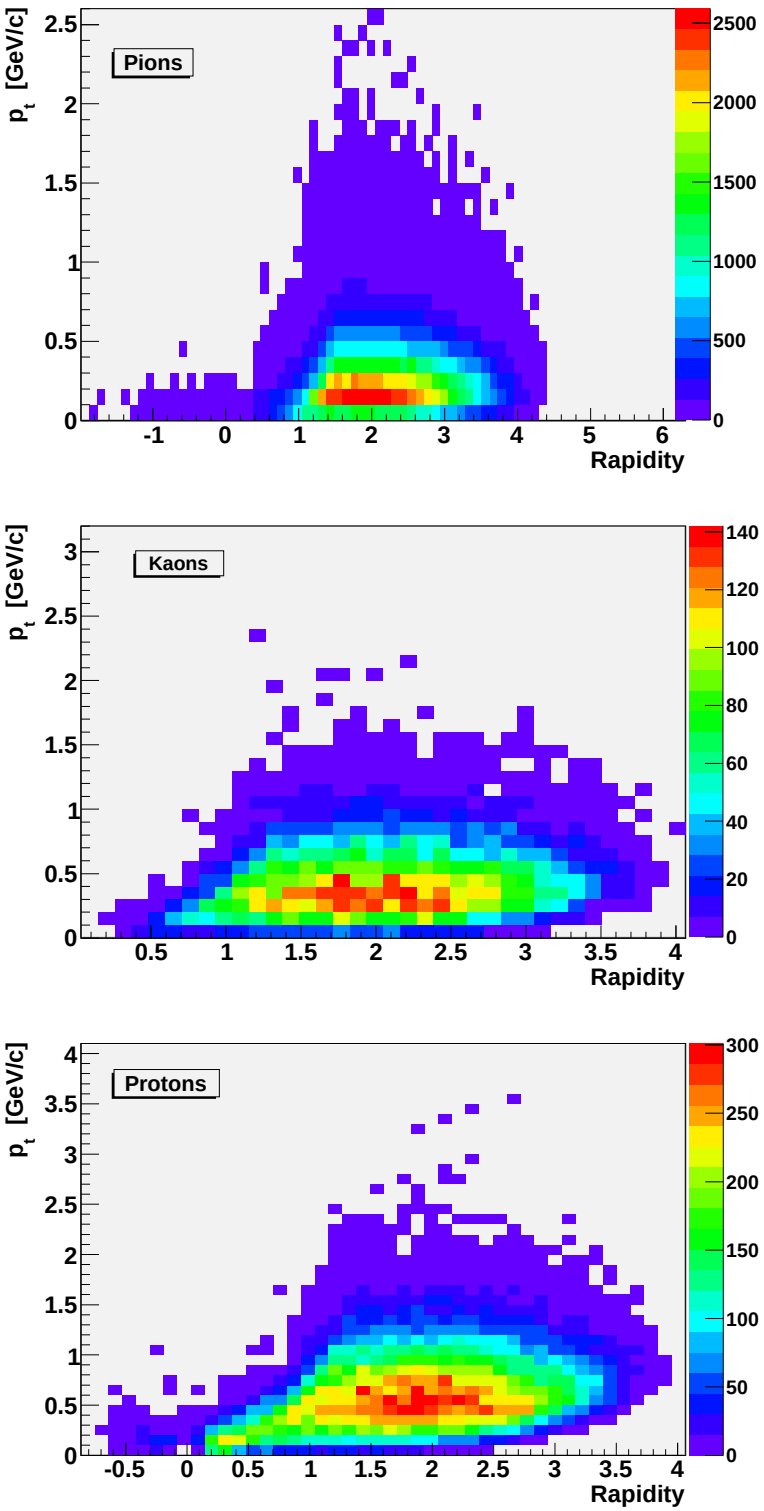

Figure 2.4: *Acceptance region for rapidity and transverse momentum for $\pi^{\pm}$ (top panel), $K^{\pm}$ (middle panel) and protons (bottom panel)*

2.3.2 The Silicon Tracker System (STS)

The Silicon Tracking System is the central component of the CBM experiment. It serves for track and momentum measurement of charged particles produced in the collision. A particular challenge for the STS is to achieve high track reconstruction efficiency in a high track density environment (typically, several hundreds charged particles per central Au+Au event within the acceptance of the STS). The requirements for precise and fast tracking in a combination with the high hit rates expected, put strong constraints on the material budget, the radiation tolerance and the readout speed of the STS.

In Figure 2.5, left, a schematical layout of the STS and the MVD is shown. The STS comprises 8 detector stations placed at 30, 35, 40, 50, 60, 75, 95, 100 cm distance from the target, and is fully based on low-mass Silicon micro-strip detectors with a pitch of 60 μm. The stations are placed inside a dipole magnet which provides the bending power required for momentum determination with an accuracy of about $\Delta p/p = 1\%$. The required time resolution of the STS is of the order of 10 ns, corresponding to a collision rate of 10 MHz. In the right-hand side of Figure 2.5 the modular structure of the stations is shown. Each station is made of double-sided micro-strip sensors. The strips on the front side are tilted by 7.5 degrees and on the back side by $-7.5°$ creating a stereo angle of 15 degrees. The read-out electronics is placed at the perimeter of the STS.

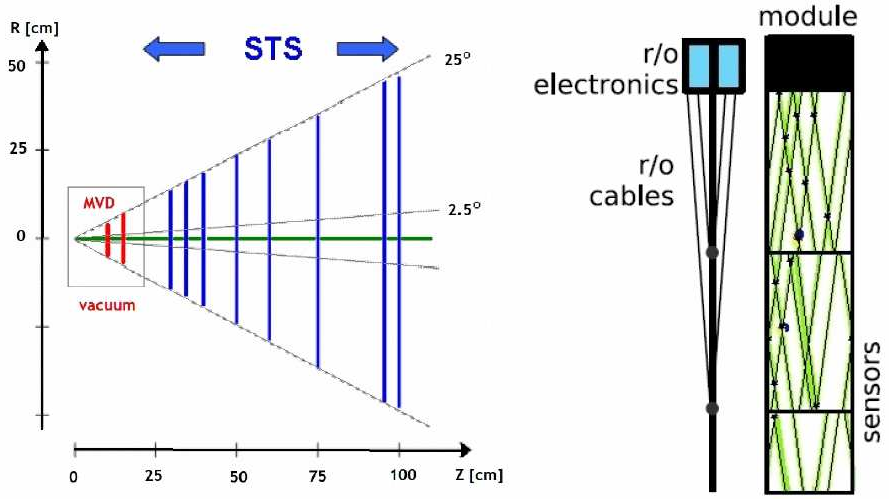

Figure 2.5: *Left: Layout of the STS and MVD stations. The locations of the stations and their polar angle coverage are indicated. Right: One STS module with the read-out electronics: side view and front view.*

2.3.3 The Superconducting Dipole magnet

Inside the dipole magnet, the charged particle trajectories are bended and their charge and momenta can be determined

The dipole magnet must host the target, the Micro-Vertex Detector (MVD), and the Silicon Tracking System (STS). Therefore its gap has to be large enough to permit the

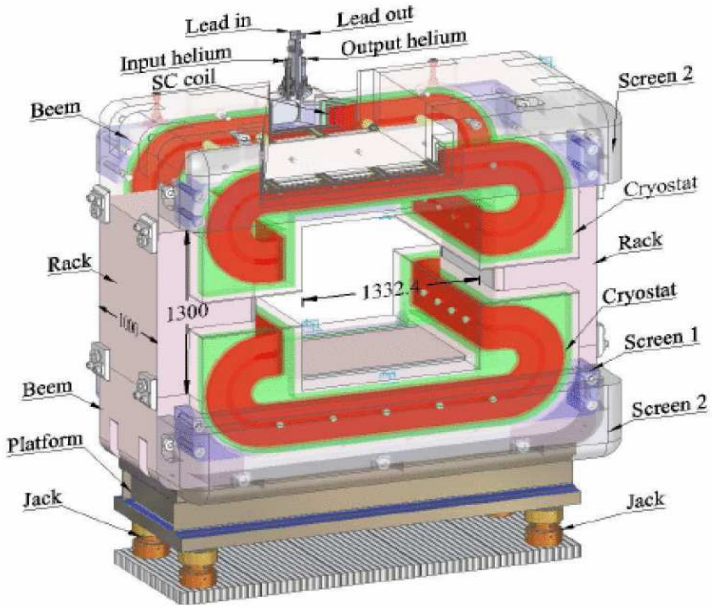

Figure 2.6: *The magnet and the coils (red) are shown.*

installation and maintenance of the STS and the MVD (not less than 1.3×1.3 m^2). For a good momentum resolution, a field of about 1.0 Tm is required in the region of the target. The angular acceptance of the magnet should cover 50° in vertical direction and 60° in horizontal direction. The conceptual design of the magnet is shown in Figure 2.6. The magnet is supplied with a yoke of magnetically soft steel with low carbon content. The upper and bottom beams form the poles of the magnet. Magnetic shields, reducing the field in the area of the RICH detector, are installed on the yoke. The superconducting coils have the "Cossack saddle" form, which allows to create a magnet with a minimal size along the beam.

2.3.4 The Time Of Flight detector (TOF)

The determination of the particle mass is done by measuring its momentum, p, and its time of flight:

$$m = \frac{p}{\gamma\beta c} = \frac{p\sqrt{1-\beta^2}}{\beta c} \tag{2.2}$$

where:

$$\beta = \frac{L}{c\Delta t} \tag{2.3}$$

L is the flight path length of the particle and Δt is the time difference between the start and stop signal of the TOF detector. A diamond pixel (or micro-strip) detector provides the start signal for the TOF measurement and can directly count beam particles at intensities of up to 10^9 ions/s. The TOF wall consists of approximately 60,000 independent cells providing a time resolution of about 80 ps. It will be composed of a large area (150 m^2) of Resistive Plate Chambers (RPC). The distance between the start detector and the TOF

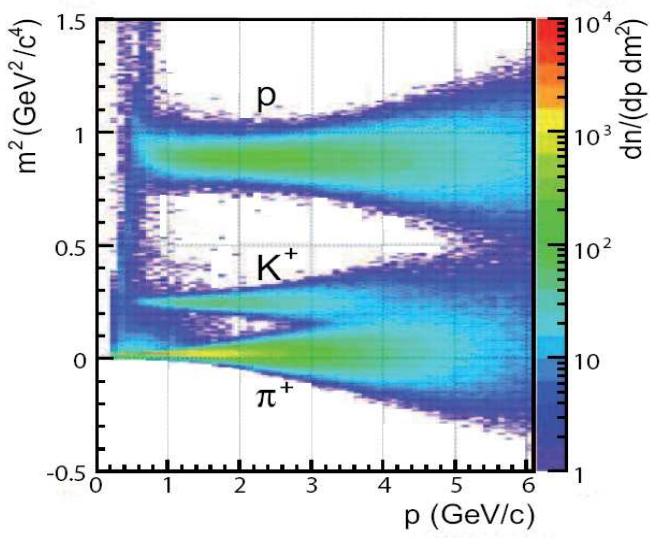

Figure 2.7: *Squared mass as a function of momentum of hadrons reconstructed by TOF in central Au+Au collisions at* 25 *AGeV beam energy [116].*

wall, of about 10 m, results in a time difference of 400 ps for pions and kaons of 3 GeV/c momentum. In order to handle the high beam intensity, the RPC chambers must cope with rates of up to 20 kHz/cm^2. Figure 2.7 shows the separation ability of TOF for pions, kaons and protons as obtained from realistic simulations [116]: a separation of kaons and pions can be achieved up to laboratory momenta of about 3.5 GeV/c, while protons can be identified up to 7 GeV/c.

2.3.5 The Transition Radiation Detector (TRD)

The TRD contributes to the electron identification and tracking of charged particles. For discriminating electrons from pions in the momentum region of a few GeV/c, a TRD exploits, one hand, their different energy loss through ionisation. On the other hand, electrons produce additional transition radiation which is then used by the TRD for their identification. Transition radiation is produced when a relativistic particle traverses an inhomogeneous medium, in particular the boundary between materials with different dielectric constants. Currently, the TRD is envisaged to be a system composed of three stations with three to four layers each, located at distances of 5 m, 7.25 m, and 9.5 m from the target. The total active area covered is about 600 m^2. Each layer consists of a radiator where the transition radiation is produced by electrons, and of a gaseous detector in which the deposited energy of charged particles and the transition radiation can be measured.

2.3.6 The Ring imaging Cherenkov detector (RICH)

Cherenkov counters contain two main elements: a radiator through which the charged particle passes and a photodetector. When a charged particle traverses the radiator with a velocity greater than the speed of light in that medium, Cherenkov light is produced. In

the RICH detector, this light cone is reflected by a mirror to a position sensitive photon detector, which allows to reconstruct the produced rings. The light is emitted under a constant Cherenkov angle δ with the particle trajectory, given by:

$$\cos\delta = \frac{1}{\beta n} \tag{2.4}$$

where n is the refractive index of the medium and β is the velocity of the particle in the medium.

In CBM, the RICH detector will serve for electron identification with momenta up to $10 - 12\ GeV/c$ and for π identification for higher momenta in order to improve the K/π separation which quickly deteriorates for $p > 4\ GeV/c$ if only time-of-flight information is used. A pion suppression of $10^2 - 10^3$ has to be provided by the RICH. In the current CBM detector layout the RICH would be placed behind the magnet (roughly 1.5 m downstream the target) and in front of the first transition radiation detector. It consists of a $\sim 3\ m$ long gas radiator, two arrays of spherical hexagonal mirrors, two photodetector planes and the corresponding support structure. High detection efficiency of electrons is required which calls for 10-15 hits per electron ring at minimum. As global tracking has to connect tracks in the STS and TRD, the RICH detector should not exceed 3 m and a material budget of 3-4 % radiation length in order to reduce multiple scattering. A large acceptance of 25° in polar laboratory angles has to be covered to identify the vector mesons in a wide range of rapidity and transverse momentum.

2.3.7 The Electromagnetic CAlorimeter (ECAL)

In CBM, a "shashlik[3] type calorimeter will be used to measure direct photons and neutral mesons decaying into photons. The calorimeter will be composed of modules which consist of about 140 layers of lead and scintillator material, with cell sizes of $3 \times 3\ cm^2$, $6 \times 6\ cm^2$, and $12 \times 12\ cm^2$.

2.3.8 The Projectile Spectator Detector (PSD)

The Projectile Spectator Detector is a forward hadron calorimeter which will be used to determine the collision centrality and the orientation of the reaction plane. The detector is designed to measure the number of non-interacting nucleons from a projectile nucleus in heavy ion collisions. The currently planned setup of the PSD consists of 12×9 modules, each with 60 lead scintillator layers with a surface of 10×10 cm^2. The scintillation light is read out via wavelength shifting (WLS) fibers by Multi-Avalanche Photo-Diodes (MAPD) with an active area of $3 \times 3\ mm^2$ and a pixel density of $10^4\ /mm^2$

2.3.9 The Muon Chambers (MuCh)

The second detector configuration in CBM (lower part of Figure 2.3) includes a Muon Chamber system. In this configuration, vector mesons like ρ, ω, ϕ, and J/Ψ, will be recon-

[3]The term "shashlik" refers to a pile of alternating slices of absorber (e.g. lead) and scintillator materials (crystal or plastic) used in calorimetry.

structed via their decay into dimuons instead of dielectrons. A possible setup for the Muon Chamber system is presented in Figure 2.8. The alternating absorber and detector layers

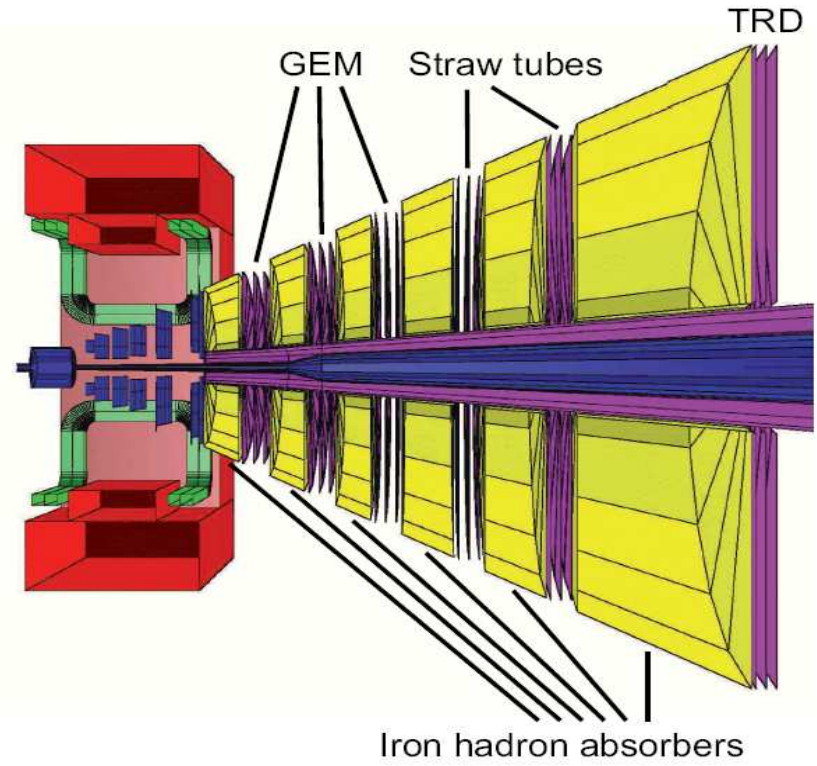

Figure 2.8: *The CBM muon detection system consisting of alternating layers of iron absorbers (yellow) and muon chambers (purple).*

serve respectively for hadron suppression and track reconstruction. Candidate technology for the detectors located in the absorber gaps are GEMs and straw tubes. The tracking and momentum determination of particles is done with the STS. The current design of the muon detection system foresees 18 detector stations and 6 segmented iron absorbers. In this case, the total material budget would correspond to 13.5 times the nuclear interaction length. The total area covered by the muon chambers is about 70 m^2.

2.3.10 Data Acquisition System (DAQ)

The need to measure rare probes like for example J/Ψ and open charm imposes the use of high interaction rates. The design of the DAQ system of CBM is motivated by the wish to operate the detector at a maximum collision rate of 10 MHz for Au+Au collisions. This motivated to design the DAQ of CBM as a free-streaming system without low level trigger. The functionality of the trigger is replaced by a self-triggered front-end electronics which recognises hits in the related sub-detector. The information on those hits is complemented with a time-stamp which is generated from a central time distribution system. Hereafter, the data is streamed in a push mode towards the central DAQ. The latter will presumably base on highly parallel multi-core computing systems which perform high level operations such as event building, real time tracking, and secondary vertex finding.

The Monolithic Active Pixels Sensors foreseen for the MVD are particularly well suited for this free-streaming trigger concept. This is due to two reasons, which will be discussed in detail in the following chapters: on one hand, and unlike to all other sensing systems used in CBM, MAPS are sensors using a frame readout which imposes a native data-push format. Moreover, the sensors foreseen for the MVD host integrated data sparcification circuits which allow for an efficient reduction of the data stream independently of any external trigger.

As discussed later in more detail, open charm reconstruction at CBM will take place at a reduced collision rate in the order of 10^5 collisions/s.

The trigger system for open charm reconstruction foresees to perform event building, tracking and secondary vertex finding by means of real time computing. Provided an interesting open charm candidate can be found based on the momentum and vertexing information delivered by the MVD and the STS, the data recorded by the other sub-detectors is analysed and the event is written on tape. This approach calls for robust and fast tracking algorithms which can be executed on multi core computing environments such as modern CPUs or GPGPUs (General Purpose Graphic Processing Units). The demanding task to develop such algorithms and computing systems is eased by the fact that open charm reconstruction in CBM will be carried out at a reduced collision rate in the order of 10^5 collisions/s. This collision rate is only moderately higher than the bandwidth of the mass storage system of CBM which will presumably allow to write 25 kHz [54] collisions/s on tape without pre-processing.

CHAPTER 3

The CBM Micro-Vertex Detector

This chapter is dedicated to the Micro-Vertex detector. It is divided in two main parts. In the first part, the operating conditions and the corresponding requirements are discussed and the choice of Monolithic Active Pixel Sensors (MAPS) is motivated. In the second part, we summarise the main features and limitations of the MAPS sensors and the present status of the R&D developments. The chapter ends with considerations on the technical design of the MVD detector.

3.1 Detection strategy for open charm particles

The major task of the CBM Micro-Vertex Detector is the reconstruction of D mesons in heavy ion collisions at FAIR energies. The strategy of the D-meson reconstruction in CBM is based on the separation of the displaced decay vertex from the primary collision vertex. This is illustrated in Figure 3.1, which shows a D^0 particle flying out of the primary collision point (PV) and decaying into a pion and a kaon pair. The particles produced in the collision (primary particles) are drawn with the dashed black lines; the products of the D^0 decay (secondary particles) are drawn in full red lines. The tracks reach the micro-vertex detector which has to reconstruct the vertices with sufficient precision to distinguish the primary vertex from the secondary one. This task is in so far challenging as the decay length of charmed mesons is very small (see Table 3.1). An excellent vertex resolution is therefore required.

Among the D-mesons, the D^0 particle is considered as the most difficult to detect. This is due to its very short lifetime (see Table 3.1). The task is further complicated by the fact that the measurements will be performed at beam energies close to the kinematical production threshold. According to the HSD model predictions shown in Figure 3.2, the D-mesons are presumably produced with very low multiplicities (below 10^{-3}) at FAIR energies, while pions and kaons will be abundantly produced (multiplicity of charged hadron is of the order of 10^2). Consequently, D-mesons have to be separated from an important combinatorial

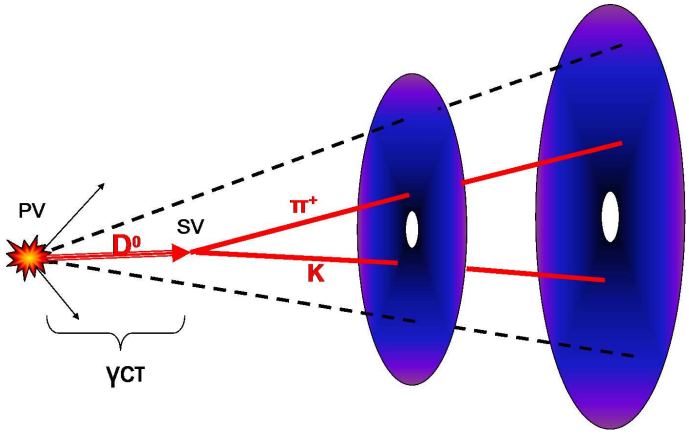

Figure 3.1: *Detection strategy for open charm mesons in CBM (see text).*

Particle	Quark content	Mass [MeV]	$c\tau$ [μm]	Decay channel	Branching ratio
D^+	$c\,\bar{d}$	1869.57 ± 0.16	311.8	$D^+ \rightarrow K^-\pi^+\pi^+$	$(9.13 \pm 0.19)\%$
D^-	$\bar{c}\,d$	1869.57 ± 0.16	311.8	$D^- \rightarrow K^+\pi^-\pi^-$	$(9.13 \pm 0.19)\%$
D^0	$c\,\bar{u}$	1864.80 ± 0.14	122.9	$D^0 \rightarrow K^-\pi^+$ $D^0 \rightarrow K^-\pi^+\pi^+\pi^-$	$(3.87 \pm 0.05)\%$ $(8.07^{+0.21}_{-0.19})\%$
$\overline{D}^0$	$\bar{c}\,u$	1864.80 ± 0.14	122.9	$\overline{D}^0 \rightarrow K^+\pi^-$ $\overline{D}^0 \rightarrow K^+\pi^-\pi^-\pi^+$	$(3.87 \pm 0.05)\%$ $(8.07^{+0.21}_{-0.19})\%$

Table 3.1: *Some properties of open charm mesons (from [2]). $c\tau$ is the mean life of the particle (τ) multiplied by the speed of light (c). Typical hadronic decay channels, which will be measured in CBM, and their corresponding branching ratios are indicated.*

background. Therefore, open charm measurements in nucleus-nucleus collisions at FAIR energies are very challenging, in particular in the case of heavy systems such as Au+Au. In the following, the detection of $D^0 \rightarrow K^-\pi^+$ in central Au + Au collisions at 25 $AGeV$ will be considered as a representative benchmark for assessing the performance of the MVD. Among the decay channels available, the decay into $K^-\pi^+$ was chosen as it is relatively easy to reconstruct since it has two charged hadrons.

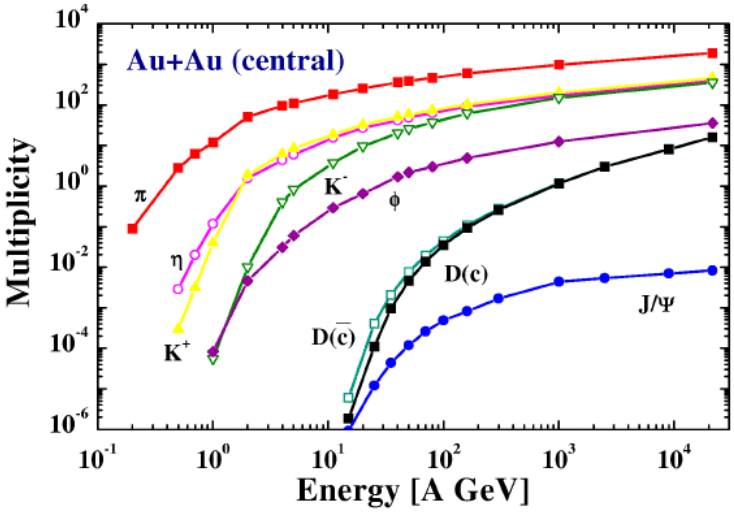

Figure 3.2: *HSD transport model predictions [53] for the multiplicity of mesons produced in central Au+Au collisions as function of the incident beam energy.*

3.2 Detection environment and requirements

3.2.1 Expected hit densities

Figure 3.3 shows the average number of hits in an MVD detector station as a function of its distance from the target. This figure has been obtained from detailed GEANT simulation studies performed for Au+Au collisions at different incident energies [61]. The results are shown for two cases: a) only for particles produced in the nuclear collision (dashed lines) and b) including delta electrons (full lines). The latter are electrons knocked out from the target by the primary beam. Note that, for this particular study, additional stations were placed in different distances from the target in order to sense the particle density at different potential locations for those stations. The material budget of these stations was 50 μm in order to minimise the production of secondary particles. The geometry was chosen as such in oder to save computing time. Alternatively, one would have to study the particle density on each station separately.

Assuming a 1% interaction target in these simulations, each nuclear collision is complimented by 100 Au beam ions passing the target without producing a nuclear interaction. These beam ions may however knock out delta electrons from the target. The delta electrons with momentum below 10 MeV/c are deflected out of the acceptance by the field of the dipole magnet. The tracks of delta electrons with higher momentum are bended by the field and are therefore concentrated in a well localised region (called hereafter "hot spot") on the MVD stations.

In Figure 3.3 one sees that if delta electrons are omitted from the analysis, the average number of hits per collision is below 200 and is roughly independent from the position of the station (dashed lines). On the other hand, when the delta electrons are included, they dominate the average number of hits per collision reaching 1600 hits/collision for a station

located at 5 *cm* (full lines). This number decreases with increasing distance from the target.

The hit density per mm^2 and per collision in the hot spots as a function of the position of the MVD disc is shown in Figure 3.4. The full (dashed) lines correspond to the results of the simulations with (without) the inclusion of δ electrons. The results are presented for Au+Au collisions at three beam energies, 15 $AGeV$, 25 $AGeV$, 35 $AGeV$. Like in the previous figure, one sees that the delta electrons dominate the hit density (per collision) which is up to 3.5 for the first station at 5 *cm*. Without delta electrons, the hit density (per collision) is below 0.5 $hits/mm^2$ for all stations.

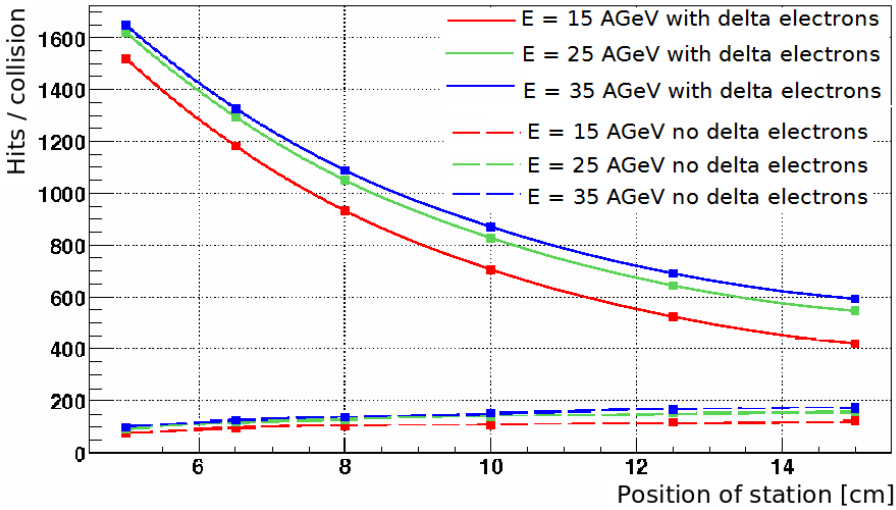

Figure 3.3: *The average number of hits on one MVD detector station per Au+Au collision as a function of the position of this station. Two cases are shown: with (full lines) and without (dashed lines) the inclusion of the contribution of delta electrons (see text). Three different incident energies were studied: 15, 25 and 35 AGeV [61].*

From these results, one concludes that at such high hit densities, up to 3.5 $hits/mm^2/collision$, the use of silicon pixel detectors with high granularity is imposed.

3.2.2 Expected radiation doses

The intense particle flux expected on the MVD will cause sizable radiation doses in particular for the station situated close to the target [55].

In silicon pixel detectors, one distinguishes the so-called ionising and non-ionising radiation doses. The term ionising radiation refers to interactions between the radiation and the penetrated silicon material, which deposit energy into the electron cloud of the silicon. Non-ionising radiation deposits energy to the nuclear cores of the detector material which may displace the latter from their position in the crystal lattice. In general, all particles may cause both types of radiation damage. However, neutral particles, e.g. neutrons, provoke only small ionising radiation damage since they rarely interact with the electron cloud. Light particles, namely photons and slow electrons, cause small non-ionising radiation damage as momentum conservation hampers the displacement of the nuclear core.

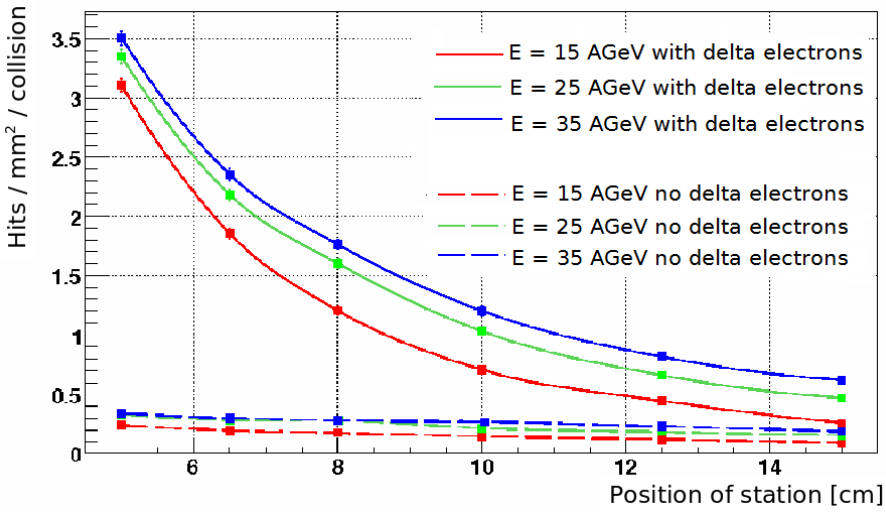

Figure 3.4: *Number of hits per mm^2 and per Au+Au collision in the hot spot region (see text) as a function of the position of the MVD detector station for three different incident energies: 15, 25 and 35 AGeV [61].*

As the microscopic and macroscopic damage caused by ionising and non-ionising radiation damage in Si is quite different, it is generally accepted to perform a separate dosimetry for each type of damage.

The expected ionising and non-ionising radiation doses in the CBM experiment were evaluated with systematic simulations [55, 56]. They were normalised for one typical CBM running year which is assumed to have an effective duration (i.e., beam on target) of $\sim 5 \times 10^6$ s (about two months). Assuming a nominal beam intensity of 10^9 beam particles per second and an interaction probability of 1% in the target, one expects that roughly 5×10^{13} collisions will take place during this period.

In reference [55] the expected radiation doses in the MVD detector were evaluated using GEANT3 [152] complemented by the GCalor [153] package. The UrQMD model was used to simulate heavy ion collisions. The generation of delta electrons was done with GEANT by propagating Au ions (created with a dedicated ion generator) through the target.

The non-ionising dose provoked by the different particles was calculated with the help of the NIEL factor which normalises the radiation damage with respect to the one caused by 1 MeV neutrons [154, 155]. For the ionising dose, it was assumed that all charged particles are minimum ionising. It was found that the radiation dose impinging the MVD detector stations may reach up to 70 μRad and 30.2 n_{eq}/cm^2 per Au+Au collision at 25 $AGeV$ for, respectively, ionising and non-ionising radiation dose.

To obtain the ambitioned requirements on the radiation hardness of the MVD one has to normalise the numbers according to the beam intensity. As discussed in Section 2.2, CBM will operate in two major phases: the first phase starts with the measurements at the SIS-100 synchrotron. The second phase starts at SIS-300 and includes the open charm measurements in A+A collisions. Currently, for the second phase at SIS-300, two stages are foreseen for open charm measurements with the CBM-MVD. The detector requirements

will be more relaxed for the first stage, while an upgrade is foreseen for the second stage. Due to various technological constraints, which will be discussed later in this thesis, it seems reasonable to operate a first generation MVD with a collision rate of $\sim 10^5$ $collisions/s$. Under these conditions, the start version of the CBM-MVD at SIS-300 should be tolerant to 10^{13} n_{eq}/cm^2 and ~ 2 $MRad$ per CBM running year [132].

The design of the MVD at SIS-100 will not be discussed in this thesis as the detector requirements for the measurements of open charm at p-p and p-A collisions at SIS-100 are less stringent due to the lower particle multiplicities.

3.2.3 Spatial resolution and material budget

The reconstruction of the secondary vertex of open charm particles imposes strong constraints on the vertex resolution. The latter determines the requirements of two key parameters, the spatial resolution and the material budget of the MVD stations. As mentioned earlier, the secondary vertex is reconstructed by extrapolating tracks from the MVD to the target. The precision of this extrapolation depends dominantly on the precision of the position and momentum measurement performed by the detector. The relevant position measurement is typically carried out by the most upstream MVD accepting the track. The better the spatial resolution of this station is, the better the accuracy of the position measurement. The momentum is measured by the MVD and the STS and its precision depends mostly on the precision of the STS. The uncertainty on the extrapolation is however dominantly caused by the direction of the momentum $\vec{p}$, which is modified by multiple scattering. The most crucial effect is the multiple scattering in the most upstream MVD station. As the related modification of the particle trajectory cannot be measured, it has therefore to be minimised by reducing the material budget of the station.

The combined influence of the spatial resolution and the material budget of the detector on the vertex resolution has been studied systematically [156]. Figure 3.5 shows the dependence of the secondary vertex resolution of $D^0 \rightarrow \pi^+ + K^-$ on both parameters. The detailed assumptions on the detector geometry used in the study are presented in Table 3.2. The study relies on an elder geometry of CBM as proposed in [52] and is meanwhile considered as outdated. However, it is similar enough to the current standard geometry so that there is no significant difference in the secondary vertex resolution between the results obtained with both MVD detector geometries. The MVD stations (stations (1), (2) and (3) in the Table 3.2) were assumed to be pixel-based. Their thickness and spatial resolution were varied in the simulations (Figure 3.5) in order to investigate their influence on the D^0-meson secondary vertex resolution. The thickness of the MVD detector layers is given in μm of silicon for each individual detector stations. It represents the full material budget of the station including support structure, cables and cooling system. The STS stations (stations (4) to (7) in Table 3.2) were assumed to be composed of 300 μm thick silicon strip detectors.

The secondary vertex resolution was determined by the distribution of the difference between the reconstructed secondary vertex position and the real vertex position. This distribution can be fitted with a Gaussian function and the standard deviation of the fit function is defined as the vertex resolution. The detector spatial resolution was simulated with a Gaussian smearing of the real position of the particle (known in the simulations).

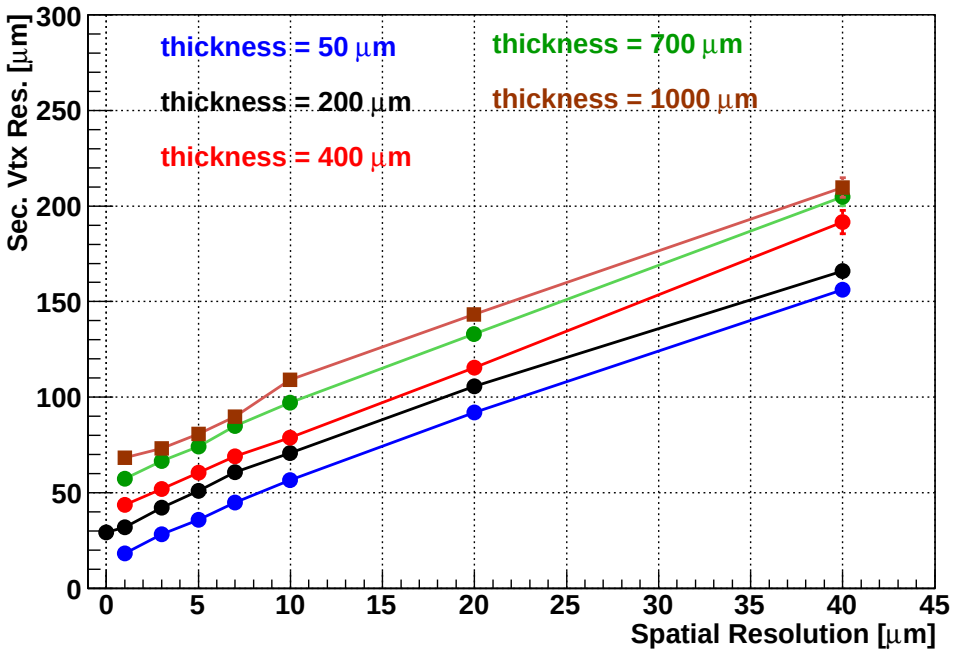

Figure 3.5: *The impact of the thickness (in μm of Silicon) of the MVD stations and the detector spatial resolution on the z-coordinate (along the beam direction) of the secondary vertex resolution for D^0 decay measurements with CBM.*

Station	**z**	$\mathbf{R}_{Inner}$ **[mm]**	$\mathbf{R}_{Outer}$ **[mm]**	Technology
1	5 cm	5.5	25.0	Pixel
2	10 cm	5.5	50.0	Pixel
3	20 cm	10.5	100.0	Pixel
4	40 cm	20.5	200.0	Strips
5	60 cm	30.5	300.0	Strips
6	80 cm	40.5	400.0	Strips
7	100 cm	50.5	500.0	Strips

Table 3.2: *Distance from the target, inner and outer radii for each of the tracking detector stations of the CBM experiment. The first three stations (pixels) constitute the MVD vertex detector. Note that this geometry is different from that of Figure 2.5*

As expected, the resolution on the secondary vertex deteriorates with an increasing material thickness and with a less precise detector (Figure 3.5). To achieve, for example, a vertex resolution of 50 μm, a material budget of $\sim$ 200 μm and a spatial resolution of 5 μm are required; alternatively 400 μm thick detectors with spatial resolution of 3μm may be used.

3.3 Pixel detector technologies

The extremely high particle densities expected in the MVD detector stations (see Section 3.2.1) impose the use of silicon pixel detectors. Traditionally, Hybrid Pixels [72] and Charge Coupling Devices (CCD) [72] were used for this purpose.

Hybrid pixels are silicon semiconductor detectors in which the readout electronics and the pixel sensors are fabricated separately and then connected to each other by ball bonding (hence the name hybrid). Each readout cell contains a full amplifying chain with integrated discriminator logic and data buffer. The pixels can have a surface as small as $\sim 100 \times 100\ \mu m^2$. Hybrid pixels have very good time resolution ($25\ ns$) but are not necessarily able to handle high rates[1]. Their spatial resolution[2] is $\sim 30\ \mu m$ and their radiation tolerance may reach ($10^{15}\ n_{eq}/cm^2$) [72]. However, due to the presence of two separate chips bonded to each other and due to the balls used for bonding, the material budget of this device (including support structure, cooling, cables etc.) is substantial ($\sim 1\%\ X_0$).

CCDs are based on the principle of a sidewards depletion of a double-diode structure [72]. The charge is confined in a single well by potential barriers. The stored charge packets can be transferred along each column towards the readout electronics. The very high granularity (pixel size $\sim 10\ \mu m$) complemented by a large area of the detector (millions of pixels) make CCDs a very attractive solution for tracking devices. Moreover, CCDs show small noise and can be thus thinned down to low material budget ($\sim 0.1\%\ X_0$ for the sensor thickness). The readout is a relatively slow process and it takes a substantial amount of time to readout a large sensor ($\gtrsim 50\ \mu s$). Moreover, CCDs have a poor radiation hardness ($\lesssim 10^{10}\ n_{eq}/cm^2$), as a substantial part of the signal charge is trapped by radiation induced effects during the transfer.

Table 3.3 lists the requirements of the start up phase of the CBM-MVD at SIS-300 (see for example Section 3.2.2, for more details see [132]) and compares them with the present and expected performances of MAPS sensors [132]. In CBM, the construction of the detectors will begin in 2015 and first data will be taken in 2018 [**?**]. Given that further progresses will be done during the R&D of the MAPS sensors, one might foresee an upgrade of the MVD after few years of operation (e.g. use sensors developed by 2018). From this table it is obvious that Hybrid pixels and CCDs are not adapted for the CBM-MVD. On one hand, hybrid pixels feature the required radiation hardness and time resolution but do not match the requirements of CBM in terms of spatial resolution and material budget. They do not therefore reach the sensitivity needed for open charm reconstruction at CBM (see Figure 3.5). On the other hand, CCDs provide the required spatial resolution and material budget for the starting phase of the CBM-MVD but show insufficient radiation hardness and time resolution.

[1] The time resolution of a detector corresponds to the time precision with which it can identify a particle hit. This should not be confused with the bandwidth needed to transport the data to the data acquisition system. In the particular case of MAPS, the time resolution and the readout time are equal.

[2] Derived from the typical pixel pitch assuming digital readout.

	Start phase (SIS-300)	MAPS 2010	MAPS 2015	MAPS 2018
Spat. Res [μm]	$\lesssim 5$	~ 5	~ 5	~ 5
Mat. Budget [X_0]	$\sim 0.3\%$	$\sim 0.05\%$	$\sim 0.05\%$	$\sim 0.05\%$
Rad. Hard. [n_{eq}/cm^2]	$few\ 10^{13}/year$	$> 10^{13}$	$> 10^{14}$	$> 10^{14}$
Time resolution	$few\ 10\ \mu s$	$110\ \mu s$	$\sim 30\ \mu s$	$few\ \mu s$

Table 3.3: *Required performances for operating the CBM-MVD at SIS-300 compared to the present and future MAPS sensors performances [132]. The material budget required for the start phase refers to a complete detector (including support structure, cables etc.) while the material budget of MAPS refers to sensors only (see text).*

3.4 Monolithic Active Pixel Sensors

As the established technologies were ruled out, the use of the Monolithic Active Pixel Sensors (MAPS) has been envisaged. MAPS is a silicon detector technique which allows integrating on the same substrate the detector element and the processing electronics. This new technology was proposed in 1999 by the IReS[3]-LEPSI[4] (Strasbourg) group to be used for devices for high-energy charged particle tracking [67]. Since then, numerous MAPS prototypes with different characteristics (pixel architecture, substrate type, epitaxial layer thickness) have been built and tested and have shown very promising performances in terms of charged particle tracking.

This technology provides a good compromise between rate capability and sensitivity according to the requirements for the CBM-MVD as listed in Table 3.3. MAPS sensors may be thinned down to $\leq 0.05\%$ X_0 without any performance loss [124]. Due to their small pixel pitch ($< 30\ \mu m$) their spatial resolution can be better than 3 μm in case of analogue readout and $\sim 5\ \mu m$ in case of digital readout.

Moreover, the fabrication of MAPS is based on standard industrial processes, which includes a low production cost. The processing electronics is integrated on the same substrate as the sensing element, which gives a better mechanical stability than for other technologies and eases the detector integration. They also have relatively low power dissipation ($1\ W/cm^2$). It has been demonstrated that MAPS devices with 10 μm pixel pitch can tolerate a non-ionising dose of about 10^{13} n_{eq}/cm^2. The latter value could be improved to reach 10^{14} n_{eq}/cm^2 [125]. Latest MAPS chip generations include complex microelectronic circuits that allow to perform on-chip signal processing such as CDS[5] and data sparcification [126]. Their performance has been substantially improved over the last few years. The present limits are indicated in Table 3.3.

3.4.1 Operation principle of MAPS

A cross section of a typical MAPS device is presented in Figure 3.6. A MAPS sensor is composed of three differently P-doped silicon layers. A moderately doped epitaxial layer,

[3]Institut de Recherches Subatomiques
[4]Laboratoire d'Electronique et de Physique des Systèmes Instrumentaux
[5]CDS:Correlated Double Sampling, see Chapter 4

which forms the sensitive volume of the device, lies in between two highly doped layers: the substrate and the P-wells. During the fabrication of a MAPS sensor, the substrate serves as the seed crystal for the growth of the epitaxial layer. It also contributes to the mechanical stability of the device. The doping levels of the substrate and the P-wells are several orders of magnitude higher than of the epitaxial layer.

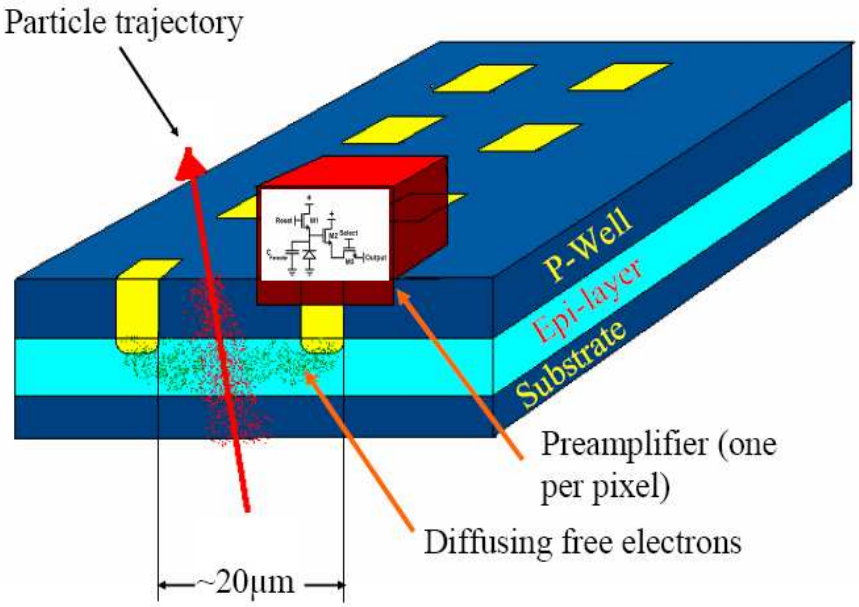

Figure 3.6: *Schematic view of a cross section of a MAPS device [55]. The epitaxial layer is shown in cyan and the collecting diodes are indicated by the yellow areas. The red box is a representation of one pixel and does not correspond to a real implementation. The distance between two collecting diodes is typically* $\sim 20\ \mu m$.

The epitaxial layer forms the undepleted sensitive volume of the device. A minimum ionising particle[6] penetrating this layer generates roughly 80 electron/hole pairs per micrometer particle trajectory in the volume.

The electrons diffuse in the epitaxial layer but cannot leave it due to the repulsive field generated by the P^+/P^- junctions [70].

They are collected by regularly implanted N-wells which form together with the epitaxial layer the charge collection diodes.

The charge collection time for a typical pixel pitch of 20 μm, was found to be $\lesssim 100\ ns$ [70] which is substantially longer than for conventional depleted detectors.

The typical thickness of the epitaxial layer is $10 - 20\ \mu$m. The typical charge from a MIP of (80 electrons per μm)$\times$(15 μm)$\simeq$ 1200 electrons. Due to the charge collection by

[6] A minimum ionizing particle (MIP) is defined as a relativistic particle with charge $Z = \pm e$. According to the Bethe-Bloch formula, the minimum energy deposit occurs for a factor of $\beta\gamma \approx 3 - 4$, which defines the speed of this particle. The MIP is the charged particle, which is most difficult to detect when passing a sensor. It is therefore regularly used to benchmark detectors.

thermal diffusion, this charge is distributed over a cluster of roughly 3×3 pixels.

The signal is low as compared with the signal generated by a MIP in the 300 μm thick sensitive volume ($80 \times 300 \simeq 2.4 \times 10^3$ electrons). This small amount of signal requires a low noise readout chain in order to provide a high signal-to-noise ratio, allowing thus for high detection efficiency.

3.4.2 Pixel architectures and readout concept

3-Transistor pixel architecture

The first stage of this readout chain is formed by a pre-amplifier integrated in each pixel. The most established architecture of this amplifier is found in the 3-Transistor (3T) pixel. A simplified schematic view of this pixel is shown in Figure 3.7.

The collection diode of this pixel is denoted as "D_{coll}". The reset transistor M1 is used to connect the collecting diode periodically to the bias voltage which is to compensate for a voltage drop at the parasitic capacity of the diode (C_{par}) which is due to leakage current. The transistor M2 constitutes one part of a source follower which is used for buffering the node K. The current source of the source follower is located outside the pixel. The transistor M3 is a row selection switch and is used to select all pixels in a row to read out. As discussed later, the column selection switch is located outside the pixel.

With this preamplifier, the pixel forms a charge integrating device and performs continuous charge integration within time between two consecutive reset operations. These are denoted with the circles with red colour, and with the circles with cyan colour, in Figure 3.8 which shows the signal encoding of the 3T pixel. In this figure, three readout cycles are

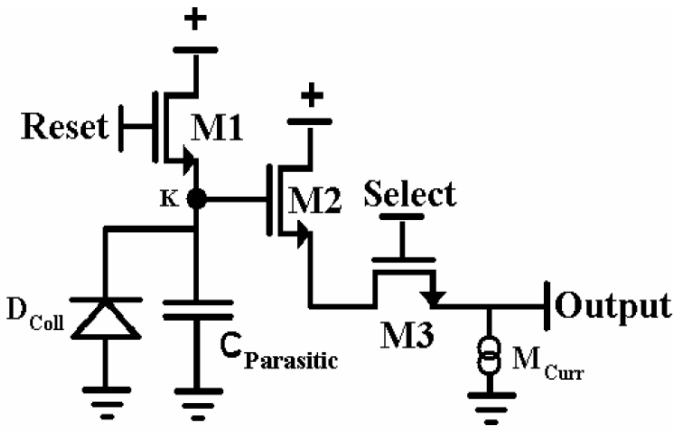

Figure 3.7: *Schema of a 3T pixel layout.*

shown. The middle one represents a cycle with the passage of a particle. The integration time $\tau_{1,2}$ of the pixel starts at the first sampling (red circle) and ends at the second sampling (consecutive cyan circle). Between these two points, and while the switch M1 is opened, a voltage drop occurs on the capacitor ($C_{Parasitic}$), which has as an origin the leakage current

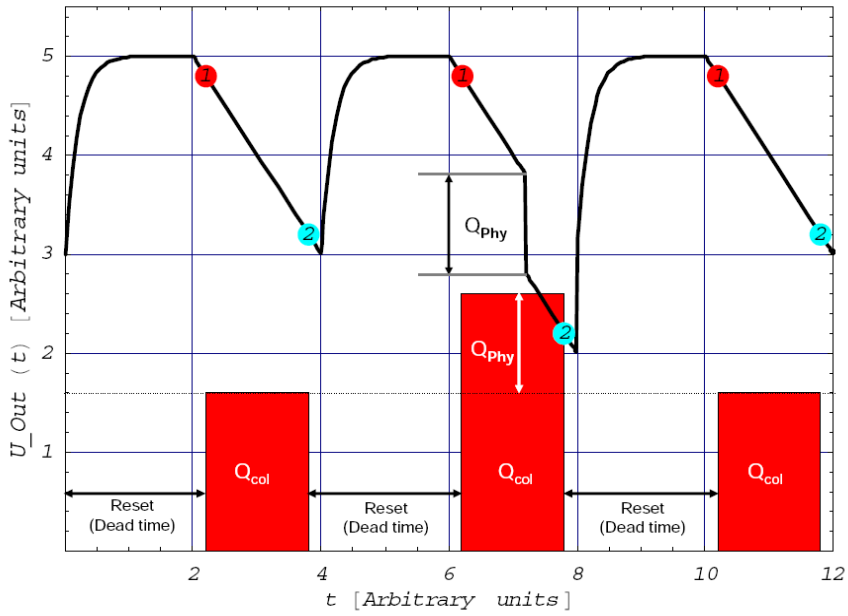

Figure 3.8: *Signal encoding for the 3T pixel [55]. The potential U_{out} corresponds to the node K of Figure 3.7. The bar diagram corresponds to the difference in potential between points (1) and (2).*

of the collecting diode. In this period of time, the pixel is twice connected with the readout system and the potential is converted by an external ADC[7]. After this time, the switch M1 is closed, which resets potential of the node K to the initial level. The time of reset, more precisely the time between the point 2 and point 1 of the next cycle, forms the dead time of the detector.

In the second cycle shown in the picture, the passage of a charged particle provokes a rapid voltage drop as the related signal electrons are collected by the diode. This voltage drop is added to measured signal amplitude of the one caused by the leakage current.

The charge collected during an integration time is derived using the Correlated Double Sampling (CDS)[8], which computes the voltage difference between the readout 2 and 1.As illustrated in Figure 3.8, this difference is enhanced due to the charge collected after the passage, Q_{phys}.

Self-Biased pixel architecture

An obvious weak point of the 3T-pixel is the dead time caused by the reset of the pixel. This issue was solved with an improved pixel design, the so-called Self-Bias pixels (SB-pixels, see Figure 3.9).

The concept of SB pixels is to replace the reset transistor (M1, in the left side of Figure 3.7) by a forward biased diode (D_{Bias}). The biasing diode continuously compensates

[7] Analogue to Digital Converter
[8] for more details on the CDS, the reader is referred to Chapter 4.

for the leakage current and stabilises the potential of the pixel. The reset cycle and the related dead time become therefore obsolete.

Figure 3.10 shows the signal encoding of the SB pixel. Several frames are shown before and after the passage of a particle. Initially, the voltage is at a constant level (frames denoted as F-3, F-2, F-1). Between F0 and F1, a particle deposits a charge Q_{phy} which turns into a drop of the pixel potential. This is followed by a recharge process (frames F1 to F12) which must have a substantially slower time constant than the time between two pixel readouts.

Despite it is in principle not mandatory, CDS is also used for SB pixels since it allows to compensate variations of the charge of the pixel capacity. These variations depend on the history of the pixel and can be substantial. Moreover, CDS provides a differential shaping of the output signal of the pixel which eases signal discrimination. After CDS, the indicated signal is slightly lower than expected from the charge deposited by the particle. This is due to the fact that the recharge process of the pixel removes a small fraction of the signal already before readout.

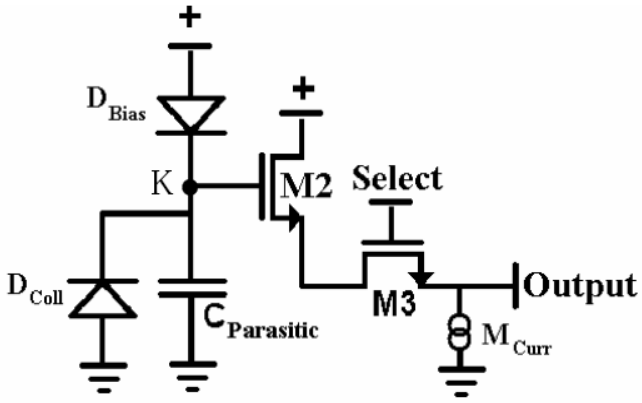

Figure 3.9: *Schema of a self-biased pixel. The reset transistor (M1) has been replaced by a bias diode.*

Readout

Conventional MAPS chips are designed as an array of pixels with the readout and processing electronics located at the periphery of the chip. Any pixel in the array is connected to analogue output and can be accessed by selecting the line and row by means of two shift registers. The pixels are read sequentially which will be referred to as *serial readout*. Their output signal is multiplexed and driven by an output amplifier to the outside world. Once all pixels in the matrix have been read out, the process re-starts from the first pixel. In general, the time resolution, which expresses the time precision with which the detector identifies an impact, is equal to the readout time of a frame. Note that for MAPS the time resolution and the readout time are equal and these terms will be used in an equivalent

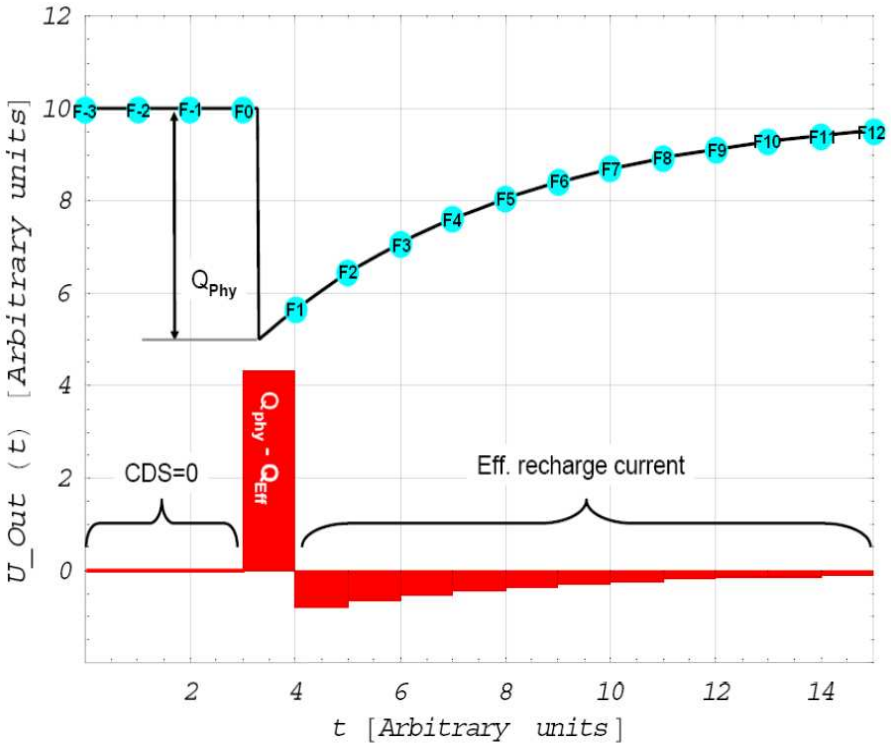

Figure 3.10: *Signal encoding for the self-biased pixel [55]. The potential U_{out} corresponds to the node K of Figure 3.9. The bar diagram corresponds to the difference in potential between two consecutive points (shown in light blue).*

way in the following. A typical readout time for the serial readout approach is of the order of 1 ms.

The time needed to read out a complete pixel matrix is obviously proportional to the time needed to read out an individual pixel and on the number of pixels in a matrix. A speed up can therefore be reached by subdividing this matrix and performing the readout by several parallel output channels.

3.5 Development status of MAPS sensors

In this section, we summarise the features of the latest generations of MAPS sensors, MIMOSA-25[9] [125] and MIMOSA-26 [126]. MIMOSA-25 shows very good performances in terms of radiation tolerance and MIMOSA-26 includes integrated signal processing which are two important features for the design of the CBM Micro Vertex Detector.

The standard CMOS technology used for conventional MAPS sensors with an undepleted, low resistivity epitaxial layer (see Section 3.4.1), seems to reach a limit in radiation tolerance at the fluence of the order of 10^{13} n_{eq}/cm^2 [131]. MIMOSA-25 chip is the first sensor prototype fabricated with a process that uses a high resistivity epitaxial layer with a commercially available technology [127], which allows for a depletion depth of several

[9]standing for Minimum Ionising MOS Active pixel sensor

micrometers[125], instead of a fraction of micron in the case of low resistivity. Due to the presence of a larger depleted area, the path length of the charge carriers is shorter, which leads to a faster charge collection and an improved charge collection efficiency. Thus, this technological evolution is expected to substantially improve the radiation tolerance of MAPS, up to $10^{14} n_{eq}/cm^2$) [128]. However, the feature size[10] used for this technology (0.6 μm) makes the design of complex MAPS with integrated signal processing difficult.

The option to build full reticle size MAPS sensors with integrated signal processing was for the first time investigated with MIMOSA-26, shown in Figure 3.11. This sensor was fabricated with a technology that uses smaller feature size (0.35 μm). The size of the chip is 21.5×13.8 mm and the sensor matrix is composed by 576×1152 pixels of 18.4 μm pitch. The pixel design is based on self biased diode architecture. The thickness of the epitaxial layer is 14 μm. In MIMOSA-26 all the pixels in a row are read out simultaneously and the rows are

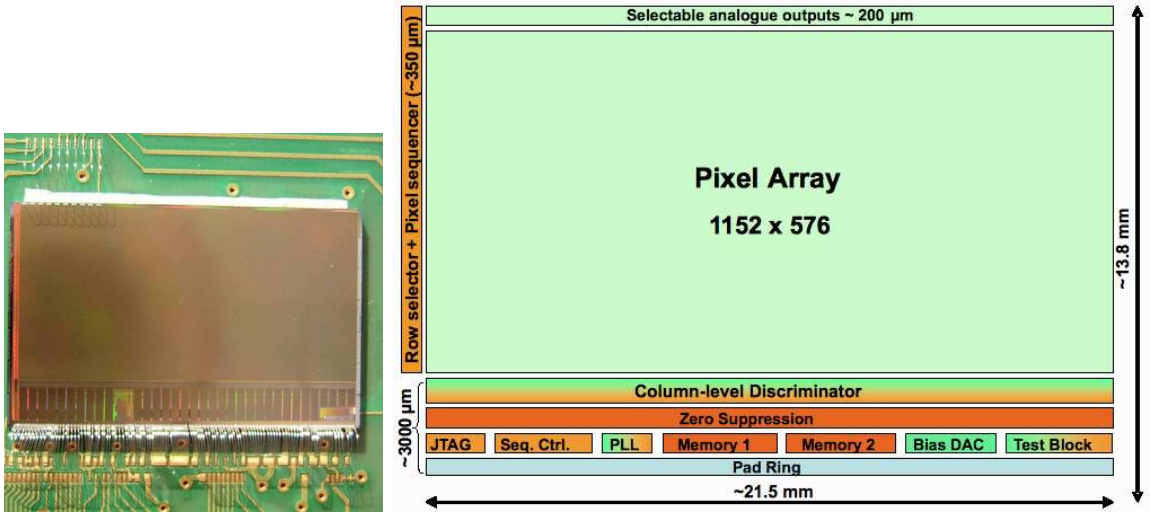

Figure 3.11: *Left: Photograph of the MIMOSA26 sensor bonded on a PCB. Right: Schematic view of the MIMOSA-26 sensor [126].*

read one by one in a *rolling shutter* mode. This approach helps achieving a readout time of 115.2 μs at an operation frequency of 80 MHz. On one side of the sensor (the top, as it is shown in Figure 3.11), an analogue output is implemented for test purposes. On the other side (the bottom part of the sensor, as it is shown in Figure 3.11) the signal processing units are located. Each pixel includes a preamplifier and circuits performing analog correlated double sampling (CDS). Each end of column is equipped with a discriminator. The binary data generated by those discriminators are compressed by a zero suppression logic [129] in order to restrict the delivered information to the most essential one. The zero suppression logic selects only pixels that give a signal above the discriminator threshold. The address and length of the consecutive fired pixels are then stored in embedded memories. The advantage of this concept is that it allows for a reduced amount of data flow which may be then stored and treated. MIMOSA-26 has been fabricated with two different substrates:

[10]The feature size corresponds to the minimum transistor channel length possible to implement in a given CMOS process.

one with a standard resistivity epitaxial layer ($\sim$ 10 $\Omega \cdot cm$) and the other with a high resistivity epitaxial layer ($\sim$ 400 $\Omega \cdot cm$), both in 0.35 μm technology. Hereafter, we will discuss only the properties of the latter.

Preliminary results [130, 128] performed in the laboratory with a ^{106}Ru β source, indicate that the charge collected on the seed pixel is about twice larger than with a standard epitaxial layer, while the noise stays nearly unchanged. Even after a fluence of 10^{13} n_{eq}/cm^2, the signal-to-noise ratio remains above 15.

The ionising radiation tolerance of MIMOSA-26 is currently under study. Preliminary beam test results demonstrate excellent performances of the sensor after an exposure to $\sim$ 300 $KRad$ soft X-rays [136]. The tolerance of this sensor to higher doses is currently being studied. Given that the radiation tolerance needed for the start version of the CBM-MVD for SIS-300 has already almost been reached with sensors with serial readout[11] [55], it will be assumed in the following that the ongoing R&D will allow increasing the radiation tolerance of MIMOSA-26 against ionising radiation to the necessary level ($\sim$ 2 $MRad$) for the start version of the MVD at SIS-300.

3.6 MVD detector design considerations

Several considerations have to be taken into account for building a complete MVD detector composed of MAPS. The integration of MAPS sensors into a complete MVD detector is a project being currently carried out by the CBM-MVD Collaboration constituted by the Institut für Kernphysik (IKF) at the Goethe University Frankfurt/Main and the Institut Pluridisciplinaire Huber Curien (IPHC). The system integration of the MVD is guided by two main requirements: the need for low material budget combined with vacuum operation.

The strategy for building a detection system fulfilling those requirements will presumably base on the following concept:

- Due to the presence of the signal processing units, a part of the sensor is inactive, thus an overlap of the MAPS sensors has to be foreseen in order to obtain a detector with 100% active area.
- Moreover, the sensors need to be cooled down to -20 degrees in order to control their radiation induced leakage current. This and the need to operate the sensors in vacuum require the use of a cooling system.
- Thin flexprint cables are used to transfer the data form the sensors to a front-end electronics board located outside the detector acceptance. All these elements need to be stabilised with a support structure.

So far, the precise geometry of the MAPS chip to be used for the MVD is not defined. However, the chip will likely be derived from MIMOSA-26 which shows promising performances in terms of non-ionising radiation hardness and on-chip data processing [137]. The dimensions of the chip correspond to the larger reticle size available ($\sim 20 \times 6$ mm^2).

The readout speed of MAPS depends on the length of the pixel column. In order to make the sensor sufficiently fast, the future chip will be composed of shorter columns than MIMOSA-26. The shape of the sensor as currently envisaged is shown in the left part of

[11] MIMOSA-15 sensor has demonstrated an ionising radiation tolerance up to 1 $MRad$

Figure 3.12. The sensitive area of the chip is in light blue while the signal processing units are in light grey. The arrangement of the sensors on the first MVD station are shown on the right part of the figure [133].

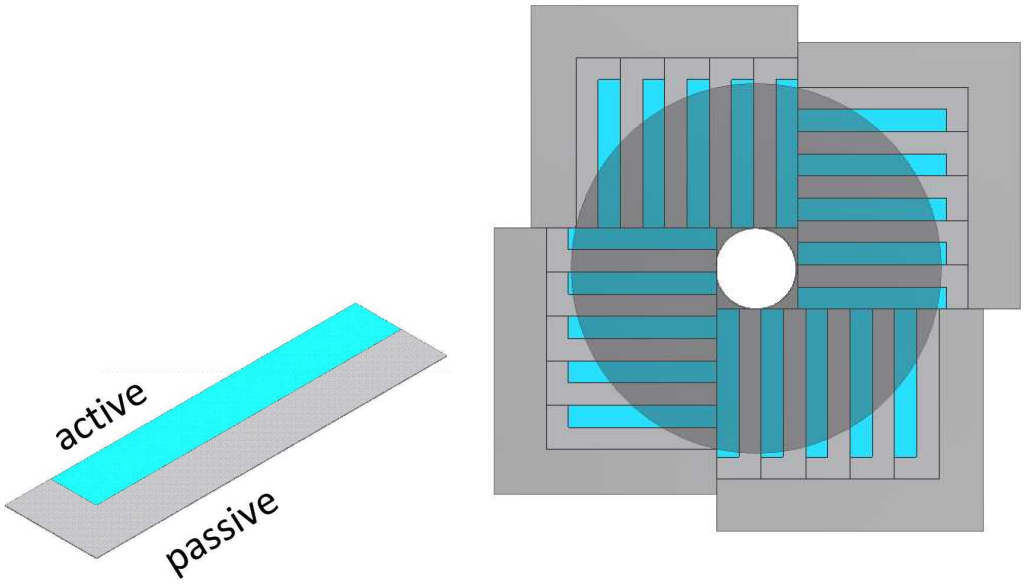

Figure 3.12: *Schematic representation of a possible shape of the future MAPS chip (left). It has 6 mm in width (3 mm active surface) and 23 mm in length (20 active surface, in blue). On the right hand side, a possible arrangement of the sensors on the front side of the first MVD station located at 5 cm downstream the target is shown. The shaded disc represents the MVD as implemented currently in the simulation. On the back side of the station (not shown here), the sensor arrangement is such that 100% of the area of the detector is covered with sensitive volume [133].*

As guide line an active cooled support structure for the sensors is considered. This structure might base on the high heat conduction of diamond or on micro-pipes transporting a coolant to the sensors. The material budget of the system is of central concern, since the necessary cooling infrastructure and the cables needed to transport the signal outside the chip would introduce a substantial material budget, making the required high-resolution vertex measurements difficult.

For the heat evacuation and support structure, industrial CVD[12] diamond is foreseen due to its excellent mechanical stiffness and, in particular, heat conduction.

The conventional approach would require to have long cables inside the acceptance, all along the sensor length, in order to drive the signal out. This solution would lead to an excessive amount of material budget.

An attractive solution to this problem is proposed within the ULISI[13] [135] project. Within this project, a thin film of polyimide is foreseen for the integration of read-out

[12]Chemical Vapor Deposition
[13]Ultra-light silicon tracking and vertex detection systems for frontier precision experiments

and power lines, in order to achieve minimum system thickness. The cross section of the proposed ladder[14] is shown in Figure 3.13. The ladder is composed of MAPS sensors, of the support structure and the thin polyimide layers which will provide a kind of envelope to enclose the metal lines which drive the signal outside the MVD. According to this approach, the first (second) MVD station would have a material budget of 0.3% X_0 (0.5% X_0).

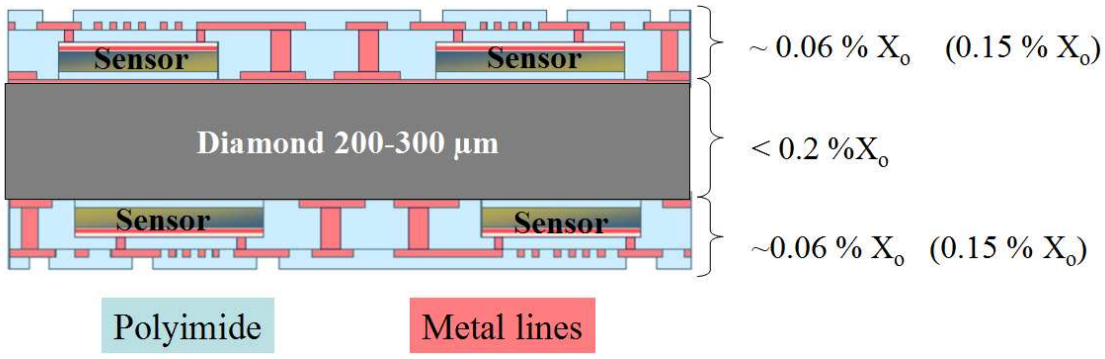

Figure 3.13: *Cross sectional view of the sensor module [134]. The thickness in radiation length of each layer is indicated on the right part of the figure. The numbers in parenthesis correspond to the estimation for the second station.*

The second MVD station, being larger (the difference between the inner radius and the outer radius is $\Delta r \simeq 45\ mm$), is more challenging to build. One of the challenges comes from the limitation to build large area MAPS sensors. The available device size is limited to the reticle size of the CMOS process which is only a few cm^2. A novel process consists in stepping a reticle across a wafer of silicon in a way that smaller arrays can be stitched together to construct large area sensors ("stitching"). Like this, it becomes possible to build larger area sensors that could equip the second MVD.

3.7 Summary

In this chapter the operating conditions for the CBM-MVD were presented. The corresponding requirements for the technology to equip this detector were discussed.

Established technologies such as CCDs and Hybrid pixels were ruled out as their performances did not match the requirements of the MVD in terms of material budget and spatial resolution (for hybrid pixels) and radiation hardness and speed (for CCDs). The choice of MAPS sensors for equipping the CBM-MVD sensors has been motivated. This technology provides the best compromise between radiation hardness, readout speed, material budget and spatial resolution. The main features and limitations of MAPS sensors and the present status of the R&D developments have been summarised.

[14] with the term ladder we refer to the elementary building element of the detector, including sensors, support etc.

CHAPTER 4

Experimental study of the response of MAPS to charged particles

In order to judge if the design of the CBM-MVD is suited for open charm detection, a precise simulation tool is needed. Building this tool required a good knowledge of the response of MAPS sensors to charged particles. Under the conditions of the CBM experiment, particles emerging from the collision are expected to impinge the MVD detector with various incident angles. It is therefore important to investigate the response of MAPS sensors to those particles. This consideration motivated a dedicated beam test.

MAPS sensors are regularly tested in the beam of the CERN-SPS accelerator in order to characterise the sensors in terms of signal-to-noise ratio, noise and spatial resolution for minimum ionising particles[1]. Despite the regular tests, the response of MAPS sensors to particles with various incident angles was so far covered by few studies [2] [148, 150, 151]. In [148, 150] only a small range of particle incident angles (0°-20°) was studied, which is insufficient for a complete characterization of the response of MAPS sensors. A systematic study was therefore undertaken in order to collect the necessary data. The study was carried out with a MAPS prototype, called MIMOSA-17[3] [100], using a pion beam of 120 GeV/c at the CERN-SPS.

In this chapter the experimental setup and the sensor under test are described. Details of the data analysis methods, which include the cluster finding and tracking algorithms, are given. Finally the results are presented and discussed.

[1] A minimum ionizing particle (MIP) is defined as a relativistic particle with charge Z = ± e. According to the Bethe-Bloch equation, the minimal energy deposit occurs for a Lorentz factor of $\simeq 3$, which defines the speed of this particle. The MIP is the charged particle, which is most difficult to detect when passing a sensor. It is therefore regularly used to benchmark detectors. Pions of momentum 120 GeV/c ($\gamma \sim 1000$) experience an energy loss which is very close to their minimum energy loss in silicon.

[2] The measurements presented in [151] were performed in parallel to this work.

[3] MIMOSA stands for **M**inimum **I**onizing particle **MOS** **A**ctive pixel sensor.

4.1 The experimental setup

The experimental setup used is composed of two main components: the detector under test (DUT) and a silicon pixel telescope (called hereafter "beam telescope"). The latter is a device composed by several layers of position sensitive silicon detectors which allow reconstruction of a particle's trajectory with very good accuracy. The tracks reconstructed by the telescope are used as references for characterising the response of the detector under test: the measured hit position of the particle on the DUT is compared to the predicted position from the reference track. In this way, it is possible to characterise the DUT in terms of spatial resolution, detection efficiency and signal-to-noise ratio. Both the beam telescope and the DUT where composed of MIMOSA-17 sensors.

4.1.1 The MIMOSA-17 sensor

A drawing of MIMOSA-17 is shown in Figure 4.1. The sensor was produced with the AMS 0.35 μm OPTO process [144]. The pixel matrix is composed by 256×256 SB-pixels[4] of 30 μm pixel pitch. It has a size (length $\times$ width $\times$ thickness) of 7.68 $mm \times 7.68$ $mm \times 700$ μm and it is organised in four identical submatrices (SubMx0 to SubMx3), formed each from 256 lines and 64 columns. The readout is done from right to left and from top to bottom, as illustrated by the arrows in the picture. Each submatrix has its own analogue serial output based on a single ended voltage output buffer running up to 20 MHz which allows for a minimum readout time of 850 $\mu s/frame$.

4.1.2 The TAPI beam telescope

The PICSEL group at IPHC-Strasbourg has developed and tested a new generation beam telescope composed by CMOS Monolithic Active Pixel Sensors (MAPS) [141], the "Telescope A PIxels" (TAPI) in French, standing for *pixel telescope*. The general layout of the TAPI telescope foresees four reference planes based on MIMOSA-18 sensors thinned down to 100 μm (pixel pitch of 10 μm and an active area of 5×5 mm^2). For the measurements reported in this work, a preliminary version of the TAPI telescope with two reference planes based on MIMOSA-17 sensors, was used. The DUT was placed in the middle of the beam telescope.

A photo of the experimental setup, composed of the TAPI telescope and the DUT, is shown in Figure 4.2: following the beam direction (from right to left), there is a plastic scintillator detector, three consecutive planes of pixel detectors and again a plastic scintillator detector. The relative distances of the different elements of the setup are indicated in Figure 4.3. The distance of the two scintillators (S1 and S2), is approximately 160 mm. The distance of each module (Ref.1 and Ref.2) from the device under test is 63.5 mm. The DUT plane is rotated around an axis vertical to the ZU plane (see figure), called V axis (Z is the beam direction). The chosen rotation angles of the detector under test were 0°, 15°, 30°, 45°, 60° and 75° and the uncertainty on those angles was estimated to be 1°.

[4] Self-Biased pixels, see Section 3.4.2

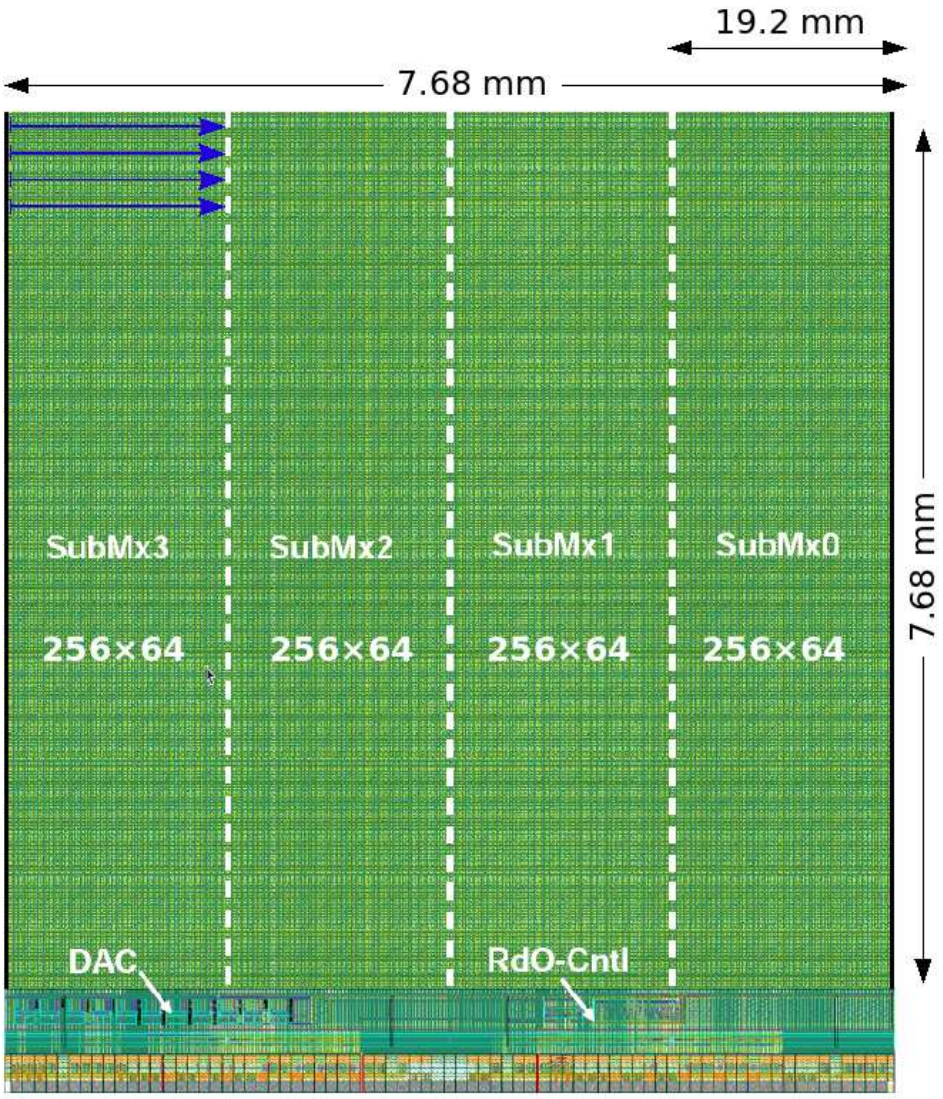

Figure 4.1: *Schema of the matrix arrangement of MIMOSA-17. There are 4 matrices with 256 rows × 64 columns each. The pixel size is* 30 $\mu m \times 30 \mu m$. *The arrows on matrix 3 (SubMx3) show the readout direction: the matrix is read line by line from left to right and from top to bottom.*

The two scintillator counters in coincidence provided a fast trigger for the data acquisition system. The first and second scintillators had an active area of 2×2 mm^2 and 10×10 mm^2 respectively. Hence, the scintillator covered the full width of a submatrix (which has dimensions (length × width) 1.62×7.68 mm^2) but only $\sim 25\%$ of its height. They were mechanically aligned with the submatrices used for the DUT and the reference planes. Note that only one matrix per MIMOSA-17 sensor was used: SubMx1 for the DUT and the upstream reference plane, SubMx2, for the reference plane downstream (see Figure 4.1).

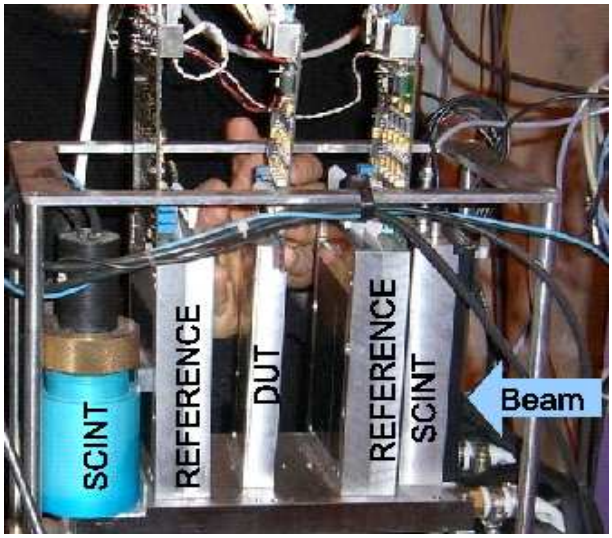

Figure 4.2: *Left: Photo of the experimental setup during the beam test at the CERN-SPS. The beam is entering from the right. The two scintillators and the three aluminium boxes containing the MAPS detectors are shown: two reference planes and the detector under test (DUT).*

4.2 The data acquisition system

The data acquisition system of the DUT and TAPI, illustrated in Figure 4.5, was developed by the PICSEL group at IPHC-Strasbourg. Each MIMOSA-17 sensor is mounted on a PCB board (proximity board) which hosts decoupling capacitors for filtering noise from the biasing voltages of the sensor and amplifiers buffering its analogue output signal. A so-called auxiliary board is connected on the proximity board. This auxiliary board holds the voltage regulators generating the biasing voltages of the chip. Moreover, it generates the differential signals needed to drive the initially single ended output signal of the sensors to the counting room. The inverse operation is performed for the slow and fast control signals steering the chip. The auxiliary board needs four outside connections (as depicted in Figure 4.4): i) power lines, ii) JTAG [5] for the slow control, iii) clock, iv) four analog outputs.

The auxiliary boards are connected to a card ("clock tree") which distributions the control and clock signals. Moreover, they deliver their analogue signal to the main acquisition board (known as USB imager board) which provides clocking and fast control signals and incorporates the four analogue to digital converters (12-bit ADCs) sampling the analogue signals delivered by the sensors. Using a clock frequency of 16 MHz, 1024 μs are needed to read a complete submatrix.

[5] Joint Test Action Group (JTAG) is the common name used for the IEEE 1149.1 standard protocol entitled "Standard Test Access Port and Boundary-Scan Architecture" generally used for test purposes. Here, this protocol is exploited for the slow control of the sensor.

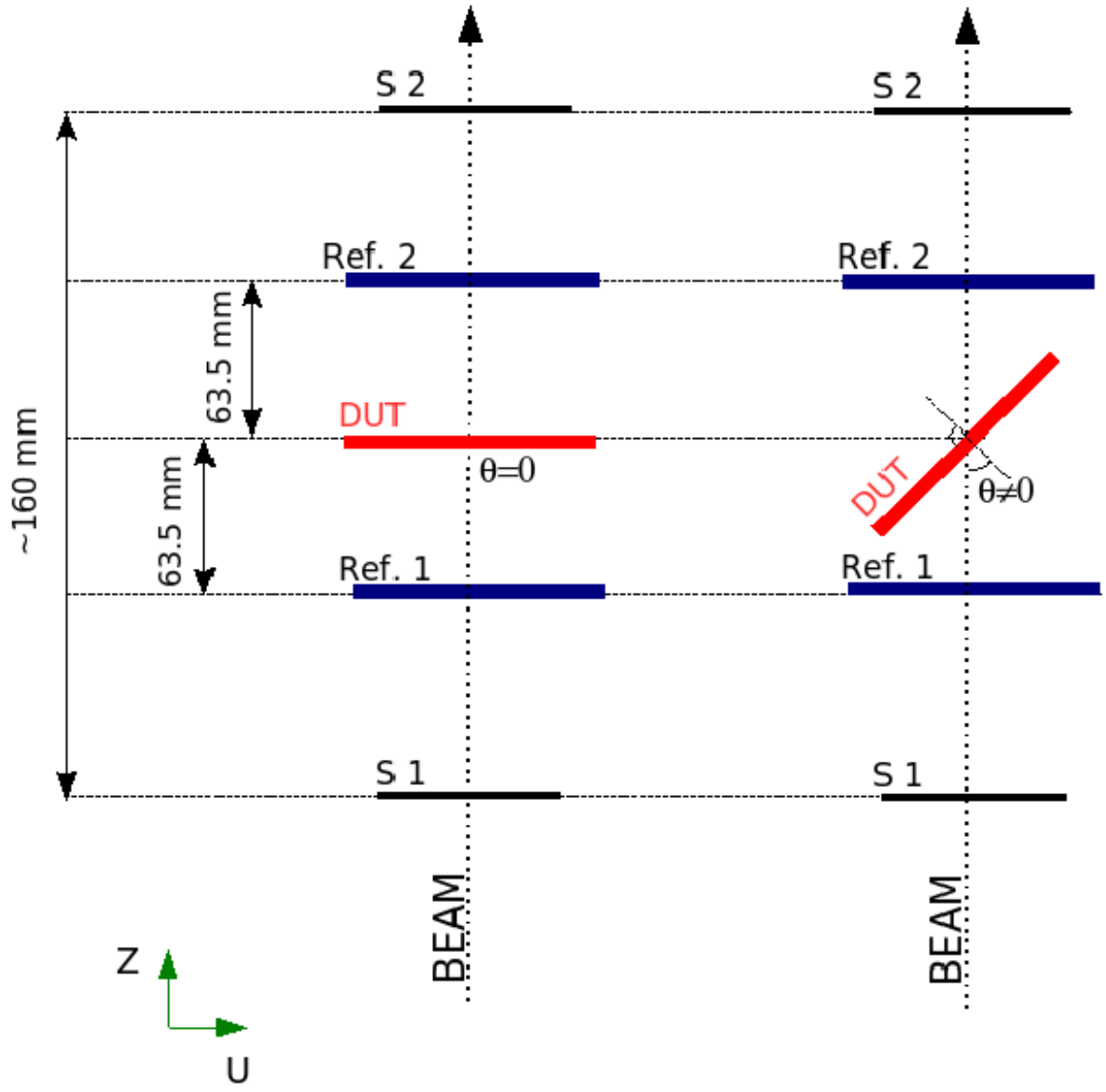

Figure 4.3: *Top view of the experimental setup. On the right-hand side, the DUT is rotated around the V axis, vertical to the ZU plane. The relative distances are indicated.*

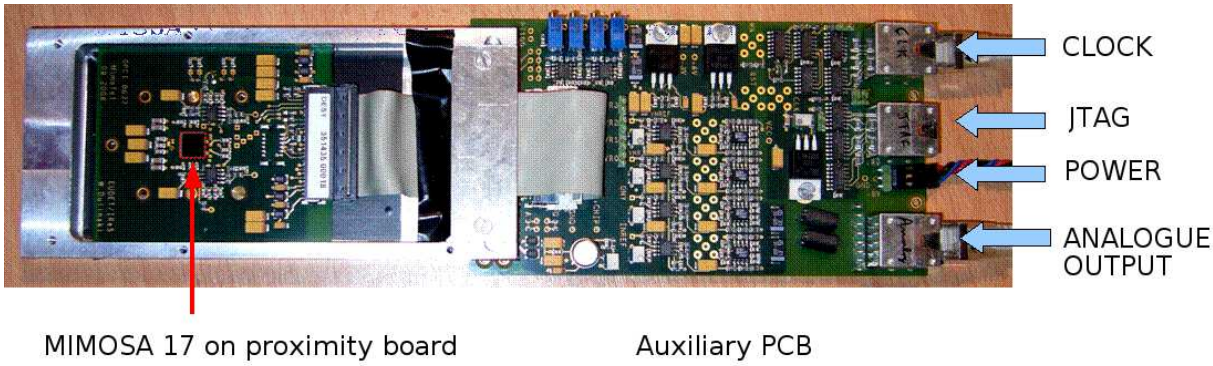

Figure 4.4: *Photograph of a MIMOSA 17 chip mounted on the proximity board and connected to the auxiliary card.*

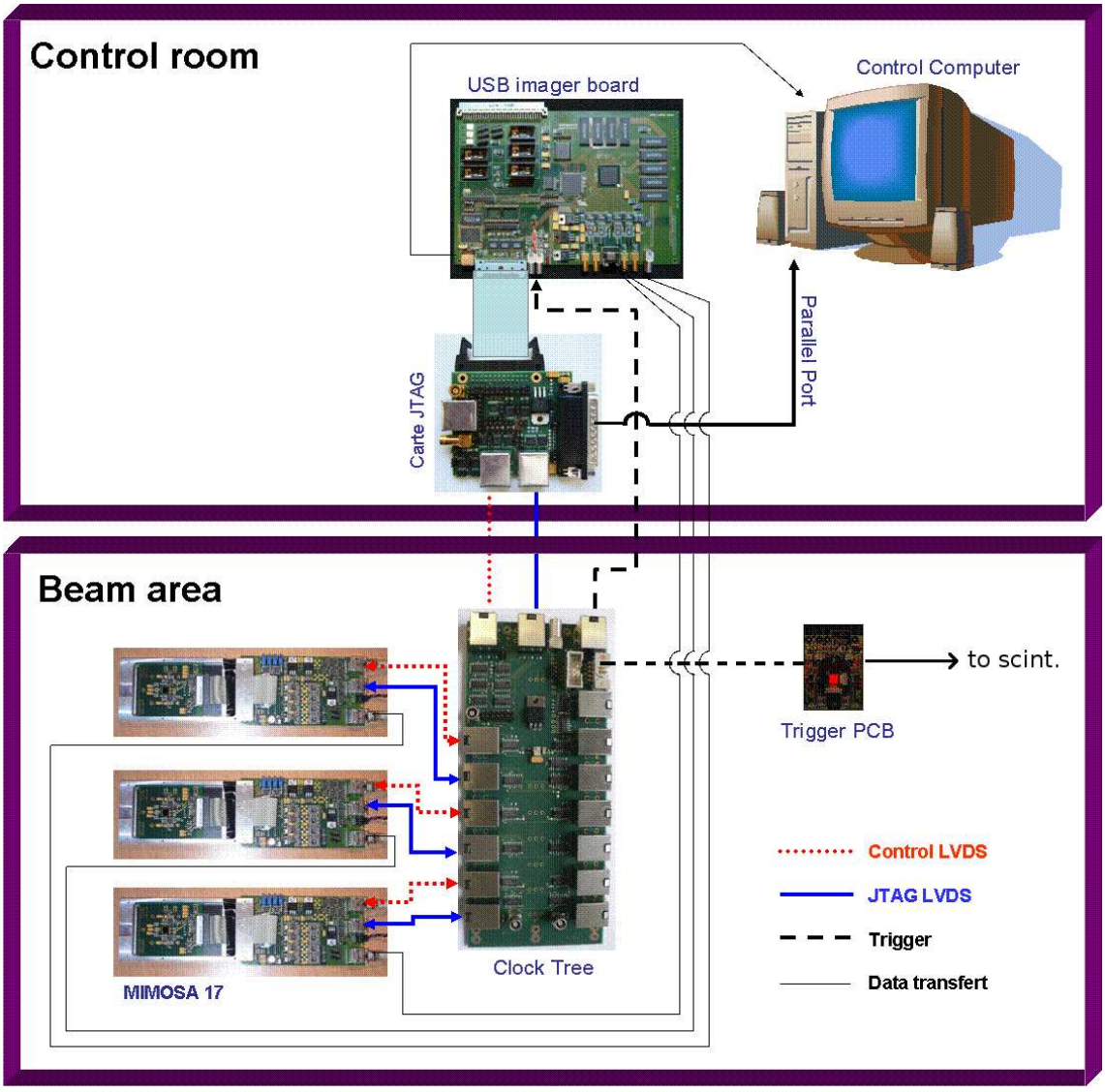

Figure 4.5: *Schema of the data acquisition system. The upper box includes the parts of the setup in the control room (JTAG card, USB imager board, control computer). The bottom box includes the elements located in the beam test area (see text).*

4.3 Signal extraction and data processing

The ability of a detector to distinguish between a signal generated by ionising particles and noise fluctuations is an important quality feature for its detection efficiency. The latter is determined by the signal-to-noise ratio of the detector. Thus, the minimization of the noise is of great importance.

The raw signal of a pixel includes several effects which need to be distinguished from the potential physical signal due to the interaction of a particle in the detector. These effects include variations of the dark signals[6] of the pixels which originate from the production tolerance of the CMOS process, namely the properties of the pixels' collection and biasing diodes. As the differences of the dark signals of different pixels exceed the order of magnitude of the signal, correcting for them is a mandatory step in the data analysis.

Moreover, the output signal of the individual pixels is affected by different types of noise which one can distinguish according to two categories: the random noise and the correlated noise. The term "correlated noise" corresponds to the type of noise that can be filtered by digital filters and data analysis (for example *common mode noise*) while the "random noise" (*shot noise, thermal noise, flicker noise*) can only be dimmed by optimising the electronics and the operating conditions.

Isolating a signal charge from the contributions of noise and variations in the dark signal requires several digital data processing steps. The latter were performed with a dedicated software called Mimosa Analysis Framework (MAF) [138] which has been developed for this purpose by the CMOS group of IPHC. In the following, the processing steps implemented in the software are summarised. For more details the reader is referred to literature [55, 70, 139].

Note that the procedure used for signal extraction depends slightly on the pixel architecture. Unlike most sources in literature, which concentrate on extracting signal from the classical 3T pixels, we will show the procedure for extracting signal for SB-pixels since this architecture is used in MIMOSA-17 sensors.

4.3.1 Signal of SB-pixels

The signal generated by a charged particle impinging a SB-pixel has been discussed in detail in Section 3.4.2. As shown in Figure 3.10 the output signal of the SB-pixel remains constant in the absence of signal charge (provided a constant temperature). If a charged particle impinges the detector, the voltage applied on the pixel capacity is reduced due to the appearance of signal charge. This fast process is followed by a slow clearing of the signal charge from the capacity. The voltage drop at the capacity is sent to the output of the chip via several buffers and digitised by means of a 12-bit ADC.

4.3.2 Correlated Double Sampling

A first step in signal processing is the correlated double sampling (CDS). This step is carried out by subtracting two consecutive samples obtained from the ADC (e.g. F1 and

[6] The dark signal is the signal a pixel generates in the absence a particle.

F0 in Figure 3.10). In SB-pixels this step corresponds to a differential shaping of the output signal if the sensor. As shown in Figure 3.10, the signal after CDS does not contain the dark signal of the pixel as the latter has been canceled out in this subtraction. Moreover, during the clearing process, the pixel shows now a negative output signal which can be easily separated from the positive signal caused by the signal charge.

After CDS processing, the signal $s_k(n)$ on the pixel numbered k and in the n^{th} acquired frame can be expressed as the result of contributions corresponding to the physical signal (generated by an impinging particle) $s_k^{phys}(n)$, the random noise $s_k^{rand}(n)$, the recharge current $s_k^{recharge}$ and the common mode noise $c(n)$. In case of reasonably low occupancy and non-irradiated[7] sensors, the recharge current contribution is usually small with respect to the signal of a crossing particle (see Figure 3.10).

$$s_k(n) = s_k^{phys}(n) + n_k^{rand} + c(n) + s_k^{recharge} \tag{4.1}$$

Figure 4.6 shows two consecutive images of the raw data of a pixel matrix, before applying the CDS procedure. Figure 4.7 shows the result after subtracting the two frames, i.e. after CDS.

The methods applied for estimating and filtering out each contribution, in order to extract the potential physical signal $s_k^{phys}(n)$, are described below.

4.3.3 Common mode noise estimate

Due to its origin, which is external to the chip, the common mode noise (CMN) affects a group of pixels. For MIMOSA-17 the CMN is estimated for each event after CDS correction, assuming that the number of pixels with signal charge and of pixels being recharged is negligible. Under this assumption, one can approximate the CMN by computing the mean signal of a group of pixels, for example all pixels in a row. Once this mean value is known, it is subtracted from the signal of all pixels in the group. This reduced the CMN to a value, which is limited by the uncertainties of the approximation.

Figure 4.8 shows an example of the common mode noise estimation for a given frame. The charge indicated on the pixels after CDS and common mode noise subtraction is shown in Figure 4.9.

4.3.4 Random noise estimate

The random noise is estimated for each pixel: first, the distribution of the raw signal $s_k(n)$ is formed after the CDS and CMN correction, typically for $M = 100$ events. In the absence of hits and recharge process, this distribution has a Gaussian shape. In the case of self-biased pixels, the centre of the distribution is ~ 0, and its standard deviation provides an estimate of the random noise. For each additional event analysed, the noise is updated. The update is made by interpreting the noise as a moving average of a squared sum of a pixel signal, assuming no charge contribution from a signal particle (physical charge): $n(i)_1 = \sqrt{Q(i)_1^2 + (M \times N(i)_0)^2}$ with $M \approx 100$. $N(i)_1$ is the updated value of the noise of the i^{th} pixel, N_0 is the current one and $Q(i)_1$ is the indicated charge on the pixel i.

[7] For a discussion on irradiation effect on MAPS sensors see [55].

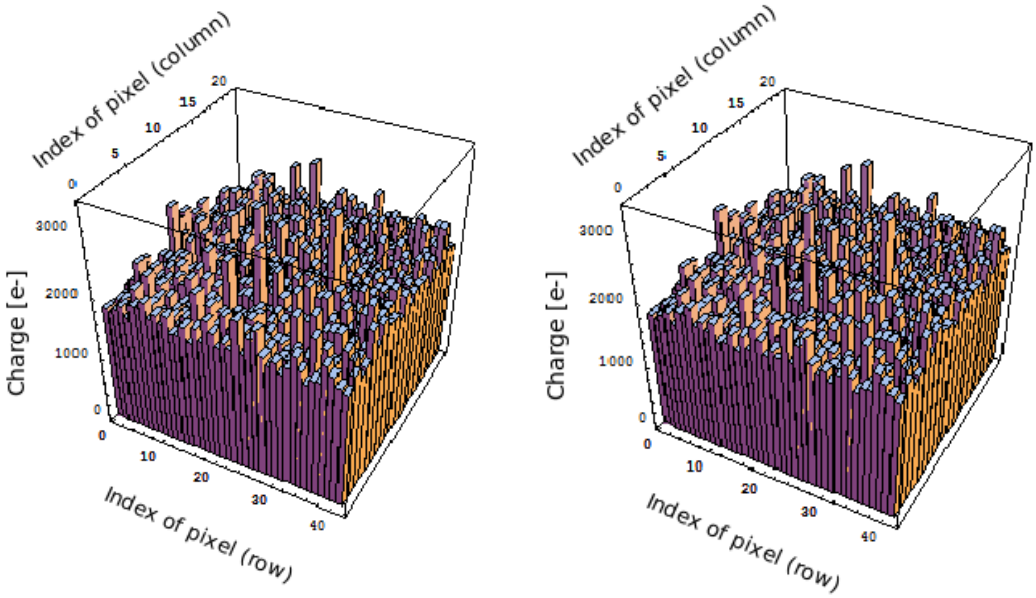

Figure 4.6: *Example of the raw data before applying the Correlated Double Sampling (CDS) procedure. Two consecutive images of the pixel matrix are shown.*

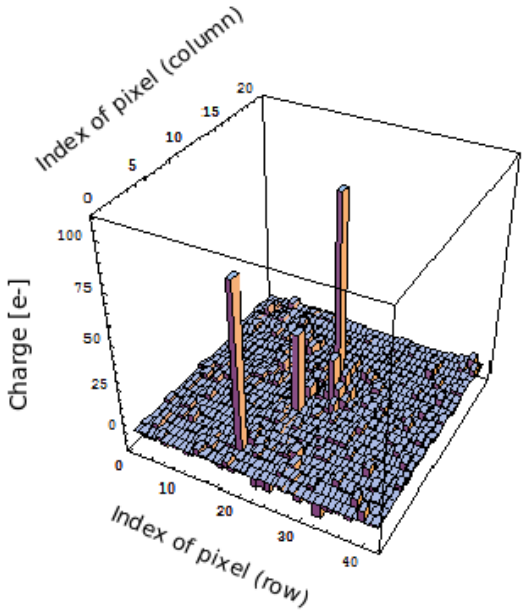

Figure 4.7: *Example of an image of a pixel matrix after CDS processing (see text).*

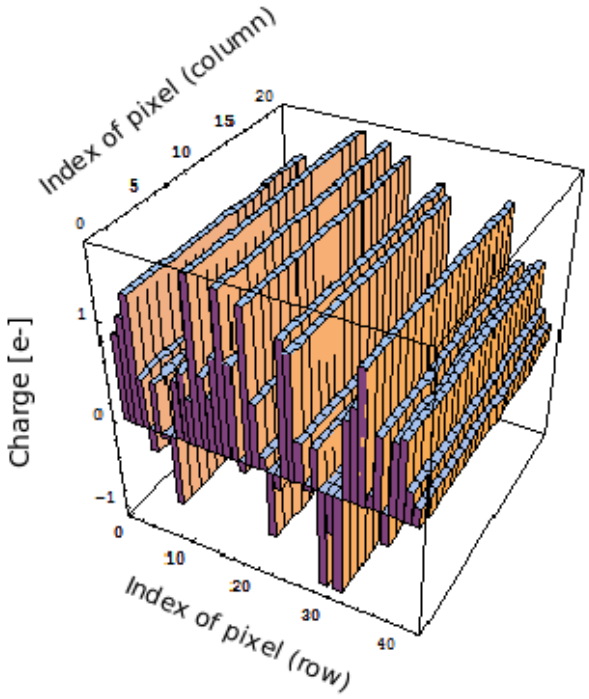

Figure 4.8: *Common mode noise calculation: the average value (over a line) of the amplitude of the charge is shown. This noise is later on subtracted from the measured signal.*

Note that, since the indicated charge is derived after CDS, it is possible to obtain negative values. The latter are obtained mainly when the estimated noise dominates the collected physical charge, or if the pixel is under recharge. This observation will be useful for the interpretation of some of the results on the response of the sensor to charged particles (Section 4.8).

4.4 Cluster reconstruction

A charged particle crossing a MAPS detector generates an amount of electrons which then diffuse in the sensitive volume until they are collected by several neighbouring diodes, forming thus a cluster of firing pixels. The reconstruction of the impact point (i.e. hit) of the charged particle is based on the information provided by the clusters. For this, two steps are undertaken: first, the clusters of pixels are identified and next, the reconstruction of the impact point is performed.

The reconstruction algorithm for clusters is based on the signal-to-noise ratio (SNR) of the individual pixels:

$$SNR = \frac{s_k(n)}{n_k} \tag{4.2}$$

where $s_k(n)$ is the charge measured on the k^{th} pixel, on the n^{th} event, and n_k is the estimated random noise of the k^{th} pixel as explained in Section 4.3.4.

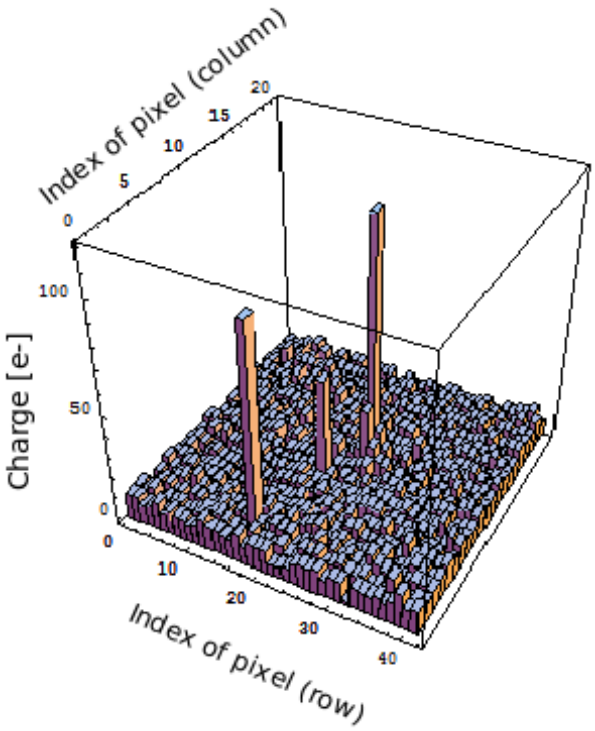

Figure 4.9: *The charge indicated on pixels after CDS and common mode noise subtraction.*

First, all the pixels in the matrix having a pulse height above a given threshold are selected. Pixels, which fulfill the following condition are *seed* pixel candidates:

$$\frac{q_0}{n_0} > T_1 \tag{4.3}$$

q_0 and n_0 are the signal and noise of the pixel. T_1 is a discrimination threshold, used as an input parameter, in units of signal-to-noise ratio. The signal-to-noise ratio is used because it allows eliminating the so-called hot pixels showing high noise fluctuations but no significant signal charge. Once a seed pixel is identified, one defines the first, the second and the third pixel coronas around it as illustrated in Figure 4.10. The seed pixel has by definition the index 0. The first pixel corona is defined by the pixels with indices from i=1 to i=8, the second one has indices from i=9 to i=24 and the third one is defined by pixels from i=25 to i=48. Typical cluster sizes are geometrical regions of N=5 × 5 or N=7 × 7 pixels. This is motivated by the observation that this number of pixels is sufficient to collect the diffusing charge. This group of pixels is now considered as a cluster *candidate*. In order to be accepted, it has to fulfill the additional condition for N=8:

$$\frac{\sum_{i=1}^{N} s_i}{\sqrt{\sum_{i=1}^{N} n_i^2}} > T_2 \tag{4.4}$$

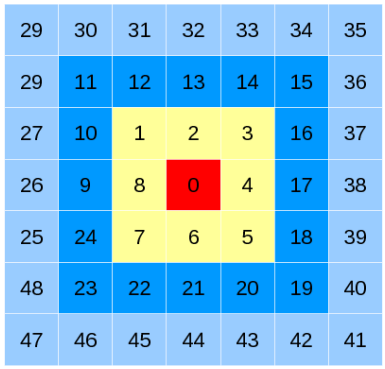

Figure 4.10: *Illustration of the first (yellow), second (blue) and third (light blue) coronas around the seed pixel, shown in red.*

The condition requires that the first pixel corona shows a SNR above a second discrimination threshold T_2. Note that the central pixel (i=0) is not included in the sum. During the analysis it was observed that many clusters contain more that one seed pixel candidate. In order to avoid double counting, a seed pixel candidate, which is located in the accepted cluster of another seed pixel with higher SNR, is considered as neighbour of the latter. The candidate is therefore removed from the list of seed pixel candidates and cannot generate its own cluster. The cluster finding algorithm repeats the process until all clusters are identified.

An illustration of the different steps in cluster reconstruction is shown in Figure 4.11. An example of the charge on each pixel is shown. Mostly two pixels with relatively high charge are observed. One of the pixels, appearing with high charge on the left panel, shows a small value of SNR on the right panel, due to a high noise. Finally, the bottom panel shows the example where only pixels with $SNR > 5$ are selected. For MAPS devices, typical signal-to-noise ratios used for identifying pixels with significant charge are usually in the range of $SNR = 3-7$. Once the clusters are identified, their impact point is reconstructed.

4.5 Hit position algorithms

There are three commonly used methods for reconstructing the impact point of particle from its charge distribution in a cluster. They rely on the use of purely digital information of fired pixels (first method), building the centre of gravity of the signal charge of a cluster (second method) and on refining the latter approach by using an eta function (third method). These different methods are described below.

4.5.1 Digital hit position

The digital hit position is defined as the centre of the seed pixel and is equivalent to the case where only one pixel is fired. Since the probability that a particle hits any part of the pixel is uniform, the probability density function for a continuous uniform distribution on

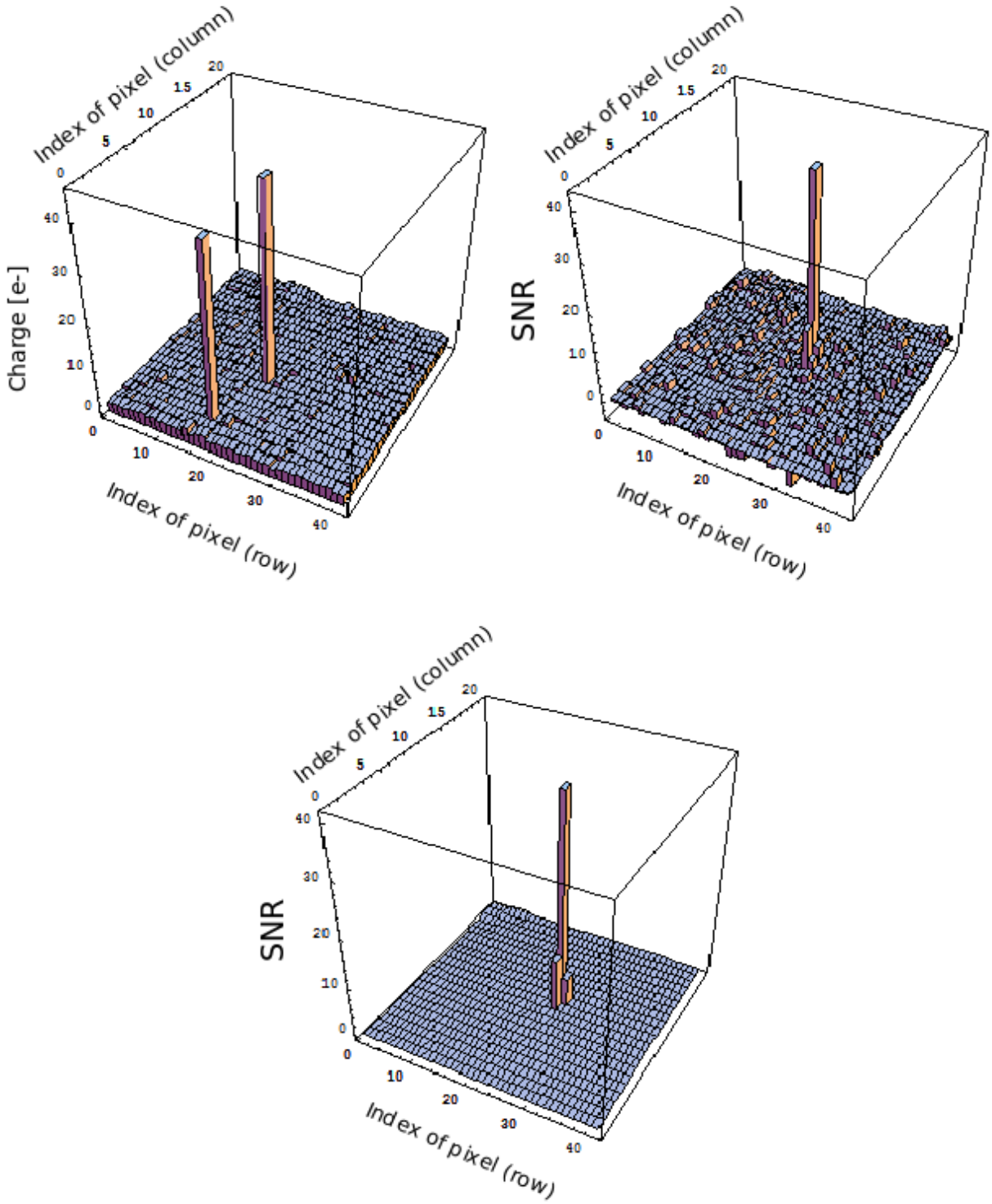

Figure 4.11: *Illustration of the cluster reconstruction procedure: Top left: noise calculated on all the pixels of the matrix: two pixels show a relatively high noise. Top right: The signal-to-noise ratio for all pixels is shown. Bottom: The pixels that have passed the selection criteria have formed a cluster.*

the interval [α, β] is used:

$$F(u) = \begin{cases} 0 & \text{for } u < \alpha \text{ , } u > \beta \\ \\ \frac{1}{\beta - \alpha} & \text{for } \alpha \leq \text{u} \leq \beta \end{cases} \tag{4.5}$$

The calculation of the standard deviation σ_u, also called *root mean square* (RMS), of the continuous distribution gives the spatial resolution of the digital method:

$$\sigma_u = \sqrt{< u^2 > - < u >^2} \tag{4.6}$$

Given that

$$< u >= \int_{-\infty}^{+\infty} uF(u)\ du = \frac{\beta + \alpha}{2} \tag{4.7}$$

and

$$< u^2 >= \int_{-\infty}^{+\infty} u^2 F(u)\ du = \frac{\beta^2 + \alpha^2 + \alpha\beta}{3} \tag{4.8}$$

then the standard deviation is given by:

$$\sigma_u = \frac{\beta - \alpha}{\sqrt{12}} \tag{4.9}$$

Replacing $\alpha = -\frac{P}{2}$ and $\beta = \frac{P}{2}$, where P is the pixel size in a given dimension,

$$\sigma_u = \frac{P}{\sqrt{12}} \tag{4.10}$$

Note that in the MAF analysis framework, the digital method is used slightly modified. Once a cluster is identified, the centre of gravity of the position of all pixels belonging to this cluster is computed (see next section). This method allows for a resolution slightly better than what is predicted by Equation 4.10.

In Figure 4.12, the measured residuals of MIMOSA-17 are shown for tracks impinging perpendicular to the sensor plane. The residuals are defined according to $r = u_{track} - u_{hit}$, where u stands for the readout direction in the detector coordinate system, u_{hit} indicates the measured hit position in the detector and u_{track} represents the expected hit position according to the projection of the track to this sensor. The distribution is roughly uniform from $-P/2$ to $P/2$, where $P = 30\ \mu m$ is the pixel pitch. The shape of this distribution is determined by the convolution of two distributions. Those are the uniform distribution of hits on the pixel and the gaussian distribution of the combined uncertainty of the track and hit position uncertainties. The few entries outside the limits of the pixel area which can be explained by misidentification of the seed pixel: it cannot be excluded that there are cases where the seed pixel is the one with the higher charge amplitude instead of the highest SNR[8]. Moreover, the precision of the track extrapolation is limited.

[8] Alternatively, one might also define the seed pixel as the one with the highest charge amplitude. However, in this case it is not excluded that a pixel with exceptionally high noise might be misidentified as seed.

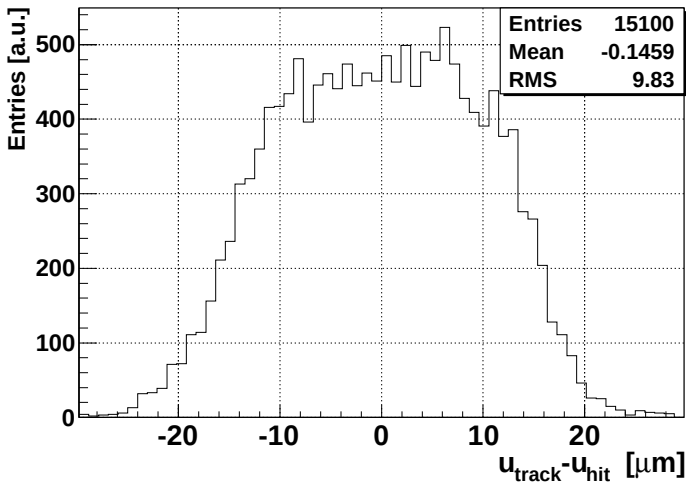

Figure 4.12: *Residuals between the measured hit position using the digital hit position method and the position expected from the extrapolation of the track (see text).*

4.5.2 Centre of gravity hit position

The centre of gravity is a refined method used for calculating the position of the hit by taking advantage of the information from all pixels in the cluster. It is defined as follows:

$$u = \frac{1}{Q_{tot}} \sum_{i}^{N} q_i \times u_i \tag{4.11}$$

with

$$Q_{tot} = \sum_{i}^{N} q_i \tag{4.12}$$

where N is the total number of pixels in a cluster, q_i is the charge measured on the i_{th} pixel and u_i is the u-coordinate of the centre of this pixel. The equivalent relations hold for the vertical dimension, called v hereafter. In Figure 4.13 distributions of the residuals are fitted with a Gaussian function. The limits of the fit were chosen to be roughly 3 times the statistical RMS of the distributions. The RMS of the histogram shown in Figure 4.13 is 5.5 μm (4.9 μm) in the u (v) dimension. The corresponding standard deviation from the Gaussian fitting function is $[4.4 \pm 0.1]$ μm (u dimension) and $[4.4 \pm 0.1]$ μm (v dimension). The root mean square (RMS) of the histogram is larger than the σ of the Gaussian fit, which means that the distribution if not perfectly Gaussian. This is likely caused by the small number of entries found in the tails of the distribution. The latter might originate from bad track reconstruction but also from effects like excessive scattering of individual pions in the detector material.

4.5.3 Eta function hit position

When determining the hit positions by means of centre of gravity of the charge, one makes the assumption that the charge collected on a pixel is inversely proportional to the

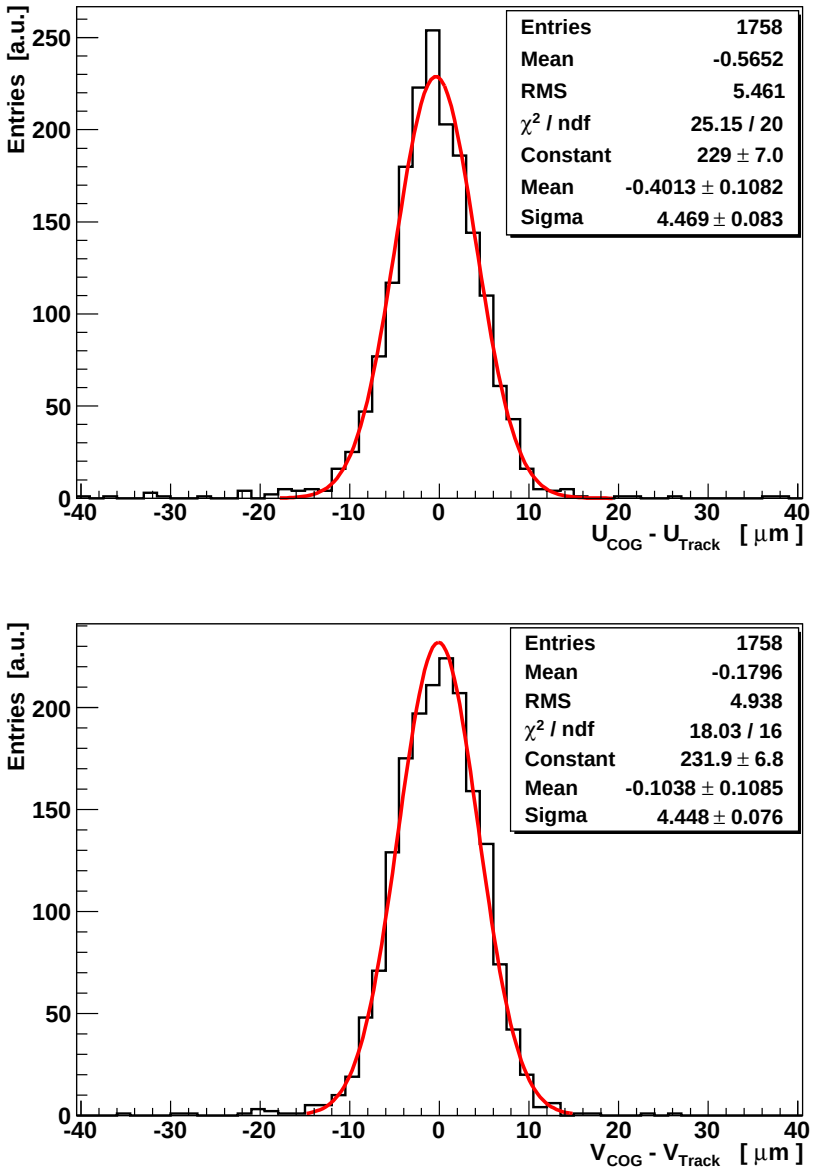

Figure 4.13: *Residuals for centre of gravity hit position for the horizontal (u) and vertical (v) dimension.*

distance of the pixel from the point where the charge was generated. To illustrate this, we assume for simplicity a cluster composed only of 2 pixels (indexed 1 and 2). The total charge in the cluster is the sum of the charge collected by pixels 1 and 2 $Q_{tot} = q_1 + q_2$ and the charge fractions are $\eta_1 = q_1/Q_{tot}$ and $\eta_2 = q_2/Q_{tot}$ for the right and left pixel respectively. The position of the centres of the two pixels are denoted as u_1 and u_2. The calculation of the centre of gravity along the u direction gives:

$$u^{cog} = \frac{1}{Q_{tot}} \sum_{k=1,2} u_k \times q_k \tag{4.13}$$

$$
\begin{aligned}
&= u_1 - \eta_2 \times (u_1 - u_2) && (4.14)\\
&= u_1 - \eta_2 \times P && (4.15)\\
u^{cog}(\eta_2) &= u_1 - \eta_2 \times P && (4.16)
\end{aligned}
$$

where $P = u_1 - u_2 = \text{const}$ is the pixel pitch. From the last set of equations it is observed that the centre of gravity method assumes that there is a linear relation between the charge fractions (η_1 or η_2) and the distance between the centres of two pixels ($u_1 - u_2$). Given the complex mechanisms behind the charge sharing in MAPS, which is among others influenced by small build-in-voltages generated by doping gradients in the silicon of the active volume, there is no reason to believe that this mechanism should be linear. Indeed, a non-linear behaviour has been regularly observed in MAPS. This is illustrated in Figure 4.14, which shows the distribution of the hits inside a pixel. The projections of the hits on the u and v directions are shown in Figure 4.15, left and right, respectively. It is observed that these distributions are not uniform despite one expects a uniform distribution of tracks over the pixel area.

In order to compensate for the underlying non-linearity of the sensor response, the so-called "eta method" is applied. The method used considers the integral of the η distribution, where $\eta = u^{cog} - u^{dig}$ (or $\eta = v^{cog} - v^{dig}$ for the v-direction). Be $N(\eta)$ the number of hits between $-P/2$ and η. u^{cog}, v^{cog} are the coordinates of the hit calculated with the centre of gravity method and u^{dig}, v^{dig} are the coordinates of the hit calculated with the digital method:

$$f(\eta_0) = \int_{-p/2}^{\eta_0} \frac{dN}{d\eta} d\eta \tag{4.17}$$

η_0 is a measured value of η. If the relation of the hit position and the relative charge of the pixels was linear, the η-distribution should be flat. As shown in Figure 4.14 this is however not the case.

The hit position according to the eta function method is given by:

$$u(\eta) = \frac{P}{N} f(\eta) - P/2 \tag{4.18}$$

where N is the total number of hits:

$$N = \int_{-P/2}^{P/2} \frac{dN}{d\eta} d\eta \tag{4.19}$$

In Figure 4.16 the distribution of hits inside a pixel obtained with the eta method is shown. The non-uniformity has been eliminated with the use of the eta method. Figure 4.17 shows the distribution of the hits in the pixel in the u (left panel) and v (right panel) direction separately.

As will be motivated later, the centre of gravity method is used in the simulation of MAPS response.

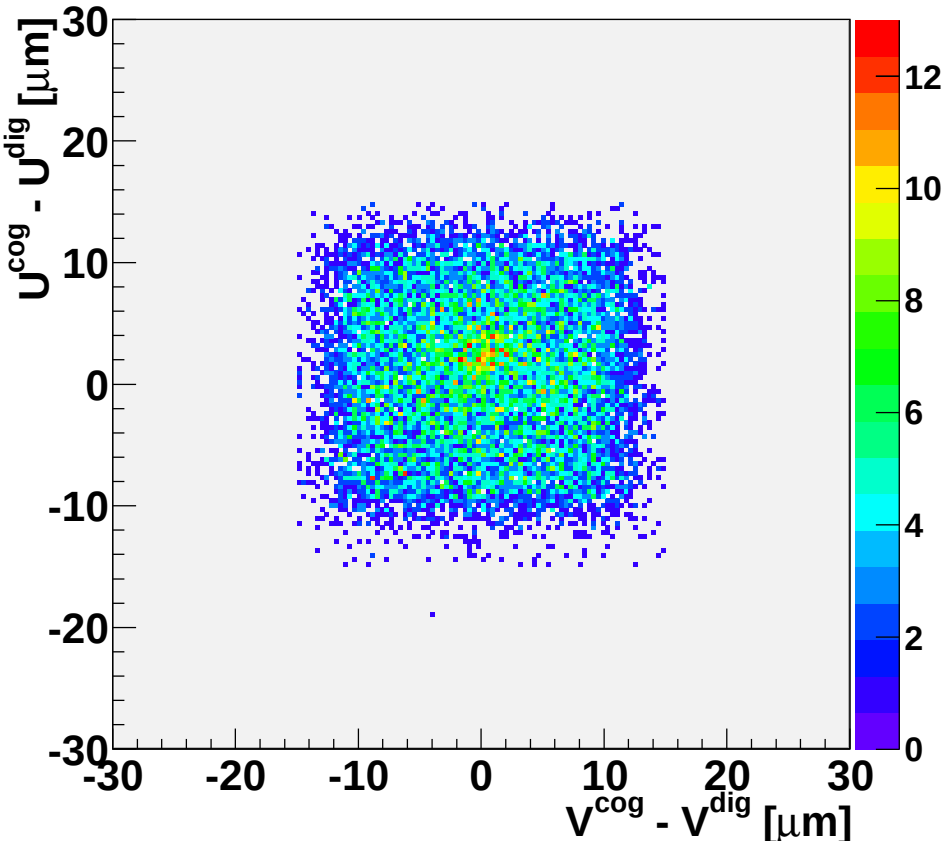

Figure 4.14: *The distribution of hits, reconstructed with the centre of gravity method, inside a pixel.*

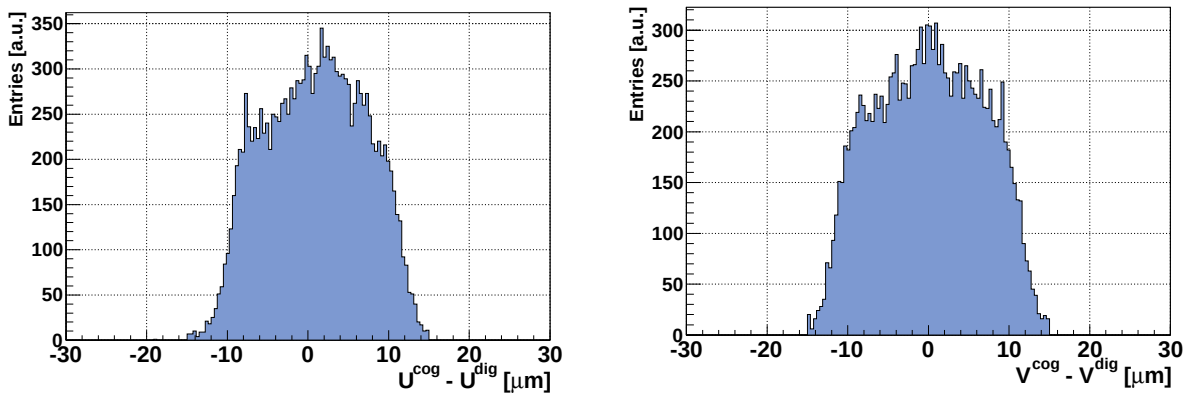

Figure 4.15: *The distribution of hit position, inside the pixel, obtained with the centre of gravity method: along the u-direction (left) and the v-direction (right). The distributions are not uniform.*

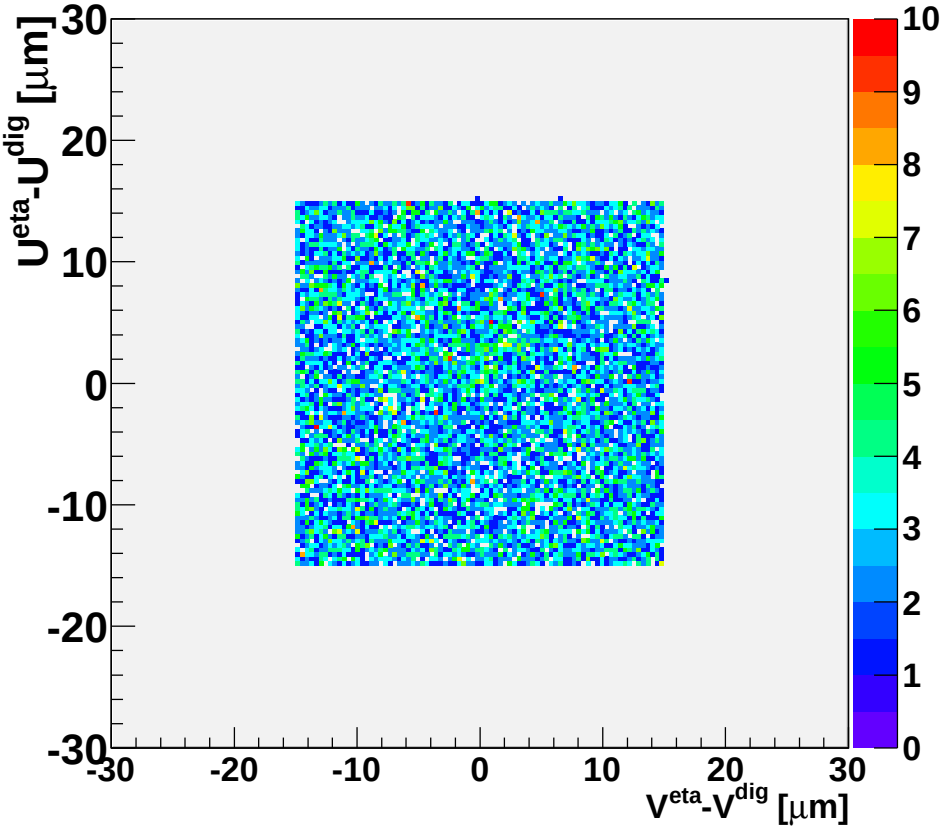

Figure 4.16: *The distribution of hits, reconstructed with the eta method, inside a pixel.*

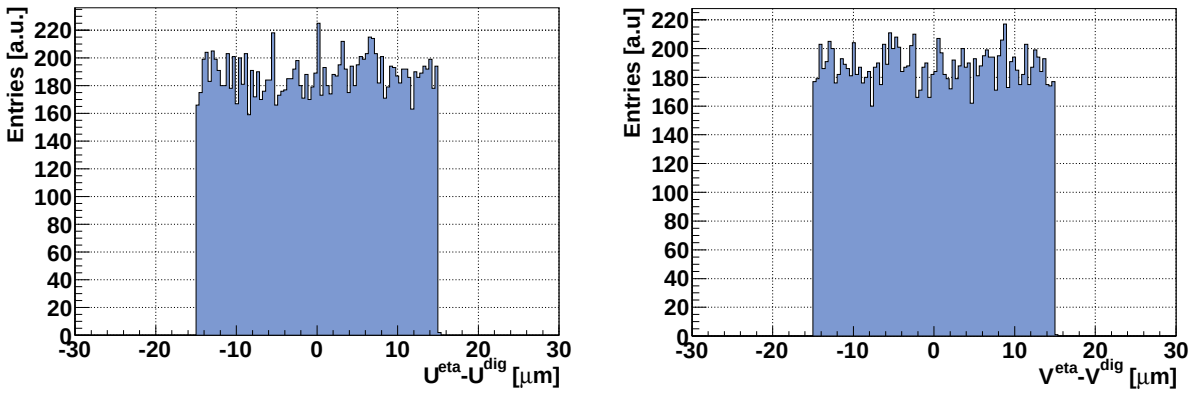

Figure 4.17: *The distribution of hit position, inside the pixel, calculated with the eta method: along the u-direction (left) and the v-direction (right). The distributions are uniform, as expected (see text).*

4.6 Tracking and alignment

When a particle passes through the TAPI telescope, its position is registered in the local coordinate systems of the three individual detectors (the two reference detector planes and the DUT) which are independent from each other. In the experimental setup showed in Figure 4.18, there are two coordinate systems: one is related to the telescope, denoted as (Tu, Tv) and the other one is related to the detector under test (Hu, Hv). The alignment is an iterative procedure which aims in the best possible coincidence of these two frames by modifying the plane position along the directions of (u,v) and one rotation angle, ϕ, around the beam axis. Unless mentioned otherwise, u is defined by the data read-out direction and is along a line of pixels and v is the direction of a column of pixels and is perpendicular to u. In the following, the alignment of the telescope planes is described in the general case.

The origin (0,0) of the plane to be aligned, hereafter called secondary reference or SR-plane, is located at the center of the matrix under study. The coordinate system of the telescope is defined by one (or two) planes chosen as references (primary reference planes or PR-planes). The SR plane coordinate system can be adjusted by two offsets, u_{off} and v_{off}, and by one rotation angle parameter ϕ_{off} around the beam axis. For each event, the

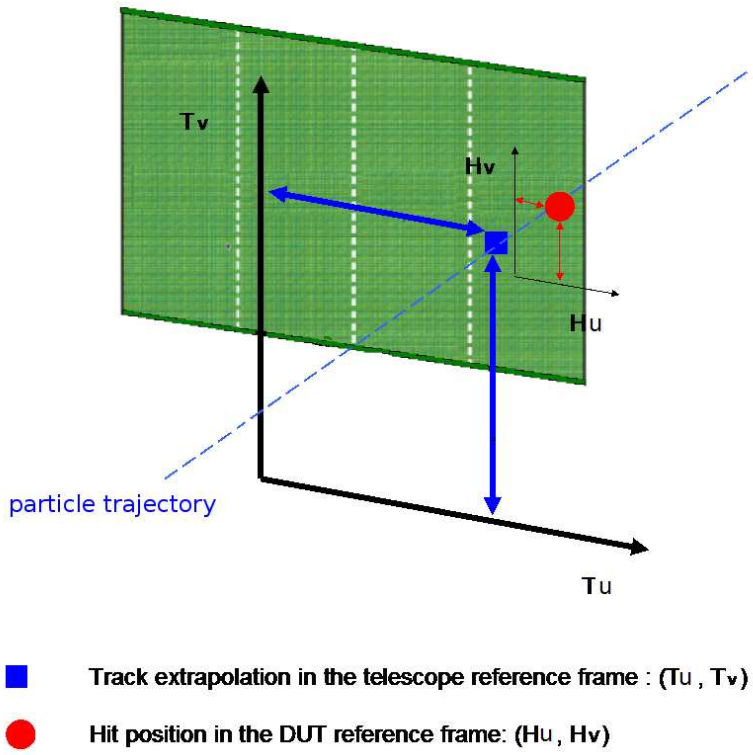

Figure 4.18: *Illustration of reference frames. The telescope reference frame is illustrated with blue colour and the DUT reference frame is in red.*

position of the hits is defined on the PR-planes. Only events with one hit per PR-plane are

selected, in order to avoid associating hits from different particles in a single trajectory, and thus deteriorating the telescope precision. Tracks are reconstructed with a simple linear fit given the absence of any magnetic field. In the particular case where only one plane is used as primary reference, the tracks are reconstructed using a hit on this plane and under the assumption that they are vertical to the plane. The alignment of the SR-planes is done as follows:

If (u_h, v_h) are the coordinates of the calculated hit position in the SR-plane coordinate system and (u_t, v_t) are the coordinates of the predicted hit position by intrepolating their associated track to the SR-plane, then:

$$u_h = u_{off} + u_t \times \cos\phi + v_t \times \sin\phi \tag{4.20}$$

where u_{off} is the offset in the u direction and ϕ is the rotation angle around the beam axis (z-axis). Correspondingly, for the v direction:

$$v_h = v_{off} - v_t \times \sin\phi + u_t \times \cos\phi \tag{4.21}$$

In general, the rotation angle is very small ($\phi \approx 0$) and consequently it holds $\cos\phi \approx 1$ and $\sin\phi \approx \phi$

We define the quantities $r_u = u_h - u_t$ and $r_v = v_h - v_t$ which (with the use of equations 4.20 and 4.21) become:

$$u_h - u_t = u_{off} + v_t \times \phi \tag{4.22}$$

$$v_h - v_t = v_{off} - u_t \times \phi \tag{4.23}$$

The quantities r_u and r_v are plotted as a function of v_t and u_t respectively and can be fitted with a linear function to obtain the offsets u_{off} and v_{off} and the rotation angle ϕ. In the following it is explained how these plots are produced and why the alignment needs to be an iterative process.

Hits on the SR-plane were attached to identified tracks reconstructed by the PR-planes of the telescope provided that the distance between the predicted and the measured hit position does not exceed a certain value. This value is initially chosen with a relatively high value in order to accept a reasonable amount of hits despite the initial misalignment.

For a sample of 200 tracks, hits are searched within a given distance: $|r_u| < L_u$ and $|r_v| < L_v$ where L_u and L_v are defined limits. These have to be sufficiently large initially in order to include all hits in a plane. This step is in principle sufficient to obtain the values of the offset and the rotation angle. However, it may happen that the hits found in these limits are not only due to the particle impact but also because of other sources (i.e noise). The contribution of other sources may be reduced by decreasing the values of L_u and L_v. Therefore the alignment is in general an iterative process which updates the limits L_u and L_v in each iteration step. Initially, all the offsets are assumed to be zero. In a first iteration the value for the offsets is provided. Afterwards, this value is then used as initial value for the next iteration. The iterations stop when the difference between the updated value of the offsets and the previous one is less than 0.5 μm. Figure 4.19 shows an example of the functions $r_u = f(v_t)$ and $r_v = f(u_t)$ and the distributions of the residuals r_u and r_v.

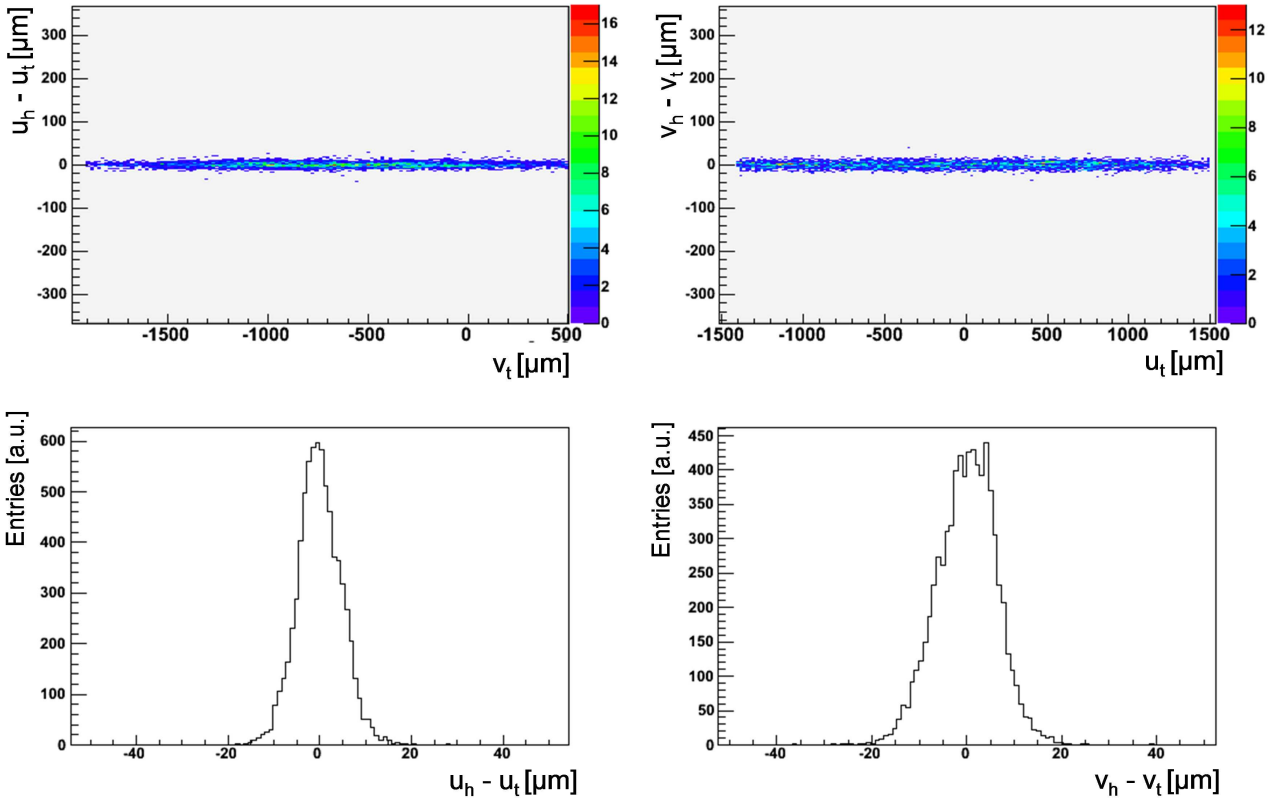

Figure 4.19: *Example of good alignment. Top panel: The functions* $r_u = u_h - u_t = f(v_t)$ *and* $r_v = v_h - v_t = f(u_t)$*. Bottom panel: The distributions of the residuals* $r_u = u_h - u_t$ *and* $r_v = v_h - v_t$*.*

4.7 Alignment of the DUT

The alignment of the DUT is different than the one described above for the secondary reference planes of the telescope. The difference consists in the number of parameters used for the alignment. For the telescope planes, only three parameters are used (two translations and one rotation) which allows to solve Equations 4.22 and 4.23 analytically. This approach gives a satisfactory alignment for the telescope.

In the case of the DUT, six parameters are used (three for rotation and three for translation along the u, v, z directions. The transformation of the hit coordinate from the telescope reference frame to the DUT reference frame is done as following:

$$\vec{A}_{DUT} = R \cdot \vec{A}_{tel} + \vec{T} \tag{4.24}$$

where $\vec{A_{DUT}}$ is the vector of the hit coordinates on the DUT plane, R is a rotation matrix depending on 3 angles, $\vec{A_{tel}}$ is the vector of the hit coordinates on the telescope plane, and $\vec{T}$ a 3-component vector corresponding to 3 translations. The translations are defined in the DUT reference frame. Solving Equation 4.24 analytically is quite complex, therefore the approach is chosen to solve it numerically. This is done by defining the following quantity:

$$c^2 = \sum_i (\vec{A}_{DUT,i} - \vec{A}_{tel,i})^2 \tag{4.25}$$

The sum is over the number of tracks. By replacing Equation 4.24 into Equation 4.25 and minimising the quantity c^2 the vectors $\vec{R}$ and $\vec{T}$ are defined. The minimisation is done with the help of the MINUIT package [146].

4.8 Results

The characterisation of a sensor's response to charged particles is done by examining several different observables, namely: the distribution of the charge in a cluster, the charge collection properties of the individual pixels of the cluster (especially the seed pixel, as defined in Section 4.4) and the signal-to-noise ratio (SNR) of the seed pixels. All the results presented here are obtained with the η-method for the cluster reconstruction unless mentioned otherwise.

4.8.1 Collected charge and signal-to-noise ratio estimate

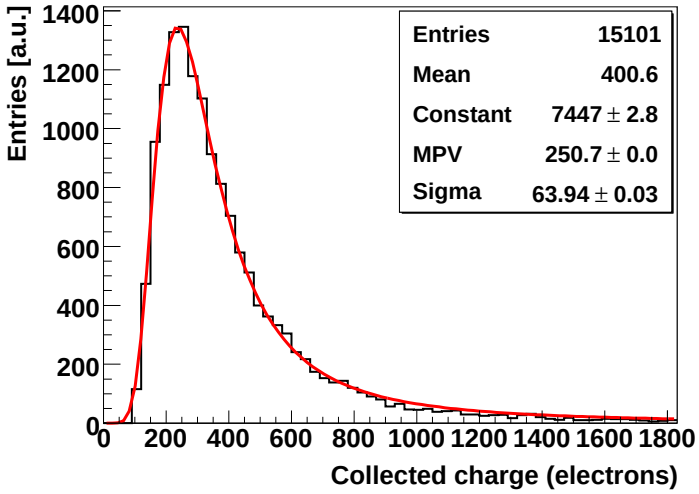

Figure 4.20: *Distribution of the charge collected in the seed pixel (tracks perpendicular to the sensor) and the Landau fit.*

The energy loss of a charged particle penetrating a thin layer of silicon is described by a Landau distribution [143]. The average number of electron-hole pairs created in the silicon is proportional to this energy loss. The number of collected charge carriers in silicon detectors differs from the number of generated carriers due to recombination and imperfections of the collection mechanisms. In the particular case of MAPS, charge carriers may remain uncollected as they diffuse away from the collection diodes until they recombine. However, despite the collection process is rather complex, it has been regularly observed that the distribution of the collected charge in MAPS has the shape of a Landau distribution [70, 145]. The distribution of the charge collected on the seed pixel for tracks perpendicular to the sensor is shown in Figure 4.20. The most probable value of the distribution, as obtained from the fit, is used to characterise the charge collected by the seed pixel.

The signal-to-noise ratio of the seed pixel of all accepted clusters is plotted in the histogram shown in Figure 4.21. This distribution can be fitted with a Landau function, as

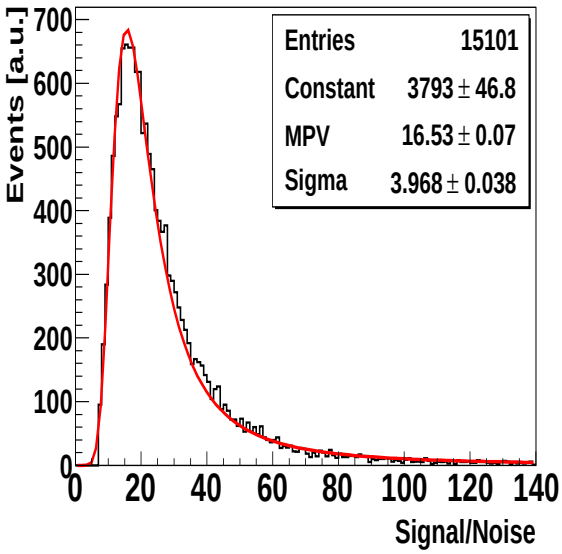

Figure 4.21: *Signal to noise ratio distribution of the seed pixel.*

shown in the figure. The result of the fit gives a most probable value (MPV) for the SNR amounting to 16.53 ± 0.07.

Figure 4.22 shows the estimated random noise distribution of the seed pixels. The mean value of the histogram provides an estimate of the typical noise of the sensor. For this measurement, the noise of the sensor was estimated to 14.8 ± 1.2 electrons, expressed in units of Equivalent Noise Charge (ENC).

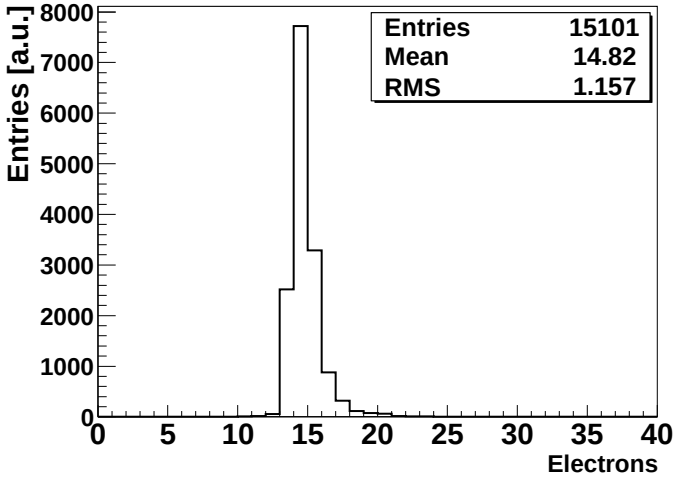

Figure 4.22: *Noise distribution of the seed pixels of MIMOSA-17.*

The relative charge among pixels within the same cluster is studied by examining the so-called accumulated charge distribution over those pixels. The plot shown in Figure 4.23, accounts for the fact that the total signal charge generated by an impinging particle is

distributed over a cluster of pixels. Experience shows that the pixels of a cluster form groups which are smaller than $M = 7 \times 7$) pixels. Therefore for each cluster the signal of 7×7 pixels was recorded. To obtain the plot, we sum the signal charge collected by a subset of the $N < M$ pixels showing the highest charge in one cluster. For every value $1 < N < M$, this sum is filled into a separate histogram H_N. After all clusters are analysed accordingly, each of those histograms contains a Landau distribution. The most probable value of the signal charge of the subset of N pixels, Q_N, is obtained by fitting the Landau distribution observed in the histogram H_N. The accumulated charge as a function of the number of pixels in a cluster is shown in Figure 4.23. It is observed that the accumulated collected charge increases with the number of pixels, reaches a maximum at $N = 32$ and then decreases for $N > 32$. The shape of this distribution is explained in the following. In Section 4.3.4 it has been shown that the indicated charge can take positive or negative values. Moreover, since in the analysis software the pixels of a cluster are ordered by the (signed) value of their pulse height, the pixels indicating negative charge appear last. Therefore, the accumulated charge over the pixels first increases and starts to decrease when the sum over pixels includes negative charge (ordered last).

Another feature to be noted in Figure 4.23 is the observation of the same value of the charge collected for N=14 and N=49 pixels. This is due to the fact that for $14 < N < 49$ the noise dominates the collected signal, and has an average value of approximately 0. The shaded area shows the part where the noise of the pixels is significant with respect to the physical charge.

With these results one learns that for MIMOSA-17 the most probable value of the cluster charge is approximately 900 electrons (shown for 49 pixels); 30% of it is collected by the seed pixel (250 electrons). 80% of the total cluster charge is collected by 9 pixels.

4.8.2 MAPS detector response to particles with different incident angles

Until now we were focused on particles with incident angle $\theta = 0°$ (perpendicular to the detector plane). In the following we study the response of MAPS to particles with different incident angles.

Figure 4.24 shows the accumulated charge as a function of the number of pixels for particles impinging the sensor with different incident angles. For small incident angles, 0° and 15°, there is no significant difference in the way the charge is shared among the pixels in the cluster nor in the total charge collected in the cluster. For angles above 30°, the total charge of the cluster increases and this effect becomes more pronounced as the particle incident angle increases. This is illustrated in Figure 4.25 which displays the total charge in the cluster as a function of the particle incident angle. The solid line shows the function used to fit the data, which is:

$$f(\theta) = \frac{\alpha}{\cos\theta} \tag{4.26}$$

where α is a free parameter adjusted by the fitting procedure and θ is the particle incident angle. The fit with least squares method gives $\alpha = 951.8 \pm 2.3$. The dependence on $\cos\theta$ of the total charge collected can be explained with geometrical arguments. If θ is the rotation

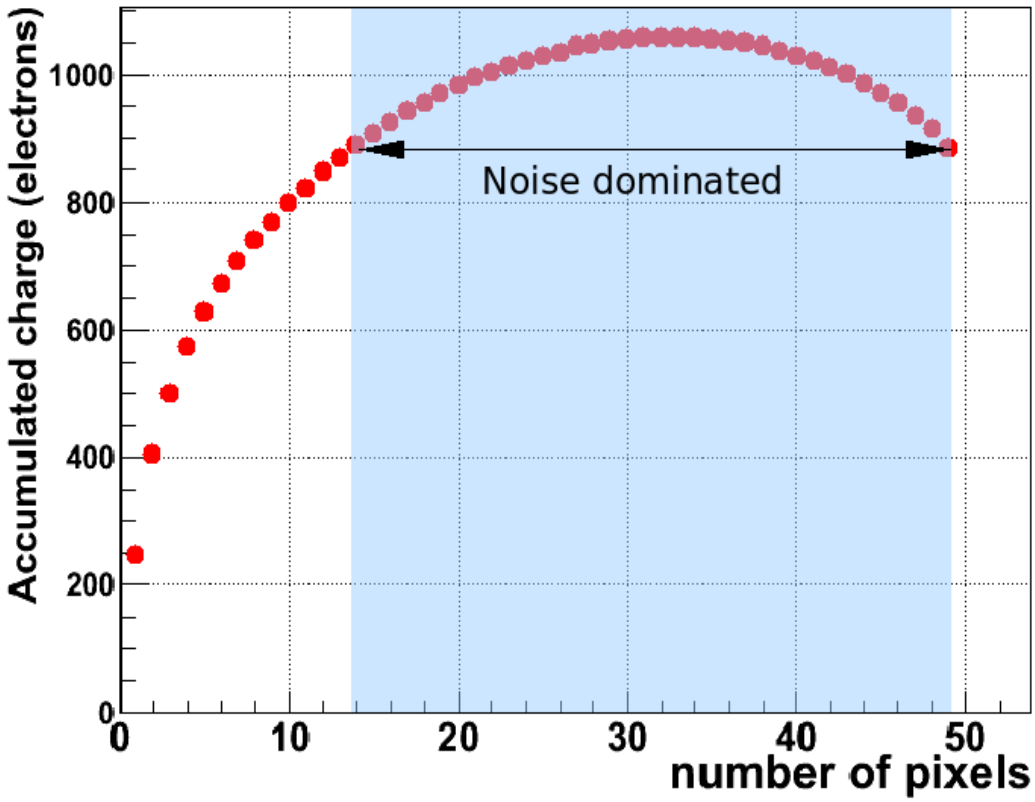

Figure 4.23: *Accumulated charge graph as a function of the number of pixels (see text). The shaded area shows the part of the graph where the charge on the pixels is dominated by the noise.*

angle around the v axis (see Figure 4.3), and L is the length of the trajectory inside the sensitive volume, then the projection, l, of the particle trajectory along the u direction is:

$$l = L \times \cos\theta \tag{4.27}$$

The average total charge Q_{gen} *generated* by the passage of a charged particle depends on the length, L, of the trajectory inside the sensitive volume and is approximately 80 electron/hole pairs per micrometer for MIPs [143]. This can be applied to the 120 GeV/c pions used in the measurement as their dE/dx is reasonably close to the one of MIPs and since $dE/dx \ll E$. Given the above mentioned approximations, the total generated charge can be written:

$$Q_{gen} = 80 \times L \tag{4.28}$$

Combining equations 4.27 and 4.28, the dependence of the total charge collected from the particle incident angle can be derived:

$$Q_{gen} = \frac{80 \times l}{\cos\theta} \tag{4.29}$$

In the epitaxial layer, a part of the generated electrons is recombined (see section 3.4.1) before being collected. This leads to a decreased amount of total collected charge Q_{coll}

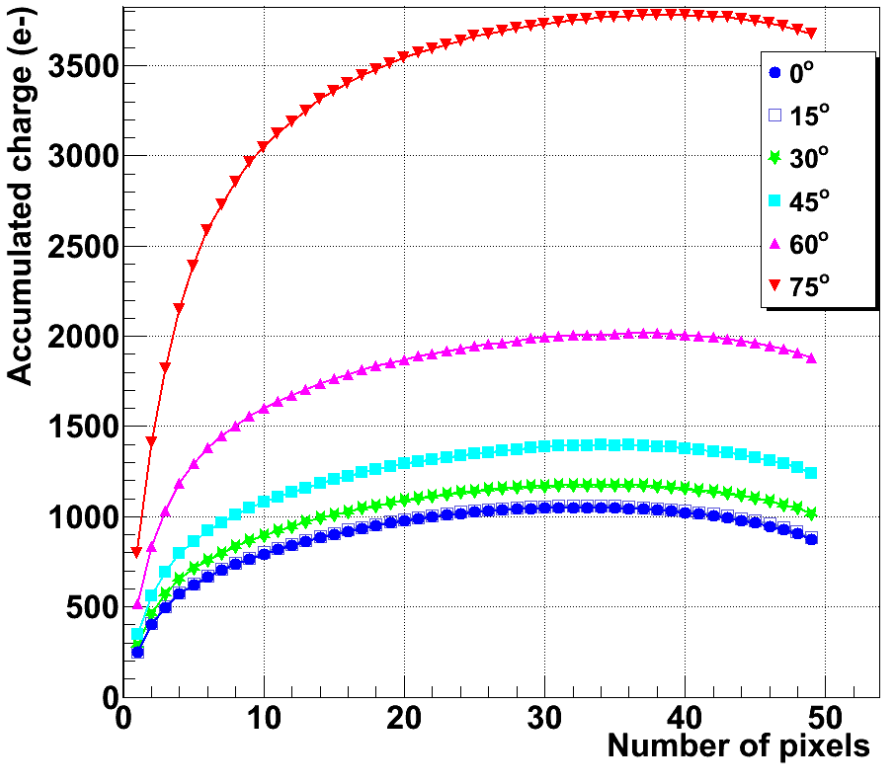

Figure 4.24: *The accumulated charge on pixels for charged pions impinging the MAPS sensor with different incident angles.*

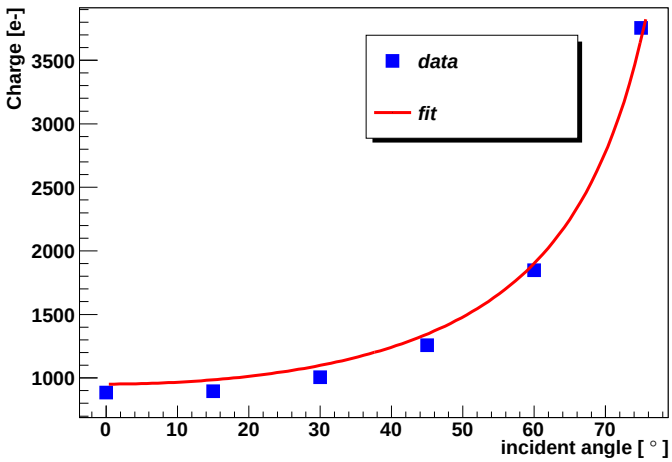

Figure 4.25: *Charge (MPV) collected by clusters composed of* 7×7 *pixels of the MIMOSA-17 sensor. The error bars are smaller than the size of the markers.*

with respect to the amount of generated charge. The ratio of the collected charge over the generated one defines the *charge collection efficiency* (E_{cc}) of the device:

$$E_{cc} = \frac{Q_{coll}}{Q_{gen}} \tag{4.30}$$

The E_{cc} of MIMOSA-17 has been measured for clusters with 3×3 pixels, in the laboratory with the use of an ^{55}Fe source. For the MIMOSA-17 sensor (DUT), this quantity has been found to be 74% [142]. From equations 4.27 to 4.30 the total charge collected in a cluster is found to be inversely proportional to the cosine of the incident angle, assuming that a) l is constant and b) E_{cc} is independent of the particle incident angle:

$$Q_{coll} = \frac{E_{cc} \times 80 \times l}{\cos\theta} \tag{4.31}$$

The last relation justifies the choice of the fit function in Equation 4.26. The parameter α then corresponds to $E_{cc} \times 80 \times l$ and gives a rough experimental measure of the average thickness of the epitaxial layer, l, which is found to be $l = 15.2 \pm 1.2\ \mu m$. This is compatible with the value $l = 14\ \mu m$ provided by the manufacturer's specifications.

4.8.3 Cluster shape

The spatial distribution of the charge in a cluster is shown in Figure 4.26 for different particle incident angles. These distributions were obtained as following: For each accepted cluster, the seed pixel is by definition the one with the highest signal-to-noise ratio. This pixel is being located in the middle of a matrix of 7×7 pixels. The charge values of the three pixel coronas are added to the matrix according to their position relative to the seed pixel. In this matrix the convention is followed such that the direction of a line is defined by the readout direction (see Figure 4.1).

To obtain Figure 4.26, the distribution of the charge on each pixel of the considered clusters was produced and fitted with a Landau function. The most probable value, as provided by the Landau fit, is plotted in the vertical axis for each pixel in the 7×7 matrix. It should be noted here that this approach is different than the one used for the accumulated charge (Figure 4.23); for the latter, the charge corresponds to the most probable value as obtained by a Landau fit of the distributions of *summed* charge over a number of pixels. Here, the charge is obtained by a Landau fit of the distribution of the charge collected on *individual* pixels, according to their geometrical position in the cluster.

For small incident angles, the shape of the cluster obtained with the above method seems symmetric with respect to the central pixel. This is expected in the case of tracks perpendicular to the sensor plane due to the charge diffusing process in MAPS. In fact, as we will see below, there are some significant asymmetries. At an incident angle of 75°, this symmetry is no longer present: one sees that the pixels with column indices (-1, +1) have clearly higher most probable charge than the pixels with line indices (-1, +1). This evolution is expected, as the direction of the particle incident angles is such, that they penetrate the pixels along a line. For high incident angles, more pixels are penetrated, resulting in an elongated cluster shape. For $\theta = 0°$, the charge along the central[9] column

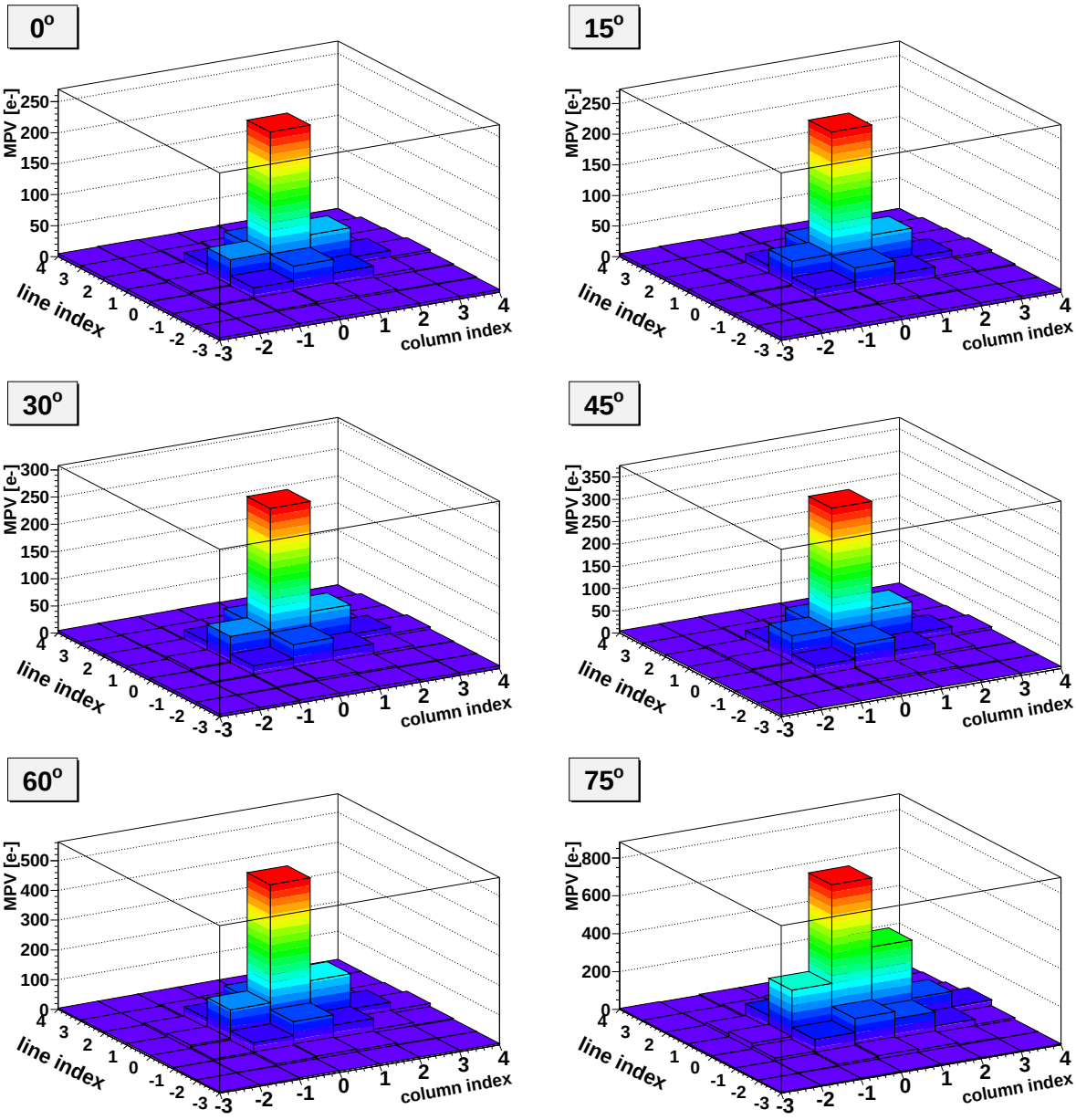

Figure 4.26: *The MPV of the charge on each pixel is shown for particles impinging the sensor with different inclination angles. The size of the array is always 49 pixels. Note the color scale.*

as a function of the pixel's index is shown in the top panel of Figure 4.27.

For tracks at normal incidence, the charge on the pixel with column index +1 is 65.1 ± 0.5 electrons while the charge on the pixel with column index -1 is 53.1 ± 0.8 electrons (bottom of Figure 4.27). This difference is likely not related to the properties of the chip. A similar observation was made already with MIMOSA-9 and MIMOSA-4 [55]. In reference [55] it was argued that, due to insufficient impedance matching, the serial ana-

[9]The term "central" used for a line (column) denotes that the line (column) index is 0.

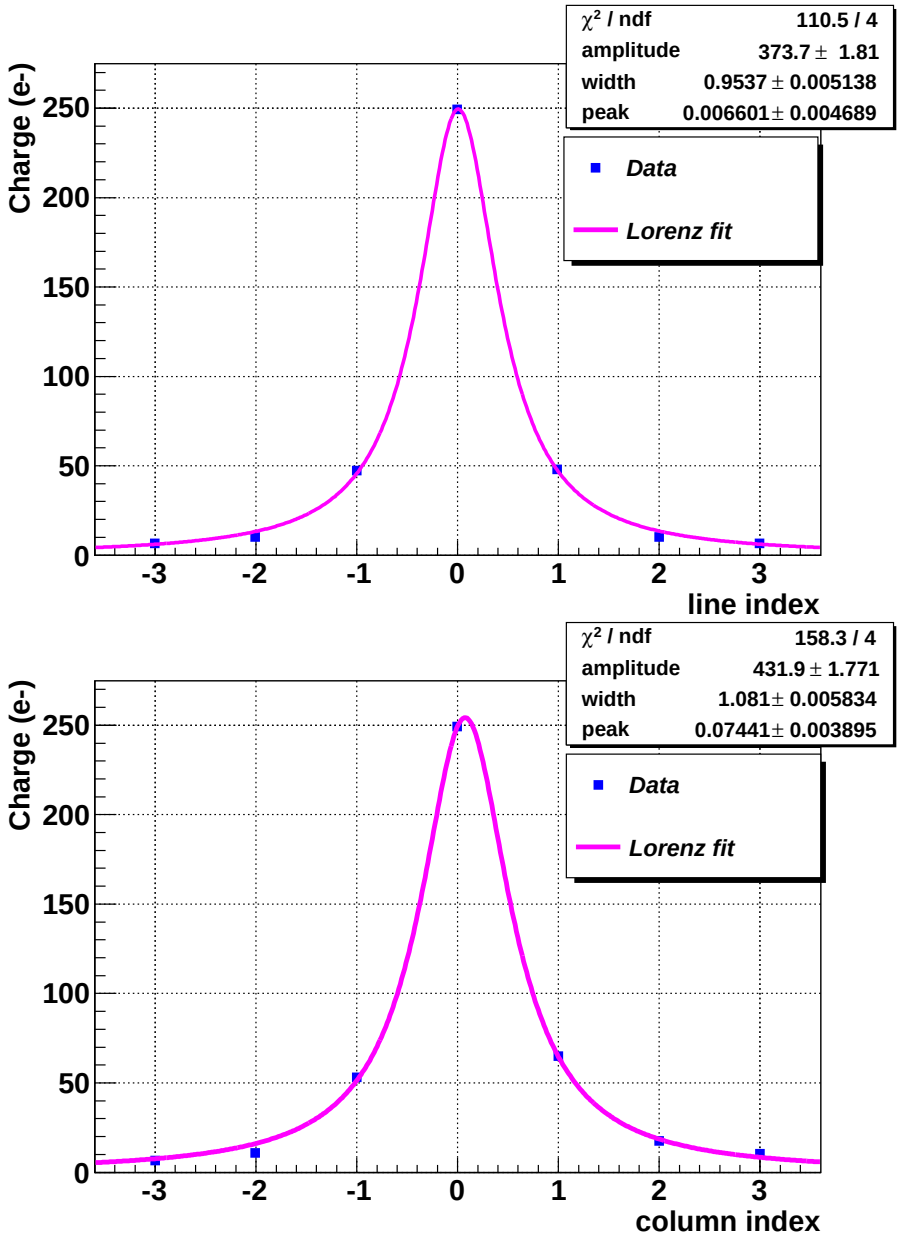

Figure 4.27: *Top: The MPV of the charge on each pixel as a function of the line index. The Lorentz fit on the data is also shown. Bottom: Same, for column indices. The error bars, as obtained from the fit with the Landau function, are smaller than the marker size.*

logue voltage signals of the sensors are reflected in the 40 m long differential signal cables used in the beam test. The latter was suspected to increase the charge indication of pixels which are consecutively read after pixels with a high signal. This would explain why additional charge is observed in the direction of the pixel read out. This explanation had been supported by the observation that replacing the long cables by short ones (1 m) alleviates the effect quite substantially.

In accordance with this explanation one observes in the top panel of Figure 4.27, that the charges among the pixels with line indices -1 and +1 are roughly equal and also match the charge of the pixel with column index -1 (bottom panel).

During this work it was found empirically that such a distribution can be fitted with the Lorentz function:

$$\mathcal{L}(x) = \frac{A \times \frac{G}{2\pi}}{(x-B)^2 + \frac{G^2}{4}} \tag{4.32}$$

where $\mathcal{L}(x)$ is the Lorentz function with parameters A (amplitude), B (peak position) and G (width). The index 0 in the top panel of Figure 4.27 corresponds to the seed pixel, the index +1 (-1) indicates the pixel belonging to the same column but the next (previous) line. The bottom panel shows the corresponding graph for pixels along the central line: the index 0 corresponds to the seed pixel, while the index +1 (-1) is the pixel which is read out next (before).

4.8.4 Spatial resolution

If one plots the distribution of the difference of the position at which the particle track (reconstructed by the telescope) intersects the DUT plane and the corresponding hit position reconstructed by the DUT device, one observes that this distribution is centered around 0 and has a width Δu_{resid}. This width is determined by the contribution of three effects: a) the intrinsic detector spatial resolution $\Delta u_{s.r.}$, b) the uncertainty due to multiple scattering $\Delta u_{m.s.}$ and c) the telescope spatial resolution Δu_T. One may express these three contributions to the Δu_{resid} as following:

$$\Delta {u_{resid}}^2 = \Delta {u_{s.r.}}^2 + \Delta {u_{m.s.}}^2 + \Delta {u_T}^2 \tag{4.33}$$

Since the measurements were performed with a high momentum particle beam (120 GeV/c), the contribution of the multiple scattering is below 1 μm. This value is negligible with respect to other contributions. One can therefore simplify Equation 4.33 as following:

$$\Delta {u_{resid}}^2 \simeq \Delta {u_{s.r.}}^2 + \Delta {u_T}^2 \tag{4.34}$$

The coordinates (u_0, z_0) and (u_2, z_2) of the reconstructed particle hits on the two reference planes are known from the measurements. As shown in Figure 4.3, the first telescope plane is located at $z_0 = 0$ mm, the DUT at $z_1 = 63.5$ mm and the second telescope plane at $z_2 = 127$ mm. Assuming a perfect alignment, the coordinates (z_1, u_1) of the intersection point of the reconstructed track and the DUT are:

$$u_1 = u_0 + \frac{u_2 - u_0}{z_2 - z_0} \times z_1 \tag{4.35}$$

If Δu_0 and Δu_2 denote the spatial resolutions of the telescope planes, the error propagation gives:

$$\Delta u_1 = \sqrt{\left(\frac{\partial u_1}{\partial u_0} \times \Delta u_0\right)^2 + \left(\frac{\partial u_1}{\partial u_2} \times \Delta u_2\right)^2} \tag{4.36}$$

Since two identical MIMOSA-17 are used for the telescope planes, it holds $\Delta u_0 = \Delta u_2 = \Delta u_{s.r.}$. The telescope precision in the u direction, Δu_T, is:

$$\Delta u_T = \Delta u_1 = \Delta u_{s.r.} \times \sqrt{\left(1 + \frac{2 \times z_1^2}{(z_0 - z_2)^2} + \frac{2 \times z_1}{z_0 - z_2}\right)} \simeq 0.7 \times \Delta u_{s.r} \tag{4.37}$$

This equation holds only for the case where the DUT is parallel to the telescope planes. In the general case where the DUT is rotated by an angle θ around the v axis, the telescope precision is:

$$\Delta u_{T,\theta} = \frac{1}{\cos\theta} \times \Delta u_T \tag{4.38}$$

Correspondingly, in v direction, the telescope resolution, Δv_T, is:

$$\Delta v_T \simeq 0.7 \times \Delta v_{s.r} \tag{4.39}$$

Combining equations 4.37 and 4.34 the spatial resolution is given by:

$$\Delta u_{s.r} \simeq 0.8 \times \Delta u_{resid} \tag{4.40}$$

The results are presented in Figure 4.28 for the three different hit position reconstruction algorithms described in Section 4.5. The resolution is displayed as a function of the particle incident angle, for both u (top panel) and v (bottom panel) directions. It is reminded here, that the u direction is defined as the readout direction and v is the direction vertical to u. For the reference planes of the telescope, the η-method is employed.

As expected, the best results among the three hit position algorithms are provided by the η algorithm. The resolution obtained with the digital hit position algorithm is substantially lower than with the two other methods.

The spatial resolution for $\theta = 0°$ is found close to 3 μm (for the center-of-gravity and the η methods) which is similar to the performances of other MIMOSA sensors [145, 150, 70]. For higher incident angles the spatial resolution gradually deteriorates and reaches a maximum of 12 μm for the highest incident angle measured ($\theta = 75°$). Moreover, one observes that the spatial resolution in v-direction is independent of the incident angle.

The digital hit position algorithm is substantially less performant than the center of gravity and the eta-methods. Using the digital method gives a position resolution of $\sim 8\mu m$ (see Section 4.5). Unlike the digital hit position algorithm, the center of gravity method and the eta algorithm use information from several pixels in the cluster in order to define the hit position and provide thus better results. However, the eta algorithm is by construction designed to overcome weak points of the center of gravity algorithm and provides thus better results.

4.9 Summary and conclusion

Data collected during a beam test experiment at the CERN-SPS were used to characterise the response of the MIMOSA-17 sensor to charged particles with different incident angles. A detailed study was carried-out in terms of cluster charge, cluster shape, cluster multiplicity and detector spatial resolution. The results show that:

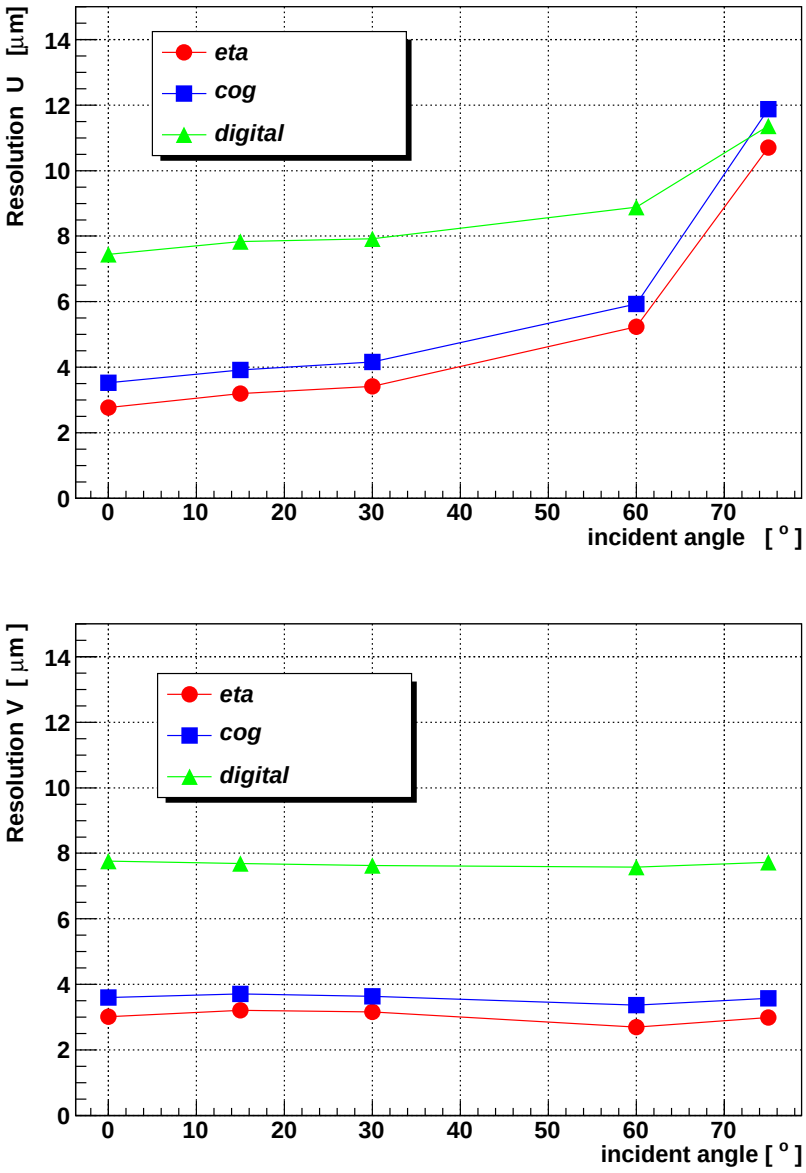

Figure 4.28: *The spatial resolution of the MIMOSA-17 sensor, obtained with three different position determination methods, as a function of the track incident angle. The error bars correspond to the uncertainty of the fit method and are smaller than the size of the symbols. Top: u direction. Bottom: v direction.*

i) The collected charge scales with the length of the trajectory inside the sensitive volume, and thus with $1/\cos(\theta)$, where θ is the particle incident angle.

ii) The average number of firing pixels in a cluster (as obtained for given thresholds on charge) is approximately independent of the incident angle for angles below 45°. For incident angles higher than 45° it gradually increases and may reach $\sim$ 17 pixels for a threshold of 45 electrons and an incident angle of 75°.

iii) The cluster shape is symmetric for small incident angles with respect to the central (seed) pixel, in both u and v directions. An asymmetry was observed on the charge repartition along the u direction. It was however stressed that this is not an intrinsic property of the sensor but a feature of the 40 m long cables used in the specific readout chain. It was observed that the profile of the cluster could be fitted with a Lorentz function. With increasing incident angles, the clusters become more elongated in the u direction.

iv) The spatial resolution is ~ 3 μm and deteriorates with increasing incident angle (θ) along the elongation axis of the cluster (u-axis) and reaches ~ 12 μm for $\theta = 75°$. The resolution along the v direction is ~ 3 μm independent of θ.

The present measurements were performed for a rotation around only one axis. Further studies are therefore needed in order to study the cluster shape or the resolution of the sensor for combined rotation around u and v.

Based on the experience gained from the above studies, we developed and evaluated a detector response model for the MVD. We present these studies in the next chapter.

CHAPTER 5

Development of a detector response model for MAPS sensors

The need for optimising the design of the CBM-MVD and for performing realistic studies on the feasibility of open charm meson reconstruction in CBM, call for detailed detector simulation. So far, related studies were performed [55, 54, 156] based on a simplified description of the response of the MVD detector to charged particles. The focus was laid on the global detector geometry while the detector response was simply represented by a Gaussian smearing of the position of impact of the particle on the silicon layer according to an a priori known spatial resolution. Obviously, this simple description neglects a number of features of the sensor response such as: cluster shape, collected charge, signal to noise ratio and noise hits. Those features are expected to have an important impact on the physics performance of the detector. This holds in particular as the high track density expected in the MVD, will presumably lead to a large number of irregular, for example merged hits, which were considered to worsen the track and vertex reconstruction quality. A reliable simulation of the MVD must be able to represent this effect which requires a precise description of the pixel response. As no suited simulation model was available in the CBM simulation framework, this tool had to be built before performing the simulation. This chapter will be dedicated to the development and benchmarking of the physics performance of this model.

The chapter starts with presenting the requirements for the simulation of an MVD detector composed of MAPS sensors.

We then present and discuss two different MAPS detector response models. The first one was found in literature [148] and meant to describe fully depleted pixel sensors. As we will see, it uses a Gauss function for the charge distribution on the pixels and will be, therefore, referred as "Gauss-model". Due to unsatisfactory performances in describing MAPS sensors, the model had to be improved; since the modified model distributes the charge on the pixels using a Lorentz function it will be called "Lorentz-model" in the following.

As the Gauss model, the Lorentz model will be benchmarked through a comparison

with experimental data. The chapter ends with a summary on the model performances and limitations.

5.1 Requirements for the CBM-MVD simulations

The main purpose of the CBM-MVD response simulation is to provide a realistic description of the response of the detector to the impinging charged particles. The response simulation model must describe in a reliable way the following aspects:

Cluster properties:
As the performance of the MVD is expected to depend crucially on the ability of the sensors to separate the clusters of nearby hits, the shape of the cluster must be well represented in the simulation model. This holds in particular for the pixels in the periphery of the cluster, whose relative contributions may become significant only as they receive charge from two particles. A pixel is considered as significant if its signal exceeds a certain threshold. On the other hand, a good description of the central pixels is crucial to represent the efficiency of the detector.
As shown in Chapter 4, the shape of the clusters depends on the incident angle. This effect is most pronounced for particles impinging the MAPS sensors with incident angles above 60°. Such incident angles correspond, in the environment of the CBM experiment, to particles with very low momentum, such as the δ-electrons. As the latter dominate the occupancy of the MVD, the dependence of the cluster shape on the incident angle needs to be well described.
Spatial resolution: The quality of track and vertex reconstruction depends on the spatial resolution of the MVD. Thus, a precise simulation of the detector spatial resolution is important.
Readout mode: Conceptually, the MAPS technology allows for placing an ADC instead of a discriminator at the end of a column. A priori, both options have advantages and disadvantages for a use in the CBM-MVD. The response model must be designed to allow simulating both, ADC and discriminator.
Fake hits: In MAPS like in every other silicon detector, it happens that a pixel fires without being hit by a particle, due to excessively high noise. An excessive amount of those so-called "fake hits" could have an impact on the occupancy and the data rates of the MVD.
Event pile-up: Presumably, the expected time resolution of the CBM-MVD will be insufficient for distinguishing individual collisions at collision rates of $> 10^5$ $collisions/s$. The simulation framework should thus allow investigating if one can tolerate a pile-up of a certain number of collisions in the MVD. This option is of importance for determining the maximum collision rate and counting statistics of the MVD.

In addition, the underlying algorithm must be fast to allow for the high statistics simulation studies needed for the optimisation of the MVD detector design and the evaluation of the physics performances of the experiment.

5.2 The "Gauss model"

This model [147] was successfully used for the simulations of an ILD [99] vertex detector based on DEPFET sensors. Later, it was demonstrated [148] that a good choice of parameters in this code allows for a fair description of the response of MAPS for small incident angles ($\sim 20°$).

Being initially developed for depleted detectors, the code simulates simultaneously the drift of a cloud of charge carriers in the electric field of depleted detectors and the expansion of this cloud by thermal diffusion. The algorithm is mainly divided in two steps:

1. Simulation of the charge generated by the impinging particle.
2. Distribution of this charge on the pixels.

The model distinguishes three layers in the structure of the sensor. Those are (left part of Figure 5.1): the sensitive layer, which represents the epitaxial layer in the case of MAPS, and the two surrounding layers representing the additional material (support, cooling structure and cables). The surface is divided into pixels. The thickness of the epitaxial layer is an input parameter of the model and was set to 14 μm for the studies performed in this work. The interface between the epitaxial layer and the downstream silicon volume is called the *collection plane*. This plane represents the assumed location of the collecting diodes.

5.2.1 Simulation of the charge generation

To simulate the generation of charge, the algorithm subdivides the particle trajectory in the active volume into segments. A so-called ionisation point is defined in the centre of a segment. The path of the particle inside the material is approximated with a straight line in order to save computing time. The equation of the line is calculated from the entrance and exit points of the particle trajectory in the full detector station (not the sensitive layer). These points are provided by GEANT which also provides the total energy E_{det} deposited by the particle in the detector. The latter (E_{det}) represents however the energy deposit in the full, active and passive material of the sensor. The energy deposited in the epitaxial layer, E_{epi} is calculated by a linear scaling of the total energy deposited:

$$E_{epi} = E_{det} \times \frac{l_{epi}}{l_{det}} \tag{5.1}$$

where l_{epi} and l_{det} are the thicknesses of the epitaxial layer and the full detector layers respectively. The average energy corresponding to each ionisation point, ϵ, is given by:

$$\epsilon = \frac{1}{n} E_{epi} + \delta\epsilon \tag{5.2}$$

where n is the number of segments and $\delta\epsilon$ corresponds to fluctuations taken from the GLANDZ method in GEANT [152].

The amount of deposited energy is translated into the number of generated electron/hole pairs. Knowing that an average deposited energy of 3.6 eV is needed to create an electron-hole pair in silicon [72].

5.2.2 Charge sharing among pixels

The next step is the distribution of electrons on the pixels. This is done by simulating the simultaneous drift and diffusion of the free electrons.

The combined movement of electrons in silicon is generally described as a superposition of a drift and a diffusion.

The equation of particle diffusion [149] is:

$$\frac{\partial \rho_N}{\partial \tau} - \mathcal{D} \times \triangle \rho_N = 0 \tag{5.3}$$

where $\frac{\partial \rho_N}{\partial \tau}$ is the change of the particle concentration, ρ_N, during a time period $\partial \tau$ and $\mathcal{D}$ is the diffusion coefficient.

The three-dimensional solution of the diffusion equation 5.3 is:

$$\rho(x, y, z, \tau) = \sqrt{\left(\frac{1}{4\pi\mathcal{D}\tau}\right)^3} \times e^{-\left(\frac{x^2+y^2+z^2}{4\mathcal{D}\tau}\right)} \tag{5.4}$$

The latter equation describes the distribution of the particle density as a Gaussian centered at the point-like origin of the electrons. The variance of this Gaussian is given with:

$$\sigma^2 = 2 \times \mathcal{D} \times \tau \tag{5.5}$$

Assuming a constant electric field, the particles are simultaneously drifting towards the collection plane with a constant average speed $\overline{v}$. They travel a distance:

$$d = \overline{v} \times \tau \tag{5.6}$$

If Equation 5.6 is combined with Equation 5.5 one obtains a relation between the drift distance and the variance of the Gaussian distribution:

$$d = C \times \sigma^2 \tag{5.7}$$

where $C = \overline{v}/2\mathcal{D}$. Note that while both $\overline{v}$ and $\mathcal{D}$ depend on the electron mobility μ_e, C is independent of μ_e. Equation 5.7 is used to describe the charge over the pixels. This is illustrated in Figure 5.1. The center of each trajectory segment is associated with the center of a Gaussian distribution. The standard deviation of this distribution is denoted as σ_i in the figure, and the drift length of the electron related to the segment is denoted as d_i. The pixel structure is represented by the thick dashed line. The relation between σ_k, σ_0, d_k and d_0 is obtained knowing that according to Equation 5.7:

$$d_k = C \times \sigma_k^2 \tag{5.8}$$

$$d_0 = C \times \sigma_0^2 \tag{5.9}$$

where C is a constant (like in Equation 5.7). From this, one obtains:

$$\sigma_k = \sigma_0 \times \sqrt{\frac{d_k}{d_0}} \tag{5.10}$$

The parameter σ_0 is adjusted by comparison with experimental data; d_0 corresponds to the epitaxial layer thickness[1]. It is assumed that the electrons reaching a pixel in the collection plane are considered to be collected by that pixel.

The charge, q_k, generated at each ionisation point is distributed over the pixels of the collection plane as following: according to a Gaussian distribution function with a σ following Equation 5.10. The integral of this function over the pixel surfaces provides the function of q_k that is distributed to a given pixel. The charge $Q(i)$ on the i^{th} pixel is given by summing up the contribution of the charge of each segment:

$$Q(i) = \sum_{k=1}^{n} q_k \times \int_{x_{min}(i)}^{x_{max}(i)} G(x, x_k, \sigma_k)\ dx \times \int_{y_{min}(i)}^{y_{max}(i)} G(y, y_k, \sigma_k)\ dy \tag{5.11}$$

with

$$G(x, x_k, \sigma_k) = \frac{1}{\sigma_k\sqrt{2\pi}} e^{-(x-x_k)^2/2\sigma_k^2} \tag{5.12}$$

and:

$$G(y, y_k, \sigma_k) = \frac{1}{\sigma_k\sqrt{2\pi}} e^{-(y-y_k)^2/2\sigma_k^2} \tag{5.13}$$

where x_k, y_k are the x and y-coordinates of the k^{th} segment, n is the total number of segments, σ_k is the standard deviation of the Gaussian function centered at (x_k, y_k). The integral limits $x_{min}(i), x_{max}(i), y_{min}(i)$ and $y_{max}(i)$ have to be adjusted to the size of the simulated pixels. To save computation time, segments located more than $3 \times \sigma_k$ are ignored when computing the charge of a pixel.

It should be mentioned that equation 5.7, on which the model is based, was derived under the assumption that the electrons drift inside an electric field. This stands in an obvious contradiction to the fact that MAPS are undepleted detectors, which do not use an electric field for collecting electrons from the active volume. Therefore the description of the charge collection process in the "Gauss model" is not suited for MAPS. Despite σ_0 is tuned to data one expects the model to provide only a first order description of the charge collection process. This expectation is indeed supported by the observations made during the benchmarking of the model, which will be shown later in this chapter.

5.2.3 Simulation of the ADC

The simulated charge Q_i is provided in units of electrons. In order to represent the ADC of the sensors, it was translated into ADC units. To do so, one assumes an ADC with N_b bits. Q_{max} and Q_{min} are the highest and lowest charges[2] respectively, which are in the dynamic range of the ADC. Then one finds:

$$E_{FSR} \;=\; Q_{max} - Q_{min} \tag{5.14}$$

[1] More precisely, d_0 is equal to the epitaxial layer thickness minus one half of the segment length (see Figure 5.1). The small values of the segment length ($\sim 1\ \mu m$) compared to the epitaxial layer thickness ($\sim 14\ \mu m$) allow for this approximation.

[2] More precisely, the ADCs measure the output voltage of the pixels which are computed from this charge, accounting for the constant charge-to-voltage conversion gain of the readout chain. As this factor, however, cancels out during cluster finding, there is not any interest in representing it in the simulation.

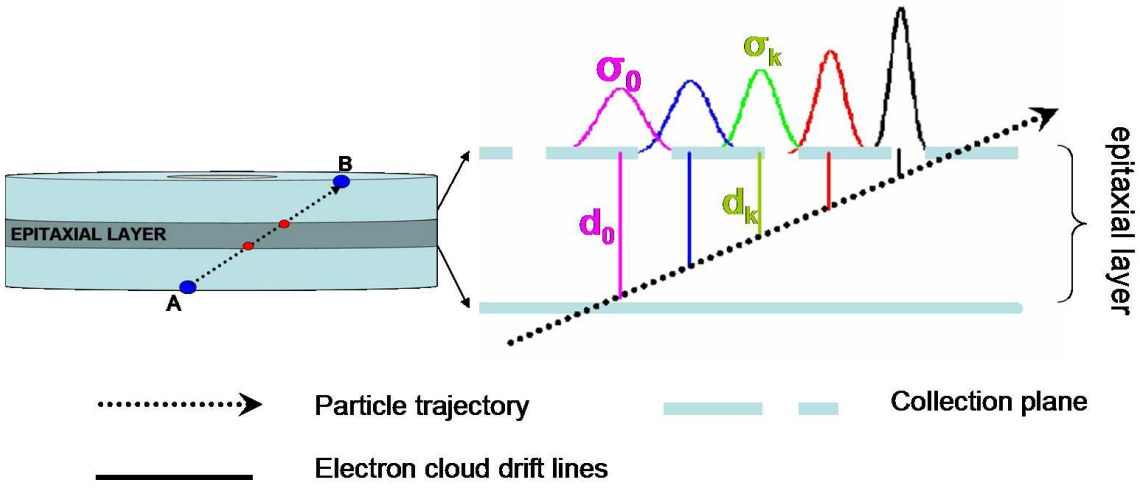

Figure 5.1: *Illustration of the charge sharing procedure based on Gaussian functions. The left part shows the side view of the detector in simulation.A zoom of the epitaxial layer is shown on the right. The thick dashed line represents the collection plane, hosting the pixels diodes. The center of each Gaussian function is located at the center of each segment of the particle trajectory. The distance covered by the electrons is denoted by d_i.*

$$N_{levels} = 2^{N_b} \tag{5.15}$$

$$Q_{res} = \frac{E_{FSR}}{N_{levels}} \tag{5.16}$$

where, E_{FSR} is the dynamic range, N_{levels} is the number of discrete values provided by the ADC and Q_{res} is its charge resolution.

The charge of the pixel in ADC units Q_{ADC} is the integer part of the fraction $\frac{Q-Q_{min}}{Q_{res}}$:

$$Q_{ADC} = \lfloor \frac{Q - Q_{min}}{Q_{res}} \rfloor \tag{5.17}$$

In the simulation model N_b, Q_{max} and Q_{min} are fully adjustable parameters and offer the possibility to vary the number of ADC bits in the simulations. Note however that the simple model does, so far, not allow simulating potential noise by flipping and offset of the ADCs. The current knowledge on these effects is insufficient for a reasonable model building.

5.2.4 Electronic noise

As discussed in Section 4.3.4, the noise of a pixel remaining after all correlated noise has been filtered out, follows approximatively a Gaussian distribution. Therefore, in simulations, the electronic noise of each pixel is represented by a random number taken from a

Gaussian distribution with a mean value[3] of 0 and with an adjustable standard deviation. The latter is set according to the measured noise of the sensor. In order to minimise the computing time, the model adds noise only on a matrix of 7×7 pixels around the seed pixel.

A fake hit[4] generator based on Gaussian noise is available in the model. It is however of limited use as it requires an excessive computing time. In the present work, this generator was turned off and the contribution of fake hits was therefore neglected. Given the measured fake hit rate of 10^{-5} for MIMOSA-26 this simplification appears acceptable [158]. Optimised algorithms accounting, among others, for Random Telegraph Signal which dominates the fake hit rate [157] are under investigation.

5.3 Cluster reconstruction algorithm

The model was complemented with a cluster reconstruction algorithm. The input of the algorithm are the so-called digis, providing the coordinates and the charge of firing pixels. The output are the reconstructed coordinates of the impact point of the particle (hits). The hits are later used as input for the tracking code. The cluster reconstruction algorithm executes two tasks: i) it identifies clusters and ii) it reconstructs the impact position of the particle corresponding to the clusters.

The natural approach would be to implement the same cluster reconstruction algorithm as in the MAF framework used in Chapter 4 for the experimental data. In this algorithm the pixels are however at some point ordered by their charge or their signal-to-noise ratio. This makes this approach not suitable for cases in which more than one pixel with a given charge is found in a cluster. This is typically the case of data acquired with a discriminator. Therefore, a new cluster finder algorithm that is suitable both for analogue and digital data had to be developed. Moreover, as the incident angles of the particles in the experiment are random, and cluster merging is expected, the cluster finder should provide the option to reconstruct any cluster shape which is not possible with MAF.

The novel algorithm scans the array of digis for pixels with charge above a certain threshold. These pixels are used as *seeds* for reconstructing a cluster. Neighbouring pixels of the seeds are checked if they pass a second, so-called neighbour threshold, which may be equal or smaller than the seed threshold.

For the neighbours that have passed the selection, the procedure is repeated: their significant neighbours are included into the cluster. A cluster is considered as completed if no more significant neighbour pixels are found.

Once the pixels belonging to a cluster have been identified, the center of gravity algorithm (cog) is used for the reconstruction of the hit. If q_i and x_i, y_i are respectively the charge and x,y coordinates of pixel i of a cluster then the x and the y coordinates of the hit are

[3] The noise is a stochastic process and therefore its average value should be 0.

[4] A fake hit is defined as a pixel that has fired without receiving a signal which is typically due to noise exceeding the detector threshold.

Name	Typical value	Value used
Epitaxial layer thickness	$10 - 20\ \mu m$	$14\ \mu m$
Pixel pitch	$10 - 30\ \mu m$	$30\ \mu m$
Segment length	few μm	$1\ \mu m$
Diffusion coefficient (σ_0)	none	$30\ \mu m$
Integral limits	none	($\pm 90\ \mu m$)
ADC settings	1-12 bits	12 bits
Noise	10-15 electrons	15 electrons

Table 5.1: *List of the model input parameters and their typical values. The values used are adjusted according to the properties of the MIMOSA-17 sensor.*

given by:

$$x_{cog} = \frac{\sum_i q_i \times x_i}{\sum_i q_i} \tag{5.18}$$

$$y_{cog} = \frac{\sum_i q_i \times y_i}{\sum_i q_i} \tag{5.19}$$

Note that the use of the η method (see Section 4.5) instead of the center of gravity method is not of advantage. This is as the non-linearities which may be corrected by the η algorithm are not represented in the simulation.

5.4 Benchmarking the Gauss model with experimental data

In order to evaluate the performance of the model, the simulated response of MAPS was compared with experimental data acquired with MIMOSA-17 at the CERN-SPS (see Chapter 4). The parameters used in the model are chosen to match the features of the MIMOSA-17 sensor. Those are: pixel size $30 \times 30\ \mu m^2$, the noise is set to 15 electrons. For the cluster reconstruction algorithm we set the two thresholds to 75 and 30 electrons.

The input parameters of this model are summarised in Table 5.1. The typical values correspond to existing MAPS sensors. The values used in the comparison with experimental data are shown in the last column.

The model is evaluated in terms of its ability to provide a realistic description of the cluster charge and the average number of significant pixels in a cluster.

5.4.1 Average cluster multiplicity

The pixel multiplicity in a cluster, N_{pixels}, is defined as the number of significant pixels in a cluster. If N_c is the total number of clusters analysed, then the average value of N_{pixels} is

$$< N_{pixels} >= \frac{\sum_{i=1}^{N_c} N_{pixels}}{N_c} \tag{5.20}$$

The average cluster multiplicity depends on the parameter σ_0 (see Equation 5.10) of the model. The latter was adjusted in a way that the simulated average multiplicity of the cluster fits the experimental results for a 0° incident angle and with a charge threshold of 75 electrons. Hereafter, with this parametrisation, the model will be evaluated for various angles and charge thresholds. As the latter is a free parameter during cluster reconstruction, the model should be able to reproduce the response of MAPS for various charge thresholds without modifying its initial parametrisation.

Therefore, we compared the experimental and simulated average number of significant pixels as a function of the incident angle, and as a function of the threshold. We used three thresholds: 45, 75 and 105 electrons, corresponding to 3, 5, 7 times the noise of MIMOSA-17. This represents the most likely range of operating a sensor in the real experiment.

A comparison of the average pixel multiplicity provided by the model and the multiplicity obtained from experimental data is presented in Figure 5.2. The discrepancy observed for a threshold set at 45 electrons is increasing with the incident angle and is of the order of 30% for maximum incident angle. However, this disagreement is not crucial, as this relatively low threshold will probably not be used for the analysis of experimental data. For higher thresholds (above 75 electrons) the simulation reproduces the data within 10%. Among the different parametrisations shown, the model shows the best results for $\sigma_0 = 30\ \mu m$ (middle panel of Figure 5.2). Therefore this value was chosen for next steps on the performance studies.

5.4.2 Charge distribution among the pixels of a cluster

The accumulated charge plot (which was described in Section 4.8) allows to compare the distribution of the simulated and the measured charge. Figure 5.3 shows the comparison between simulation and data, for 0°, 45° and 75° incident angles. The most probable value is shown in the left column and the σ_L in the right column. Both parameters of the Landau fit are used for building the accumulated charge plots.

The most probable charge of the most significant pixels is overestimated by roughly 10%. This rather small discrepancy allows to conclude that the charge distribution for these pixels within the cluster is quite accurately reproduced. The discrepancy becomes however more important for higher incident angles. Moreover, the width of the distribution, the parameter σ_L, shows large discrepancies of 50% or above.

5.4.3 Discussion on the performance of this model

It was shown that a good choice of the σ_0 parameter allows the model to reproduce the average number of significant pixels per cluster with a precision better than 10%. However,

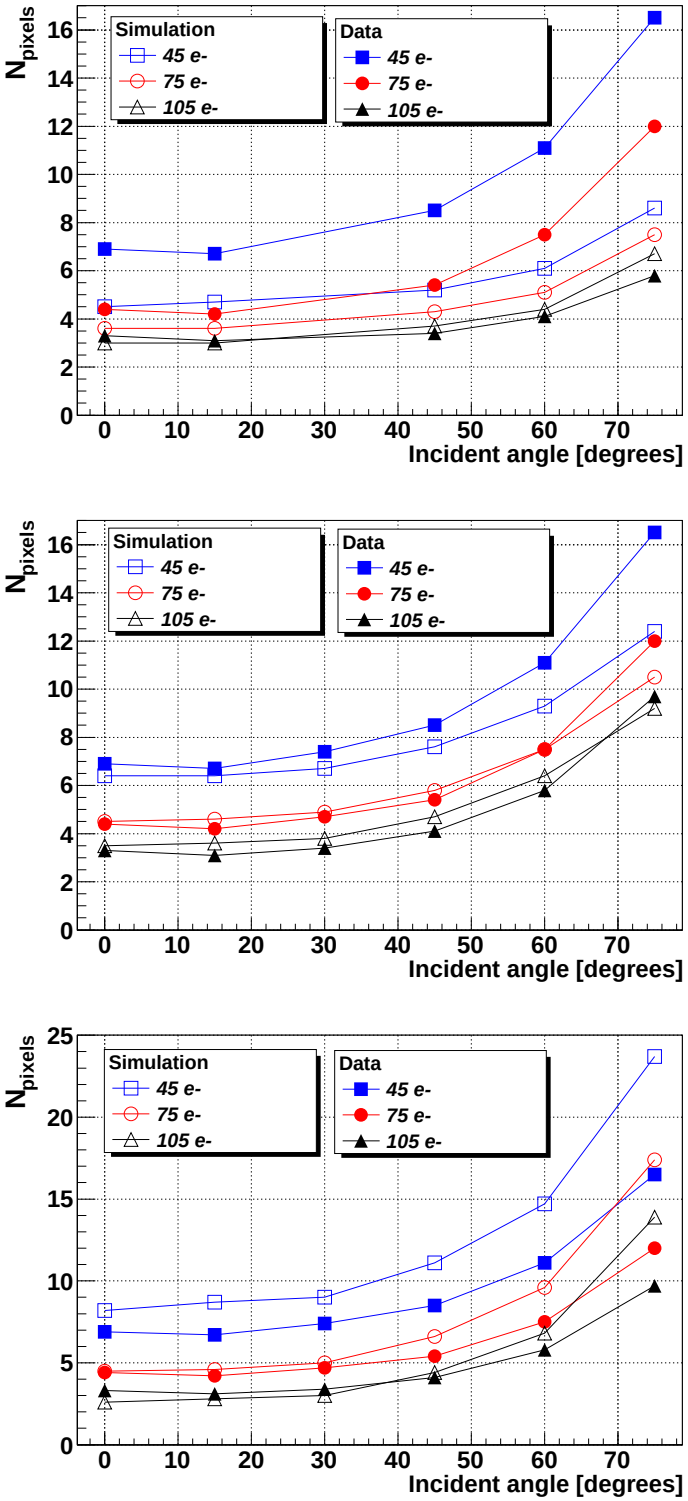

Figure 5.2: *The average number of pixels within a cluster as a function of the incident angle. The experimental results (full symbols) are compared to the results of the simulations for three different values of the σ_0 parameter:* 18 *µm (top panel),* 30 *µm (middle panel) and* 55 *µm (bottom panel). The comparison is shown for different values of the charge threshold: 45 electrons (blue rectangles), 75 electrons (red circles) and 105 electrons (black triangles).*

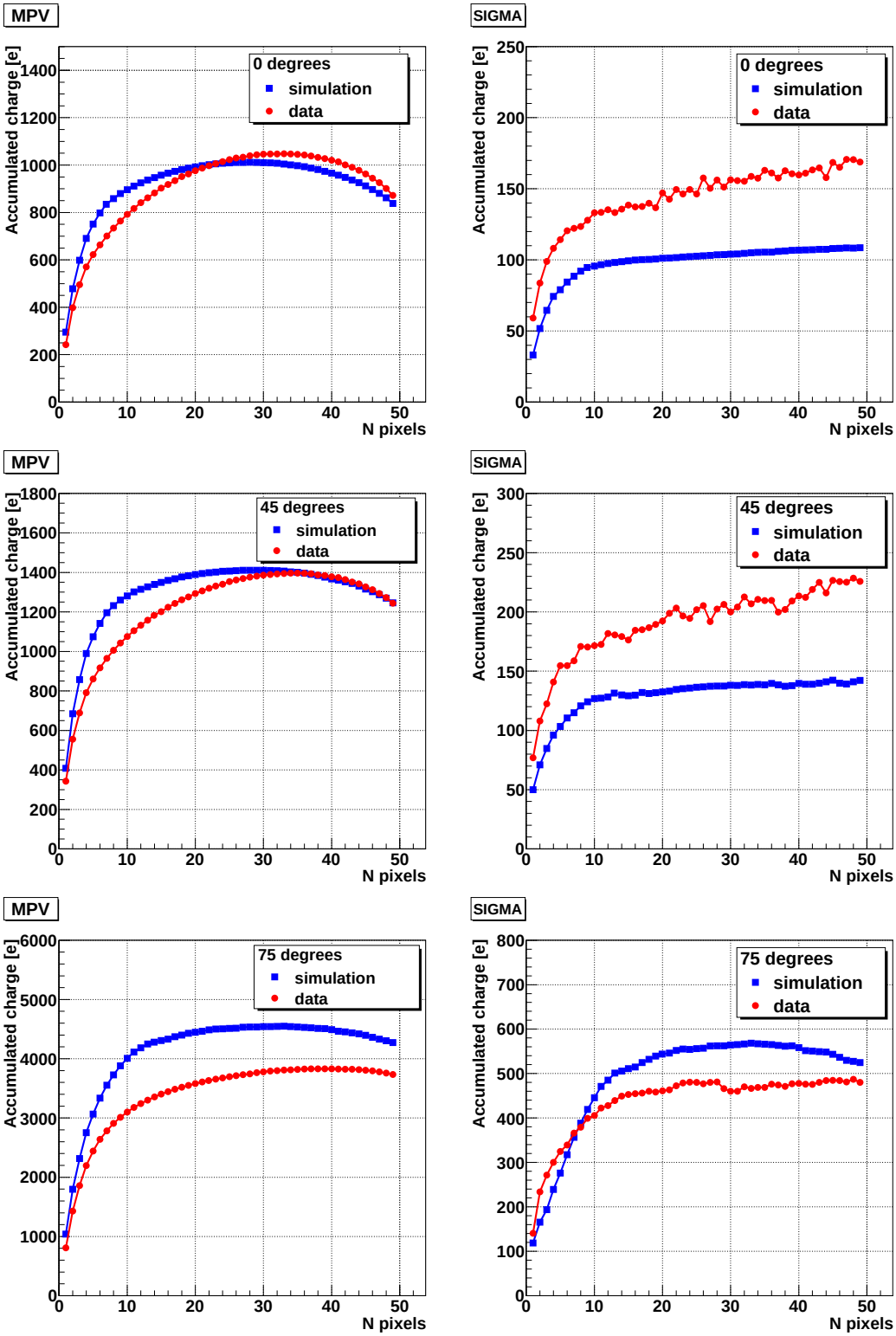

Figure 5.3: *Comparison of the accumulated charge plots obtained from MIMOSA-17 data (red) and the Gauss model (blue). The left column corresponds to the most probable values as obtained from the fits with the Landau function, while the σ_L (from the same fit) is shown on the right-hand side column. The incident angles are 0°, 45° and 75° from top to bottom respectively.*

the distribution of the charge on the pixels inside the cluster is not well reproduced. Only the most probable charge in the most significant pixels ($N_{pixels} \leq 5$) is reproduced with a 10% accuracy. The charge of the pixels with intermediate values of $5 \leq N_{pixels} \leq 10$ (as plotted in Figure 5.3) is substantially overestimated in the simulation. This effect becomes more pronounced for higher incident angles. It is reminded that the pixels appearing last (large N_{pixels}) in the plot in Figure 5.3 are the ones receiving less charge [5]. Geometrically, these are the pixels located mainly in the outer coronas (periphery of the cluster). With the parameters used here, the model tends to distribute more charge to the central, most significant pixels and fails to correctly represent the charge on the outer coronas (mainly large N_{pix}). The use of this model might lead to substantial overestimation of the rate of merged clusters.

The primary goal of the simulation, which is to assess the expected performance of the experiment for open charm measurements, requires a precise estimate and description of this rate. Therefore the Gauss-model was not considered as sufficiently precise for the purpose of this work.

An obvious explanation of the failure of the model lies in the initial assumptions made. As mentioned in the beginning of this chapter, the model was initially developed for fully depleted sensors. It is thus implicitly assumed that the electron cloud is directed by means of an electric field to the collection diode which is not present in the undepleted MAPS.

5.5 The Lorentz detector response model

The limits of the Gauss model motivated the development of a more appropriate model that can describe accurately the cluster shapes for all incident angles. In this approach, a parameterisation of the experimental data is performed. It consists thus in describing the response of the detector without taking into account the physics process of charge creation and diffusion. The approach of the previous model to approximate the trajectory inside the epitaxial layer with a straight line and to divide it in segments was kept but the model for the charge generation and distribution on the pixels was completely reworked. The charge of the pixels inside the cluster as well as its shape are parameterised from experimental data.

5.5.1 Charge generation

In this model, the total charge collected by a cluster is taken randomly according to a Landau distribution[6]. The parameters of the latter are determined by fitting the experimental distribution of the total charge collected by a pixel array with 5×5 pixels. The size of this array is sufficient to register the full signal charge. Only experimental data from tracks perpendicular to the detector plane are used. Figure 5.4 shows the Landau distribution used as input in the model. Inclined tracks are simulated by scaling the charge obtained from the random number according to the length of the particle trajectory in the

[5] See Chapter 4

[6] It was discussed in Chapter 4 that the collected charge measured by a cluster of pixels after the passage of a charged particle in a MAPS sensor follows with good approximation a Landau distribution.

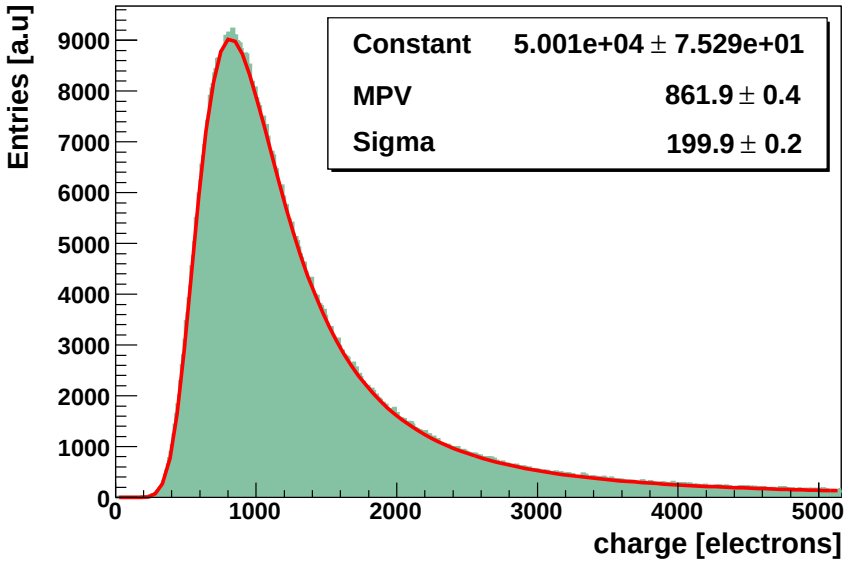

Figure 5.4: *The simulated Landau distribution for tracks perpendicular to the detector plane. The Landau fit is shown in red line. The most probable value (MPV) of the distribution and the parameter sigma are indicated.*

epitaxial layer. This is a reasonable procedure: as was shown in Section 4.8.2, the measured collected charge on a cluster may be derived by scaling the charge according to the trajectory length inside the epitaxial layer.

5.5.2 Charge distribution on pixels

It was shown in Chapter 4 that the charge corresponding to the central line (or column) of pixels can be fitted with a Lorentz function[7]. Therefore, it seemed natural to use this function as a starting point in the model, in order to distribute the charge on the individual pixels of a cluster. Figure 5.5 shows a schematic view of charge sharing in the Lorentz model. The parameters of the Lorentz function used were defined as described in Section 4.8.3 (see Figure 4.27). Being inspired by the response model based on Gauss functions, we placed the centre of each Lorentz function at the centre of each trajectory segment. However, unlike in the Gauss model, the width of the Lorentz functions was kept constant, independently of the position of the related ionisation point. The charge distributed on each pixel is determined by multiplying the generated charge (from random sampling of the measured Landau) by the value of the Lorentz function at the coordinates of the center of a pixel. The contributions of the Lorentz functions of several ionising points are added. The charge on the pixel i is given by:

$$Q_i = \frac{1}{n} \times Q_{Landau} \times \sum_{k=1}^{n} \frac{A \times \frac{G}{2\pi}}{(x_k - x_i)^2/P^2 + (y_k - y_i)^2/P^2 + G^2/4} \tag{5.21}$$

[7]The central line (or column) is the one that includes the seed pixel.

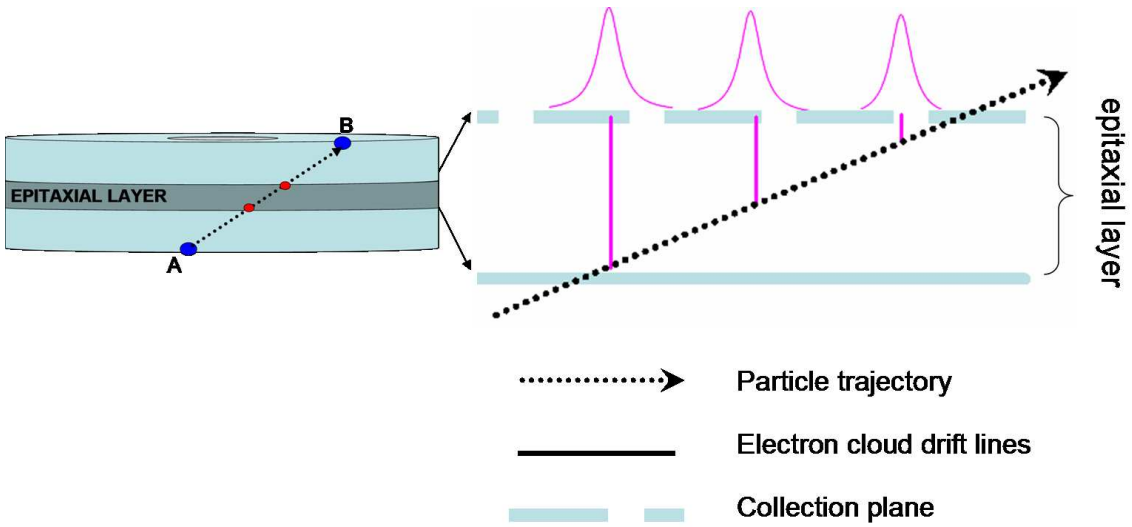

Figure 5.5: *Illustration of the charge sharing procedure among pixels in the Lorentz model. The left part of the figure is an enlargement of the epitaxial layer. The centre of each Lorentz function at the centre of the particle trajectory segments.*

where Q_{Landau} is the charge taken from the measured Landau charge distribution; A, G are parameters defined in Section 4.8.3; P is the pixel pitch, which is needed to obtain the correct units for the charge. x_i, y_i are the coordinates of the center of pixel i, x_k, y_k is the position of the ionisation point and n the number of ionisation points. This equation is inspired from Equation 5.11 and is empirically obtained in the context of this work.

5.5.3 Implementation of event pile up for the MVD

Due to its limited readout time, the MVD detector will likely operate with a moderate collision pile up. Since pile up does not affect in the same way all detectors[8] this effect must be implemented in the response model of the MVD.

During one readout cycle, the MVD will accumulate hits from few nuclear collisions and from the electrons knocked out of the target. The latter (also called δ-electrons) originate from the passage of beam ions through the target. The field of the dipole magnet of CBM deflects a part of the δ-electrons before they can reach the vertex detector. Nevertheless, the remaining electrons are sufficiently numerous to be of concern for the occupancy of the MVD.

To simulate a pile up of N events, we merge the hits originating from one central collision and N-1 minimum bias collisions. This combination is motivated by the fact that in CBM a selection of central collisions is foreseen. Therefore, among the number (N) of event pile-up we want to make sure that we have at least one central collision in simulation. To take into account the contribution of delta electrons, we include the hits resulting from $k \times N$ ions

[8]The STS, with a readout time of in the order of 10 ns is sufficiently fast to operate without pile up at a nominal collision rate of 10 MHz

traversing the target, where k is the inverse of the interaction probability of the target used in simulation. For example, if the target has an interaction probability of 1% then $k = 100$.

The central collisions, the minimum bias collisions and the ions are saved in separate files. For clarity, we distinguish the "main-file", the "pile-up file" and the "δ-electron file" accordingly.

Typically one simulates 10^4 central Au(25 $AGeV$)+Au collisions without pile up (N=1), and a target with an interaction probability of 1% (k=100). Then $10^4 \times k \times N = 10^4 \times 100 \times 1 = 10^6$ ions crossing the target would be needed in order to simulate the corresponding δ-electrons. This approach is extremely consuming in terms of CPU time and memory. In order to overcome this limitation, a sufficiently large number of ions, M, producing the δ-electrons are simulated (typically few 10^3). The corresponding particle hits on the MVD are saved in an independent file ("δ-electron file"). For each nuclear collision, the detector response model then "reads" the δ-electron file and randomly chooses $k \times N = 100 \times 1 = 10^2$ ions. The hits from these ions are added on the MVD stations. Special care is taken in order not to choose the same ion multiple times for the same nuclear collision. In this approach, one is able to obtain $\binom{M}{k \times N}$ different combinations of ions. Provided that M is sufficiently large, this approach allows to simulate the δ-electrons for a large number of nuclear collisions.

Similar approach is followed for the simulation with event pile-up. Typically 1000 minimum bias collisions are simulated and saved in an independent file ("pile-up file"). Then, if one wants to simulate the pile up of N=5 events and the corresponding δ-electrons, one has to add the hits from one central event from the "main-file", 4 events from the "pile-up file" and 500 ions from the "δ-electron file" to the MVD stations.

5.5.4 Comparison between simulation results and experimental data

The Lorentz model was parameterised with data obtained for particles impinging the detector with an incident angle of 0°. It remains to demonstrate that it reproduces accurately the response of MAPS for larger incident angles. Figure 5.6 shows the average cluster pixel multiplicity as a function of the incident angle. The simulated results reproduce the experimental data with a precision better than 10%, if high charge thresholds (above 75 electrons) are used. For the lowest threshold considered (45 electrons), the simulation overestimates the cluster pixel multipicity, but the discrepancy stays below 15%. This is however only of academical interest as this low threshold is not suited for a real detector operation.

The most probable value of the integrated cluster charge as a function of the pixel number N_{pixels} for incident angles from 0° to 75° is shown in Figure 5.7. All obtained results agree within 10%. The standard deviation (σ_L) of the integrated cluster charge as a function of the pixel number N_{pixels} for incident angles from 0° to 75° is shown in Figure 5.8. Differences are mainly observed for σ_L for 75°: the simulation overestimates σ_L by 30%.

Figures 5.9 and 5.10 illustrate that the geometrical shape of the cluster is in accordance with the experimental one for different particle incident angles (45° to 75°). The plots show the most probable value of the charge as obtained from the Landau fit of the charge distribution of the pixels. The left column shows the shape as obtained by simulation and the right column shows the shape as obtained from the experimental data.

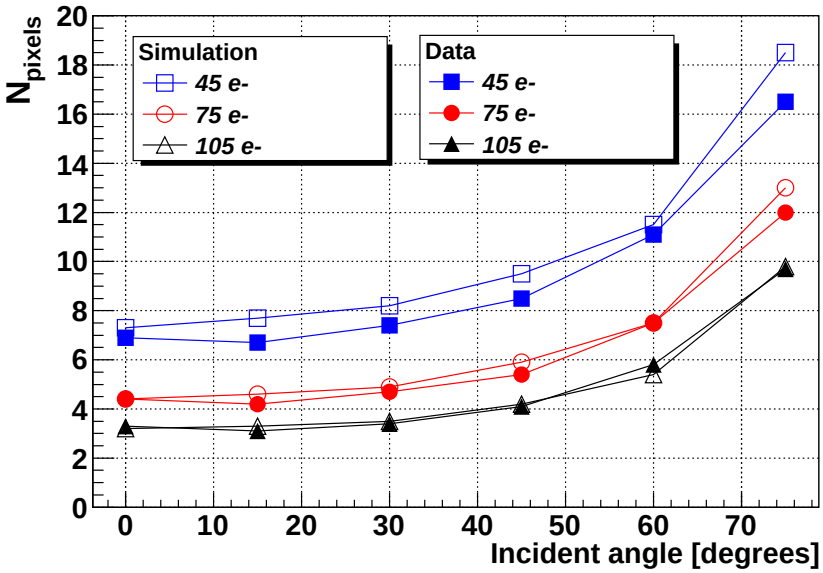

Figure 5.6: *Comparison of the average number of significant pixels in a cluster as obtained from the Lorentz model and experimental data.*

The cluster shapes are well reproduced. Note that for the experimental data, the charge on the right side of the seed pixel (column index +1) is in general higher than for the pixel left of the seed (column index -1). This effect, as it has been discussed in Chapter 4, is not a feature of the sensor and it should therefore not be reproduced by the simulation model.

5.6 Summary and conclusion on the detector response models

Two different detector response models for MAPS were implemented and tested against experimental data obtained for the MIMOSA-17 sensor. In the first model, initially developed for depleted pixel detectors, the mechanism of diffusion of the charge is based on a Gaussian function. This model was compared with experimental data and showed weaknesses in reproducing the charge on the outer pixels of a cluster, which is essential for realistic simulations of the MVD. It was therefore important to develop another model that allows a better description of the response of MAPS sensors to charged particles. This new model, so-called Lorentz model, is based on a parameterisation of the measured response of MAPS. The mechanism of charge diffusion is based on the measured profile of the cluster which follows a Lorentz distribution. The model parameters were tuned according to data measured in a beam test at the CERN-SPS for tracks at normal incidence on the sensor surface. The model predictions for those tracks as well as for inclined tracks (up to 75°) were compared with measured data. The model describes within 10% accuracy the most crucial parameters for simulations purposes of the CBM-MVD, which are the cluster pixel multiplicity and the charge sharing among the pixels in the cluster. A discrepancy of 30% is observed for the parameter σ_L, which corresponds to the width of the charge distribution

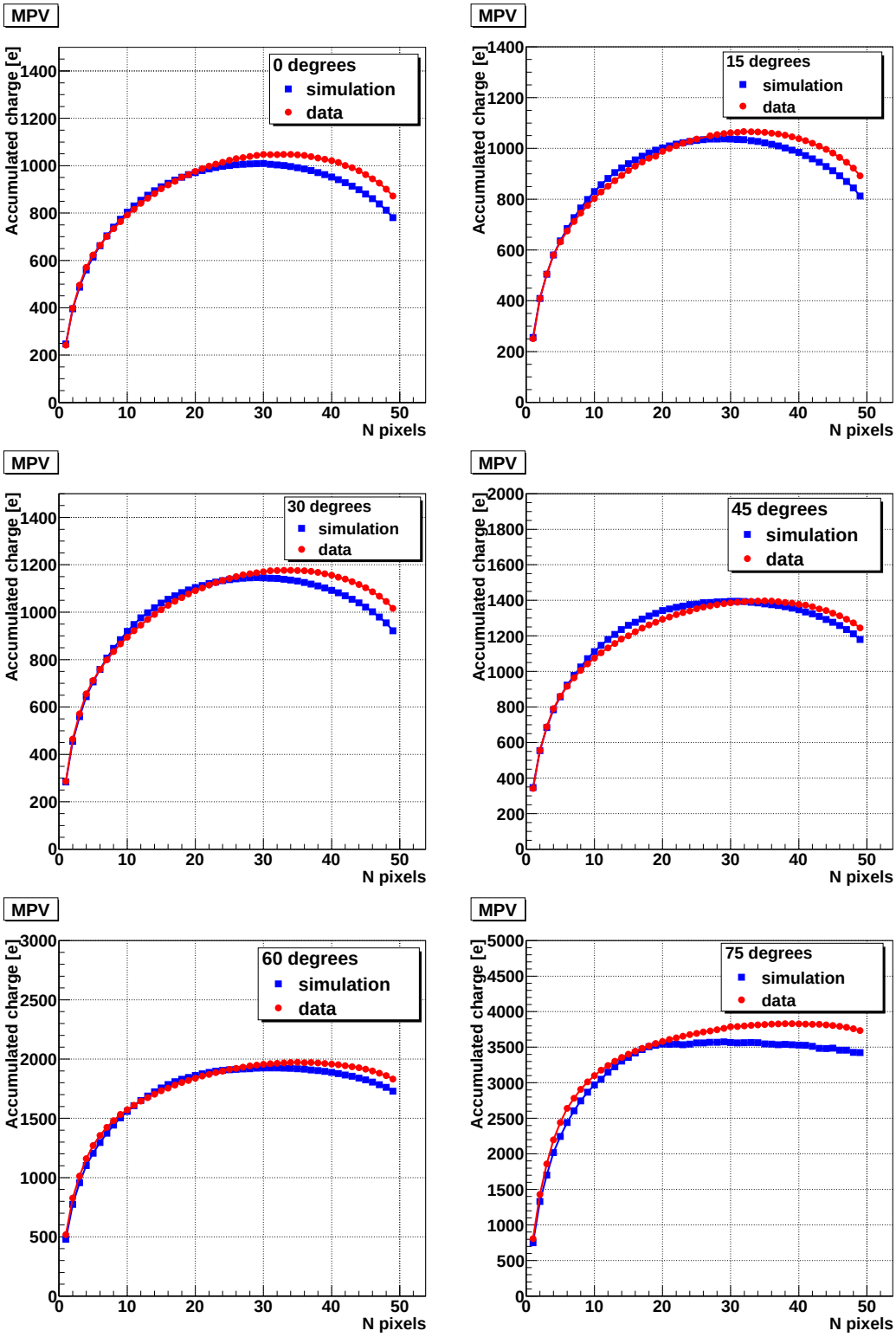

Figure 5.7: *Comparison of simulated and experimental data for the most probable value (MPV) of the integrated cluster charge as a function of the pixel number N_{pixels} for different particle incident angles.*

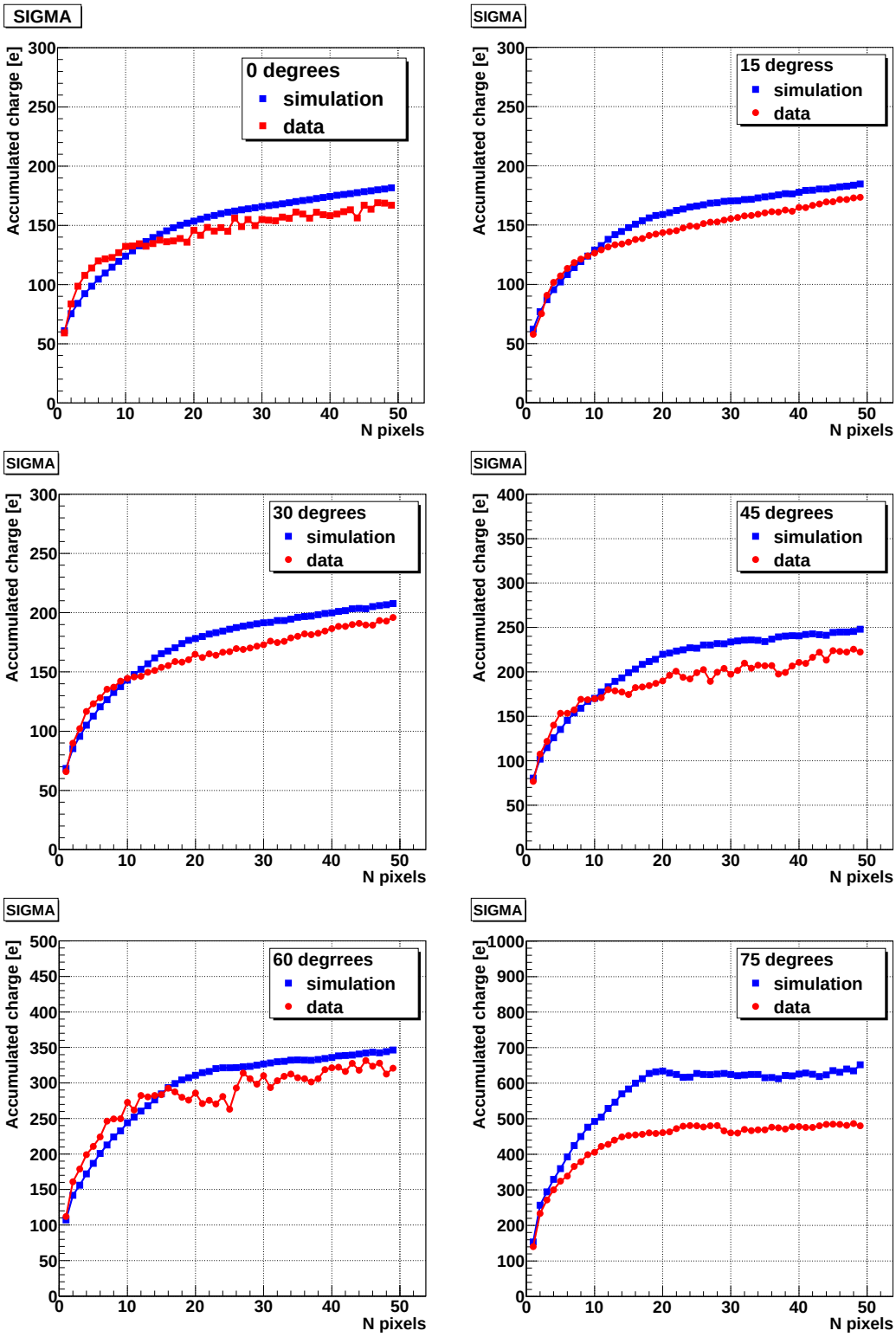

Figure 5.8: *Comparison of simulated and experimental data for the σ_L of the Landau fit.*

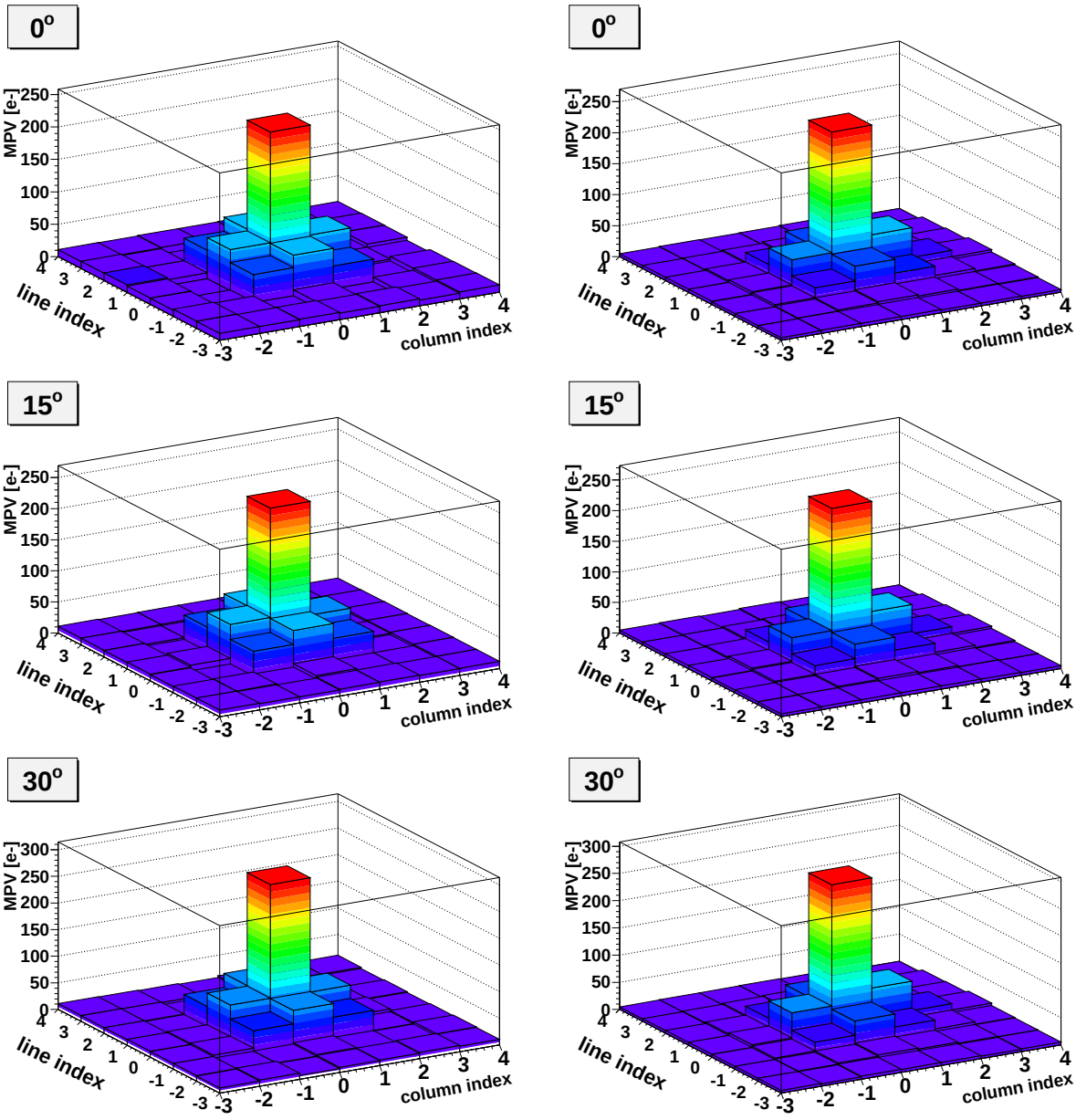

Figure 5.9: *The simulated MPV (left column) and the experimental MPV (right column) of the charge on each pixel is shown for particles impinging the sensor for different particle incident angles (*0°,15°, 30°*).*

on the pixels. Overall, the Lorentz model has demonstrated better performances than the Gauss model. Due to its good performances it was chosen to be used for the simulations of the CBM-MVD. As input from measured data is needed, the Lorentz response model is not able to predict the properties of MAPS but it can reproduce accurately their response profiting from a rich data base of the properties of different MAPS prototypes obtained in numerous beam tests.

The implementation of this detailed MVD response model in the CBM simulation frame-

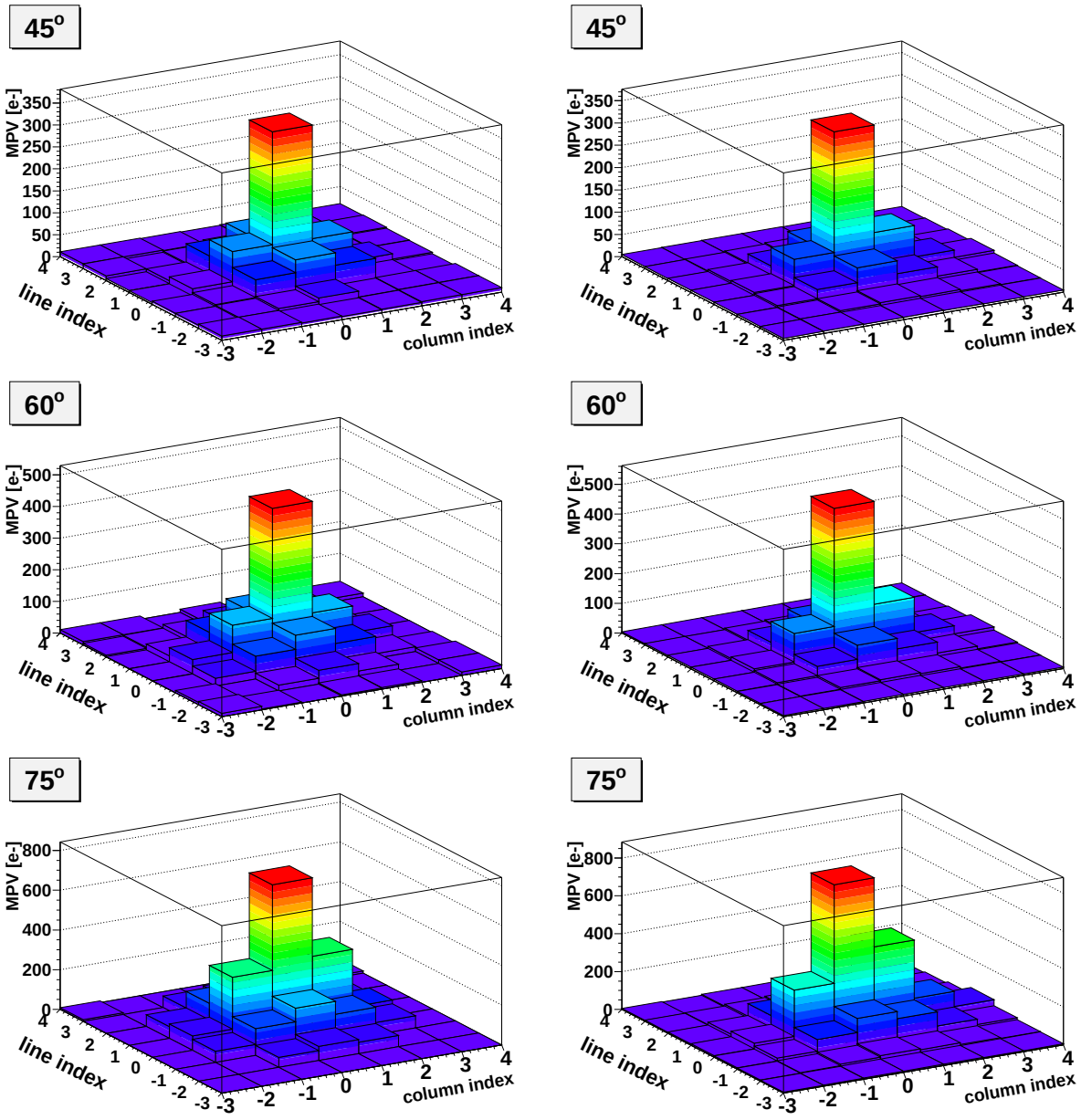

Figure 5.10: *The simulated MPV (left column) and the experimental MPV (right column) of the charge on each pixel is shown for particles impinging the sensor with different particle incident angles* 45°, 60°, *and* 75°. *Note that the color scale is not the same for different incident angles.*

work allows us to perform realistic simulation studies to assess the physics capabilities of the CBM experiment. Moreover, it offers the possibility to compare the expected performances for different MAPS sensors. This last point is crucial for the design and the optimisation of the MVD detector. The model allows to investigate the possibility to pile-up a certain number of events in the MVD detector. This is extremely important for high statistics measurements which are needed for detailed studies of open charm particles. A detailed

MVD response simulator is also very important for the evaluation of data flow which is a necessary input for the elaboration of data compression strategies.

In the next chapter, we will use the model to address the first two topics mentioned above.

CHAPTER 6

Performance for the reconstruction of open charm particles

Simulation studies are needed in order to assess the expected physics performance of the CBM experiment for open charm particle measurements in nucleus-nucleus collisions. The low production multiplicities of open charm mesons at FAIR energies impose the use of high beam intensities which would allow measuring sufficient statistics. The increased particle flux due to high beam intensity induces problems of occupancy and radiation damage. These harsh requirements turn into the need to operate the Micro Vertex Detector as close as possible to its technological limits. In order to obtain a realistic picture of the limits of MAPS and the physics potential which could be reached using this technology, accurate and quantitative simulations are required. A core element of those simulations is the detector response model for MAPS sensors which has been the object of the previous chapter.

The chapter starts with a short introduction on the interest of measuring open charm mesons with CBM. Next, the simulation procedure is described and the MVD detector setup used in the simulations is presented. Then, the physics performance of the MVD is benchmarked using the D^0 meson in its hadronic decay channel leading to a (π^+, K^-) pair. The chapter ends with a discussion on the simulation results, their implications regarding the physics program of the CBM experiment and some suggestions for future improvements.

6.1 Introduction

Since most of the charm quarks are carried away in D-mesons in the final state, data on open charm are crucial for a deep understanding of charm production. Moreover, the effective masses of D-mesons are expected to be modified in the hot and dense nuclear medium (see Chapter 1). Experimental investigations of these effects should shed light on the question of chiral symmetry restoration in dense hadronic matter. As of today there are no measurements of open charm at FAIR energies.

At FAIR energies, charmed mesons are difficult to measure. They are very rare as they are produced close to the kinematical threshold. The strategy of reconstruction of these

particles in CBM is based on the reconstruction of their decay vertex. Due to the very low average proper decay length of open charm mesons ($c\tau$ is few 100 μm, see Table 3.1) the separation of the primary interaction vertex and the secondary decay vertex is a challenge. In order to demonstrate the feasibility of open charm measurements in CBM, detailed simulation studies accounting for the detector response are required. Among the open charm mesons, the D^0 particle is considered as the most difficult to measure, mainly due to its very short decay length ($c\tau = 123$ μm). It is therefore used as a benchmark in the simulations.

In the CBM experiment, D^0 mesons will be reconstructed in their hadronic decay channel $D^0 \rightarrow \pi^+ + K^-$. The identification of D^0 particles can be done via the reconstruction of the invariant mass of pairs of opposite charge particles. Due to the high track multiplicities, the uncorrelated pairs are expected to create a huge combinatorial background. Typically, in a central Au+Au collision at 25 $AGeV$ roughly 1000 charged particles are emitted. A major part of them are pions, while the multiplicity of D^0 mesons is only of the order of 10^{-5}. Knowing that a pion is one of the decay products of D^0, the need to reduce the combinatorial background by several orders of magnitude is imposed. For this purpose, several selection criteria can be applied. Among them, the topological cuts, such as the distance of the decay vertex from the primary collision vertex, are the most efficient. The expected number of D^0 particles to be measured, depends on the duration of the CBM run period and the collision rate.

6.2 CBM run period and collision rates

In order to evaluate the physics potential of the experiment, it is necessary to estimate the expected statistics for open charm particle measurements. The number of measured D^0 particles will depend on the detection efficiency, on the collision rate at which the MVD will be able to operate and on the duration of the measurements.

6.2.1 CBM run period

In Chapter 2, it was mentioned that at the FAIR accelerator up to four research programs could be run in parallel. FAIR beams are expected to be available about 4 months per year. This would be the typical CBM run period (CRP). To evaluate the expected statistics during this period, a 50% operating efficiency will be assumed in the simulations, which corresponds to an effective data taking time (termed hereafter as t_{RCP}) of approximately 2 months, i.e. 5×10^6 s.

It is important to note that due to radiation hardness limits of the MVD detector stations, in particular those located most upstream, the open charm measurements (requiring the MVD detector) might not be possible over this whole period. This will depend on the collision rate at which the MVD will operate, which itself depends on the time resolution of the MAPS sensors.

6.2.2 Evaluation of the expected radiation dose

The non-ionising radiation dose per Au+Au collision at 25 $AGeV$ incident energy, D_{coll}, expected in the first MVD station is estimated to be $D_{coll} = 30.2\ n_{eq}/cm^2$ [55] (see also Section 3.2.2). This holds for the most exposed part of the first station located 5 cm downstream the target. The corresponding ionising radiation dose is estimated to be 6.7 μRad per collision [55]. The ionising radiation is dominated by knock-on electrons coming from the target. Due to their presence, the most exposed part of the first station is not located at the same position as for the non-ionising dose. Due to this reason, the total dose cannot be obtained by summing up the two contributions mentioned above. Comparing the non-ionising dose with today's radiation tolerance of MAPS, which is close to $3 \times 10^{13}\ n_{eq}/cm^2$, one concludes that roughly 10^{12} Au+Au collisions can be measured before the detector is damaged. Concerning the ionising radiation dose, current MAPS sensors can tolerate up to 1 $MRad$ [55] and research on this field is ongoing. Therefore, in the present studies this limitation is not accounted for.

Due to the limited radiation tolerance of MAPS sensors, the working assumption currently in CBM is to replace the most exposed MAPS sensor(s) for each CBM run period. The possibility to replace the MVD during a run will not be considered here.

6.2.3 Collision rates

As discussed in Chapter 3, the goal of the ongoing R&D for the MAPS sensor foreseen for the first open charm measurements at SIS-300 is a readout time of 30 μs, and a radiation tolerance well above $3 \times 10^{13}\ n_{eq}/cm^2$.

Due to the high beam intensities required in CBM several collisions might be piled-up in the MVD detector. The number N_{pileup} of collisions piled up in the MVD is a function of the collision rate (R_C) and the MVD detector readout time (t_{res}):

$$N_{pileup} = R_C \times t_{res} \tag{6.1}$$

Note that the equation is considered for $N_{pileup} \geq 1$.

The radiation dose per CBM run period (corresponding to an effective data taking time t_{CRP}), denoted here as D_{year}, depends on the collision rate:

$$D_{year} = R_C \times t_{CRP} \times D_{coll} \tag{6.2}$$

Note that the number of collisions measured within one t_{CRP} is given by $R_c \times t_{CRP}$. For example, for a sensor with 30 μs readout time, the collision rate should be approximatively $3 \times 10^4\ collisions/s$ in the case of no pile-up in the MVD (i.e., $N_{pileup} = 1$) and 10 times higher ($3 \times 10^5\ collisions/s$) with 10 pile-up events in the MVD ($N_{pileup} = 10$).

Figure 6.1 shows a graphical representation of the dependence of the number of pile-up events on the collision rate and the readout time of the detector. The right hand scale shows the dose per t_{CRP}. The shaded area covers a range of the plausible radiation tolerance of MAPS ($10^{13}-10^{14}\ n_{eq}/cm^2$). The dashed vertical lines show the number of pile-up collisions corresponding to the marked D_{year}; for example, N_{pileup} amounts to 20 collisions at a dose of $10^{14}\ n_{eq}/cm^2$ for a sensor with $t_{res} = 30\ \mu s$.

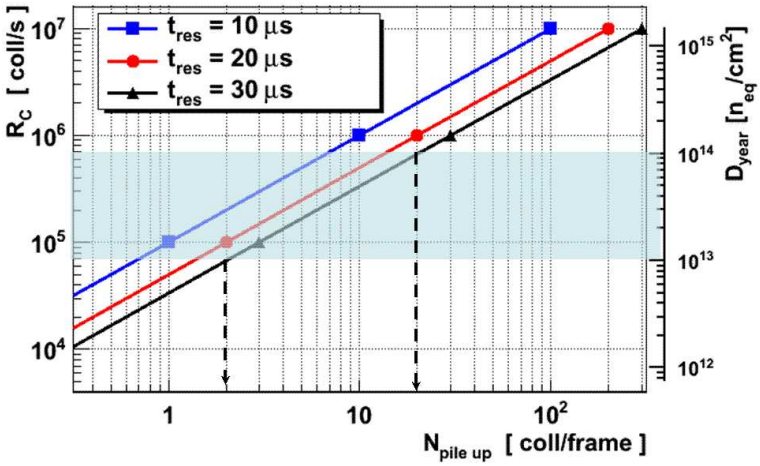

Figure 6.1: *The collision rate (R_C) and the corresponding number of pile-up collisions in the MVD, N_{pileup}, for different assumptions on the detector readout time (t_{res}). The scale on the right side shows the corresponding radiation dose per t_{CRP}.*

This figure illustrates the highest collision rates that may be reached within one t_{CRP}. The corresponding radiation dose is within the limits in radiation hardness of the MVD detector. Note that for such high interaction rates, a collision pile up is to be expected.

6.3 Simulation procedure and software tools

The simulation studies presented in this work were performed using the CbmRoot software, which is part of the FairRoot software [73]. The latter is a ROOT [68] based simulation and data analysis framework. The Virtual Monte-Carlo (VMC) interface of ROOT (TGeoManager) can be used to interface different particle transport Monte-Carlo engines like Geant3 and Geant4 with ROOT. This allows to use the same analysis code and geometry definition with the different engines. Figure 6.2 displays the structure of the FairRoot framework [73]. The latter consists mainly of three different branches CbmRoot, PandaRoot and R3BRoot (not shown in the figure) which share the same base classes. FairRoot delivers base classes which enable the users to construct their detectors and/or analysis tasks in a simple way. Moreover an interface for reading magnetic field maps is also implemented. The storage of all information collected by the different sensitive detectors is done on an event by event basis (an event means in this context one interaction between a beam ion and the target). All relevant objects are stored into binary ROOT files. An interface class (CbmMCPoint) is provided to define the structure of registered hits in a detector. All registered hits will be collected into dedicated lists, one list corresponding to one detector entity. The ROOT class TTree is used to organise the output data into a "ntuple like" data structure. For the related data analysis, the CbmRootManager provides methods to read this information.

The event reconstruction and analysis software is organised in so-called tasks. The CbmTask is an abstract class which can be used to create specialised algorithms inheriting

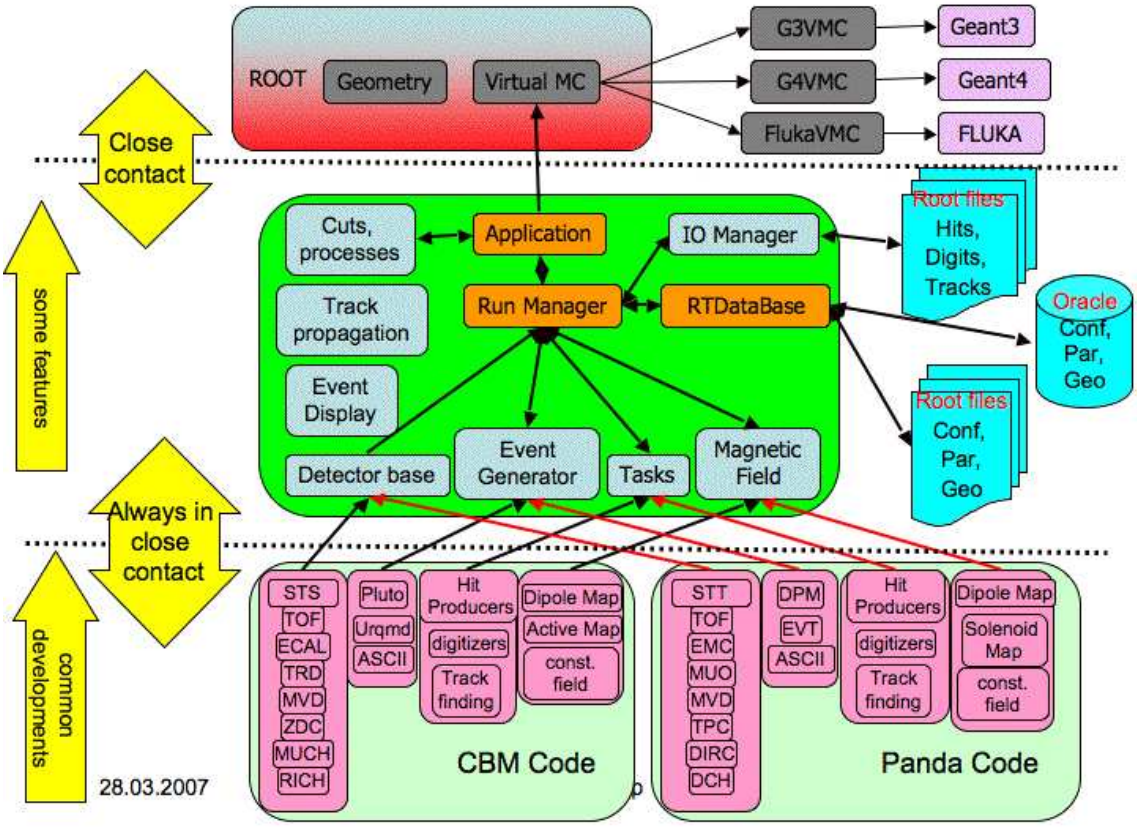

Figure 6.2: *Structure of the FairRoot simulation framework [73].*

from it. For each event, various tasks or reconstruction algorithms are created. Each task defines the relevant input data and parameters and creates its particular output data. The relevant input data and parameters are retrieved from the input file and the output data objects are stored in the output file. The successive steps of the simulation procedure are described in more detail in the following.

6.3.1 Simulation procedure

The successive steps of the simulation procedure are depicted in Figure 6.3. In this figure, the middle column (pink) lists the order (from top to bottom) and the type of the different tasks to be executed. The right column (light blue) describes the output files produced from one task, which serve as input files for the next task. The left part of the figure provides a brief explanation of each task.

As shown in the figure, the first step consists in the generation of the particles entering a detector. Those are composed from three dominant contributions which are: the nuclear collision particles (noted "UrQMD" in the figure), the π^+, K^- pairs coming from a D^0 decay (noted as "Thermal model" in the figure) and the δ-electrons generated inside the target by the passage of beam particles in the target (noted as "beam particles"). The term "event" corresponds to one UrQMD collision in which may be embedded the D^0 decay particles. The thermal model and the UrQMD generators create different output files (see the first blue box on top). The thermal model generates one file containing only signal particles. The UrQMD model is used to create two independent files: one containing only central collisions (0 fm impact parameter) and one containing minimum bias collisions (any impact parameter). By doing so, it is easier to overlap collisions in order to simulate collision pile up. The signal pairs are embedded only in the central collisions (one pair per collision). The "beam particles" generator is generating ions (e.g. Au ions) which are then are directly injected in the GEANT simulation. The interaction of the beam particles with the target generate the δ-electrons. Note that the δ-electrons are also saved in a separate file, not shown in the figure.

The generated particles are then processed by the GEANT3 simulation package [152] to add the detector effects. GEANT3 allows simulating the behaviour of particles as they interact with the different detector elements and physical structures of the experiment. The output data type (MCPoints) provides the position, the type and the momentum of the particles impinging each detector.

The next step is to simulate the response of each sub-detector including its subsequent electronics (for example, the number of firing pads, the detector inefficiencies, electronic noise, etc.). The detector response models use as input the data stored in the MCPoint object and provide the number of fired pads (pixels or strips), their pulse height and their position on the detector. The output data type is called Digi and includes the above mentioned information. Afterwards, specific algorithms for the reconstruction of the particle impact position (hits) are used. Once the hits are reconstructed, then the track reconstruction takes place; this consists of the track finding and the track fitting procedures. The former associates the hits to a track and the latter performs a fit of the tracks in order to extract the track parameters, e.g. the particle momentum. Finally, the tracks are used for

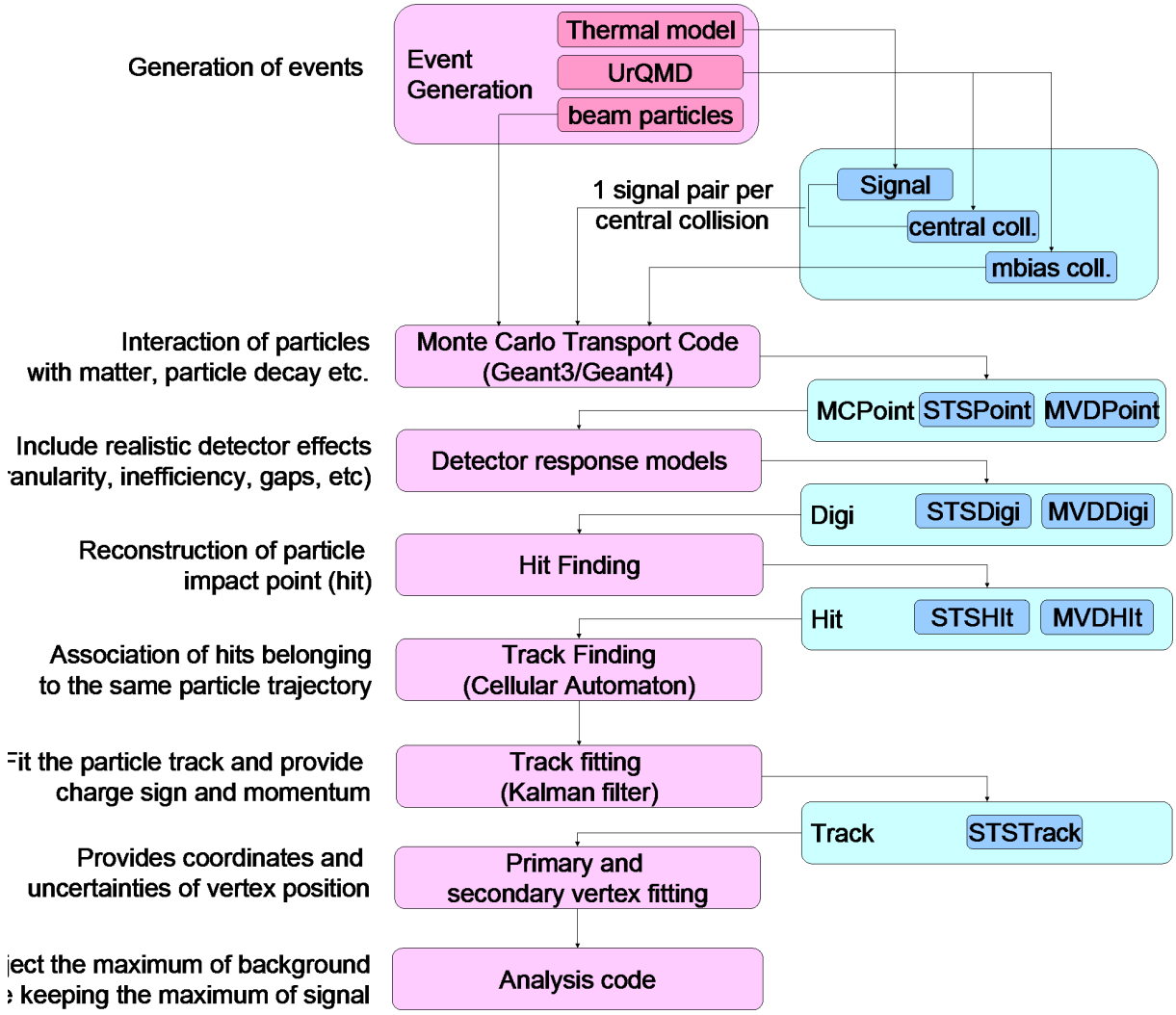

Figure 6.3: *Simulation procedure: The middle column represents the consecutive tasks that should be executed from top to bottom in the simulation chain. The right column describes the output files produced from one task which serve as input files for the next task. In the left column, the tasks are explained (see text).*

the primary and secondary vertex reconstruction and then the physics analysis may take place.

In the following, the details regarding the above mentioned procedure are described.

6.3.2 Event generators

Given the extremely low (3.75×10^{-5}) production multiplicity of D^0 at FAIR energies, a very large number ($\sim 7 \times 10^5$) of nuclear collisions should be simulated in order to produce one $D^0 \rightarrow \pi^+, K^-$. To this, one has to add the effect of the reconstruction efficiency which is typically of the order of few percent, and therefore few 10^9 collisions need to be simulated in order to reconstruct one D^0. Since the computation time needed for such a simulation is unrealistic, the approach to embed one $D^0 \rightarrow \pi^+ + K^-$ in each central Au+Au collision was

adopted. Therefore, the signal had to be generated separately than the background. Later on in the analysis, proper normalisation factors are applied to recover the correct numbers of signal particles. The simulations presented in this chapter were performed for central Au+Au collisions at an incident energy of 25 $AGeV$, which constitute a good benchmark case to assess the expected performance of CBM for open charm particle measurements [54].

The Ultra-Relativistic Quantum Molecular Dynamics (UrQMD) transport model [75] is used to generate central Au+Au events at 25 $AGeV$. For each event, the model provides the number (multiplicity) of produced particles, the identity and the momentum of each of those particles. A brief description of this model is given in Chapter 1.

The signal, e.g. D^0 particles, was generated using a thermal model [76] with a temperature parameter T = 300 MeV (Equation 6.3) and assuming a Gaussian rapidity distribution with a standard deviation of $\sigma_Y = 1.0$ (Equation 6.4). The choice of the latter value is somewhat arbitrary. Note however that UrQMD gives for pions the same width in rapidity. The centre of mass rapidity is $Y_{cm} = 2$ for collisions at 25 $AGeV$. The transverse momentum and the rapidity ($Y = 0.5\frac{E - p_L}{E + p_L}$) of D^0 follow the distributions $F(p_t)$ and $F(Y)$ respectively:

$$F(p_t) = p_t \times e^{-\sqrt{({p_t}^2 + m^2_{D^0})}/T} \tag{6.3}$$

$$F(Y) = \frac{1}{2\pi\sigma^2_Y} \times e^{-\frac{(Y-Y_{cm})^2}{2\sigma^2_Y}} \tag{6.4}$$

The decay of D^0 into a (π^+, K^-) pair is done in its rest frame, according to the rules of kinematics (energy and momentum conservation). Then the Lorentz transformation of the π^+, K^- momenta from the center-of-mass to the laboratory frame is performed. The coordinates (x_0, y_0, z_0) of the decay vertex of D^0 are calculated taking into account the probability $P(r_0)$ that D^0 with momentum $\vec{p}$ and mass M_{D^0}, travels a distance r_0 or greater before it decays. This probability is given by:

$$P(r_0) = e^{-M_{D_0} r_0 \Gamma/|\vec{p}|} \tag{6.5}$$

where $\Gamma = 1/c\tau$ is the inverse of the average decay length. Solving the above equation, the distance r_0 traveled by D^0 is:

$$r_0 = -\frac{|\vec{p}| \times c\tau \times \ln P(r_0)}{M_{D^0}} \tag{6.6}$$

The probability $P(r_0)$ is given by a random number generator which generates numbers between 0 and 1.

Finally, the coordinates of the decay vertex are: (x_0, y_0, z_0)=$(r_0\frac{p_x}{p},\ r_0\frac{p_y}{p},\ r_0\frac{p_z}{p})$, where (p_x, p_y, p_z) are the (x,y,z) components of the particle momentum.

Since the UrQMD model does not include the production of D^0 mesons, the estimation of the Hadron String Dynamics model (HSD) [39, 40], was used for the D^0 production multiplicity. In the HSD model, the multiplicity of D^0 particles in central Au(25 $AGeV$)+Au collisions is predicted to be 3.7×10^{-5} [54].

At this level, one event is defined by one central Au+Au collision in which one signal pair (π^+,K^- from D^0 decay) is embedded.

The distributions of pions and kaons originating from the D^0 decay are illustrated in Figure 6.4. The top panel shows the momentum distribution. It is interesting to notice that a substantial amount of the particles have a momentum above 1 GeV/c. The middle panel shows the transverse momentum distribution of pions and kaons, and the lower panel shows the transverse momentum of D^0 particles as a function of their rapidity.

As discussed in Chapter 3, the contribution of the so-called δ or *knock-on* electrons[1] dominates the hit density in the MVD. Therefore, in order to perform realistic simulations, one needs include them in the studies. The δ-electron production was simulated as following: Au ions with an energy of 25 $AGeV$ were generated by means of a dedicated ion generator. They were then propagated by GEANT through the target. The interaction between Au ions and the target produces the δ-electrons. The obtained kinetic energy distribution of the secondary electrons is within 30% agreement with the theoretical predictions [159].

6.3.3 Simulation of detector response

As shown in Figure 6.3, the next step is the simulation of the detector response. Different models are used for each detector type.

The MVD detector response model developed within this work is described in detail in Chapter 5. Here it is reminded that the response model of the MVD allows to simulate clusters of pixels firing after the passage of a charged particle. It also allows to take into account important effects such as the contribution of δ-electrons from the target and the pile-up of several collisions in the MVD.

The implementation of the STS detector response is described in [163]. This model includes all the physical processes related to the passage of a charged particle, from the charge generation to the digital output signals. The simulation includes charge sharing between strips, charge collection inefficiency, Lorentz drift due to the presence of a magnetic field, channel dead time and electronic noise.

6.3.4 Cluster and hit reconstruction

The information stored in the "Digi" object is used in order to reconstruct the clusters of firing pads in the different detectors.

For the MVD detector, the particle impact point is reconstructed by calculating the center of gravity of charge on the pixels belonging to a cluster (see Section 5). The output data type is called "Hit" (see Figure 6.3) and provides the coordinates of the reconstructed impact as well as the corresponding uncertainties. The hits are used in order to reconstruct particle trajectories.

For the STS detector, the algorithm used is described in [163]. Provided that a strip has a signal of at least 4000 electrons, it is used to construct a cluster. Several adjacent strips are grouped together in a cluster. The particle impact position is given by the center of gravity algorithm (cog):

$$X_{cog} = \frac{\sum_{cluster} S_i x_i}{\sum_{cluster} S_i} \tag{6.7}$$

[1] It is reminded that the δ-electrons are produced when a beam ion crossing the target is knocking orbiting electrons out of atoms.

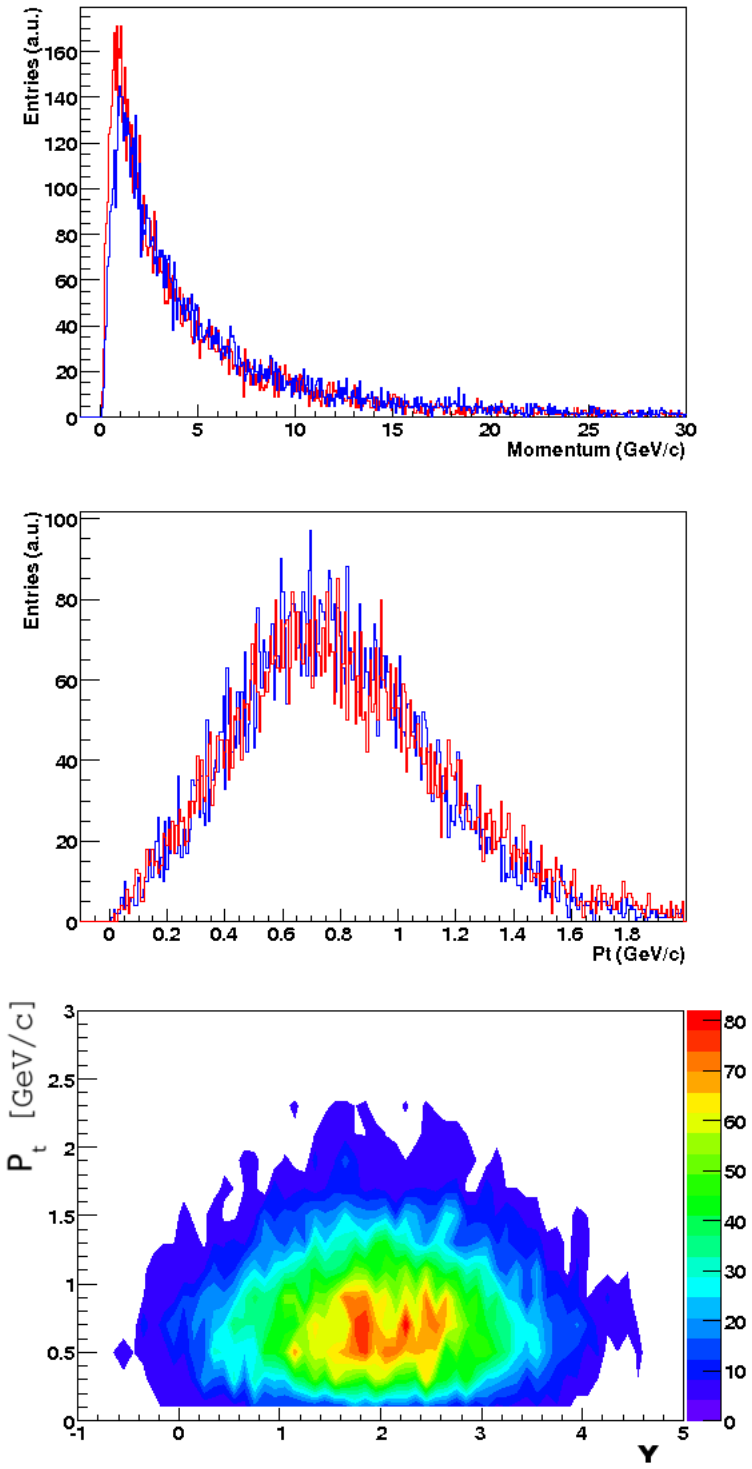

Figure 6.4:
Upper panel: The momentum distribution of pions (red) and kaons (blue) from a D^0 decay. Note that a major part of the momentum is above 1 GeV/c. Middle panel: The transverse momentum of pions (red) and kaons (blue) from a D^0 decay. Lower panel: The transverse momentum distribution of D^0 as a function of rapidity in the laboratory frame. The centre of mass rapidity at 25 AGeV is 2.

where x_i is the position of the i^{th} strip included in the cluster and S_i is the signal on this strip; the sum is over all the strips included in a cluster. Next, the association of two clusters lying on opposite sides of the double-sided sensor is performed.

6.3.5 Track reconstruction

The track reconstruction in CBM is performed with the Cellular Automaton algorithm [77]. The latter builds segments of tracks, called *triplets*, by connecting hits in three consecutive detector planes. Triplets are combined until a complete track is reconstructed. The algorithm provides the option to use the MVD in the track reconstruction. In this case, the MVD detector planes are used in the same way as the STS planes. Priority is given to long tracks with momentum $p > 1\ GeV/c$ which point to the target. Next, tracks with lower momenta are addressed.

When all possible hits have been assigned to tracks, the tracks are fitted with the Kalman filter method [78] in order to define the track parameters (curvature, momentum). The advantage of the Kalman filter method with respect to other methods, e.g., least squares, is that it allows to include noise and other inaccuracies in the calculation. In the case of track reconstruction, Kalman filter allows to include the effect of multiple scattering in the particle trajectory.

The performance of track reconstruction as function of the momentum is shown in Figure 6.5. Two cases are shown: the performance using the STS only (black rectangles) and the performance using both the STS and MVD (red circles). The efficiency here is defined as the ratio of the number of reconstructed particle trajectories to the number of Monte-Carlo tracks having 4 consecutive Monte-Carlo hits in the detector planes [160]. This criterion is used as the track reconstruction algorithm needs at least three hits in order to define the curvature of a track and therefore the momentum of a particle. A track is considered as successfully reconstructed if 70% of all associated reconstructed hits belong to the same particle [160]. The track reconstruction efficiency is roughly 95% for tracks with momentum above 1 GeV/c for both detector setups. However, a substantial drop is observed for particles with lower momenta, since these particles are suffering from multiple scattering, which makes their reconstruction difficult. The performance for the low momentum particles is substantially improved when the MVD is used. This can by explained by taking into account two facts: first, the low momentum particles ($P < 1\ GeV/c$) are strongly bended inside the magnetic field and have an increased probability to leave the CBM acceptance. Second, given that the MVD stations are located closer to the target, the probability that they accept a hit from a low momentum particle is increased. For these reasons, the track reconstruction efficiency for low momentum particles is improved when the MVD is used. As will be discussed later, in the case of D^0 reconstruction, the particles with $P < 1\ GeV/c$ are excluded from the analysis. Therefore, the presence of δ-electrons or collision pile-up, which affects only the MVD stations, has no impact in the track reconstruction efficiency of the high momentum particles.

Another figure of merit used to characterise the performances of the STS and the track reconstruction software is the momentum resolution, defined as the ratio $\Delta p/p_{MC}$ expressed in percent. Δp is defined as the difference between the reconstructed particle momentum and the real one (p_{MC}), provided by GEANT. Figure 6.6 shows the momentum resolution

as a function of the particle momentum for three different STS setups: a) 8 silicon strip stations, b) 6 silicon strip stations and c) 2 hybrid pixel stations and 4 silicon strip stations. Configuration a) is used in this work. In all cases, the momentum resolution is between 1.2% and 1.6% which is a satisfactory performance.

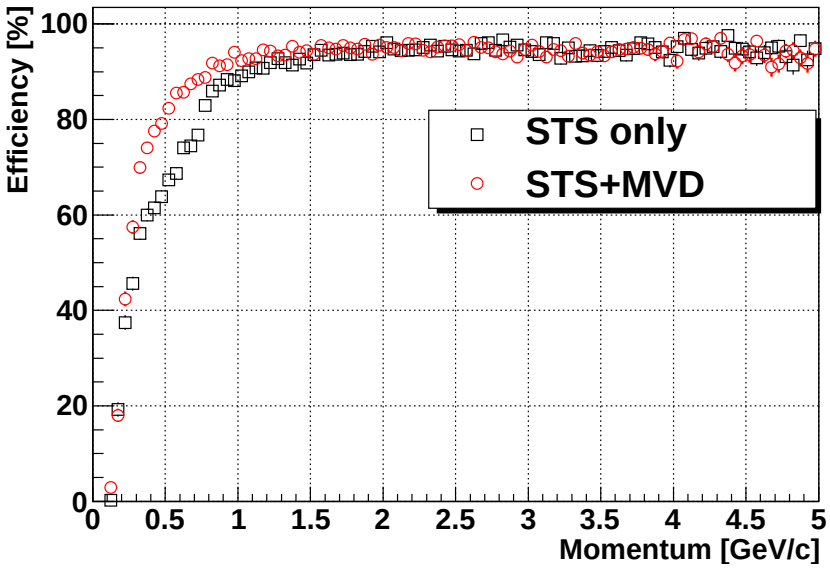

Figure 6.5: *Tracking efficiency of all charged particles from 100 Au+Au collisions at 25 AGeV (see text).*

6.3.6 Primary vertex reconstruction

The precise reconstruction of both the primary and secondary vertices is of crucial importance for D-meson measurements. As the identification of these particles is based on the separation of their decay vertex from the primary collision point, the determination of both vertices has to be performed with excellent precision. Especially for the D^0 meson which has a $c\tau = 123\ \mu m$, an excellent vertex reconstruction is mandatory.

The reconstruction of the primary vertex is based on the Kalman filter. The primary vertex position is determined by using the track estimates obtained after the track fitter. Each track is initially extrapolated to the center of the target (along the Z-direction) and is considered as an independent measurement of the vertex position. All tracks intersecting the target are used in order to estimate the position of the primary vertex.

Figure 6.7 illustrates typical results of the primary vertex resolution. The distributions are fitted with a Gaussian function. The standard deviation (σ) as derived by the fit shows that the resolution is below 1 μm for the (X,Y) dimension and below 5 μm along the Z-direction (beam direction), which is excellent. The resolution in Z is less good than in X and Y due to the fact that the tracks are extrapolated towards the target (along the Z-direction) and therefore the uncertainties along this dimension are somewhat larger. Overall, the

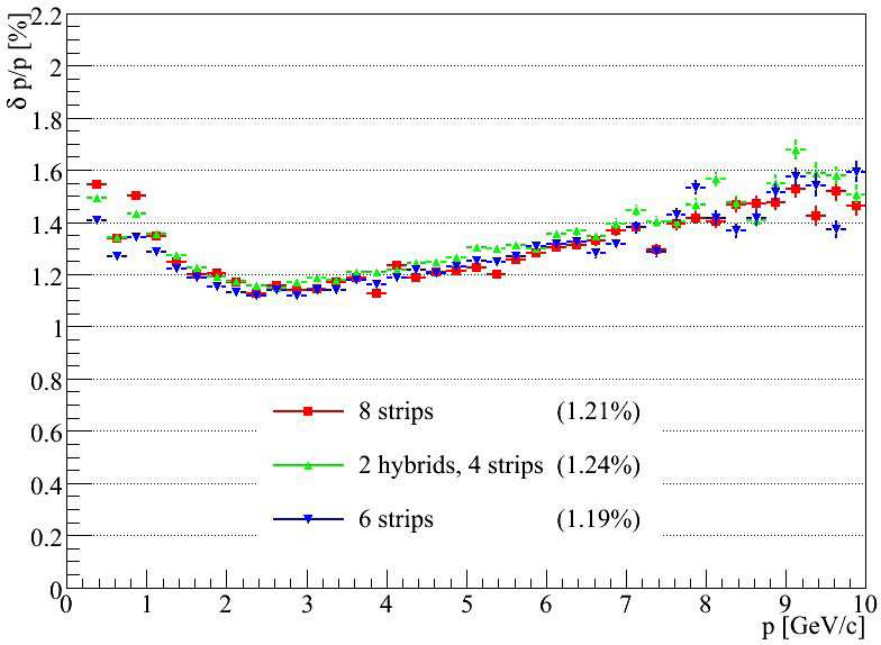

Figure 6.6: *The performance of the STS is shown, in terms of momentum resolution, as a function of the momentum [42]. Three detector configurations have been considered: a) 8 strips, b) 6 strips and c) 2 hybrid pixels and 4 strips. Configuration a) is used in the present work.*

excellent primary vertex resolution is mainly due to the MVD: its high granularity which allows to handle high track densities, offers the possibility to locate the stations at a small distance from the target (5 *cm*). This, combined with the low material budget of the stations allows minimising the track extrapolation errors.

6.3.7 Secondary vertex reconstruction

The secondary vertex is reconstructed in a similar way as the primary vertex. In the case of D^0 decaying into two particles, the secondary vertex is composed of only two tracks. The position of the vertex is the point of closest approach of the two tracks. This is calculated as following: first, the equations describing the two tracks are first determined (this is provided by the track reconstruction algorithm). Then one assumes a point situated on one trajectory and calculates its distance to the second trajectory. By minimising this distance, the position of the vertex can be determined[2].

The vertex is located on the line connecting the points of closest approach of the two tracks. The coordinates of the vertex given by the Kalman filter with the use of an additional constraint that the vector of the combined momentum of the two tracks is required to point to the primary vertex.

The secondary vertex resolutions along the X,Y,Z directions are shown in Figure 6.8,

[2]A detailed example of the track fitting in the case of two straight tracks can be found in [62]

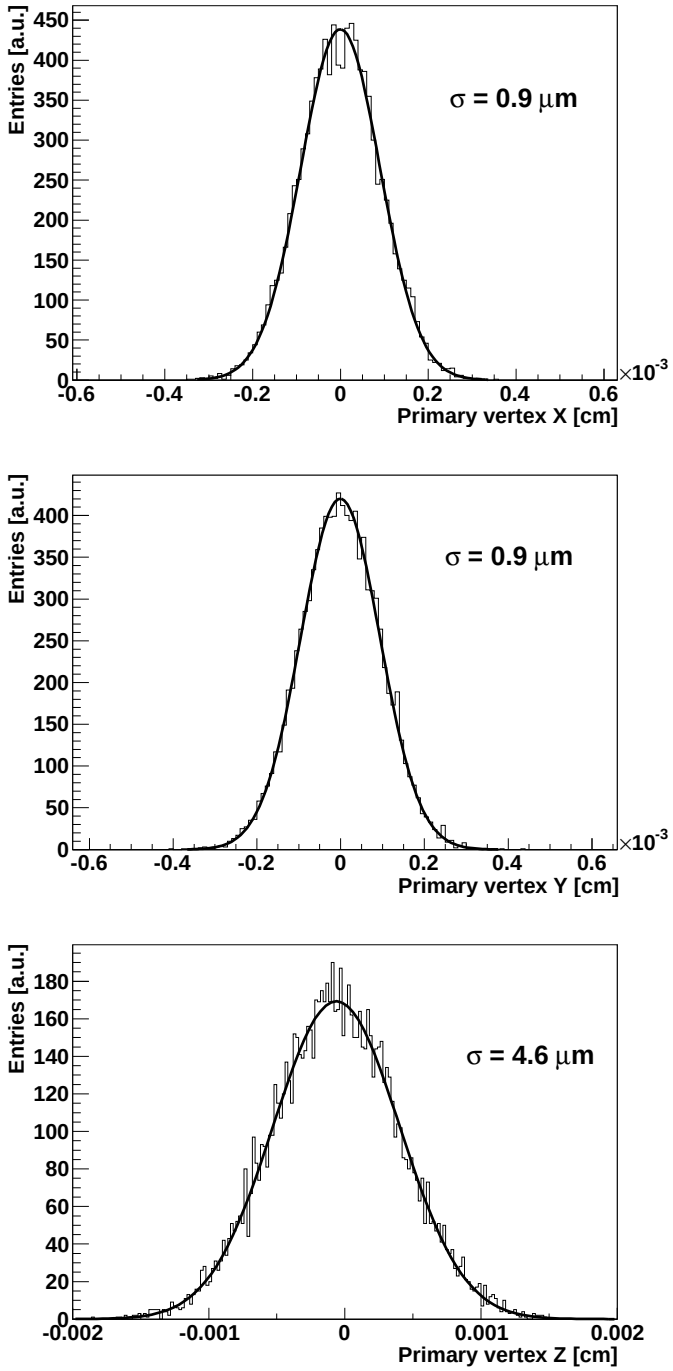

Figure 6.7: *Difference between Monte Carlo and reconstructed position of the primary vertex for central Au(25 AGeV)+Au collisions. The results are shown for the X (top), Y (middle) and Z (bottom) directions. The distributions are fitted with a Gaussian function.*

from top to bottom, respectively. The distributions are reasonably well fitted with a Gauss function. This fit allows to obtain an estimation of the width of the distribution and therefore of the spatial resolution. The "tails" of the distributions are mainly due to: a) low momentum tracks which are affected by multiple scattering and b) by uncertainties in the track reconstruction, mainly occurring when hits are not found in any of the STS or MVD stations. Similar to the primary vertex reconstruction, the Z-direction resolution ($\sigma_Z = 61\ \mu m$) is worse than in X ($\sigma_X = 10\ \mu m$) and Y ($\sigma_Y = 10\ \mu m$), since the extrapolation of the tracks is done along this direction.

6.4 Detector setup in the simulations

The detector setup is composed by the MVD and the STS stations (see Section 2.3). These detectors are located inside the dipole magnet. The structures included are described below.

The target is a golden plate with a radius of 0.25 mm and a thickness of 250 μm corresponding to an interaction probability of 1% with a 25 $AGeV$ Au ion beam.

The MVD is located in vacuum inside the beam pipe, which is a carbon tube of 0.5 mm thick and has a special modification around the MVD detector in order to allow for it to be located in the vacuum.

The MVD geometry consists of 2 stations situated at 5 cm and 10 cm downstream the target. In the simulation, the detector planes are represented by Si disks of 300 μm and 500 μm thickness respectively. They are oriented vertical to the beam axis and have an inner hole for allowing the passage of the beam particles. The inner hole corresponds to 2.5° polar angle and the outer radius corresponds to 25° polar angle which is the acceptance of CBM for the MVD. Details of the geometry such as gaps between sensors as well as the support structure are not implemented.

The STS detector is represented by 8 silicon disks located at 30, 35, 40, 50, 60, 75, 95, 100 cm from the target. The thickness of each station is 400 μm. The strip structure is represented in the simulation and for a more realistic representation, the z-position of the strips is randomly displaced for a few μm with respect to the center of the volume.

The magnet is represented by a mechanical iron structure located in the region around the target (see also Section 2.3.3). The magnitude of the magnetic field is about 1 T around the target region. Note that the field is not constant. This magnitude allows at the same time to have a good separation of positive and negative particles and a large acceptance.

For an on-line reconstruction of D^0 only the STS and the MVD detectors will be used. With these detectors only the momentum and the sign of charge of particles can be measured but the mass identification is not possible. Without having any information on the identity of the particles, an assumption is made about their mass: all the positive particles are assumed to be pions and all the negative particles are assumed to be kaons.

The use of particle identification is discussed in details later.

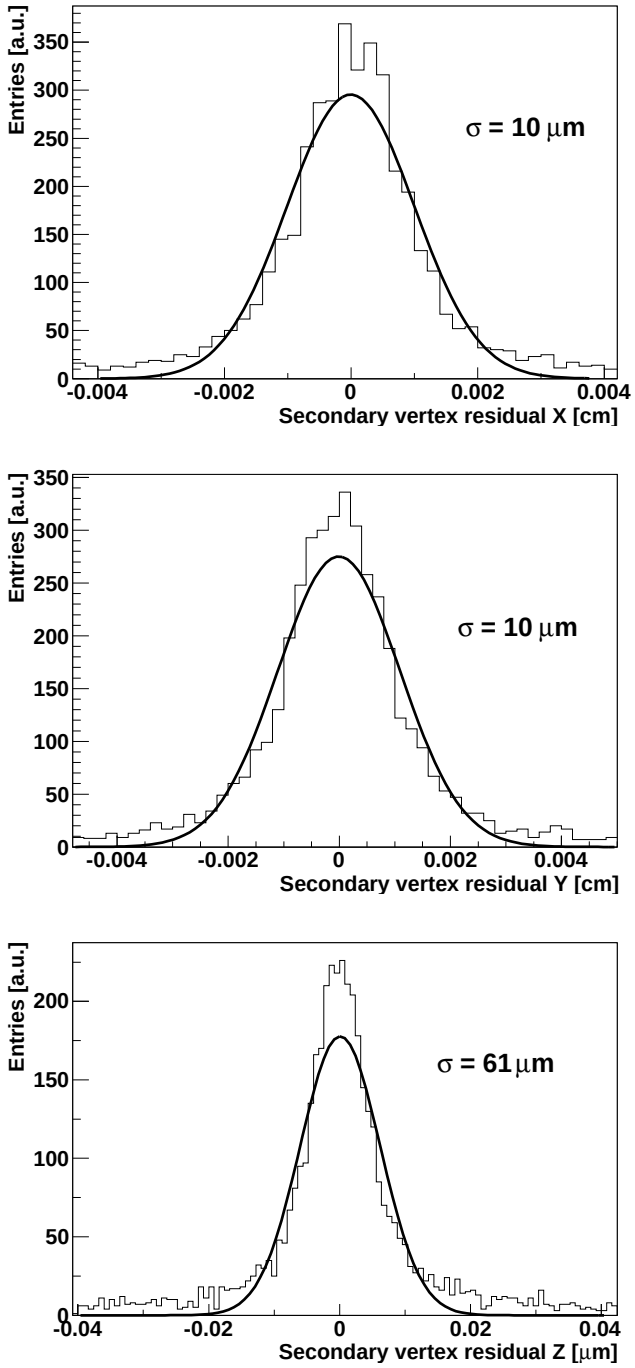

Figure 6.8: *Difference between Monte Carlo and reconstructed position of the decay vertex of $D^0 \rightarrow \pi^+, K^-$ in central Au(25 AGeV)+Au collisions. The results are shown for the X (top), Y (middle) and Z (bottom) directions. The fit shown is performed with a Gauss function. Note the different range in the Z direction.*

6.4.1 Detector simulation

The details of the geometry of the MVD are described in Chapter 3. Here we make a short reminder and complement it with details on the readout setting assumed. The MVD is assumed to be composed of MIMOSA-26 sensors which have a pixel pitch of 18.4 μm. The thickness of a complete detector, including support and heat evacuation structures is 300 μm and 500 μm of Si for the first and second station respectively. The electronic noise was simulated by a Gaussian distribution centered at 0 and a standard deviation of 15 electrons. For the studies presented below, the readout is assumed to be performed with a discriminator (1-bit ADC). This choice is motivated by the advantages that the digital readout presents: it allows for a fast readout and minimises the sensor's power consumption.

The discriminator threshold is set to 75 electrons (1 ADC unit) for cluster reconstruction. The threshold corresponds to 5 times the value of the average electronic noise simulated, which is 15 electrons,. This setting is motivated by the need to have good compromise between good cluster reconstruction efficiency and low fake hit rate.

6.4.2 Particle identification

The open charm feasibility studies presented here, are mainly based on the performances of the MVD and STS detectors. This choice was motivated by two facts: unlike the other detectors, the MVD and STS are mandatory for open charm detection in CBM. On the other hand, priority was given to study the impact of the MVD on the open charm reconstruction. Therefore, the particle identification detectors (RICH, TRD and TOF) were not included in the present simulations and the impact of particle identification could not be studied in a realistic way. However, in order to obtain an idea of the importance of particle identification, the latter was modeled in a simple way as described below.

First, it is reminded that, since the MVD and STS do not provide any particle identification, all positively charged particles are assumed to be pions and all negatively charged particles are assumed to be kaons. This is because the decay of D^0 is to a positive pion and a negative kaon. The additional information on particle identification will help excluding other particles. For example, a particle identified as electron (e.g. by the RICH detector) is rejected. During the analysis, the reconstructed tracks are matched to the corresponding Monte-Carlo track. From this, information is available about the particle type. The momentum range within which, each detector (RICH, TRD and TOF) may identify particles is known from other simulation studies [54]. Combining the above information, one may model the particle identification capabilities of CBM.

Table 6.1 indicates the momentum range where charged particles can be identified. The excellent identification capabilities of the TOF detector allow us to assume that all protons are identified. Moreover, the combined use of the RICH and TRD detectors offers very good electron and positron identification. In principle, the identification of kaons is also possible by the TOF detector. However, given their average decay length ($c\tau = 3.7\ m$) a substantial part of kaons decays before reaching the TOF, which is located 10 m downstream the target. Therefore, the contribution of kaon identification could not be taken into account. Detailed simulations are needed in order to estimate this effect which is expected to further improve the physics performance.

	RICH	TRD	TOF
protons			all
$\pi^{\pm}$			up to $\sim 3.5\ GeV/c$
$e^{\pm}$	up to $6\ GeV/c$	from $1\ GeV/c$	from $1\ GeV/c$

Table 6.1: *Particle identification capabilities of different sub-detector systems of CBM as used in the present studies. These numbers are based on detailed simulation studies [54].*

6.5 Reconstruction of open charm particles

The aim of this simulation is to investigate quantitatively the performance of the MVD for D^0-meson reconstruction using a realistic detector setup. Due to the very short lifetime of D^0 mesons, the reconstruction of this particle is chosen to be used as a benchmark for the feasibility studies of open charm particle measurements. The study is focused on the hadronic decay channel of $D^0 \rightarrow \pi^+,\ K^-$ mainly because it has the smallest branching ratio (3.8%). The simulations were performed for central Au+Au collisions at an incident energy of 25 $AGeV$. This system is among the heaviest that CBM can measure, and this energy is close to the production threshold of D^0. Only central collisions are studied in order to address the case with highest track multiplicites. Therefore, this collision system was chosen for the feasibility studies.

6.5.1 The simulation strategy

There are two main challenges in performing realistic open charm particle reconstruction in the environment of the CBM experiment. First, one needs to generate an enormous amount of events in order to obtain reliable results. Typically, 7×10^5 events need to be simulated in order to produce one D^0 particle decaying into a (K^-, π^+) pair. Another very important issue is to achieve an efficient rejection of the combinatorial background, at least by several orders of magnitude in the D^0 invariant mass region. Both points will be addressed in the following sections.

D^0 particles decay before they reach the first MVD detector station (located at a distance of 5 cm to the target) due to their short lifetime. This means that D^0 can only be measured via its decay products. The latter have to be charged particles, in order to be detected by the MVD and the STS.

This condition is fulfilled by two decay channels, which are $D^0 \rightarrow K^-\pi^+$ and $D^0 \rightarrow K^-\pi^+\pi^+\pi^-$. Within this work, the D^0 decaying into a (K^-, π^+) pair was addressed. This choice was, on one hand, motivated by a non-negligible gain in terms of combinatorics and computing time: the search for a four particle vertex is by a factor of 100 more time consuming than a two-particle vertex. On the other hand, this decay channel shows a smaller branching ratio which suggests that in case this channel can be reconstructed, reasonably good results can be found also when analysing the decay to K^-, π^+, π^+, π^-. The latter assumption has been supported by independent studies [80] which suggest that CBM is in principle able to perform the reconstruction of $D^0 \rightarrow K^-\pi^+\pi^+\pi^-$.

The reconstruction of open charm is based on the reconstruction of its invariant mass spectrum. At this step, only information from the MVD and the STS detectors is used. Information for particle identification will be used later. This means that one has to assume that positive particles are pions and negative ones are kaons. By combining all pairs of opposite charge sign particles, it is possible to calculate the invariant mass of the potential mother particle. Be $(E_1, \vec{p}_1)$ and $(E_2, \vec{p}_2)$ the four-momenta of the decay products, with E_i being the energy of the i^{th} particle and $\vec{p_i}$ its momentum, then the invariant mass of the mother particle is:

$$m_{inv} = \sqrt{(E_1 + E_2)^2 - (\vec{p_1} + \vec{p_2})^2} \tag{6.8}$$

The energy is calculated from the energy-mass equation:

$$E^2_{1,(2)} = m^2_{1,(2)} + |\vec{p^2_{1,(2)}}| \tag{6.9}$$

Using the above equations one can reconstruct the invariant mass of pion and kaon pairs. This includes D^0 and its combinatorial background.

6.5.2 The Super-Event technique

Taking a D^0 production multiplicity of 3.75×10^{-5} in central Au($25\ AGeV$)+Au collisions [54] and knowing that the branching ratio of $D^0 \rightarrow K^+, \pi^-$ channel is 3.8 %, one finds that 7×10^5 collisions are required to produce one D^0 decaying into pion and kaon. In order to obtain reasonable statistics for the open charm study, an extremely large number of collisions should be simulated (several hundreds of millions). For reasons of limited CPU calculation time it is not reasonabe to simulate such a high number of events. In order to overcome this problem, the Super-Event technique was used in the present work. This technique is inspired by the event-mixing technique used to estimate the combinatorial background for experimental data.

In order to identify D^0 particles on the basis of their invariant mass distribution, each positively charged track is combined with each negatively charged one. In the conventional analysis, this operation is performed using the tracks from the same collision. In the Super-Event technique, one combines the tracks belonging to different collisions. Assume that from a single central Au+Au collision, p is the number of positively charged particles and n is the number of negatively charged particles. Then, the number of combinations of two opposite charged particles is equal to p×n. If the tracks from N central collisions are combined using the Super-Event technique, then the number of pairs found would be $(N \times p) \times (N \times n) = N^2 \times p \times n$ This corresponds to N^2 *equivalent* events. With this approach, it is possible to raise the statistics by a factor of N and overcome the CPU time limitation. In order to check the validity of this technique, an artificial event was built from the tracks of $N = 33$ events generated with the UrQMD model and was compared to the background generated from $N^2 = 33^2 = 1089$ individual UrQMD events. Figure 6.9 shows the combinatorial background obtained using ordinary events (black histogram) and the Super-Event technique (red histogram). As can be seen in this figure, the two distributions are in excellent agreement, validating therefore the use of the Super-Event method.

In the Super-Event technique, only the background from uncorrelated pairs is represented. However, the decay of other particles, such as hyperons and $\overline{D}^0$ might also lead to

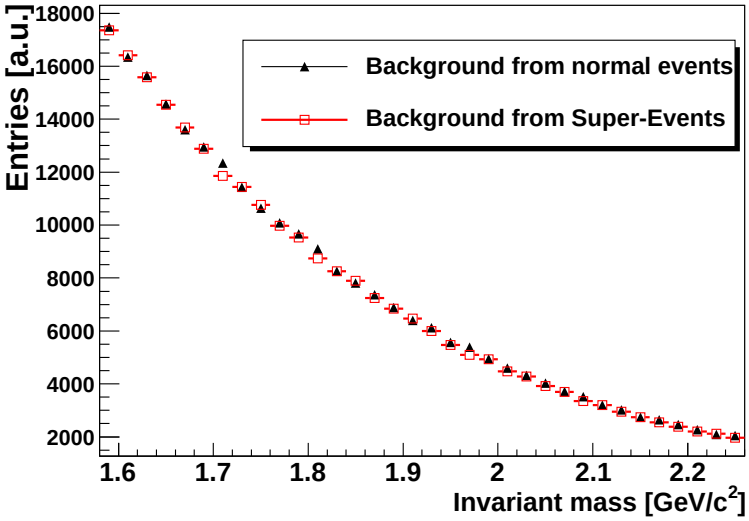

Figure 6.9: *Combinatorial background generated with ordinary events (black triangles) and with the super-event technique (red circles). The magnitude and shape of the combinatorial background obtained with the Super-Event technique are similar to those obtained with ordinary events.*

significant contributions in the invariant mass region around the D^0 mass peak. As will be discussed in the next section, these contributions can be substantially reduced by applying appropriate selection cuts in the reconstruction procedure.

6.5.3 The background rejection strategy

The strategy for identifying the open charm signal mainly relies on the separation of the displaced decay vertex of open charm from the primary vertex of the collision. The combinatorial background consists of all uncorrelated pairs of opposite charge particles. Knowing that for each central Au+Au collision at 25 *AGeV* several hundreds charged particles are entering the detector acceptance, and assuming that half of the particles combined are negative and half of them are positive, then roughly 10^5 candidate pairs are created per collision. In order to extract the signal under these conditions one needs to apply several selection criteria that reject a substantial fraction of the combinatorial background without affecting significantly the signal. An important criterion relies on the fact that the invariant mass of the candidate pairs must be close to the mass of D^0 particles. The remaining background can be then further reduced by applying selection criteria on any variable that can be different for the signal and the background. The selection criteria are distinguished into two categories that are described in detail below: the single track cuts and the cuts on the track pairs.

Single track cuts

The first step in the selection procedure consists in imposing conditions on individual tracks. The goal here, is to select only tracks that are likely to originate from decay particles of D^0. This first step is very important for reducing the combinatorial background as it reduces the number of candidate tracks that form pairs: both the computing time and the number of pairs are reduced significantly. The following cuts are introduced:

- *Primary vertex sigma cut (PV-sigma):*

  Since the pions and kaons coming from the decay of D^0 are secondary particles their trajectory should not intersect with the primary collision vertex. This cut corresponds to the minimum impact parameter cut. The latter is the distance between the primary vertex and the impact point of the extrapolated track to the target plane. This distance is divided by the extrapolation uncertainty of the track and is thus given in units of this uncertainty, noted as σ_{PV}. It is therefore called PV-sigma.

- *Impact parameter cut (IP-cut):*

  A second selection criterion also based on the impact parameter cut is used. This is a maximum value of the impact parameter below which the tracks are accepted. This is based on the fact that the D^0 particle has a limited lifetime and therefore the impact parameter of its decay products should not exceed a certain value (maximum impact parameter cut).

- *Momentum cut (p-cut):*

  The momentum of most of the tracks coming from D^0 particle decay is above 1 GeV/c (this is shown in Figure 6.4), so this criterion rejects all the particles with momentum less than 1 GeV/c.

- *Transverse momentum cut p_t-cut:*

  This cut is based on the fact that the mass of D^0 is significantly higher than the one of its daughter particles. Therefore, a significant amount of energy is released in the decay. Due to this effect, it is likely that the decay particles have a higher transverse momentum than many background particles. This is observed on their respective transverse momentum distributions.

After the application of these cuts, roughly 95% of all background tracks are rejected. The most efficient cut at this point is the PV-sigma cut, since a major part of the background tracks comes from the primary collision. For signal tracks, roughly 30% survives this step. The typical values used for these cuts are given in Table 6.2.

Cuts on track pairs:

At this level of selection, all tracks that have passed the previous selections are combined into pairs with opposite charge sign in order to form D^0 candidates.

- *Secondary vertex cut (SvZ-cut):*

  D^0 particles are produced in the primary collision and then they fly a short distance before they decay. This defines a minimum distance above which it is interesting to search for candidate vertices.

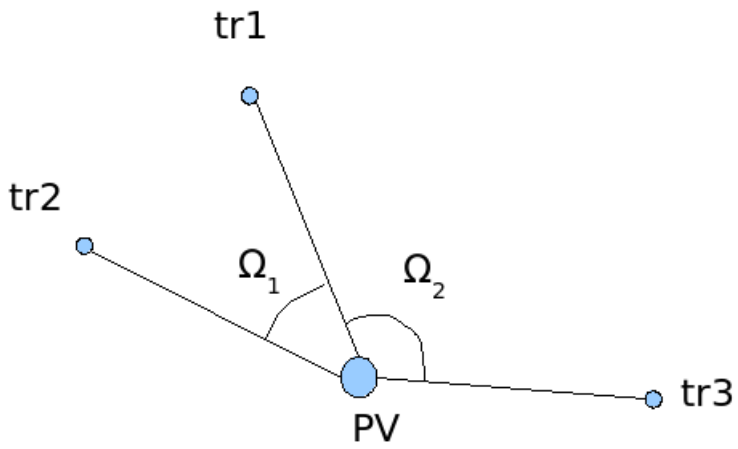

Figure 6.10: *Illustration of the IPAngle cut: On the target plane, the small opening angles (for example Ω_1) are rejected, while the larger ones (Ω_2) are accepted. The primary vertex is denoted as PV; tr1, tr2 and tr3 are the extrapolated points of three arbitrary tracks to the target transverse plane.*

- *Secondary vertex χ^2 cut (SvChi-cut)*:
  The SvChi-cut corresponds to the distance of closest approach of two tracks divided by the quadratic sum of track uncertainties. It is given in units of sigma, noted for clarity σ_{χ^2}, where sigma is the square root of the quadratic sum of the track uncertainties. It is used as a kind of measure of the vertex quality.
- *D^0 impact parameter cut (IPD0-cut):*
  As mentioned above, the D^0 particles are produced in the primary collision and therefore, the extrapolation of their trajectory should point to the primary collision vertex. A minimum value of the impact parameter of the D^0 candidate is set, below which the candidates are accepted.
- *The IPAngle cut*:
  This is a cut on the opening angle of the extrapolated tracks on the target plane, illustrated in Figure 6.10. Small angles (like Ω_1 shown in Figure 6.10) are rejected. The opening angle should be larger than 140 degrees.
- *The opening angle of the daughter particles (cosA-cut and cos12-cut):*
  Ideally, the opening angle of the daughter particles in their center of mass frame, should be 180 degrees. In order to account for the track and momentum reconstruction tolerances, a minimum opening angle of 140 degrees is required. This is the $\cos A$ cut. In the laboratory frame, the opening angle between the tracks of the daughter particles is restricted to a minimum value in order to exclude vertices from tracks which are almost parallel. For such tracks it is very difficult to define a point of closest approach, that is a secondary vertex. Therefore for such tracks, the secondary vertex resolution is bad. This cut, called cos12-cut, eliminates such cases.
- *Armenteros-Podolanski cut ($\tilde{p}_t$-cut):* A hyperon decay can be misidentified as a D^0 decay and thus contribute to the physics background of D^0. The Armenteros-Podolanski cut is a geometrical cut which is used to exclude the vertices produced by hyperon

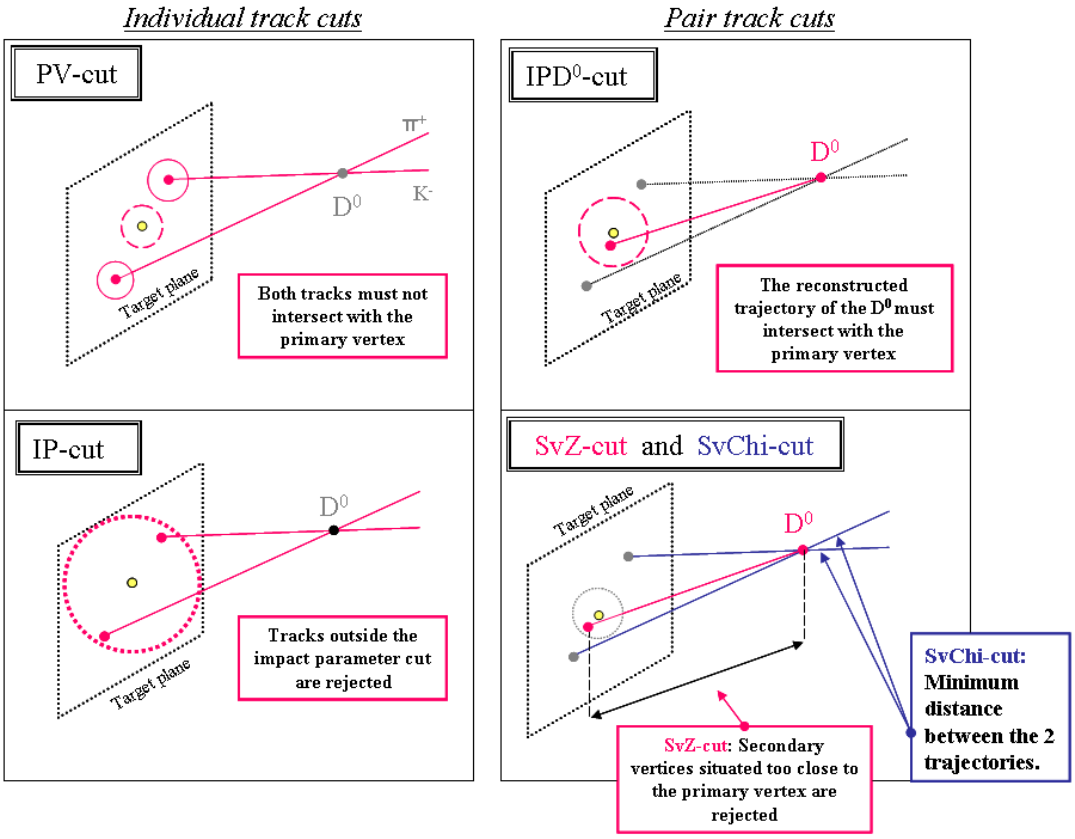

Figure 6.11: *Illustration of the most important cuts used in the D^0 reconstruction procedure. Left panel: The PV-sigma cut (PV-cut) and the IP-cut are illustrated. Right panel: The D^0 impact parameter cut (IPD^0), the secondary vertex Z cut (SvZ-cut) and the SvCi-cut are illustrated.*

Cut variable	Value	Background remaining (%)	Signal remaining (%)
PV-sigma cut	$PV > 4.5 \times \sigma_{PV}$	5	50
SvZ-cut	$SvZ > 360\ \mu m$	8	70
IPD0	$IPD0 < 7.2 \mu m$	95	99
IP-cut	$IP < 600\ \mu m$	90	95
SvChi-cut	$SvChi < 1.12 \times \sigma_{\chi^2}$	60	70
Pt-cut	$Pt > 300\ MeV$	70	99
P-cut	$P > 1\ GeV$	75	99

Table 6.2: *Isolated effect of most important cuts on signal and background distributions.*

decays (Λ, $\overline{\Lambda}$ and K^0_s). This cut allows eliminating a large fraction of the secondary vertices corresponding to the decay of Λ ($\overline{\Lambda}$). Let α be $\alpha = \frac{P_L^+ - P_L^-}{P_L^+ + P_L^-}$ and

$\tilde{p}_t = P^- \times \sqrt{1 - (\frac{P_L^-}{P^-})^2}$. $P^{-(+)}$ is the momentum of the negative (positive) particle, $P_L^{-(+)}$ is the longitudinal momentum of the negatively (positively) charged particle.

6.5.4 Cut optimisation procedure

There exist more than one method to optimise a set of selection cuts $(c_1, c_2, ...c_n)$. A very common and simple method is the sequential optimisation (also called "single cut" optimisation) of each individual cut. This method is described in detail in [76]. It consists in maximising the significance for each cut c_i:

$$Sign(\vec{c}) = \frac{S(c_i)}{\sqrt{S(c_i) + B(c_i)}} \tag{6.10}$$

$S(c_i)$ and $B(c_i)$ represent the number of signal and background pairs respectively, after applying the cut c_i. The value of the cut that maximises this function is the optimum one. An example of this approach is shown in Figure 6.12, where the cut to optimise is the position of the reconstructed secondary vertex along the beam axis, v_z . In the upper (middle) panel of the figure, the distribution of v_z is plotted for signal (background) pairs, and the lower panel shows the significance as a function of v_z. The arrows indicate the optimised value of the secondary vertex cut (SvZ-cut).

This optimisation method has however some drawbacks. First, this approach of optimising the cuts one after the other does not take into account the possible correlation between two cuts. This might lead to different results if the cuts are optimised in a different order. Moreover, the identification of a maximum might be difficult, in particular when the distributions of the significance for a given cut c_i have a relatively wide plateau at their maximum.

Figure 6.13 illustrates that this method does not necessarily find the optimal cuts in the two dimensional case. The red arrows show the results obtained if one optimises sequentially two cuts (Cut1 and Cut2). It can be seen that the results depend on the order in which the two cuts are optimised.

The method adopted in the present work consists in a multidimensional analysis in which the significance is calculated using simultaneously all cuts. The advantage of this method is that it takes into account the correlations between all the cuts, it is easy to use and less computer time consuming. There are two drawbacks: the first one is that this method needs a large computing memory. The second drawback is that the method might converge to a local maximum. The latter can be found within a given neighbourhood of the data set, whereas a global maximum is found in the entirety of the data set. In order to make sure that the algorithm is not converging in a local maximum, several iterations of optimisation are performed. In each iteration, a different data set is used as input for the algorithm. If the cut values provided are similar for several iterations, then the result is accepted. This approach is described more in detail in [55]. It consists in maximising the significance function which is expressed as a vectorial function of cuts:

$$Sign(\vec{c}) = \frac{S(c_1, c_2, ..., c_n)}{\sqrt{S(c_1, c_2, ..., c_n) + B(c_1, c_2, ..., c_n)}} \tag{6.11}$$

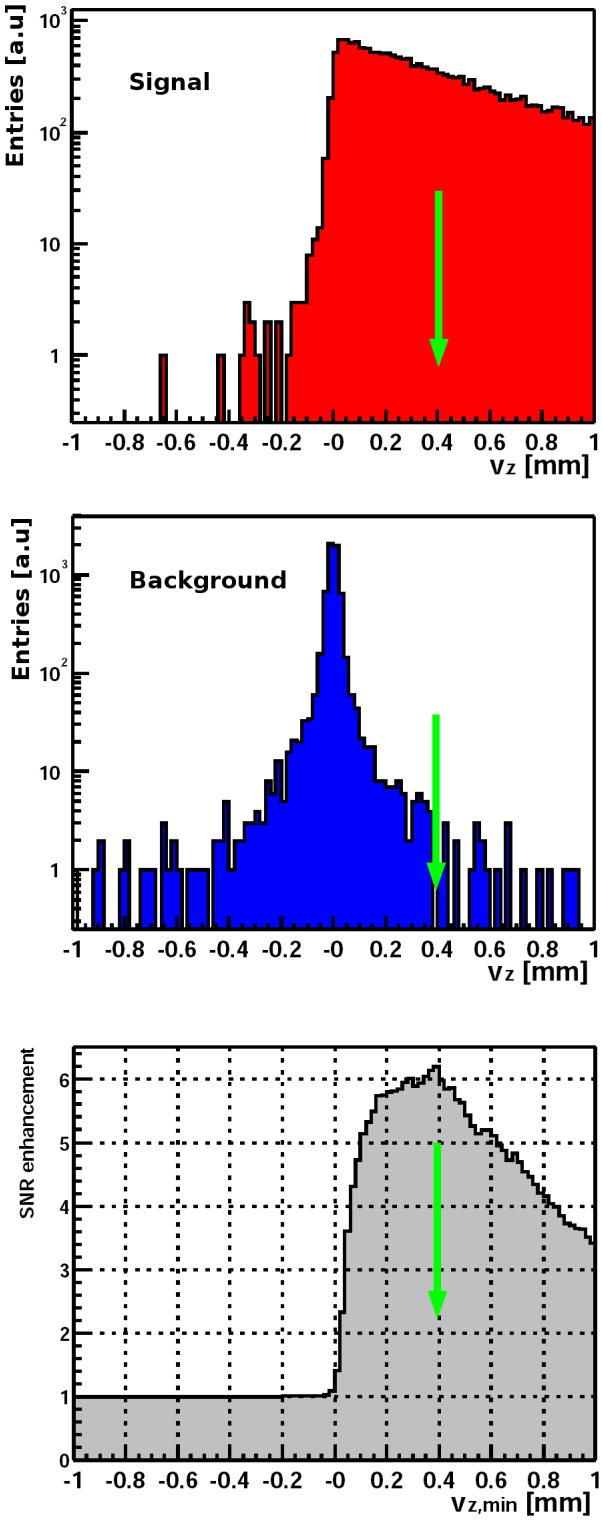

Figure 6.12: *The distribution of the distance of the secondary vertex to the target along the beam axis (v_z). Top panel: secondary vertex for signal pairs is on top. The middle panel illustrates the v_z distribution for background pairs and the lower panel shows the significance as a function of v_z. The arrow indicates the value of v_z for which the significance is maximised. The figure is taken from reference [76].*

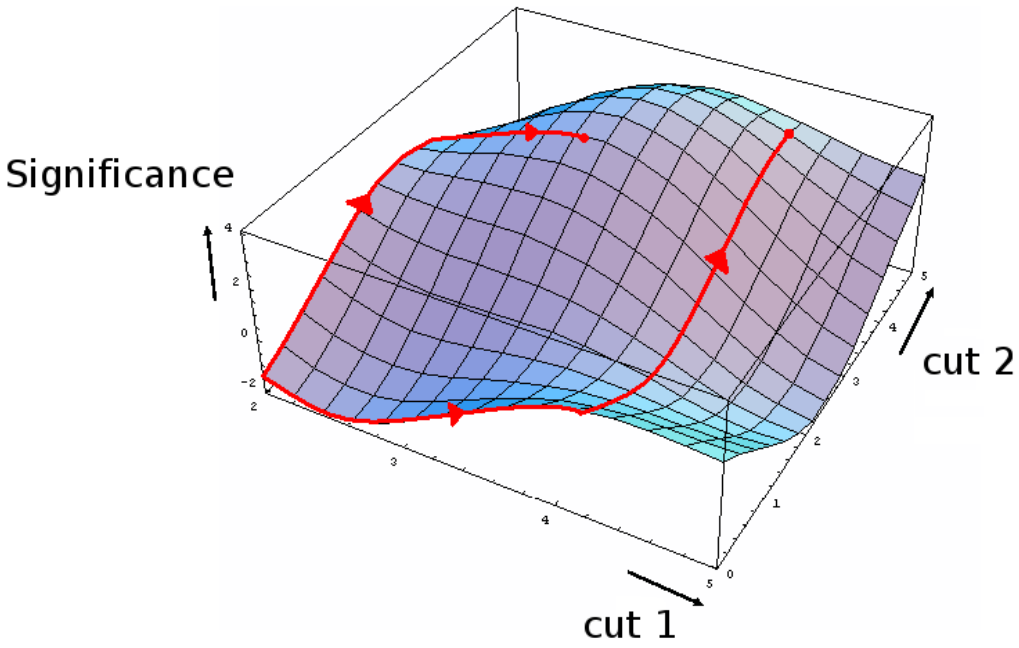

Figure 6.13: *Schematic representation of the problem arising from the use of the sequential cut optimisation method in the multidimensional case. The scale is linear. The procedure of optimising one cut after the other corresponds to choosing the paths marked in red within the two-dimensional function. One observes that the result depends on the order in which the cuts are optimised [55].*

Searching for an optimal set of cuts becomes then equivalent to a maximum search on the significance function. Mathematically, the extreme of a continuous function is found when its first derivative becomes zero. As the analytic form of the $Sign(\vec{c})$ function is unknown, a simplified iterative approach was used: it consists in varying one cut by small steps and comparing the corresponding value of $Sign(\vec{c})$. For example, assume that the cut c_i is being optimised and the step size is a small positive number h. The value of the significance is calculated for three cut values: c_i, $c_i + h$ and $c_i - h$. Among them, the cut value is chosen for which the significance is higher. Once this procedure has been followed for all cuts, the next iteration starts, in which the step h is reduced. The process continues for all cuts and stops when the step size is sufficiently small.

In order to minimise the algorithm's computer memory needs, it is important to reduce the size of the input files. For this purpose, a pre-selection step is required, which aims in reducing the amount of pairs and, consequently, the size of the file to be analysed. This step is applied in the same way to the background and signal histograms. The pre-selection is based on the PV-sigma cut (pairs with $PV - sigma < 4.5$ are rejected) and on applying an ideal proton identification. Moreover, a selection is applied on the invariant mass: only a region between 1.7 GeV/c^2 and 2.2 GeV/c^2 is used. This region is sufficiently large to include all signal pairs. The choice of these cuts represents a compromise between a sufficient background reduction and a minimum impact on the optimisation. Typically, after the cut optimisation with the multi-dimensional method, pairs with $PVsigma < 6$ are rejected.

The same value is usually obtained with the sequential cut optimisation method. The excellent particle identification capabilities of the TOF detector allow making the realistic assumption that all protons may be identified and rejected. It is therefore concluded that the pre-selection step does not introduce a bias in the optimisation.

The invariant mass distributions of opposite charge particle pairs obtained by applying this set of pre-cuts are shown in Figure 6.14. The left panel corresponds to the uncorrelated pairs (background). The right panel corresponds to the correlated pairs (signal).

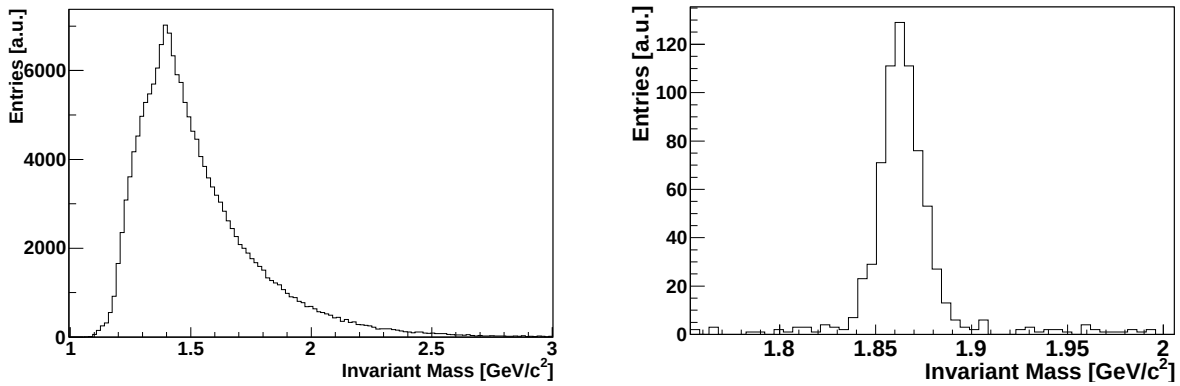

Figure 6.14: *Invariant mass distributions for the uncorrelated opposite charge particle pairs (left) and for the correlated opposite charge particle pairs (right). Only pre-selection cuts have been applied.*

6.5.5 Cut values

Table 6.3 lists the values of all cuts used in the analysis. The so-called "manual" cuts (i.e. the ones added independently of the cut optimisation algorithm) are denoted with a $^{(*)}$.

Figure 6.15 shows the invariant mass distributions of opposite charge particle pairs obtained after applying all selection cuts. The left panel corresponds to the uncorrelated pairs (background) and the right panel corresponds to the correlated pairs (signal). The distributions have been fitted with an exponential function and a Gauss function respectively. The distributions of Figure 6.15 will be used in the following section to evaluate the expected performance for D-meson measurements in CBM.

6.6 Results

As an output of the cut optimisation procedure one obtains two histograms which are shown in Figure 6.15. Those histograms contain the invariant mass of the remaining signal candidates (right panel) and background (left panel).

The signal and background are extracted from the histograms by fitting them, integrating the fit functions over the invariant mass region of interest and normalising those integrals according to the anticipated statistics of a CBM run.

Cut	[units]	Pre-selection	Optimisation	Manual+Optimisation
PV-sigma (or PV)	$[\sigma_{PV}]$	$> 4.5^{(*)}$	> 6.6	> 6.6
SvZ-cut	$[\mu m]$	-	> 550	> 550 and $< 2 \times 10^{3(*)}$
IPD0	$[\mu m]$	-	< 20	< 20
SvChiT-cut	$[\sigma_{\chi^2}]$	-	< 2.6	< 2.6
Pt-cut	[MeV/c]	-	> 315	> 315
P-cut	[GeV/c]	-	> 1	> 1
Proton rejection		yes		yes
IPAngle-cut		-	< -0.80	< -0.80
IP-cut	$[\mu m]$	-	-	$< 700^{(*)}$
$\cos A$-cut		–	-	$< 0.8^{(*)}$
$\cos 12 - cut$			< 1	< 1
$\tilde{p}_t$**-cut**		–	-	$> 0.22^{(*)}$
IM-cut	$[GeV/c^2]$			$> 1.7^{(*)}$ and $< 2.2^{(*)}$

Table 6.3: *List of cuts used for open charm reconstruction. The column with the "Pre-selection" shows the value of the cuts fixed before applying the cut optimisation algorithm. The column "Optimisation" lists the values provided at the output of the algorithm and the last column shows the combined cuts used as final in the analysis. The numbers marked with* $^{(*)}$ *denote the cut values added manually.*

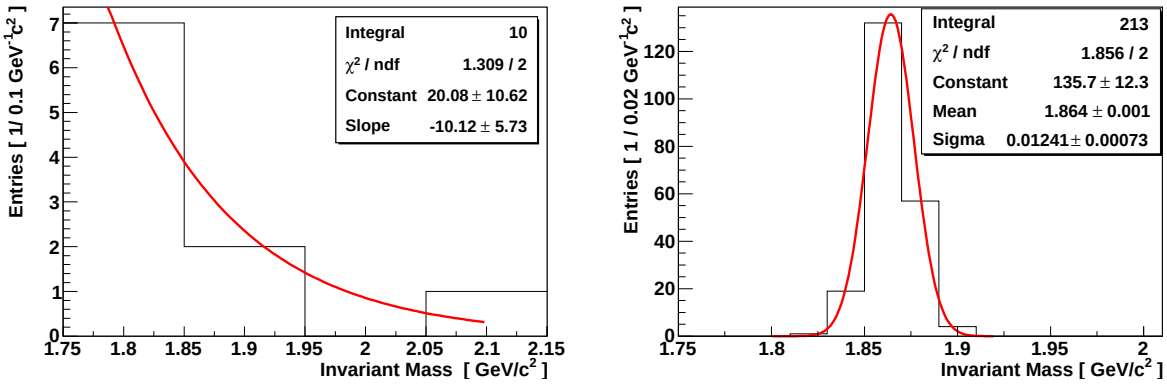

Figure 6.15: *Invariant mass distributions for the uncorrelated opposite charge particle pairs (left) and for the correlated opposite charge particle pairs (right) after applying all cuts. For the background* 9.5×10^7 *events were used and for the signal* 10^4 *(π^+, K^-) pairs.*

The approach of fitting signal and background was chosen to cure the fact that after applying the optimised cuts, the invariant mass region of interest does not contain any background pairs. This is considered as an artifact of the "low" statistics used in the simulation. The fit of the background aims to obtain a more realistic background estimate.

6.6.1 Invariant mass resolution

The first step in the procedure is to define the invariant mass region of interest based on the invariant mass resolution of the experiment. To do so, we performed a Gauss fit on the signal peak (right panel of Figure 6.15). We chose to fit this distribution within a range: $m \pm 2 \times RMS$, where m is the arithmetic mean and RMS is the root mean square of the distribution. The fitting procedure provides the mean value of the Gauss function, μ, which corresponds to the measured invariant mass of the D^0 meson. The standard deviation, σ, obtained from the fit function, corresponds to the invariant mass resolution of the experiment.

The mass of D^0 meson used as input in the simulations was $m_{D^0} = 1864.8\ GeV/c^2$, taken from reference [2]. Following this method, the mass of the D^0 particle was found to be $\mu \pm \sigma = (1864.2 \pm 12.4)\ MeV/c^2$, which is consistent with the input value within the errors bars. The width of the distribution originates from detector effects rather than from the width of the resonance mass of D^0, which is very small (and not taken into account in the present simulations).

The very satisfactory invariant mass resolution of only $\sim 12\ MeV/c$ can be considered as a success of the tracking algorithm and the very accurate silicon tracking system, which provides a momentum resolution of 1.2%. It is particularly helpfull as the D^0 mesons can be found in a narrow invariant mass window. This leads to a better extraction of the signal and therefore of a good signal-to-background ratio.

6.6.2 Estimate of the detection efficiency

The detection efficiency for D^0 is obtained by comparing the number of signal pairs found in the mass region of interest after applying all cuts with the number of pairs initially put into the simulation, N_{input}^{signal}.

While N_{input}^{signal} is known, one obtains the number of remaining pairs by integrating the Gauss fit function (described in Section 6.6.1) within the invariant mass region of interest. The latter is selected as $[\mu - 2\sigma, \mu + 2\sigma]$ (μ and σ is the mean and standard deviation respectively of the Gauss fit function). This choice is motivated by the fact that roughly 95.5% of all the signal entries are included in this region of the Gauss function. One obtains the integral I_S representing the number of remaining pairs in the simulation. The detection efficiency ϵ is derived according to:

$$\epsilon = \frac{I_S}{N_{input}^{signal}} \tag{6.12}$$

It is found to be $\sim 2\%$.

6.6.3 Expected signal for a CBM running period

In order to estimate the signal for a CBM running period, one has to normalise I_S according to the relation between N_{input}^{signal} and the number of $D^0 \rightarrow \pi^+, K^-$ decays expected for this running period ($N_{generated}^{D^0}$). $N_{generated}^{D^0}$ is derived according to:

$$N_{generated}^{D^0} = N_{coll}^{centr} \times M \times R_{Br} \tag{6.13}$$

where M is the D^0 particle production multiplicity, and R_{Br} is the branching ratio of $D^0 \rightarrow \pi^+$, K^- and N_{coll}^{centr} is the anticipated number of central collisions recorded during the running period. Knowing $N_{generated}^{D^0}$ and the detection efficiency ϵ, one can derive the expected particle yield from a run (S) according to:

$$S = N_{generated}^{D^0} \times \epsilon \tag{6.14}$$

Combining Equations 6.12 and 6.13 into Equation 6.14, we find:

$$S = N_{coll}^{centr} \times M \times R_{Br} \times \frac{I_S}{N_{input}^{signal}} \tag{6.15}$$

Assuming the production multiplicity predicted by HSD for central Au+Au collisions ($M = 3.74 \times 10^{-5}$) then 4.4×10^2 D^0 are expected to be measured within one typical CBM run period. If SHM multiplicity is used, ($M = 2.05 \times 10^{-4}$) then 2.4×10^3 D^0 particles are expected. It is reminded that these results were produced under the assumption that there is no collision pile up in the MVD (1.5×10^{10} *collisions* during one typical CBM running year).

6.6.4 Extraction of the background

While the statistical uncertainties of the signal estimate are reasonably low, the small number of background pairs imposes important uncertainties on the background estimate. A naive approach to estimate those uncertainties would be to propagate the uncertainties of the fit parameters. This method can however not be applied as it requires the uncertainties of the background to be small with respect to the related estimates. This is not fulfilled in our case.

In order to overcome this obstacle, we estimated the uncertainty of the background by means of a Monte-Carlo approach. To do so, we fitted the background of the simulation (see left part of Figure 6.15) with a suited fit function which will be referred to as F_0^{Bg} hereafter. We used this fit function and its parameters as an input for a random generator, which was used to generate a set of new histograms, h_i^{Bg}. The number of entries n_i^{Bg} of the i-th histogram was obtained from a Poissonian smearing of the number of entries in the original histogram.

The "invariant mass" of those "background pairs" was generated by a random generator based on the initial fit function F_0^{Bg}. This approach was to represent the random fluctuations of the number and the invariant mass of the remaining background pairs.

For each histogram obtained, a fit was performed. The fit function obtained was integrated in the mass region of interest and the integral I_i^{Bg} was scaled to the anticipated statistics of the CBM running period.

The related scaling factor is derived by the ratio of the number of central collisions expected in the experiment, N_{coll}^{centr}, to the number of collisions used in the simulation, N_{bg}^{input}. One obtains:

$$B_i = I_i^{Bg} \times \frac{N_{coll}^{centr}}{N_{bg}^{input}} \tag{6.16}$$

By filling all normalised background estimates B_i into one single histogram one may build the distribution of background estimates. This can be conceptually used to obtain an estimate on the background and the uncertainties of this background.

6.6.5 Extraction of S/B and significance

The precise values of the background are of limited interest for this work. In order to estimate the quantities of interest which are the S/B ratio and the significance of the open charm peak, the above mentioned concept has been extended to those quantities. To do so, for each background estimate B_i the signal estimator was generated. This was done by generating an estimator I_i^S by means of a Poissonian smearing of the original signal integral I_S (see Section 6.6.2). Hereafter, I_i^S was normalised according to Equation 6.15 to the statistics of the CBM running period. One obtains an estimator for the signal S_i.

An estimator for the S/B ratio is derived by dividing S_i to B_i and filled hereafter into a histogram. By doing this for all samples i, one obtains a distribution for the S/B ratio as shown in Figure 6.16. The S/B ratio of the reconstructed D^0 signal was defined as the median of this distribution (shown in Figure 6.16). The uncertainties were defined as one standard deviation from the median. This means that the central 68% of all entries are

within the error bars. As the distribution is not symmetric, one obtains different upper and lower limits. This is illustrated in Figure 6.16 where the standard deviation for the upper limit (σ_1) is larger than the one for the lower limit (σ_2).

The same concept was applied for the significance, which was derived according to $S_i/\sqrt{S_i + B_i}$. Figure 6.17 shows the distribution of $S_i/\sqrt{S_i + B_i}$ values. In the figure the median and the error bars are shown.

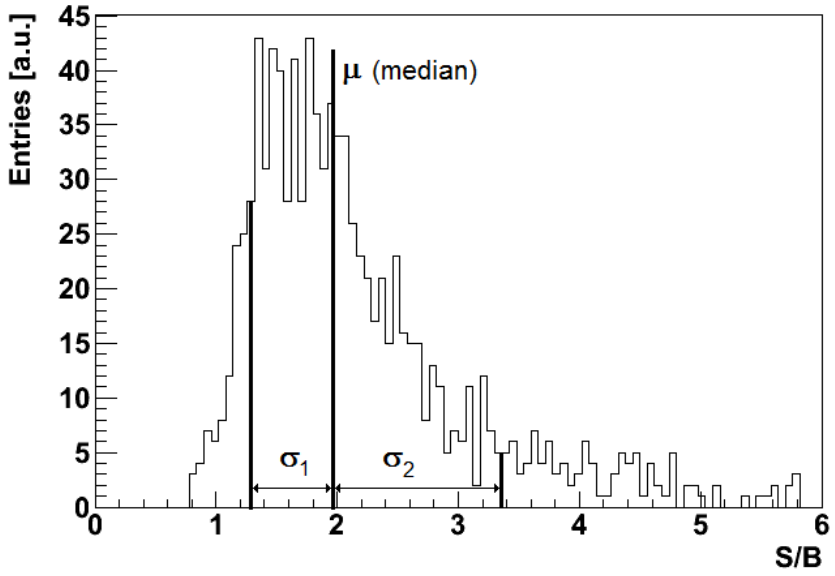

Figure 6.16: *The distribution of S_i/B_i. The median and the upper (σ_1) and lower limits (σ_2) are shown (see text).*

6.6.6 Expected invariant mass distribution for a typical CBM run period

An illustration of the invariant mass distribution corresponding to 1.5×10^{10} central Au+Au collisions is shown in Figure 6.18. This figure was obtained based on the fit functions for signal and background shown in Figure 6.15. The functions were normalised to the statistics (1.5×10^{10} central Au + Au events) corresponding to one CBM run year at 3×10^4 *collisions/s* and afterwards they were added. The fluctuations represent the expected statistical uncertainties in the bins after measuring 1.5×10^{10} central collisions. Note that the shape of the background shown in this figure underlies substantial uncertainties, and should therefore be considered as an illustration only.

Table 6.4 summarises the results for the expected performance of the D^0, $\overline{D}^0$ and combined $D^0 + \overline{D}^0$ measurements in central Au(25 $AGeV$) + Au collisions assuming a collision rate of 3×10^4 *collisions/s*. The simulation has been performed only for the D^0 meson. For the $\overline{D}^0$ particle, it was assumed that the detection efficiency is the same as for D^0. This is a reasonable assumption as the properties of D^0 and $\overline{D}^0$ in terms of invariant mass, average decay length, and branching ratio are identical. However, a complete feasibility study for

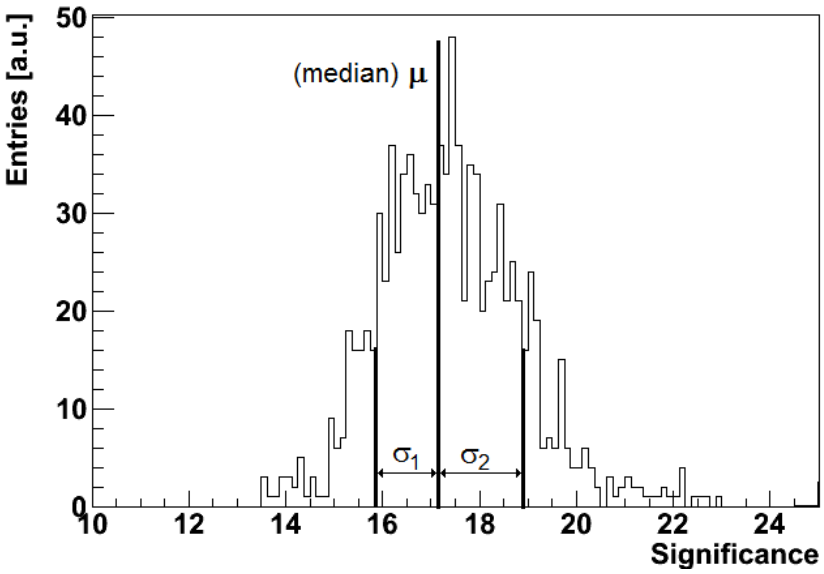

Figure 6.17: *The distribution of* $S_i/\sqrt{S_i + B_i}$. *The median and the upper* (σ_1) *and lower limits* (σ_2) *are shown (see text).*

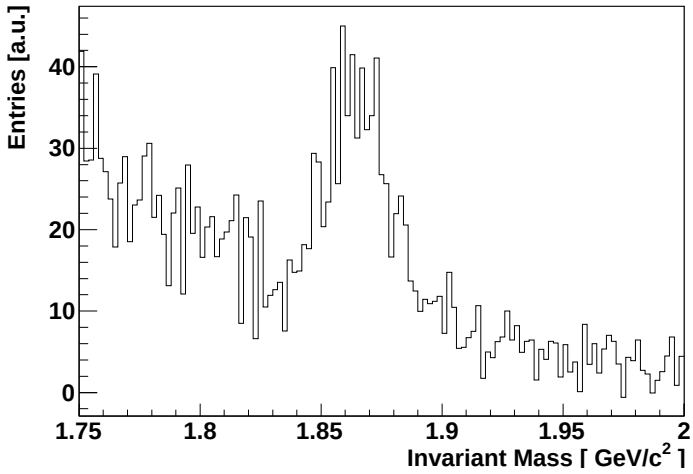

Figure 6.18: *Invariant mass distribution of opposite charge pairs as expected for* 1.5×10^{10} *central Au+Au collisions at* 25 *AGeV and after all cuts are applied (see text).*

$\overline{D}^0$ would be necessary as the combinatorial background might differ due to the different assumptions on the identity of charged particles: in the D^0 case, all unidentified positive particles are assumed to be pions while all unidentified negative particles are assumed to be kaons. In the $\overline{D}^0$ case, this assumption should be inverted. The different multiplicities for the positive and negative particles might be at the origin of a different combinatorial background. In this work, we simply assumed that the background for D^0 and $\overline{D}^0$ is the same. The numbers marked with a $^{(*)}$ in the table denote that the results are derived based on this assumption.

For the production multiplicity of D^0 and $\overline{D}^0$ mesons, the predictions of two different models HSD [54] and SHM [161] are used. In both models the production multiplicity of $\overline{D}^0$ is roughly 3 times higher than for D^0. In HSD, which is a purely hadronic model, the $\overline{D}^0(\bar{c}u)$ is more frequently produced at low energies, due to the associated production with Λ_c, Σ_c baryons. In SHM, which assumes the formation of a thermalised quark-gluon plasma, this difference in multiplicity is due to the fact that the net baryon density is high at FAIR energies. This means that the number of u quarks is higher than the number of $\overline{u}$ quarks, although the number of c quark is equal to the number of $\bar{c}$ quarks, as they are produced in pairs. Therefore, the production of $\overline{D}^0 = \bar{c}u$ is favoured over the production of $D^0 = c\overline{u}$.

		D^0	$\overline{D}^0$	$D^0 + \overline{D}^0$
Multiplicity	HSD	3.74×10^{-5}	1.12×10^{-4}	1.49×10^{-4}
	SHM	2.05×10^{-4}	6.15×10^{-4}	8.20×10^{-4}
mean proper decay length $c\tau$ $[\mu m]$		122.9	122.9	122.9
decay channel		$K^-\pi^+$	$K^+\pi^-$	$K^\mp\pi^\pm$
Branching ratio		3.89%	3.89%	
sec. vertex resol. $[\mu m]$		42 ± 0.1		
Reconstruction Efficiency		2%	$2\%^{(*)}$	
Mass resolution $[MeV/c^2]$		12.4 ± 0.7		
S/B	HSD	$1.95^{+1.41}_{-0.63}$	$5.85^{(*)}$	
	SHM	$10.8^{+7.95}_{-3.45}$	$32.4^{(*)}$	
Significance	HSD	$17.18^{+1.62}_{-1.38}$	$29.72^{(*)}$	
	SHM	$48^{+2.4}_{-2.2}$	$81.6^{(*)}$	
Expected number of particles	HSD	4.4×10^2	1.3×10^3 $^{(*)}$	1.7×10^3 $^{(*)}$
	SHM	2.4×10^3	7.2×10^3 $^{(*)}$	9.6×10^3 $^{(*)}$

Table 6.4: *Reconstruction efficiency, mass resolution, signal-to-background ratio, significance and number of expected particles for D^0 measurement in central Au+Au collisions at 25 AGeV beam energy. The normalisation is done for 1.5×10^{10} central Au(25 AGeV)+Au collisions, corresponding to a runtime of roughly 8 weeks (see text). Numbers marked with $^{(*)}$ are based on the results obtained from the study of D^0 particles (see text). The "sec. vertex resol." is the secondary vertex resolution along the beam direction.*

6.6.7 Expected statistics for other D-meson species

In order to obtain a complete information about the charm production in CBM, it is important to measure all open charm meson species (e.g. $D^{\pm}$). The feasibility of other open charm species was investigated in another work [80, 81] within the collaboration. In [81] it was found that the reconstruction efficiency for $D^+ \to \pi^+\pi^+K^-$ and $D^- \to \pi^-\pi^-K^+$ is a factor of 1.7 lower than for $D^0 \to \pi^+K^-$ particles. One might expect therefore a detection efficiency of 1.18% for D^+ and D^- mesons.

CBM will allow measuring D-mesons via different hadronic decay channels. For example, The decay of the D^0-meson into four hadrons ($D^0 \to \pi^+\pi^+\pi^-K^-$) can be reconstructed. It was found in [80] that the detection efficiency for this channel is about 9 times lower than for the $D^0 \to \pi^+K^-$ decay. Therefore, the detection efficiency $D^0 \to \pi^+\pi^+\pi^-K^-$ is expected to be about 0.22%. Note that for the decay of D^0 to four hadrons, the detection efficiency is substantially lower than for the two particle channel. This is mainly due to geometrical acceptance effects. The requirement that all four hadrons issued from a D^0 decay are within the acceptance, is more difficult to fullfil. Same considerations apply for the $D_s^+ \to K^+K^-\pi^+$ decay (studied in [81]), for which the detection efficiency is expected to be 0.45%.

Table 6.5 lists the total reconstruction efficiency, the multiplicity, branching ratio (BR) and expected statistics for the D-mesons discussed above. Note that only the study for $D^0 \to \pi^+K^-$ has been performed in this work.

Particle	Tot. eff.	BR	Multiplicity		Expected statistics	
			HSD	SHM	HSD	SHM
$D^0 \to \pi^+K^-$	2%	0.0389	3.74×10^{-5}	2.05×10^{-4}	4.4×10^2	2.4×10^3
$\overline{D}^0 \to \pi^-K^+$	2%	0.0389	1.12×10^{-4}	6.15×10^{-4}	1.3×10^3	7.2×10^3
$D^0 \to \pi^+\pi^+\pi^-K^-$	0.22%	0.077	3.74×10^{-5}	2.05×10^{-4}	10^2	5.2×10^2
$\overline{D}^0 \to \pi^-\pi^-\pi^+K^+$	0.22%	0.077	1.12×10^{-4}	6.15×10^{-4}	2.8×10^2	1.6×10^3
$D^+ \to \pi^+\pi^+K^-$	1.18%	0.095	4.17×10^{-5}	2.10×10^{-5}	7.0×10^2	3.5×10^2
$D^- \to \pi^-\pi^-K^+$	1.18%	0.095	8.91×10^{-5}	6.30×10^{-5}	1.5×10^3	1.1×10^3
$D_s^+ \to K^+K^-\pi^+$	0.45%	0.053	5.43×10^{-6}	1.4×10^{-4}	20	5×10^2
Sum					4.4×10^3	1.4×10^4

Table 6.5: *Expected statistics for open charm mesons for* 1.5×10^{10} *central Au(25 AGeV)+Au collisions (see text). The multiplicities are taken from references [80, 81]*

The expected number of D-mesons depends on the model used to estimate their production multiplicity. If one uses the SHM production multiplicities then roughly 10^4 $D^0 + \overline{D}^0$ mesons are expected. If the HSD predictions are used, then the expected statistics is lower by a factor of approximately 5. From the results presented in Table 6.5, one observes that a substantial fraction (80%) of the expected statistics of D-mesons comes from the D^0 and $\overline{D}^0$ mesons. Note that the expected statistics is evaluated only on the basis of central collisions. Further simulation studies are required to estimate the number of D^0 particles from non-central collisions.

With the expected statistics (typically a few thousand D^0 particles), it is possible to determine quantities such as production yields and particle yield ratios with relatively good precision. A better precision can be achieved with higher statistics. Observables requiring higher statistics such as differential spectra, are more difficult to determine with good precision. In order to achieve more statistics one can investigate the possibility to operate the MVD at a higher collision rate. The simulation studies presented in this section were performed assuming a collision rate of 3×10^4 $collisions/s$. Above this rate an event pile-up is expected in the MVD because of its limited time resolution (30 μs). It is therefore important to study the possibility to pile-up several collisions in the MVD. This is the topic of the next section.

6.7 Simulation studies with event pile up in the MVD

Given the high granularity of the MVD detector one may consider to take advantage of this feature and operate with higher collision rates. It is important to note here, that if there is an event pile-up in the MVD it does not necessarily mean that events are also piled-up in other detectors, e.g. the STS. The separation of the individual collisions is based on the time information from the STS. The latter, due to its fast readout time (of the order of 10 ns) is able to separate individual collisions at a collision rate up to 10 MHz. At this rate it would in principle be possible to pile-up some 10^3 collisions in the MVD but the limitation arises mainly from the consequent excessive occupancy and the resulting high rate of merged pixel clusters in the MVD stations.

6.7.1 Estimate of the tolerable number of pile up events in the MVD

The goal here is to investigate how many events can be piled up in the MVD without deteriorating significantly the reconstruction performances. As a full simulation requires substantial computing resources it was first investigated what would be the tolerable limit in event pile up by examining the rate of merged clusters in MAPS sensors composing the MVD stations. The next step was to perform a complete study to demonstrate whether the D^0 measurement is indeed feasible with a certain number of pile up events in the MVD.

The term "merged cluster" used hereafter is referring to two or more clusters on the MAPS sensors which are located so close to each other that they overlap. The cluster finding algorithm (described in Section 5.3) used in the present simulations is not able to recognise and separate those overlapped clusters. In consequence, the information on the position of the contributing hits is distorted in the composed cluster. This effect may have substantial impact on the precision of the reconstruction of the corresponding tracks.

We used the number of correctly reconstructed clusters as a criterion in order to define an upper limit of the number of pile up events tolerable by the MVD. In order to characterise a cluster as correctly reconstructed, or "unambiguous", it has to originate from a unique particle hit. All other cases, e.g. where one cluster is produced from multiple hits, are considered as "ambiguous".

We require that at least 95% of all clusters should be unambiguous for each MVD station separately. This is considered as a reasonable requirement for good track reconstruction.

The study was performed using a 1-bit ADC for the MAPS sensors readout (see Chapters 3 and 5). The ADC parameters are such that a threshold of 75 electrons is used for the identification of firing pixels. This value was used as a compromise between a good detection efficiency and a low fake hit rate.

We sample four representative cases of event pile up in the MVD, $N_{pileup} = 1, 5, 10, 20$ within the range defined in Figure 6.1. To simulate a pile up of N events, we merge the hits originating from 1 central collision, N-1 minimum bias collisions and $100 \times N$ Au ions traversing the target (see Section 5.5.3).

Table 6.6 lists the fraction, expressed in percent, of the correctly reconstructed clusters over all clusters for the first and second MVD stations.

Pile up	1	5	10	20
1st station	99.0%	96.0%	92.6%	88.9%
2nd station	99.8%	99.1%	98.3%	97.1%

Table 6.6: *Fraction of the unambiguous clusters for the 2 MVD stations. The columns correspond to different assumptions on the number of pile up events.*

From the results shown in Table 6.6 the requirement for 95% of unambiguous clusters is fulfilled for $N_{pileup} \leq 5$. The results suggest that the reconstruction of open charm with a pile up of more than 5 collisions is challenging with the present status of the hit and tracking reconstruction software.

Therefore, it was decided to perform a complete simulation study in order to evaluate the expected performance for D^0 measurements with $N_{pileup} = 5$ collisions.

6.7.2 Reconstruction of D^0 particles with event pile up in the MVD

For the studies presented here, it is assumed that the collision rate is increased by a factor of 5 with respect to the study presented previously (where the collision rate assumed was 3×10^4 *collisions*/*s*). Provided that this collision rate can be handled by the MVD without drawbacks in terms of track reconstruction, one expects this increased rate to turn into a five times higher number of reconstructed open charm particles. Under this assumption, the S/B ratio would remain unchanged while the significance of the signal increases by a factor $\sqrt{5}$. In the following, we aimed to study if the assumed good reconstruction is achieved. This was in so far questionable, as the increased collision rate turns into a pile up of collisions in the MVD by the same factor. The related increased occupancy was expected to form an extreme challenge to the hit and track reconstruction algorithms of CBM.

For the simulation study with event pile up, the procedure followed is the same as described in Section 6.5. A total of 6.7×10^7 events were generated using the Super-Event technique (see Section 6.5.2).

The pre-selection cuts were not modified but the cut optimisation was performed in order to adapt the cuts to the new data sample. The cuts obtained from the optimisation are listed in Table 6.7. The values of the cuts added independently of the cut optimisation ("manual" cuts) are denoted with a $^{(*)}$.

Cut	[units]	Pre-selection	Optimisation	Manual+Optimisation
PV-sigma (or PV)	$[\sigma_{PV}]$	$> 4.5^{(*)}$	> 7.4	> 7.4
SvZ-cut	$[\mu m]$	-	> 300	> 300 and $< 2 \times 10^{3(*)}$
IPD0	$[\mu m]$	-	< 7.8	< 7.8
SvChiT-cut	$[\sigma_{\chi^2}]$	-	< 1.05	< 1.05
Pt-cut	[MeV/c]	-	> 750	> 750
P-cut	[GeV/c]	-	> 1	> 1
Proton rejection		yes		yes
IPAngle-cut		-	< -0.80	< -0.80
IP-cut	$[\mu m]$	-	-	$< 600^{(*)}$
$\cos A$-cut		–	-	$< 0.8^{(*)}$
$\cos 12 - cut$			< 1	< 1
$\tilde{p}_t$**-cut**		–	-	$> 0.22^{(*)}$
IM-cut	$[GeV/c^2]$			$> 1.7^{(*)}$ and $< 2.2^{(*)}$

Table 6.7: *List of used cuts for open charm reconstruction. The column with the "Pre-selection" shows the cuts fixed before applying the cut optimisation algorithm. The column "Optimisation" lists the values provided at the output of the algorithm and the last column shows the combined cuts used as final in the analysis. The numbers marked with* $^{(*)}$ *denote the cut values added manually.*

In addition to the proton identification, the identification of other particles (as described in Section 6.4.2) was also applied.

6.7.3 Results on the simulation studies with event pile up

Figure 6.19 shows the invariant mass distributions of all opposite charge pairs after applying all cuts for the background (left panel) and the signal (right panel). The background was fitted with a constant, as shown in the figure. The uncertainties of the fit were handled as described in Section 6.6.5.

The results of the study are displayed in Table 6.8 which includes also the expected performances for $\overline{D}^0$ and $D^0 + \overline{D}^0$. The latter were obtained assuming that the reconstruction efficiency for the $\overline{D}^0$ particle and the remaining background are the same as for D^0.

An illustration of the invariant mass distribution of pion and kaon pairs as expected for 7.5×10^{10} central collisions is presented in Figure 6.20. This figure was produced in a similar way as Figure 6.18.

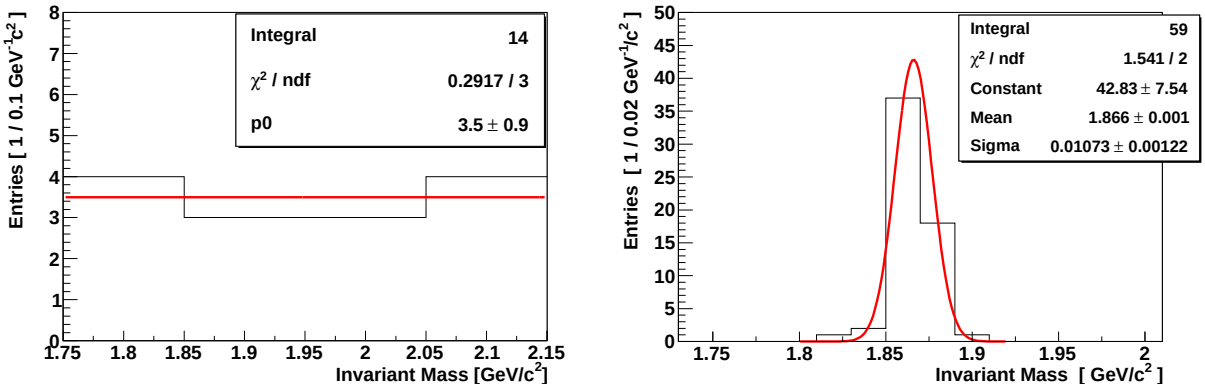

Figure 6.19: *Invariant mass distributions of opposite charge pairs after applying selection cuts. Left: Uncorrelated pairs (background), right: correlated (signal) pairs. The fit functions are shown.* 6.7×10^7 *events and* 7×10^3 *signal pairs were used for this simulation.*

Comparing the results obtained on D^0 meson reconstruction from the two studies, one observes that due to the pile-up, the signal-to-background ratio is reduced by a factor slightly larger than 4. Moreover, the detection efficiency deteriorates from 2% to 0.7% which reduces the gain in terms of counting statistics from the ambitioned factor of 5 to a factor of 1.8. Consequently, the siginificance of the D^0 peak remains unchanged within error bars.

Table 6.9 lists the expected statistics for other charm mesons. The results were derived as described in Section 6.6.7. Assuming SHM production multiplicities, 2.5×10^4 D-mesons are expected during one typical CBM run period.

Figure 6.21 shows the distribution of D^0 particles in the transverse momentum-rapidity plane. The top panel corresponds to the initial (4π) distribution used as input in the

		D^0	$\overline{D}^0$	$D^0 + \overline{D}^0$
Multiplicity	HSD	3.74×10^{-5}	1.12×10^{-4}	1.49×10^{-4}
	SHM	2.05×10^{-4}	6.15×10^{-4}	8.20×10^{-4}
mean proper decay length $c\tau$ $[\mu m]$		122.9	122.9	122.9
decay channel		$K^-\pi^+$	$K^+\pi^-$	$K^\mp\pi^\pm$
Branching ratio		3.89%	3.89%	
sec. vertex resol. $[\mu m]$		50 μm		
Reconstruction Efficiency		0.72%	0.72%	
Mass resolution $[MeV/c^2]$		10.7 ± 1.2		
S/B	HSD	$0.43^{+0.18}_{-0.11}$	$1.29^{(*)}$	
	SHM	$2.4^{+0.96}_{-0.63}$	$7.2^{(*)}$	
Significance	HSD	$15.6^{+2.8}_{-2.2}$	$46.8^{(*)}$	
	SHM	$56.25^{+5.5}_{-6}$	$168.75^{(*)}$	
Expected number of particles	HSD	7.9×10^2	2.4×10^3 $^{(*)}$	3.2×10^3 $^{(*)}$
	SHM	4.3×10^3	1.3×10^4 $^{(*)}$	1.7×10^4 $^{(*)}$

Table 6.8: *Reconstruction efficiency, mass resolution, signal-to-background ratio, significance and number of expected particles for open charm reconstruction in central Au+Au collisions at 25 GeV beam energy. The "sec. vertex resol." is the secondary vertex resolution along the beam direction. The results correspond to* 7.5×10^{10} *central collisions (see text). The numbers marked in* $^{(*)}$ *denote that the results are obtained assuming that the reconstruction efficiency and the shape of the background distribution for* $\overline{D}^0$ *are the same as those of* D^0 *particles (see text).*

Particle	Tot. eff.	BR	Multiplicity		Expected statistics	
			HSD	SHM	HSD	SHM
$D^0 \rightarrow \pi^+ K^-$	0.72%	0.0389	3.74×10^{-5}	2.05×10^{-4}	7.9×10^2	4.3×10^3
$\overline{D}^0 \rightarrow \pi^- K^+$	0.72%	0.0389	1.12×10^{-4}	6.15×10^{-4}	2.4×10^3	1.3×10^4
$D^0 \rightarrow \pi^+ \pi^+ \pi^- K^-$	0.08%	0.077	3.74×10^{-5}	2.05×10^{-4}	1.7×10^2	9.5×10^2
$\overline{D}^0 \rightarrow \pi^- \pi^- \pi^+ K^+$	0.08%	0.077	1.12×10^{-4}	6.15×10^{-4}	5.2×10^2	2.8×10^3
$D^+ \rightarrow \pi^+ \pi^+ K^-$	0.45%	0.095	4.17×10^{-5}	2.10×10^{-5}	1.3×10^3	6.7×10^2
$D^- \rightarrow \pi^- \pi^- K^+$	0.45%	0.095	8.91×10^{-5}	6.30×10^{-5}	2.9×10^3	2×10^3
$D_s^+ \rightarrow K^+ K^- \pi^+$	0.16%	0.053	5.43×10^{-6}	1.4×10^{-4}	35	8.9×10^2
Sum					8.1×10^3	2.5×10^4

Table 6.9: *Table on expected performances for open charm mesons for* 7.5×10^{10} *central Au(25 AGeV)+Au collisions (see text). The multiplicities were taken from [80, 81]*

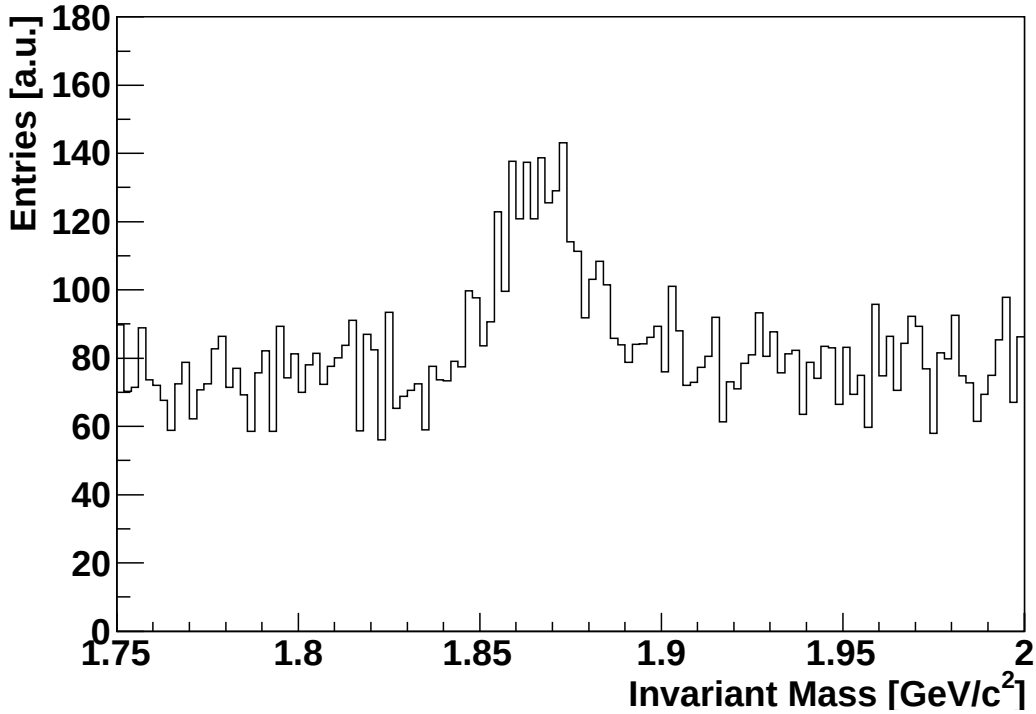

Figure 6.20: *Invariant mass distribution of opposite charge pairs after applying selection cuts as it is expected for one CBM run period at* 7.5×10^5 *central collisions/s.*

simulations. The middle panel illustrates the effect of geometrical acceptance. The detector acceptance allows covering a large fraction of the forward hemisphere in the centre of mass and the mid-rapidity region (around Y=2). The bottom panel shows the distribution after all cuts have been applied. Although there is a reduction of the number of D^0 expected to be measured, a large fraction of the phase space around the mid-rapidity region remains covered.

6.7.4 Impact of particle identification

In order to evaluate the importance of particle identification in CBM, its effect on the D^0 measurements in CBM was explored. Given that no detector with particle identification capabilities was included in the simulation, the effect of particle identification was modeled in a rather simple way, as described in Section 6.4.2. Four cases are explored: i) only RICH, ii) RICH and TRD and iii) RICH, TRD and TOF iv) ideal pion and kaon identification over the full momentum range. In all four cases an ideal proton rejection provided by the TOF was assumed as this rejection was part of the pre-selection cuts.

These assumptions on particle identification were considered as reasonable as they account for the realistic performances of the detectors. Note however, that the geometrical acceptance of these detectors was assumed to be the same as the one of the tracking detectors. Moreover, ideal track reconstruction was assumed and the decay of pions and kaons

was not accounted for.

Table 6.10 lists the performances for different assumptions on particle identification assuming particle multiplicities provided by the HSD model. As the cuts listed in Tables 6.3 and 6.7 were not modified, the total signal efficiency (which includes the geometrical acceptance and the reconstruction efficiency) is not affected by the particle identification cuts and remains 2% (0.7%) for the no pile up (pile up of 5 events) case. However, the additional particle identification reduces the background. This is not of substantial importance for the electron identification, provided by RICH and TRD, as electrons do not contribute substantially to the background in the invariant mass region of interest. The most crucial detector for background rejection is the TOF which is assumed to separate all kaons and pions up to 3.5 GeV/c. This detector allows to increase the S/B ratio for the open charm reconstruction by a factor of approximately 6 (no pile up) or 3 (pile up of 5 events). If ideal particle identification is applied, the background is almost completely removed and therefore a reasonable estimate for the S/B cannot be obtained. In this case a lower limit is given. This comparison illustrates the need for a high performance TOF detector in CBM, allowing for excellent pion to kaon separation.

6.8 Summary and discussion

The purpose of this chapter was to study the feasibility of open charm mesons measurements in nucleus-nucleus collisions with the CBM detector. D^0 particles decaying into a pion and a kaon were chosen to benchmark the performance of the experiment as they are considered as the most difficult to detect, mainly due to their short average proper decay length and their small production multiplicity. The MVD detector plays a crucial role in the reconstruction of these mesons as it provides an excellent secondary vertex resolution. The latter is needed in order to reconstruct and separate the decay vertex of D^0 particles from the nuclear collision vertex.

Detailed simulations were carried out including a realistic MVD detector response description. The foreseen characteristics of the MAPS sensors that will equip the MVD detector stations, were taken into account in these simulations: a pixel pitch of 18.4 μm, a readout time of 30 μs, a radiation tolerance of 3×10^{13} n_{eq}/cm^2 and a realistic estimate of the material budget. The particle identification system of CBM was modeled as follows: it was assumed that the TOF detector of CBM may reject all protons and distinguish pions from kaons up to a momentum of 3.5 GeV/c. Moreover, the assumption was made that the RICH and the TRD may reject electrons. The contribution of δ-electrons produced by the passage of beam particles in the target was included. Two feasibility studies were performed for the measurement of the D^0 mesons in the case of central Au+Au collisions at 25 $AGeV$ beam energy.

In the first study, it was assumed that there is no event pile-up in the MVD detector. The collision rate was chosen such that one collision occurs per readout frame of the MVD, i.e. 3×10^4 $collisions/s$. The reconstruction of the D^0 particle was based on building its invariant mass distribution. Several selection criteria were used to reduce the very high combinatorial background due to uncorrelated (π, K) pairs. After optimising the underlying selection cuts, we found a signal-to-background ratio in the D^0 invariant mass region of

	S/B		Sign.	
	pu1	pu5	pu1	pu5
only proton rejection	0.18	0.11	8.2	8.9
RICH	0.25	0.13	9.2	9.5
RICH & TRD	0.25	0.13	9.2	9.5
RICH & TRD & TOF	1.95	0.43	17.18	15.6
ideal	> 6	> 2	21	28

Table 6.10: *The performance of open charm detection depending on the use of RICH, TRD and TOF. The results are shown for two cases: only one collision per readout cycle (pu1) and for a pile up of 5 collisions (pu5).*

$1.95^{+1.41}_{-0.63}$ and $10.8^{+7.95}_{-3.45}$ depending on the assumption made on the D^0 production multiplicity (3.74×10^{-5} for HSD and 2.05×10^{-4} for SHM respectively). The total reconstruction efficiency of $D^0 \rightarrow \pi^+, K^-$ particles was found to be 2%. This includes the detector acceptance, the single track reconstruction efficiency and the efficiency of the selection cuts. Assuming SHM multiplicities, one expects 9.6×10^3 ($D^0 + \overline{D}^0$) particles within a typical CBM run period (i.e. two months beam on target). For HSD multiplicities, this turns into 1.7×10^3 particles per run period. The significance of D^0 particles was found to be $48^{+2.4}_{-2.2}$ (SHM) and $17.18^{+1.62}_{-1.38}$ (HSD). If the HSD multiplicities are considered, then the physics potential of CBM is limited essentially to yield and particle ratio measurements. In order to increase the physics potential of the experiment further, higher statistics is needed. It was therefore studied whether operating the MVD with a higher collision rate and, consequently, a moderate number of pile up events, would be feasible.

First, a dedicated study was performed in order to identify the tolerable number of collision pile up by the MVD. In this study, we identified the fraction of merged clusters in the MVD stations for different assumptions on collision pile up. We required a maximum of 5% merged clusters per station in order to define a tolerable collision pile up. From this criterion it was found that pile up should not exceed a value of five collisions per readout cycle of the MVD.

This result led to the second feasibility study in which it was assumed that 5 collisions (1 central and 4 peripheral) occur within one readout frame of the MVD. The assumed collision rate amounts then to 1.5×10^5 *collisions*$/s$. The total reconstruction efficiency for D^0 particles was found to be about 0.7%. According to the multiplicity predicted by the HSD (SHM) model, roughly 3.2×10^3 (1.7×10^4) $D^0 + \overline{D}^0$ particles are expected. The S/B of D^0 particles is $2.4^{+0.96}_{-0.63}$ and the significance is $56.25^{+5.5}_{-6}$ (assuming SHM).

The results suggest that, in contrast to our expectations, increasing the collision rate from 3×10^4 *collisions*$/s$ to 1.5×10^5 *collisions*$/s$ does not significantly extend the physics potential of CBM. This is because the higher occupancies related to the pile up of collisions deteriorate the reconstruction performance of the detector: the reconstruction efficiency is reduced by a factor of ~ 3 (from 2% to 0.7%) and the signal-to-background ratio decreases from $1.95^{+1.41}_{-0.63}$ to $0.43^{+0.18}_{-0.11}$ (assuming HSD model predictions for D^0 particles). The origin of this decreased efficiency is due to the high occupancy of the vertex detector, which translates into a high hit density and a non-negligible number of merged clusters. The track reconstruction algorithms of CBM are not yet adapted to handle this issue. It will be subject of future studies to study the precise origin of the effect and to identify software and hardware optimisations which may alleviate this effect. The impact of merged clusters on the physics performances may be alleviated with the usage of an adequate cluster reconstruction algorithm. The latter should be able to disentangle a large fraction of merged hits. With the presence of such an algorithm, it is likely that the pile-up of more than 5 events can be tolerated. However, note that the collision rate (and therefore the collision pile up) might be limited by the radiation tolerance of the detector.

Independently of the collision rate study, it is found that the significance of the D^0 signal is sufficient to identify this particle and to perform yield measurements. Moreover, the central rapidity region as much as a transverse momentum region up to at least 2.5 GeV/c is covered.

Two systematic uncertainties remain. On one hand, it is worth noticing that the expected

statistics of open charm particles depends on their production multiplicity, which is difficult to estimate in the FAIR energy range. This issue was partially accounted for by using two model predictions, which might express to some extent the range of the uncertainty on D-meson multiplicities. However, as no data are presently available, one cannot exclude that both predictions overestimate the open charm production multiplicities. If so, it may be preferable to carry out the first generation measurements at the SIS-300 top energy (35 $AGeV$ for Au + Au collisions) in order to profit from the rapid raise of the multiplicities with energy.

On the other hand, it is also important to mention that the collision rate of CBM will not be constant but will vary due to fluctuations in the beam intensity and due to the Poisson fluctuations of the beam-target interactions. In this respect, the result of the study indicates that a moderate pile up caused by those fluctuations will not disturb the measurements. This observation underlines the robustness of the current detector concept.

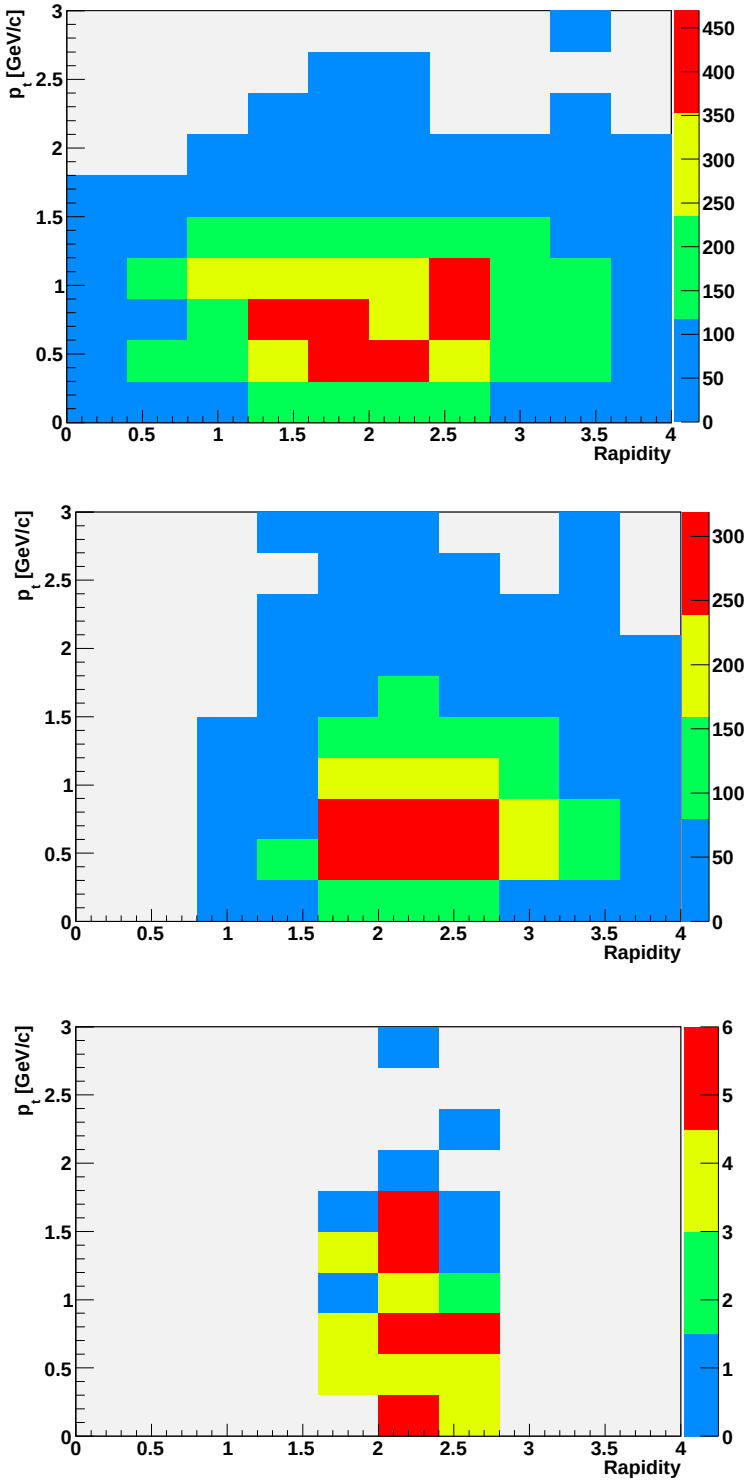

Figure 6.21: *Acceptance for $D^0 \rightarrow \pi^+ + K^-$ illustrated in the transverse momentum-rapidity plane. Top panel: The initial 4π distribution. The centre of mass rapidity is Y=2 at 25 AGeV. Middle panel: The distribution obtained taking into account the geometrical acceptance of the STS and MVD detectors. Bottom panel: The same distribution after applying all selection cuts.*

Summary and conclusion

The work presented in this thesis is a contribution to the design and development of the Micro Vertex Detector of the the CBM experiment planned at the future FAIR accelerator facility. It is focused around two main objectives: the development and evaluation of a realistic response simulation model of the MVD detector and the study of the expected performance of the CBM experiment for measuring open charm particles in nucleus-nucleus collisions at FAIR energies.

The response model was developed to serve as a tool for those performance studies. This imposed the need for the model to describe accurately the shape of hit clusters, which are generated by a high density of particles impinging the sensor with a broad range of incident angles. This was of particular importance as cluster merging was feared to deteriorate the reconstruction performances of the MVD.

A first step in building the response model was to obtain experimental data, which were to serve as reference for benchmarking and tuning the parameters of this model. To do so, a dedicated beam test was performed at CERN-SPS with 120 GeV/c pions. The analysis of the data taken during this test allowed us to characterise the response of a MAPS prototype (MIMOSA-17) for particles with a wide range of incident angles (0°-75°). It was observed that the shape of the cluster generated by particles impinging the sensor with an incident angle of 0° follows a Lorentz function. For the inclined tracks, it was found that the total charge generated in the cluster scales with the length of the particle trajectory in the sensitive volume of the sensor ($\sim 1/\cos\theta$). Moreover, for inclined tracks it was observed that the shape of the cluster is elongated along the direction of the particle trajectory.

The experimental data were compared to the results obtained using an existing simulation model, which had been previously used for modeling the response of MAPS sensors in the context of the International Linear Collider (ILC) experiments. This model, which is referred in this work as Gauss model, was found to reproduce the average pixel multiplicity of the clusters with fair precision. However, their shape could not be reproduced with sufficient accuracy to allow for a reliable description of cluster merging. This is due to the fact that the Gauss model was initially developed for fully depleted sensors which collect charge with an electric field. It therefore describes very well sensors which use the drift process to collect charge carriers. MAPS sensors however, are undepleted sensors. This means that

the charge carriers are mainly collected by diffusion. This process is not included in this model, which is therefore considered as not suitable for the description of the response of the CBM-MVD detector.

In order to better describe the response of MAPS sensors to the passage of particles with different incident angles, another simulation approach was adopted. The latter is based on a parameterisation of the measured MAPS detector response. In the new model, which is referred to as Lorentz-model, the charge produced in the active volume is randomly generated following the measured Landau distribution of the charge collected over a cluster of 5×5 pixels. This charge is then shared among the pixels of the cluster according to a Lorentz function whose parameters were adjusted to reproduce the measured shape of the cluster. The parameters of the model were tuned to reproduce the response of MAPS sensors measured for particles impinging the sensor with an incident angle of 0 degrees. Despite being simple, the model allows reproducing the data measured for different particle incident angles (from 0 to 75 degrees) with an accuracy of 10% or better.

The model was designed to allow simulating collision pile up in the MVD and the effect of δ-electrons originating from the passage of beam ions through the target. Moreover, the option to simulate MAPS being read out with ADCs instead of the currently preferred discriminators was implemented.

The MVD response model was used to carry out realistic simulation studies in order to investigate the feasibility of open charm particle measurements in CBM.

The studies were performed with the CBMRoot simulation framework. Only the MVD and STS detectors were used for event reconstruction. Their response was simulated in a realistic way. Other detectors serving for particle identification were not included in the simulation. However, their effect was modeled in a simple way. In order to represent the Time-Of-Flight detector, all protons were rejected from the combinatorial background. Moreover, it was assumed that the TOF provides a perfect pion to kaon separation for momenta of up to 3.5 GeV/c. To describe the combination of RICH and TRD detectors, the assumption was made that all electrons may be rejected.

We studied the reconstruction of open charm particles in central Au+Au collisions at an incident energy of 25 $AGeV$. The D^0 meson decaying into a (π^+, K^-) pair was chosen as a benchmark in this study. The strategy for reconstructing the D^0 particle was based on the identification and separation of its decay vertex from the primary collision vertex. The resolution of the secondary vertex was found to be about 60 μm. The momentum resolution of the STS was of in the order of 1.2% which led to an invariant mass resolution of 12 MeV/c^2. The tracking efficiency for tracks with momentum above 1 GeV/c was $\sim 95\%$.

In a first step of the simulation, it was assumed that the collision rate of CBM for open charm measurements would be chosen in order to avoid a pile up of collisions in the MVD. Accounting for a readout time of this detector of $\sim$ 30 μs, this turns into a maximum collision rate of about 3×10^4 collisions per second.

We found a signal-to-background ratio in the D^0 invariant mass region of $1.95^{+1.41}_{-0.63}$ and $10.8^{+7.95}_{-3.45}$ depending on the assumption made on the D^0 production multiplicity (3.74×10^{-5} for HSD and 2.05×10^{-4} for SHM respectively). The total reconstruction efficiency of D^0 particles was found to be 2%. This includes the detector acceptance, the single track reconstruction efficiency and the efficiency of the selection cuts. Assuming SHM multiplicities,

one expects 9.6×10^3 ($D^0 + \overline{D}^0$) particles within a typical CBM run period (i.e. two months beam on target). For HSD multiplicities, this turns into 1.7×10^3 particles per run period. The significance of D^0 particles was found to be $48^{+2.4}_{-2.2}$ (SHM) and $17.18^{+1.62}_{-1.38}$ (HSD). Note that particle identification is included in these results: ideal proton identification, pion and kaon identification up to 3.5 GeV/c from the TOF detector and electron identification from the RICH and TRD detectors. If the HSD multiplicities are considered, then the physics potential of CBM is limited essentially to yield and particle ratio measurements. In order to further increase the physics potential of the experiment, higher statistics is needed. It was therefore studied whether operating the experiment with a higher collision rate and, consequently, a pile up of a certain number of collisions in the MVD, would be feasible.

This motivated a second feasibility study in which the simulations were performed in the case of a higher collision rate. Simple considerations on the rate of overlapped clusters in the MAPS sensors suggest that a pile-up of 5 collisions in the MVD could be tolerable. This translates into a collision rate of 1.5×10^5 $collisions/s$ and a total statistics of 7.5×10^{10} central collisions per CBM running year.

The results of the simulations with a pile up of 5 events in the MVD show that the total reconstruction efficiency for D^0 particles is about 0.7%. According to the multiplicity predicted by the HSD (SHM) model, roughly 3.2×10^3 (1.7×10^4) $D^0 + \overline{D}^0$ particles are expected in this case. The S/B of D^0 particles is $2.4^{+0.96}_{-0.63}$ and the significance is $56.25^{+6}_{-5.5}$ (assuming the D^0 multiplicity predicted by HSD).

These results suggest that, in contrast to our expectations, increasing the collision rate from 3×10^4 $collisions/s$ to 1.5×10^5 $collisions/s$ does not significantly extend the physics potential of CBM. This is because the higher occupancies related to the pile up of collisions deteriorate the reconstruction performance of the detector: the reconstruction efficiency is reduced by a factor of ~ 3 (from 2% to 0.7%) and the signal-to-background ratio decreases from $1.95^{+1.41}_{-0.63}$ to $0.43^{+0.18}_{-0.11}$ (assuming HSD model predictions for the multiplicity of D^0 particles). The significance of the D^0 signal remains unchanged within the uncertanties of the simulation.

The effect of mass identification on the performance of the D^0 reconstruction was investigated. We found that the sensitivity of CBM for open charm improves substantially (S/B is increased up to a factor of 8) if information from the particle identification detectors (TOF, RICH, TRD) is used.

The studies carried out demonstrate the robustness of the overall CBM detector concept. The sensitivity of the detector depends on the rate capability of the sensor assumed in the study (which limits the number of reconstructed particles). On the other hand, the tracking algorithms were not yet optimised to operate with a large number of overlapped clusters in the MVD. It is estimated that a factor of 2 in efficiency and therefore in measured particle statistics is lost due to this effect. The performance of the experiment might be improved by refining software and detector aspects.

Optimisation of the reconstruction software should provide the possibility to identify and potentially disentangle overlapping pixel clusters by means of pattern recognition. The latter would allow the tracking algorithm to decide whether a cluster should be attached to more than one track which was, in so far, generally not done.

The design of the MVD detector might be improved by adding a third station, which was initially foreseen but was removed in order to reduce the cost of the vertex detector. Due to

this modification however, the gap between the STS and MVD was enlarged to 20 cm. This distance came out to be too high to allow obtaining an efficient track matching between the MVD and the STS. One might consider to optimise the RICH detector for hadron identification for the open charm runs. This could be done by choosing a specific radiator gas allowing for better kaon and pion identification.

The simulated performances of the sensors represent the best assumptions on the status of sensor development in 2015. Given the encouraging progress in CMOS sensor development it is fair to expect that by the time of start-up of CBM at SIS-300 substantially more performing sensors might be available. In particular, there are currently architectures discussed which might accelerate the readout time of the MVD by a factor of 5 and provide a non-ionising radiation tolerance above 10^{14} n_{eq}/cm^2. Moreover, the time scale of CBM at SIS-300 would probably allow to profit from the appearance of 3D integrated detectors, which may show even higher performances.

From these considerations it is concluded that open charm reconstruction is feasible with the CBM experiment. Implementing the above mentioned improvements might lead to substantial gain in the detector performances. The latter should allow performing more elaborated measurements requiring high statistics (e.g. elliptic flow, differential distributions).

Bibliography

[1] T. Morii, C. S. Lim, S. N. Mukherjee, "The physics of the standard model and beyond", ISBN 981-02-4571-8

[2] Particle Data Group: "Particle Physics Booklet July 2010", http://pdg.lbl.gov/

[3] G. S. Bali, Phys. Rept. 343 (2001) 1, http://arxiv.org/pdf/hep-ph/0001312

[4] K. Schweda, X. Zhu, M. Bleicher, S.L. Huang, H. Stocker, N. Xu, P. Zhuang, arXiv:nucl-ex/0610043 v1 30 Oct 2006

[5] P.Senger, "The Compressed Baryonic Matter (CBM) experiment at FAIR", presentation given at Gauhati University, Guwahati, India, March 4, 2011

[6] F. Karsch et E. Laermann, Preprint: arXiv : hep-lat/0305025

[7] F. Karsch, E. Laermann, A. Peikert, Nuclear Physics B 605 (2001) 579-599 , http://arxiv.org/pdf/hep-lat/0012023v1

[8] Z. Fodor et S. D. Katz, JHEP 0404 (2004) 050. Preprint : arXiv : heplat/0402006.

[9] M. Stephanov, Journal of Physics: Conference Series 27 (2005) 144-153

[10] http://press.web.cern.ch/press/pressreleases/Releases2000/PR01.00EQuarkGluonMatter.html

[11] E. V. Shuryak, Phys. Lett. B 78 (1978) 150.

[12] J. D. Bjorken, Phys. Rev. D 27 (1983) 140.

[13] S. Salur, Investigation of Hadronic Resonances with STAR, Disseration Thesis, Yale (2006).

[14] A. Andronic, P. Braun-Munzinger, K. Redlich, J. Stachel, Nucl. Phys.A 789 (2007) 334, nucl-th/0611023.

[15] P.Braun Munzinger, K. Redlich, J. Stachel, nucl-th/0304013

[16] I. Arsene et al., Collaboration BRAHMS, Preprint : arXiv : nucl-ex/0410020

[17] T. Matsui and H. Saltz, Phys. Lett. B 178, 416 (1986)

[18] M. C. Abreu et al. NA50 Coll Physics Letters B 450, 1999, 456-466

[19] R. Arnaldi and the NA60 Collaboration, Nuclear Physics A, Volume 783, 2007, 261-268

[20] S. Gavin, M. Gyulassy, A. Jackson, Physics Letters B, Volume 207, 1988, 257-262

[21] R. Vogt, M. Prakash, P. Koch, T. H. Hansson, Physics Letters B, 207, 1988, 263-268

[22] L. Ramello, Nuclear Physics A, Volume 774, (2006) 59-66

[23] Nucl.Phys.A757:102-183,2005, arXiv:nucl-ex/0501009v3

[24] Nucl.Phys.A757:184-283,2005, arXiv:nucl-ex/0410003v3

[25] Nucl.Phys.A757:28-101,2005, arXiv:nucl-ex/0410022v2

[26] J. Adams et al. (STAR Collaboration) Phys. Rev. Lett. 91, 072304 (2003)

[27] Y.Zhang, "Overview of charm production at RHIC", arXiv:0806.0079v1, 2008

[28] J. Adams et al. [STAR Collaboration], Phys. Rev. Lett. 92, 052302 (2004)

[29] S. S. Adler et al. [PHENIX Collaboration], Phys. Rev. Lett. 91, 182301 (2003)

[30] C. Alt et al. (NA49 collaboration) Phys. Rev. C 77, 024903 (2008)

[31] A. Andronic et al. Nuclear Physics A 772 (2006) 167-199

[32] J. Cleymans et al., Phys. Rev. C 60 (1999) 054908; P. Braun-Munzinger et al., Nucl. Phys. A 697 (2002) 902.

[33] E.L. Bratkovskaya et al., Phys. Rev. C 69 (2004) 054907

[34] P. Braun-Munzinger, J. Stachel, Phys. Lett. B 490 (2000) 196, nucl-th/0007059

[35] Larry McLerrana, "Quarkyonic Matter and the Revised Phase Diagram of QCD" arXiv:0907.4489v2

[36] Mark G. Alford et al. "Color superconductivity in dense quark matter", arXiv:0709.4635v2

[37] Letter of Intent for the NA61 experiment, CERN-SPSC-2006-001 SPSC-I-235 (2006)

[38] V. Toneev, Pos(CPOD07)057 (2007)

[39] W. Ehehalt and W. Cassing, 'Relativistic transport approach for nucleus-nucleus collisions from SIS to SPS' Nucl. Phys. A 602 (1996) 449 -486 or LANL e-print

[40] J. Geiss, W. Cassing and C. Greiner 'Strangeness production in the HSD transport approach from SIS to SPS energies' Nucl. Phys. A 644 (1998) 107-138 or LANL e-print

[41] P. Braun-Munzinger, K. Redlich, J. Stachel, nucl-th/0304013v1

[42] B.Friman et al. "The CBM Physics Book: Compressed Baryonic Matter in Laboratory Experiments", Lecture Notes in Physics, Vol. 814 ,ISBN: 978-3-642-13292-6

[43] A. D. Frawley, T. Ullrich, R. Vogt Heavy flavor in heavy ion collisions at RHIC and RHIC II (2008), arXiv:0806.1013v2

[44] R. Vogt, "The A Dependence of Open Charm and Bottom Production", arXiv:hep-ph/0111271v1 22 Nov 2001

[45] P. Shukla "Glauber model for heavy ion collisions from low energies to high energies" http://arxiv.org/abs/nucl-th/0112039

[46] NA38 and NA50 Collaborations, M. C. Abreu et al., Eur. Phys. J. C14, 443-455 (2000).

[47] J. W. Cronin et al. "Production of hadrons at large transverse momentum at 200, 300, and 400 GeV", Phys. Rev. D 11 (1975) 3105.

[48] M. Arneodo, "Nuclear effects in structure functions", Phys. Rept., 240, 301

[49] P.Senger, "Probing dense baryonic matter", Progress in Particle and Nuclear Physics, 2009, 375

[50] F. Wilczek, Physics Today 53 (2000) 22

[51] F. Weber, J. Phys. G 27 (2001) 465

[52] Conceptual Design Report of the CBM collaboration

[53] W. Cassing, E. Bratkovskaya, A. Sibirtsev, Nucl. Phys. A691 (2001) 745

[54] Technical Status Report of the CBM collaboration, January 2005.

[55] M. Deveaux, "Development of fast and radiation hard Monolithic Active Pixel Sensors (MAPS) optimized for open charm meson detection with the CBM-vertex detector", PhD thesis, Strasbourg, 2008,

[56] "Radiation dose simulations", D.Bertini, CBM collaboration meeting, 12 March 2009,

[57] S. Gorbunov, I. Kisel and I. Vassilev, CBM note, CBM-PHYS-note-2005-001

[58] https://www.gsi.de/documents/DOC-2008-Oct-165-1.pdf

[59] https://www.gsi.de/documents/DOC-2009-Feb-233-1.pdf

[60] DPG 2010, M. Deveaux

[61] Master thesis of C.Trageser, Frankfurt University

[62] V. Friese, CBM note, CBM-PHYS-note-2002-001.

[63] M. Bleicher, E. Zabrodin, C. Spieles, S.A. Bass, C. Ernst, S. Soff, L. Bravina, M. Belkacem, H. Weber, H. Stocker, W. Greiner: "Relativistic Hadron-Hadron Collisions in the Ultra-Relativistic Quantum Molecular Dynamics Model" J. Phys. G: Nucl. Part. Phys. 25 (1999) 1859-1896

[64] W.Cassing, E.L. Bratkovskaya, A. Sibirtsev: "Open charm production in relativistic nucleus nucleus collisions", Nucl. Physics A 691 (2001) 753-778

[65] B. Andersson, G. Gustafson, H. Pi, Z. Phys. C57 (1993) 485-494.

[66] T. Sjostrand, Comput. Phys. Commun. 82 (1994) 74

[67] R. Turchetta, J.D. Berst, B. Casadei, G. Claus, C. Colledani, W. Dulinski, Y. Hu, D. Husson, J.-P. Le Normand, J.-L. Riester, G. Deptuch, U. Goerlach, S. Higueret and M. Winter, "A Monolithic Active Pixel Sensor for Charged Particle Tracking and Imaging Using Standard VLSI CMOS Technology Nuclear Instruments and Methods in Physics" Research Section A 458 (2001) 677-689

[68] http://root.cern.ch/

[69] J.-P. Blaizot and J.-Y. Ollitrault, Phys. Lett. B 199, 499 (1987)

[70] G. Deptuch, "New Generation of Monolithic Active Pixel Sensors for Charged Particle Detection / Developpement d'un capteur de nouvelle generation et son electronique integrée pour les collisionneurs futurs", PhD Université Louis Pasteur 2002, Available online: http://ireswww.in2p3.fr/ires/recherche/capteurs/index.html (English, french summary)

[71] J.Baudot, "Future of Low Mass Pixel Systems with MAPS" PoS(VERTEX2010)001.

[72] G. Lutz, "Semiconductor Radiation Detectors", Springer (1999), ISBN 3-540-64859-3

[73] http://cbmroot.gsi.de/

[74] http://root.cern.ch/drupal/

[75] S. A. Bass et al: "Microscopic Models for Ultrarelativistic Heavy Ion Collisions.", Prog. Part. Nucl. Phys. 41 (1998) 225-370

[76] V. Friese, "Feasibility of the detection of D0 mesons in the CBM experiment", CBM-PHYSnote-2002-001, http://www.gsi.de/documents/DOC-2005-Aug-36-1.pdf

[77] I. Kisel et al. "CATS: A cellular automaton for tracking in silicon for the HERA-B vertex detector", Nucl. Instrum. Meth. A 489 (2002) 389.

[78] R.E. Kalman, "A new approach to linear filtering and prediction problems", Transaction of the ASME, Journal of Basic Engineering 82 (1960) 35.

[79] R. Frühwirth et al:, "Data Analysis Techniques for High-Energy Physics", Cambridge University Press; 2nd edition (2001).

[80] I.Vassiliev et al, "D0 decay feasibility study in the CBM experiment" GSI Scientific Report 2007

[81] I. Vassiliev, "Open charm measurement in the CBM experiment", CBM Collaboration Meeting, 12-16 April 2010, GSI, Darmstadt,

[82] I. Vassiliev, "Open charm simulations", CBM Collaboration Meeting, Dubna, 14-Oct-08

[83] M.Koziel, "Development of Fast and Radiation Tolerant Monolithic Active Pixel Sensors for High Energy Physics Experiments." PhD thesis, in progress

[84] F.Karsch, Lecture Notes in Physics 583, (2002) 209, Nucl. Phys. A 698 (2002)

[85] Yu.B Ivanov et al, "Relativistic Heavy-Ion Collisions within 3-Fluid Hydrodynamics: Hadronic Scenario", http://arxiv.org/pdf/nucl-th/0503088v3

[86] P. Braun-Munzinger et al. Eur.Phys.J. C1 (1998) 123

[87] M. C. Abreu et al. NA50 Coll Eur.Phys.J. C14 (2000) 443

[88] O. Linnyk et al. Nuclear Physics A 786 (2007) 183-200

[89] A. Andronic, P. Braun-Munzinger, K. Redlich, J. Stachel, Nucl. Phys.A 789 (2007) 334, nucl-th/0611023.

[90] A. Andronic et al. Physics Letters B 659 (2008) 149-155

[91] A. Andronic et al., Phys. Lett. B 673 (2009) 142.

[92] J. Phys. G: Nucl. Part. Phys. 34 (2007)

[93] R.Lacey and A.Taranenko, arXiv:nucl-ex/0610029v3

[94] R. Brockmann, W. Weise. "The chiral condensate in nuclear matter ", Physics Letters B 367 (1996) 40-44

[95] J. Randrup, J. Cleymans, Phys. Rev. C 74, 047901 (2006), arXiv:0905.2824v1 [nucl-th]

[96] J. Cleymans, H. Oeschler, K. Redlich, and S. Wheaton, Phys. Rev. C 73, 034905 (2006).

[97] Feinberg EL.Nuovo Cim. A34:391 (1976)

[98] I. C. Arsene et al., Phys. Rev. C75 (2007) 034902.

[99] The ILD Concept Group, "The International Large Detector letter of intent", arXiv:1006.3396v1[hep-ex]

[100] The IPHC-PICSEL group, MIMOSA-17 documentation, internal document.

[101] F. Klingl, S. Kirn, S.H. Lee, P. Morath, W. Weise, Phys. Rev. Lett. 82 (1999) 3396.

[102] S. Gavin, M. Gyulassy, and A. Jackson. Phys. Lett., B207 262, 1988.

[103] R. Vogt, M. Prakash, P. Koch, and T.H. Hansson. Phys. Lett., B207 263 268, 1988.

[104] E. Bratkovskaya, W. Cassing, private communication

[105] A. Tai (STAR Collaboration), J. Phys. G 30, S809 (2004).

[106] J. Adams et al. (STAR Collaboration), Phys. Rev. Lett. 94, 062301 (2005).

[107] S. Baumgart (STAR Collaboration), arXiv:0709.4223.

[108] C. Zhong (STAR Collaboration), J. Phys. G 34, S741 (2007).

[109] B. I. Abelev et al. (STAR Collaboration), Phys. Rev. Lett. 98, 192301 (2007).

[110] A. Adare et al. (PHENIX Collaboration), Phys. Rev. Lett. 98, 232301 (2007); 98, 172301 (2007); S. S. Adler et al. (PHENIX Collaboration), ibid. 96, 032301 (2006); 94, 082301 (2005); K. Adcox et al. (PHENIX Collaboration), ibid. 88, 192303 (2002).

[111] S. S. Adler et al. (PHENIX Collaboration), Phys. Rev. Lett. 96, 032001 (2006); A. Adare et al. (PHENIX Collaboration), ibid. 97, 252002 (2006).

[112] S. S. Adler et al. (PHENIX Collaboration), Phys. Rev. C 72, 024901 (2005).

[113] FAIR Baseline Technical Report, http://www.gsi.de/documents/DOC-2006-Dec-94-1.pdf, 2006.

[114] W.Cassing, E.Bratkovskaya, Physics Reports, Volume 308, Issues 2-3, 1 January 1999, Pages 65-233

[115] CBM Progress Report 2009, http://www.gsi.de/documents/DOC-2010-Apr-17-1.pdf

[116] D. Kresan and C. Höhne, Event-by-Event Fluctuations of the K/p Yield Ratio in the CBM Experiment, CBM Progress Report 2008, 2009.

[117] M. Gazdzicki and M. Gorenstein, Acta Phys. Pol. B 30 (1999) 2707c

[118] F. Karsch and E. Laermann, Quark-Gluon Plasma 3, Hwa and Wang (ed.) (2003).

[119] S.Jeon et al, "Event-by-event fluctuations" arXiv:hep-ph/0304012v1

[120] M. Stephanov, K. Rajagopal, and E. Shuryak, "Signatures of the Tricritical Point in QCD", Phys. Rev. Lett. 81, 4816–4819 (1998). arXiv:hep-ph/9806219v2

[121] M.Stephanov, Phys. Rev. Lett. 102, 032301 (2009)

[122] E. Shuryak, Phys. Lett. B 78 (1978) 150

[123] R. Rapp, Nucl. Phys. A 661 (1999) 33c.

[124] M.Winter,"CMOS Pixel Sensors for Charged Particle Tracking : Achieved Performances and Perspectives" TIPP 2009, Tsukuba (12-17 March)

[125] A.Dorokhov, "Improved radiation tolerance of MAPS using a depleted epitaxial layer", 11th European Symposium on Semiconductor Detectors, Wildbad Kreuth (7-11 June)

[126] J.Baudot, "First Test Results of MIMOSA-26, a Fast CMOS Sensor With Integrated Zero Suppression and Digitized Output", IEEE Nuclear Science Symposium, Orlando (25-31 October).

[127] M. Förtsch et al., "Integrated PIN Photodiodes in High-Performance BiCMOS Technology", Electron Devices Meeting, 2002. IEDM '02. Digest. International.

[128] G.Voutsinas, "Studies for a 10 μs, thin, high resolution CMOS pixel sensor for future vertex detectors", to be published in Nuclear Physics B.

[129] A.Himmi, "A Zero Suppression Micro-Circuit for Binary Readout CMOS Pixel Sensors", TWEPP 2009 , Paris (21-25 September)

[130] R.De Masi et al.,Nucl.Instr.and Meth.A (2010), doi:10.1016/j.nima.2010.06.339

[131] M.Deveaux et al. "Design considerations for the Micro Vertex Detector of the Compressed Baryonic Matter experiment", PoS(VERTEX 2008)028

[132] M.Deveaux et al. "Status of the Micro Vertex Detector of the Compressed Baryonic Matter experiment", PoS(BORMIO 2010)041

[133] Tobias Tischler, private communication

[134] M. Deveaux, 15th CBM collaboration meeting , 14th April 2010, GSI

[135] http://ulisi-wiki.gsi.de/

[136] M.Deveaux "Radiation tolerance of a partially depleted CMOS-sensor with column parallel readout" talk presented in the 12^{th} iWoRiD Conference, 2010, Cambridge, United Kingdom

[137] M. Winter, "From the STAR CMOS Pixel Sensors to an eRHIC Sensor: A Path guided by Synergies", talk given at the "Workshop on system integration of highly granular and thin vertex detectors", 6-9 September 2011, Mont Sainte Odile, France

[138] The IPHC-PICSEL group, MAF documentation, internal document.

[139] Dirk Meier PhD thesis: "CVD Diamond Sensors for Particle Detection and Tracking", Heidelberg University, 1999

[140] Renato Turchetta, PhD thesis, CRN/HE 91-07, N.d'ordre 1019

[141] W.Dulinski, "Beam telescope for medium energy particles based on thin submicron precision MAPS", IEEE Nuclear Science Symposium 2007, Hawai (October 27, November 3)

[142] M.Goffe, private communication.

[143] H.Bichsel, "Straggling in thin Silicon detectors", Rev. Mod. Phys. 60 (1988) 663-699 and references therein.

[144] http://www.austriamicrosystems.com/

[145] Michal Szelezniak "Development of monolithic CMOS pixel sensors for the vertex detector upgrade in STAR RHIC experiment", PhD thesis, IPHC 2008.

[146] F. James, "MINUIT Function Minimization and Error Analysis", reference manual, Computing and Networks Division CERN Geneva, Switzerland

[147] A. Raspereza, Presented at the International Conference on Linear Colliders (LCWS06), Bangalore, India, March 2006

[148] M. Battaglia, Nucl. Instr. and Meth. A 572 (2007) 274-276

[149] Helmut Mehrer, "Diffusion in solids. Fundamentals, Methods, Materials, Diffusion-Controlled Processes" Springer series in solid state science 155, ISBN 978-3-540-71486-6

[150] Arnaud Gay, "Mesure du couplage de Yukawa du quark top auprès du collisionneur linéaire. Caractérisation du premier prototype Megapixel de capteurs CMOS pour la détection des particules chargées", PhD thesis, IPHC 2004

[151] Łukasz Mączewski, "Measurements and simulations of MAPS (Monolithic Active Pixel Sensors) response to charged particles - a study towards a vertex detector at the ILC", PhD thesis, Warsaw University, 2010, http://arxiv.org/abs/1005.3710

[152] "GEANT - Detector Description and Simulation Tool",

[153] http://wwwasd.web.cern.ch/wwwasd/geant/index.html C. Zeitnitz and T.A. Gabriel, "The GEANT-CALOR interface and benchmark calculations of ZEUS test calorimeters", NIM A 349 (1994) 106-111.

[154] C.J. Dale, P.W. Marshall, G.P. Summers, and E.A. Wolicki, E.A.Burke: "Displacement damage equivalent to dose in silicon devices", Appl. Phys. Lett. 54 (5), 30. Januar 1989

[155] A. Akkerman, J. Barak, M.B. Chadwick, J. Levison, M.Murat, Y. Lifshitz: "Updated NIEL calculations for estimating the damage induced by particles and γ-rays in Si and GaAs", Radiation Physics and Chemistry 62 (2001) 301-310

[156] C. Dritsa, "Feasibility study of charmed meson detection in the CBM experiment planned at the future FAIR facility", Master Thesis, IPHC 2006

[157] M.Deveaux et al., "Random Telegraph Signal in Monolithic Active Pixel Sensors", Nuclear Science Symposium Conference Record, 2008. NSS 08. IEEE, p 3098-3105 and references therein

[158] M Deveaux et al, "Radiation tolerance of a column parallel CMOS sensor with high resistivity epitaxial layer" 2011 JINST 6 C02004 doi: 10.1088/1748-0221/6/02/C02004

[159] P.Koczon, "Knock on electrons at CBM" talk given at the CBM Collaboration Meeting March 9-12, 2005, GSI, Darmstadt.

[160] I. Kisel, personal communication.

[161] A. Andronic, personal communication.

[162] S.Seddiki,"MVD DAQ prototype", talk given in the 15^{th} CBM collaboration meeting, Darmstadt, April 2010

[163] A.Kotynia et al. "CBM Progress Report 2010", Darmstadt 2010, p.8. and references therein.

[164] C.Trageser, talk given on the 17th CBM Collaboration Meeting and Symposium on Charm, Dileptons and Deconfinement, 4-8 April 2011, "Investigation of Tracking Efficiencies for different MVD geometries"

[165] Mark G. Alford et al. "Color superconductivity in dense quark matter", arXiv:0709.4635v2

[166] I.Vassiliev, private communication

[167] S.Seddiki, private communication